

Universidade Federal do Rio de Janeiro
Centro de Ciências Matemáticas e da Natureza
Observatório do Valongo

Multiwavelength Study of Galaxy Groups in the Boötes Region

Ph. D. Thesis

Bruna Vajgel

Advisor: Dr. Paulo A. A. Lopes (OV/UFRJ)

Dr. Christine Jones (CfA)

Rio de Janeiro - Agosto 2014



Universidade Federal do Rio de Janeiro
Centro de Ciências Matemáticas e da Natureza
Observatório do Valongo

Multiwavelength Study of Galaxy Groups in the Boötes Region

Bruna Vajgel

Advisor: Dr. Paulo A. A. Lopes

Dr. Christine Jones

Presented as a requisite to obtain the Ph. D. title in astronomy

Vajgel, Bruna

V133m Multiwavelength Study of Galaxy Groups in the Boötes Region

Bruna Vajgel . – Rio de Janeiro: UFRJ/OV, 2014

206 f.

Orientador: Paulo A. A. Lopes.

Co-orientadores: Christine Jones

Tese (doutorado) - Universidade Federal do Rio de Janeiro, Observatorio do Valongo, Programa de Ps-graduao em Astronomia, 2014.

1.Galaxy Groups 2.Galaxy Populations 3.X-ray Survey

4. Optical Surveys 5. Scaling Relations

I. Lopes, Paulo A. A., II. Jones, C., coorient.

III. Ttulo.

“As estrelas são todas iluminadas ...
Não será para que cada um possa
um dia encontrar a sua?”
(Antoine de Saint-Exupery)

Acknowledgments

Numa longa jornada, muitas pessoas cruzam o nosso caminho. Umam passam e outras ficam. Mas todas nos deixam uma contribuição, todas têm algo a nos ensinar. E com elas eu aprendi. E a elas eu tenho muito a agradecer.

À minha mãe, meu pai, minha madrinha, meu irmão e meu padrasto, meus grandes pilares, minha grande fonte de inspiração e meu grande orgulho. Obrigada pela paciência, pela compreensão, pela dedicação e, em especial, pelos pequenos gestos de atenção. Foram eles que por diversas vezes fizeram o meu dia valer a pena. Sei o quão difícil pode ser conseguir um sorriso meu.

Quando eu digo que não teria conseguido sem você não é nenhum exagero. Se hoje não existem caquinhos meus espalhados por toda a cidade é porque você os recolheu e os colocou de volta. À minha querida amiga Letícia, minha grande companheira de doutorado, não só toda a minha gratidão mas também a minha total admiração.

Obrigada às minhas grandes, queridas, melhores (poderia passar horas tecendo elogios as duas) amigas, Bárbara e Ana Clara. Aquelas que eu sempre carrego no meu coração para todo lugar que eu vou.

A meu grande amigo Lucas, meu anjo da guarda na informática. Essa tese nunca teria chegado ao fim sem você. Desculpa por te ligar nas horas mais inconvenientes pra dizer que meu computador quebrou...

Um obrigada especial as queridas Raquel, Carol e Raquel. Obrigada pelas risadas, pelas fofocas, pela diversão. Vocês tornaram meus dias mais leve.

Agradeço, em especial, ao meu orientador Paulo Lopes, pelas oportunidades de trabalho e por toda sua contribuição na minha formação profissional.

I would like to thank Christine and Bill. I am really glad for the opportunity that was given to me. It was amazing to work with you

Agardeço também ao Felipe, um grande amigo que eu fiz em Boston.

Abstract

In this Ph.D. thesis, we report a comparative study between the nature of galaxy groups and clusters, to understand the similarities and the differences between those two types of systems. We present two galaxy group samples in the Boötes region: one X-ray selected based on the extended source catalog from the X-Boötes Survey (XBS); and one optically selected using the optical spectroscopic data from AGES (OBS). Group redshifts are measured from the AGES spectroscopic data. We use photometric data from the NOAO Deep Wide Field Survey (NDWFS) to estimate the group richness (N_{gals}) and the optical luminosity (L_{opt}). We estimate also velocity dispersions (σ_{gr}) and perform a virial analysis to obtain the radii (R_{200} and R_{500}) and total masses (M_{200} and M_{500}) for groups with at least five galaxy members at $z \leq 0.35$. After deriving the X-ray luminosity (L_X), we find a subsample in the optically selected catalog of X-ray non-detected and upper limit groups. The absence of X-ray emission, which is a tracer of the hot intra-group gas, may be an indication of the evolutionary stage of these systems. To investigate the nature of the X-ray non-detected and upper limit groups, we compare their properties with the selected groups with X-ray reliable emission. We also examine the performance of the group properties σ_{gr} , L_{opt} and L_X , as proxies for the group mass. Understanding how well these observables measure the total mass is important to estimate how precisely the cluster/group mass function is determined. Exploring the scaling relations built with the Boötes samples and comparing these with samples from the literature, we find a break in the L_X - M_{500} relation at approximately $M_{500} = 5 \times 10^{13} M_{\odot}$ (for $M_{500} > 5 \times 10^{13} M_{\odot}$, $M_{500} \propto L_X^{0.61 \pm 0.02}$, while for $M_{500} \leq 5 \times 10^{13} M_{\odot}$, $M_{500} \propto L_X^{0.44 \pm 0.05}$). Thus, the mass-luminosity relation for galaxy groups cannot be described by the same power law as galaxy clusters. A possible explanation for this break is the dynamical friction, tidal interactions and projection effects which reduce the velocity dispersion values of the galaxy groups. By extending the cluster luminosity function to the group regime, we predict the number of groups that new X-ray surveys, particularly eROSITA, will detect. Based on our cluster/group luminosity function estimates, eROSITA will identify ~ 1800 groups ($L_X = 10^{41} - 10^{43} \text{ ergs s}^{-1}$) within a distance of 200 Mpc. Since groups lie in large scale filaments, this group sample will map the large scale structure of the local universe.

Resumo

Nessa tese de doutorado, apresentaremos um estudo comparativo entre a natureza dos grupos e aglomerados de galáxias, a fim de entender as semelhanças e diferenças entre estes dois sistemas. Foram construídos dois catálogos de grupos na região de Boötes: um selecionado em raio-X com base no catálogo de fontes extensas do *X-Boötes Survey* (XBS); o segundo selecionado no óptico utilizando dados espectroscópicos do AGES (OBS). Também com os dados do AGES, medimos o *redshift* de todos grupos. Utilizando os dados do *NOAO Deep Wide Field Survey*, estimamos a riqueza (N_{gals}) e a luminosidade óptica (L_{opt}). Após derivadas as dispersões de velocidades (σ_{gr}), realizamos uma análise do virial para obter os raios (R_{200} e R_{500}) e a massas totais (M_{200} and M_{500}) para grupos com pelo menos 5 membros e em $z \leq 0.35$. Ao determinarmos as luminosidades em raio-X (L_X), encontramos uma sub-amostra de grupos selecionados no óptico que não possui emissão em raio-X ou possui uma emissão muito próxima do limite da emissão de fundo. A ausência ou baixa emissão em raio-X, que é um traçador do gás quente intra grupo, pode ser um indicativo do estágio evolutivo desses sistemas. A fim de investigar a natureza desses grupos com baixa ou nenhuma emissão em raio-X, comparamos suas propriedades com os demais grupos da amostra com emissão normal em raio-X. Também examinamos o desempenho das propriedades dos grupos (σ_{gr} , L_{opt} e L_X) como calibradores de massa. Entender o quão bem esses observáveis medem a massa total dos sistemas é importante para se estimar o quão precisa a função de massa de grupos/aglomerados é determinada. Explorando as relações de escala construídas com as amostras na região de Boötes e as comparando-as com amostras de aglomerados de galáxias da literatura, encontramos uma quebra na relação L_X - M_{500} em aproximadamente $M_{500} = 5 \times 10^{13} M_{\odot}$ (para $M_{500} > 5 \times 10^{13} M_{\odot}$, $M_{500} \propto L_X^{0.61 \pm 0.02}$, enquanto para $M_{500} \leq 5 \times 10^{13} M_{\odot}$, $M_{500} \propto L_X^{0.44 \pm 0.05}$). Logo, a relação massa-luminosidade de grupos não pode ser descrita pelas mesmas leis de potência que descrevem os aglomerados de galáxias. Uma possível explicação para a quebra são os processos de fricção dinâmica, interações de maré e efeitos de projeção, que podem provocar a redução das dispersões de velocidade em grupos de galáxias. Estendendo a função de luminosidade até o regime de grupos, realizamos previsões sobre o número de sistemas de baixa massa que novos levantamentos de dados, em particular o eROSITA, irão

detectar. Baseado nas estimativas da função de luminosidade de grupos e aglomerados, o eROSITA irá identificar ~ 1800 grupos ($L_X = 10^{41} - 10^{43}$ ergs s $^{-1}$) dentro de uma distância de 200 Mpc. Como grupos residem nos filamentos em larga escala, esta amostra de grupos observada pelo eROSITA irá mapear a estrutura em larga escala do universo local.

Contents

1	Introduction	1
1.1	X-ray Emission Mechanisms	3
1.2	Galaxy Population in Galaxy Groups	6
1.3	Scaling Relations	8
1.4	Aims and Outline of This Thesis	10
2	Group Samples	13
2.1	Data	13
2.1.1	NOAO Deep Wide Field Survey (NDWFS)	13
2.1.2	X-Boötes Survey	15
2.1.3	AGN and Galaxy Evolution Survey (AGES)	15
2.2	Samples	18
2.2.1	X-ray Selected Boötes Sample (XBS)	18
2.2.2	Optically Selected Boötes Sample (OBS)	25
3	Methodology	33
3.1	Virial Analysis	33
3.2	Optical Properties Determination	39
3.3	X-ray Properties Determination	42
4	Results	47
4.1	Comparison Between The Samples Selected In Optical and X-ray	47
4.2	Scaling Relations	57
4.2.1	Optically Selected Sample	57
4.2.2	X-ray Selected Sample	68

4.3 X-ray Luminosity Function	73
5 Discussion	81
6 Conclusions	85
Bibliography	87
Appendix	103
A X-ray Selected Galaxy Group Catalog - General Information	105
B Optically Selected Galaxy Group Catalog - General Information	109
C X-ray Selected Extended Source Catalog For $z \leq 0.35$	125
D Optically Selected Extended Source Catalog For $z \leq 0.35$	131
E X-ray Selected Galaxy Group Catalog - Optical and Dynamical Properties	155
F Optically Selected Galaxy Group Catalog - Optical and Dynamical Properties	159
G X-ray Selected Galaxy Group Catalog - X-ray Properties	167
H Optically Selected Galaxy Group Catalog - X-ray Properties	171

List of Figures

1.1	The Bullet Cluster	4
2.1	Transmission Filters from NDWFS	14
2.2	The X-Boötes Survey Mosaic	16
2.3	Examples of AGES Spectra of Galaxies	17
2.4	Point Source Examples	18
2.5	Extended Source Example	19
2.6	Redshift Distribution of the X-ray and Optically Selected Samples	21
2.7	The Voronoi Tessellation Applied to AGES	26
3.1	The Phase-space Diagram of Three X-ray Selected Groups	34
3.2	Distribution of N_{gals} , L_{opt} , L_{X} , σ_{gr} , R_{500} and M_{500}	38
3.3	Optical and X-ray Coordinates Offset Distribution for the OBS Groups	41
3.4	Surface Brightness Profile of XBS 06	41
4.1	Comparison of the Number of Members Distribution Between XBS and OBS Samples	49
4.2	Comparison of the X-ray Luminosity Distribution Between XBS and OBS Samples	50
4.3	Stacked Positions of the Galaxy Members	55
4.4	Stacked Phase-space Diagrams of the Galaxy Groups	56
4.5	OBS Optical Scaling Relations	59
4.6	OBS X-ray Scaling Relations	60
4.7	The X-ray Luminosity Residuals of the $L_{\text{X}}-M_{500}$ Relation	63
4.8	The Color-Magnitude Diagram of the OBS and XBS Groups	64
4.9	The Fraction of Blue Galaxies Inside the Groups	65

4.10	XBS Optical Scaling Relations	69
4.11	XBS X-ray Scaling Relations	70
4.12	Log N -Log S Relation	75
4.13	X-ray Luminosity Function of Galaxy Groups and Clusters	76
C.1	X-ray Selected Extended Source Catalog	126
C.2	Continuation of Figure C.1	127
C.3	Continuation of Figure C.1	128
C.4	Continuation of Figure C.1	129
C.5	Continuation of Figure C.1	130
D.1	Optically Selected Extended Source Catalog	132
D.2	Continuation of Figure D.1	133
D.3	Continuation of Figure D.1	134
D.4	Continuation of Figure D.1	135
D.5	Continuation of Figure D.1	136
D.6	Continuation of Figure D.1	137
D.7	Continuation of Figure D.1	138
D.8	Continuation of Figure D.1	139
D.9	Continuation of Figure D.1	140
D.10	Continuation of Figure D.1	141
D.11	Continuation of Figure D.1	142
D.12	Continuation of Figure D.1	143
D.13	Continuation of Figure D.1	144
D.14	Continuation of Figure D.1	145
D.15	Continuation of Figure D.1	146
D.16	Continuation of Figure D.1	147
D.17	Continuation of Figure D.1	148
D.18	Continuation of Figure D.1	149
D.19	Continuation of Figure D.1	150
D.20	Continuation of Figure D.1	151
D.21	Continuation of Figure D.1	152
D.22	Continuation of Figure D.1	153

D.23 Continuation of Figure D.1 154

List of Tables

1.1	X-ray and optical scaling relations predicted by the self-similar model . . .	9
2.1	Information of the Brightest Galaxy of the Group of the X-ray Selected Sample	24
2.1	Information of the Brightest Galaxy of the Group of the X-ray Selected Sample	25
2.2	Information of the Brightest Galaxy of the Group of the Optically Selected Sample	30
2.2	Information of the Brightest Galaxy of the Group of the Optically Selected Sample	31
2.2	Information of the Brightest Galaxy of the Group of the Optically Selected Sample	32
4.1	Scaling Relations of Luminosity, Velocity Dispersion and Mass of the OBS Groups	67
4.2	Scaling Relations of Luminosity, Velocity Dispersion and Mass of the XBS Groups	74
4.3	Expected Number of Groups Between $L_X^{\min} < L_X < L_X^{\max}$ Inside a Volume ($z_{\min} < z < z_{\max}$)	76
A.1	Information of position, redshift, and exposure for the 32 galaxy groups selected with the X-Boötes Survey.	106
A.1	Information of position, redshift, and exposure for the 32 galaxy groups selected with the X-Boötes Survey.	107
A.1	Information of position, redshift, and exposure for the 32 galaxy groups selected with the X-Boötes Survey.	108

B.1	Information of position, redshift, and exposure for the 162 galaxy groups selected with the AGES data.	110
B.1	Information of position, redshift, and exposure for the 162 galaxy groups selected with the AGES data.	111
B.1	Information of position, redshift, and exposure for the 162 galaxy groups selected with the AGES data.	112
B.1	Information of position, redshift, and exposure for the 162 galaxy groups selected with the AGES data.	113
B.1	Information of position, redshift, and exposure for the 162 galaxy groups selected with the AGES data.	114
B.1	Information of position, redshift, and exposure for the 162 galaxy groups selected with the AGES data.	115
B.1	Information of position, redshift, and exposure for the 162 galaxy groups selected with the AGES data.	116
B.1	Information of position, redshift, and exposure for the 162 galaxy groups selected with the AGES data.	117
B.1	Information of position, redshift, and exposure for the 162 galaxy groups selected with the AGES data.	118
B.1	Information of position, redshift, and exposure for the 162 galaxy groups selected with the AGES data.	119
B.1	Information of position, redshift, and exposure for the 162 galaxy groups selected with the AGES data.	120
B.1	Information of position, redshift, and exposure for the 162 galaxy groups selected with the AGES data.	121
B.1	Information of position, redshift, and exposure for the 162 galaxy groups selected with the AGES data.	122
B.1	Information of position, redshift, and exposure for the 162 galaxy groups selected with the AGES data.	123
E.1	Dynamical and Optical Properties For The 14 X-ray Selected Groups with $z \leq 0.35$ and at least 5 Galaxy Members	156

E.1	Dynamical and Optical Properties For The 14 X-ray Selected Groups with $z \leq 0.35$ and at least 5 Galaxy Members	157
F.1	Dynamical and Optical Properties For The 67 Optically Selected Groups with $z \leq 0.35$ and at least 5 Galaxy Members	160
F.1	Dynamical and Optical Properties For The 67 Optically Selected Groups with $z \leq 0.35$ and at least 5 Galaxy Members	161
F.1	Dynamical and Optical Properties For The 67 Optically Selected Groups with $z \leq 0.35$ and at least 5 Galaxy Members	162
F.1	Dynamical and Optical Properties For The 67 Optically Selected Groups with $z \leq 0.35$ and at least 5 Galaxy Members	163
F.1	Dynamical and Optical Properties For The 67 Optically Selected Groups with $z \leq 0.35$ and at least 5 Galaxy Members	164
F.1	Dynamical and Optical Properties For The 67 Optically Selected Groups with $z \leq 0.35$ and at least 5 Galaxy Members	165
G.1	X-ray Properties Inside 0.5 Mpc	168
G.1	X-ray Properties Inside 0.5 Mpc	169
H.1	X-ray Properties Inside 0.5 Mpc	172
H.1	X-ray Properties Inside 0.5 Mpc	173
H.1	X-ray Properties Inside 0.5 Mpc	174
H.1	X-ray Properties Inside 0.5 Mpc	175
H.1	X-ray Properties Inside 0.5 Mpc	176
H.1	X-ray Properties Inside 0.5 Mpc	177
H.1	X-ray Properties Inside 0.5 Mpc	178
H.1	X-ray Properties Inside 0.5 Mpc	179
H.1	X-ray Properties Inside 0.5 Mpc	180
H.1	X-ray Properties Inside 0.5 Mpc	181
H.1	X-ray Properties Inside 0.5 Mpc	182

Chapter 1

Introduction

Galaxies are not uniformly distributed in space. On the contrary, they show a tendency to gather together in galaxy groups and clusters. The Milky Way, for instance, is a member of a group, known as the Local Group. It is because of the tendency of galaxies to gather that clusters of galaxies were first identified as large concentrations in the projected galaxy distribution containing dozens to thousands of galaxies, clustering over a small area on the sky (Abell, 1958; Zwicky and Humason, 1961; Abell et al., 1989). Although the galaxies determine the optical appearance of a cluster, only a small fraction of the total cluster mass is contained in the stellar form.

The existence of a hot X-ray emitting gas located in between the galaxies was just discovered after the X-ray astronomy advances. The extended X-ray emission of the intracluster medium (ICM) was observed for the first time in the Coma cluster (Felten et al., 1966; Meekins et al., 1971; Gursky et al., 1971; Cavaliere et al., 1971; Forman et al., 1972; Kellogg et al., 1972). This intergalactic gas contains up to five times more baryons than the stars from the galaxy members. From the dynamics of galaxies (Zwicky, 1933, 1937), from the properties of the X-ray emission of clusters (Felten et al., 1966) and from the gravitational lens effect (Schneider, 2006), the existence of the dark matter in galaxy clusters was deduced. The mass content of galaxy clusters consists of dark matter ($\sim 85\%$), hot thermal intracluster gas ($\sim 12\%$) and galaxies ($\sim 3\%$).

According to the hierarchical model of structure formation, galaxy clusters are the largest virialized gravitationally bound systems. They are formed essentially by gravitational collapse and many have had time to reach their dynamical equilibrium (virial

equilibrium). These are recent structures which appeared only in a relatively late epoch in the cosmic history. The precise redshift that clusters started to collapse is not yet precisely determined (Boehringer et al., 2006).

In the local universe, galaxy clusters are known for having: (i) the majority of their galaxy population in the red sequence; (ii) a diffuse stellar emission; (iii) a hot intracluster medium (ICM) emitting in the X-ray; and (iv) a virialized dark matter halo. Because of their composition, these systems are excellent astrophysical laboratories to investigate the galaxy evolution in dense environments (Dressler, 1980; Goto et al., 2003, e.g.), the evolution of the thermal and dynamical structure (Balestra et al., 2007; Maughan et al., 2008; Anderson et al., 2009, e.g.), the chemical enrichment of the ICM (Cora, 2006; Heath et al., 2007, e.g.), the background galaxies at high redshift using gravitational lenses (Metcalf et al., 2003; Santos et al., 2004; Bartelmann, 2010, e.g.) and the evolution of the Universe testing the cosmological models (Rosati et al., 2002; Böhringer et al., 2002; Voit, 2005; Vikhlinin et al., 2009; Allen et al., 2011, e.g.).

Galaxy groups have lower masses, lower velocity dispersions, lower luminosities, and smaller extents than galaxy clusters. However, galaxy groups are not simply scaled down versions of rich clusters (e.g. Mulchaey (2000); Ponman (2003); Voit (2005)). Due to a group's shallow gravitational potential, feedback processes (e.g., galactic winds and AGN feedback) play an important role in the group's evolution. Feedback processes also can change the global properties and increase systematically the intrinsic scatter in their relations. Because the evolution of galaxy groups is not a simple product of gravitational mechanisms, it is complex to reproduce it in simulations and thus necessary to check the results with observations.

The matter composition in groups may also be altered by feedback processes. While, in clusters, the cluster baryonic mass is strongly dominated by the hot gas, in groups the mass of the galaxy members can exceed the gas mass (Giodini et al., 2009). When this occurs, the characteristic properties of the gas, including X-ray luminosity (L_X), X-ray temperature (T_X) and gas mass fraction (f_g), will be lower compared to the dynamical properties, including velocity dispersion (σ) and total mass (M_{Tot}). A direct consequence of this is the break in the scaling relations between galaxy clusters and galaxy groups (Davé et al., 2008; Pope, 2009; Mittal et al., 2011).

From the galaxy formation and evolution perspective, the low velocity dispersions in

galaxy groups result in frequent strong interactions between galaxies, like tidal disruption and mergers (Proctor et al., 2011). Therefore, groups provide an important test for models of galaxy formation and evolution. Consequently, there is an ongoing effort to identify and characterize groups in both the local universe and at higher redshifts (Hilton et al., 2010; Strazzullo et al., 2010; Bauer et al., 2011).

A special class of groups, first identified by Ponman et al. (1994), are the so called fossil groups. These are defined by Jones et al. (2003) as X-ray luminous structures ($L_X > 5 \times 10^{42} h^{-2} \text{ ergs s}^{-1}$) with a gap between the brightest and second brightest galaxies (Δm_{12}) greater than 2 magnitudes within half the virial radius. Fossil groups are therefore dominated by a massive central early-type galaxy surrounded by much smaller and fainter galaxies and enclosed in a hot X-ray halo. The most commonly-quoted scenario to explain the nature of such systems is that fossil groups are ancient systems, resulting of a significant galaxy merger/accretion activity, leading any large galaxies close to the central regions of the group to spiral inwards, ultimately to merge with the central galaxy (D’Onghia et al., 2005; Dariush et al., 2007; Proctor et al., 2011). If all groups will have the same fate of fossil groups, is not clear yet.

As mentioned above, the astrophysical studies of galaxy clusters and groups are too broad, therefore I will highlight the topics that are relevant to this thesis work. In Section 1.1, the main mechanisms responsible for the X-ray emission in groups are presented. In Section 1.2, information about the galaxy population of groups is provided. A comparison is also made between the populations observed in low and high mass systems. In Section 1.3, the correlations between the group’s observables and the mass are introduced. The motivations for why it is so important to have well calibrated observable-mass proxies are also listed. Finally, in Section 1.4 the aims and an outline of the thesis are listed.

1.1 X-ray Emission Mechanisms

One of the most important discoveries of the UHURU X-ray satellite was the detection of X-ray radiation from massive galaxy clusters. With the later Einstein and ROSAT X-ray satellites and more recently XMM-Newton and Chandra X-ray Observatory, X-ray emission was also detected from lower mass clusters and groups. Figure 1.1 shows an example of one of the most famous cluster observed with Chandra, the Bullet Cluster.

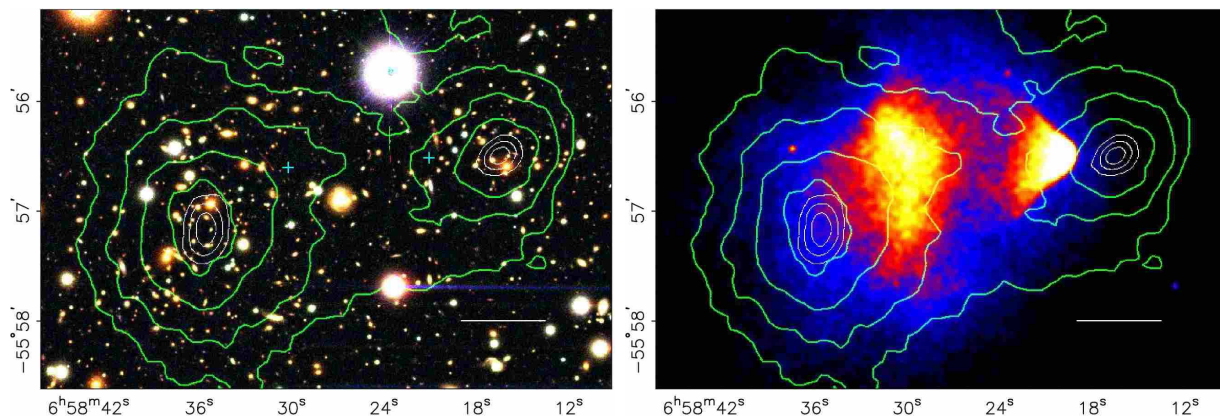


Figure 1.1 The left panel is a color image from the Magellan images of the merging cluster 1E0657–558, popularly known as “the Bullet Cluster”. The white bar indicates the 200 kpc distance from the cluster. In the right panel is a 500 ks Chandra image of the cluster. Shown in green contours in both panels are the weak lensing. This figure was taken from Clowe et al. (2006).

Galaxy clusters are X-ray sources because the galaxy formation is inefficient. Only about one tenth of the baryonic matter in the universe resides in stars, whereas the vast majority populates the intergalactic space. Most of these intergalactic baryons are extremely difficult to observe, but thanks to the compression exerted by the deep potential wells of clusters, the baryonic gas in the intracluster medium is heated to X-ray emitting temperatures ($kT \gtrsim 2$ keV). The gas temperature inferred from a cluster’s X-ray spectrum therefore indicates the depth of a cluster’s potential well (Voit, 2005).

The spectral energy distribution of the X-rays leads to the conclusion that the process responsible for the emission is the thermal bremsstrahlung (free-free radiation) from the hot gas (Felten et al., 1966). The radiation is produced by the acceleration of free electrons in the Coulomb field of protons and atomic nuclei. When an electrically charged particle is accelerated by a heavier nuclei, it emits a photon. From the properties of these emitted photons in the ICM, it is possible to infer the gas temperature of the galaxy clusters. For a cluster with mass typically between $10^{14} - 10^{15} M_{\odot}$, the temperature of the intracluster gas lies in the range of about 1-10 keV.

As mentioned above, the X-ray radiation is tightly connected to the cluster’s potential well. To draw any conclusion about the properties of the ICM from the observed X-ray

radiation and about the cluster’s mass distribution, the gas needs to be modeled. The most commonly used method to fit the X-ray surface brightness data is the β -model fitting (Cavaliere and Fusco-Femiano, 1976). This model is based on the assumption that the total mass density profile is described by an isothermal distribution. The mass profile of a cluster can be derived by a King model (King, 1962), which describes the gas density profile:

$$\rho_g(r) = \rho_{g0} \left[1 + \left(\frac{r}{r_c} \right)^2 \right]^{-3\beta/2}, \quad (1.1)$$

where ρ_{g0} is the central gas density and r_c is the core radius. The brightness profile of the X-ray emission in the β -model is, then,

$$I(R) \propto \left[1 + \left(\frac{R}{r_c} \right)^2 \right]^{-3\beta+1/2}. \quad (1.2)$$

The cluster’s X-ray emission has typically r_c between $0.1-0.3h^{-1}$ Mpc and $\beta \approx 0.65$. The β -model provides a good approximation of the X-ray surface profile, although the X-ray temperature is not constant over all cluster’s radii. Chandra and XMM-Newton observations have revealed that the gas is not really isothermal (Jones and Forman, 1984; Vikhlinin et al., 1999). Typically, the temperature decreases towards the cluster center and the outer edge ($r \gg R_c$), while it remains constant over a large range at the intermediate radii.

X-ray observations have shown the presence of diffuse X-ray emission in many groups too, but the existence of a hot luminous intra-group medium (IGM) appears to be linked to the presence of early-type galaxies (Mulchaey et al., 2006). The X-ray luminous groups are sometimes described as miniature galaxy clusters; their IGM is highly enriched, particularly in the group core; they host significant early-type galaxy populations and are often dominated by a single, centrally-located giant elliptical (Helsdon and Ponman, 2003).

On the other hand, spiral-rich groups are typically poor in hot gas, and consequently X-ray faint. Mulchaey et al. (2003) have found that spiral-rich groups tend to be less X-ray luminous than the elliptical-dominated ones, and have detected none of the twelve spiral-only groups in their ROSAT atlas of 109 systems. Osmond and Ponman (2004) have detected only galaxy-scale emission in the ten spiral-only groups in the GEMS sample.

Several studies have investigated the X-ray properties of compact groups and the diffuse hot gas in these systems (Helsdon et al., 2001; Desjardins et al., 2013; Fuse and Broming,

2013). The authors made the effort to mask the soft X-ray emission from the galaxies and reported that the remaining emission seems to be clumpy, suggesting that in contrast to clusters, the hot gas is not in equilibrium yet.

Examination of the X-ray faint, spiral-rich compact groups has suggested an evolutionary sequence, with galaxy interactions stripping the HI from spiral galaxies to form intergalactic clouds and filaments or even a diffuse cold IGM (Verdes-Montenegro et al., 2001; Johnson et al., 2007; Konstantopoulos et al., 2010). Using a combination of deep Chandra X-ray observations and radio continuum imaging to investigate the origin and current state of the IGM in the spiral-rich compact group HCG 16, O’Sullivan et al. (2014) have confirmed the presence of a faint, low temperature ($T_X = 0.30_{-0.05}^{+0.07}$ keV) intra-group medium extending throughout the ACIS-S3 field of view, with a ridge linking the four original group members. This ridge contains $6.6_{-3.3}^{+3.9} \times 10^9 M_\odot$ of hot gas and is at least partly coincident with a large-scale HI tidal filament, indicating that the IGM in the inner part of the group is highly multi-phase. They have presented evidence that the group is not yet virialized, and show that gas has probably been transported from the starburst winds of NGC 838 and NGC 839 into the surrounding IGM. Considering the possible origin of the IGM, O’Sullivan et al. (2014) have argued that material ejected by galactic winds may have played a significant role, contributing 20-40% of the observed hot gas in the system.

1.2 Galaxy Population in Galaxy Groups

The multi-component structure of galaxy clusters offers the possibility to observe these systems across the whole electromagnetic spectrum (Sarazin and White, 1988; Allen et al., 2011). In particular, the optical and near infrared (NIR) emission of galaxy clusters is dominated by starlight from galaxies. As showed by Eke et al. (2004), the majority of galaxies in the local Universe reside in small gravitationally bound groups, whose low velocity dispersion ($\lesssim 500 \text{ km s}^{-1}$) and small galaxy separations are conducive to tidal interactions and mergers between galaxy members. This means that the group environment can play an important role in the evolution of galaxies.

Tracing the properties of galaxies versus both the local environment of the surrounding galaxies and the global group/cluster environment has important implications for understanding the processes responsible for driving both the morphological transformation of

galaxies and the reduction or even the complete quenching of star formation in dense environments. In the lower density environment of groups, processes like ram pressure stripping (Gunn and Gott, 1972) are expected to be less relevant, while other processes such as galaxy-galaxy interactions and mergers are more effective (Miles et al., 2004; Taylor and Babul, 2005; Tempurin and Fritze-von Alvensleben, 2006).

Examining the morphological make-up of X-ray-bright groups, Helsdon and Ponman (2003) have shown that the brighter galaxies in these groups exhibit clear morphology-density and morphology-radius relations (Dressler, 1980; Dressler et al., 1997; Smith et al., 2005, e.g.). The group morphology-density relation is offset from the cluster relation in the sense that at a given surface density, X-ray-bright groups have a lower spiral fraction. They argue that considering a simple model to correct the group data for the effects of projection and for the expected higher merging rate in groups, that one can bring the morphology-density relation for groups into good agreement with that of clusters, suggesting that the relation may be driven by two-body interactions. The fraction of S0 galaxies in these X-ray-bright groups is at least as high as that observed in nearby clusters.

Studies of optically selected galaxy groups at low redshift have revealed them to have a heterogeneous population, varying from cluster-like to field-like galaxy populations (Zabludoff and Mulchaey, 1998). Groups showing luminous extended X-ray emission tend to have a significant fraction of early-type galaxies and a dominant early-type galaxy at the group center (Mulchaey and Zabludoff, 1998; Mulchaey et al., 2003; Osmond and Ponman, 2004).

Studying galaxy morphologies and star formation in low-luminosity clusters at $z \sim 0.25$, Balogh et al. (2002a,b) found that the galaxy populations in these systems are similar to those in massive clusters at the same redshift. On the other hand, in an investigation comparing groups optically selected at $0.3 < z \leq 0.55$ with low redshift groups, Wilman et al. (2005b,a) found that the fraction of star-forming galaxies increases with redshift in both groups and the field, but that this fraction is always lower in groups at a given epoch.

Mulchaey et al. (2006) presented the spectroscopic confirmation of a sample of nine moderate-redshift groups ($z \sim 0.23 - 0.59$) based on optical observations. Based on the initial group membership, these groups were found to have a significant fraction of early-type galaxies similar to X-ray emitting groups at low redshift. However, unlike low-redshift groups, a central, dominant early-type galaxy was not found in $\sim 40\%$ of these systems. In addition, three of the four central galaxies were found to have multiple components.

These observations suggest that X-ray emitting groups at intermediate redshift may be in an earlier phase of evolution where the central galaxy has not yet undergone its last major merger.

As it is possible to notice, the galaxy group nature is very heterogeneous. This may be a result of the large range of masses and densities represented among groups, the differences in their evolutionary stages or a bias in the sample selection techniques. Because of the low galaxy densities, groups are difficult systems to detect. That is why studies of representative samples of groups are just beginning. However to fully understand the complex nature of groups and the galaxy evolution, it is mandatory to have larger well defined group samples covering a large range of redshift.

As postulated by Zabludoff and Mulchaey (1998), if clusters evolve hierarchically by accreting poor galaxy groups, members of an infalling group may have recently experienced the hot, dense cluster environment for the first time. Therefore, galaxies in poor groups and in the field are a control sample for understanding the factors that influence the evolution of their counterparts in subclusters.

1.3 Scaling Relations

Clusters of galaxies constitute the largest gravitationally collapsed structures in the Universe, according to the hierarchical model. Hence, clusters have been widely used to constrain cosmological models (Bahcall et al., 1997; Evrard, 1989; Viana and Liddle, 1996; Carlberg et al., 1997; Vikhlinin et al., 2009). But in order to use them as cosmological tracers, it is necessary to measure their mass distribution which is the main difficulty encountered in these studies. A variety of techniques has been used today, but accurate mass estimates for large data sets are still impractical, since they are too expensive in terms of observations.

Total mass is the most important property of the galaxy clusters, but it cannot be directly measured. A simple way to estimate it for a large sample of clusters is to find an unbiased observable proxy such as X-ray luminosity, richness, X-ray temperature, optical luminosity or velocity dispersion. Establishing and calibrating such mass-observable relations are essential for determining the cluster mass function (Lopes et al., 2009b).

If clusters are formed through the gravitational collapse of homogeneous spherical overdensities of non-interacting dark matter, it is expected that the collapse process and the

Table 1.1. X-ray and optical scaling relations predicted by the self-similar model

Relation	Self-Similar Correlation
$L_{\text{opt}}\text{-M}$	$M \propto L_{\text{opt}}$
$\sigma\text{-M}$	$M \propto \sigma^3$
$L_X\text{-}\sigma$	$\sigma \propto L_X^{1/4}$
$L_X\text{-M}$	$M \propto L_X^{4/3}$
$L_X\text{-}T_X$	$T_X \propto L_X^{1/2}$

produced dark matter halo will be self-similar (Kaiser 1986). So, if a cluster is a self-similar system, its properties are expected to follow predicted relations, which are known as scaling relations. Some expected relations according to the self-similar model are displayed in Table 1.1.

A direct consequence of the self-similar model is that the lower mass systems are scaled down versions of higher mass systems. However, some works (Davé et al., 2008; Pope, 2009; Mittal et al., 2011) have reported a break in the scaling relations of galaxy clusters and galaxy groups

Scaling relations for clusters and groups, including X-ray luminosity vs. mass, X-ray luminosity vs. velocity dispersion and X-ray luminosity vs. temperature, have been investigated extensively (Finoguenov et al., 2001; Reiprich and Böhringer, 2002; Popesso et al., 2006; Rykoff et al., 2008; Lopes et al., 2009b; Vikhlinin et al., 2009; Ettori et al., 2010; Leauthaud et al., 2010). However the question of whether the relations determined for clusters also hold true for poor clusters and groups still remains unsettled.

Some studies do not support a break in the scaling relations between groups and clusters, but instead find consistent results for the whole observed mass range, although often with larger scatter for groups for the $L_X\text{-}\sigma$, $L_X\text{-}T$, $M\text{-}T$, $\sigma\text{-}T$ and $M\text{-}Y_X$ relations (e.g. Mulchaey and Zabludoff (1998); Osmond and Ponman (2004); Sun et al. (2009); Eckmiller et al. (2011)).

However, other evidence supports a break in the scaling relations at the low end of the group/cluster mass range, possibly caused by the strong influence of non-gravitational

physics on low-mass groups. In studies of poor systems, Mahdavi et al. (2000) and Xue and Wu (2000) found, respectively, $L_X \propto \sigma^{1.38 \pm 0.4}$ and $L_X \propto \sigma^{2.35 \pm 0.21}$, flatter than what they found for clusters, $L_X \propto \sigma^{5.37 \pm 0.5}$ and $L_X \propto \sigma^{5.30 \pm 0.21}$, respectively. Helsdon and Ponman (2000) ($L_X \propto \sigma^{2.4 \pm 0.4}$) and Osmond and Ponman (2004) ($L_X \propto \sigma^{2.31 \pm 0.62}$) also found significantly flatter relations in groups. For groups, Finoguenov et al. (2001) reported a steeper $M-T$ slope than for clusters. Maughan et al. (2012) found an observed steepening in the L_X-T_X relation for relaxed systems below 3.5 keV and argued it is caused by central heating that affects the intracluster medium (ICM) to larger radii in lower-mass systems.

For the next generation of surveys like eROSITA (Predehl et al., 2010) that will detect up to a hundred thousands of clusters and groups, it is essential to use reliable mass-observable proxies to estimate the total mass of the detected systems.

1.4 Aims and Outline of This Thesis

There has been considerable interest in how the X-ray and optical properties of groups differ from those of rich clusters. Such comparisons are often limited by poorly determined group properties. Most optical properties of groups are determined from existing redshift surveys. Generally, these surveys are X-ray flux limited and reach only to low redshifts. So, they typically include only the most luminous group members at moderate to high redshifts. As a consequence, properties like velocity dispersion and virial radius are underestimated. Measuring the properties of the hot intragroup gas is also challenging. Galaxy groups have lower X-ray fluxes, lower gas density contrasts and a not-well defined emission extents in which further complicates the determination of the X-ray properties. Despite that, comparisons between groups and clusters are very important to provide some insights about the nature of galaxy groups.

In this Ph.D. thesis, our main goal is to study the nature of galaxy groups in comparison with clusters and thus to better understand the similarities and the difference between those two types of systems. We construct two catalogs: one X-ray selected based in the extended source catalog from the X-Boötes Survey (Kenter et al., 2005); and one optically selected using the optical spectroscopic data from AGES (Kochanek et al., 2012). The two selected samples allow us to investigate the differences between two sets of galaxy groups, depending on their selection technique; to trace the optical and X-ray scaling relations,

testing the existence of a break between the low and high mass regime and the existence of the X-ray underluminous systems; and to determine the X-ray luminosity function. All the analysis and information concerned to the X-ray selected sample is already in the form of an published paper in the *Astrophysical Journal* (Vajgel et al., 2014). The work related to the optically selected sample will be submitted for publication in the near future.

This Thesis is organized as follows: in Chapter 2 we present the observations and the two samples, describing the two selection techniques used and the redshift estimation method. In Chapter 3 we explain the methods to estimate the group's velocity dispersion (σ_{gr}), virial radius (R_{500}), mass (M_{500}), optical luminosity (L_{opt}), richness (N_{gals}), X-ray luminosity (L_{X}) and temperature (T_{X}). Chapter 4 is divided into three sections: (i) in the first section we compare the optically and X-ray selected samples; (ii) in the second section we discuss the optical and X-ray scaling-relations; (iii) in the third section we estimate the X-ray luminosity function and, based on this, we make some predictions for the EROSITA survey. In Chapter 5 we discuss the results obtained in Chapter 4. In Chapter 6 we summarize the conclusions. The cosmology assumed in this work is $\Omega_m = 0.3$, $\Omega_\Lambda = 0.7$, and $H_0 = 100 h \text{ km s}^{-1} \text{ Mpc}^{-1}$, with h set to 0.7.

Chapter 2

Group Samples

In this section, we describe the three sets of observations covering the Boötes region used in this thesis to extract and estimate the properties of the X-ray detected galaxy groups. These observations include a deep six-band optical and IR photometric survey (Jannuzi and Dey, 1999), the Chandra X-Boötes survey (Murray et al., 2005) and the AGES (AGN and Galaxy Evolution Survey) optical spectroscopic survey of AGNs and galaxies brighter than $I = 20$ (Kochanek et al., 2012). The sets of observations are described in the chronological order they were observed.

Then, we will explain the selection of the two samples of galaxy groups. The first sample is an X-ray detected set of galaxy groups, using the X-Boötes survey. The second sample is optically selected, applying a Voronoi Tessellation technique to the AGES spectroscopic data. The AGES observations were also used to determine the redshift in the groups of both samples. During this thesis, the X-ray selected Boötes sample will be referred to as XBS and the optically selected sample as OBS.

2.1 Data

2.1.1 NOAO Deep Wide Field Survey (NDWFS)

The NOAO Deep Wide Field Survey (NDWFS, Jannuzi and Dey, 1999) is a deep optical and IR survey (B_wRIJHK , Figure 2.1 shows the transmission of each filter), mapping a total area of 18 deg^2 (two regions of 9 deg^2 each, one in the Boötes constellation and the other in the Cetus constellation) to faint flux limits ($B_wRI \leq 26$ AB mag; $JH = 21$ and

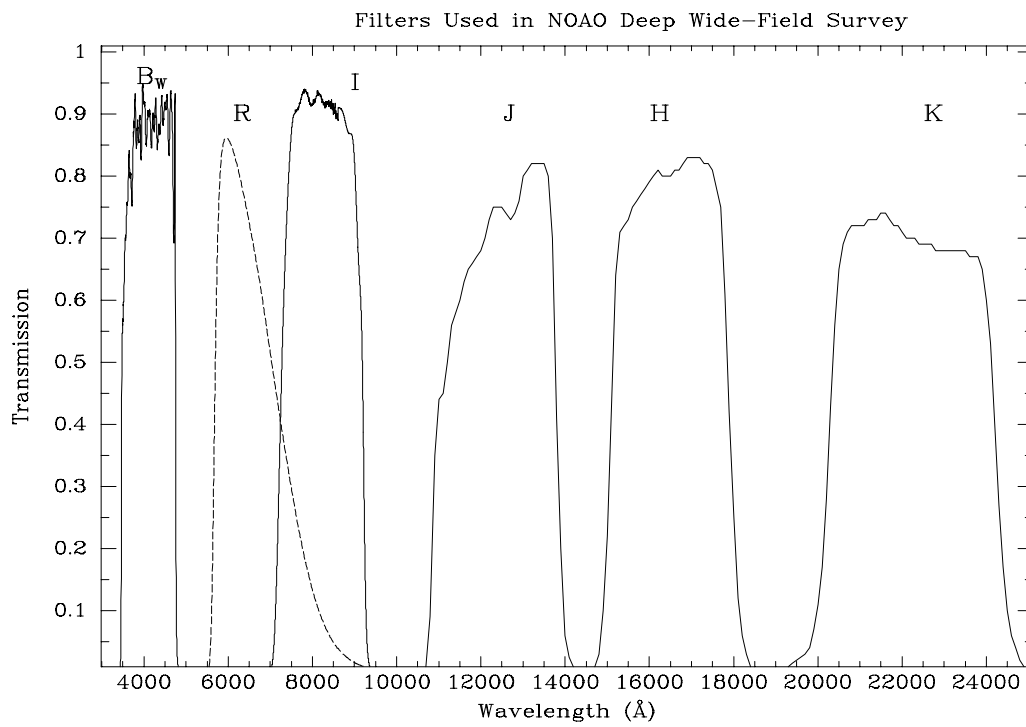


Figure 2.1 Transmission Filters from NDWFS (Figure taken from <http://www.noao.edu/noao/noadeep>).

$K = 21.4$ at 5σ detection limits). The optical imaging was done with the wide field ($36' \times 36'$) MOSAIC cameras on NOAO's 4 m telescope. The IR imaging was done with the Ohio State/NOAO Imaging Spectrograph (ONIS) on the KPNO 2.1 m telescope.

We are interested in the northern Boötes field, which covers $3^\circ \times 3^\circ$ and is centered at (J2000) RA = 14:32:06 and Dec = +34:16:48.

2.1.2 X-Boötes Survey

The X-Boötes survey (Murray et al., 2005) covers a 9.3 deg^2 area of the Boötes constellation (the north field of the NOAO Deep Wide Field Survey), centered on (J2000) R.A. $\approx 14:32:00$ and Dec $\approx +35:06:00$. The survey comprises 126 separate contiguous ACIS-I observations each approximately 5 ks in duration. This is the largest mosaic observed by Chandra (see Figure 2.2) and allows the study of large-scale structure with arcsecond angular resolution and uniform coverage (e.g. Starikova et al., 2011).

In addition to the 5 ks X-ray mosaic, in our analysis we also used all deeper Chandra observations of the Boötes field. Thus, besides the 126 5 ks ACIS-I observations, we have 76 ACIS-I observations with 10 to 40 ks of exposure and 14 ACIS-S observations with 10 to 100 ks.

2.1.3 AGN and Galaxy Evolution Survey (AGES)

The AGN and Galaxy Evolution Survey (Kochanek et al., 2012) is a redshift survey, covering 7.88 deg^2 of the Boötes field. The observations were made with the Hectospec instrument, a robotic spectrograph with 300 fibers in one degree field of view on the 6.5 m MMT telescope. Each fiber has a diameter of 1.5 arcsecond. The spectrograph is positioned in 15 different locations on the sky as shown in Figure 2 from Kochanek et al. (2012). The wavelength range is 3700 \AA to 9200 \AA , with a pixel scale of 1.2 \AA and a spectral resolution of 6 \AA (See Figure 2.3). The AGES survey was designed to investigate the AGN activity and properties of galaxies from the local to the distant Universe.

The final AGES sample comprises 21,805 redshifts for galaxies, including 4764 AGNs, to a limiting magnitude of $I < 20 \text{ mag}$. The survey is sensitive to L^* galaxies to $z = 0.5$. The median galaxy redshift is 0.31 and 90% of the redshifts are in the range $0.05 < z < 0.66$.

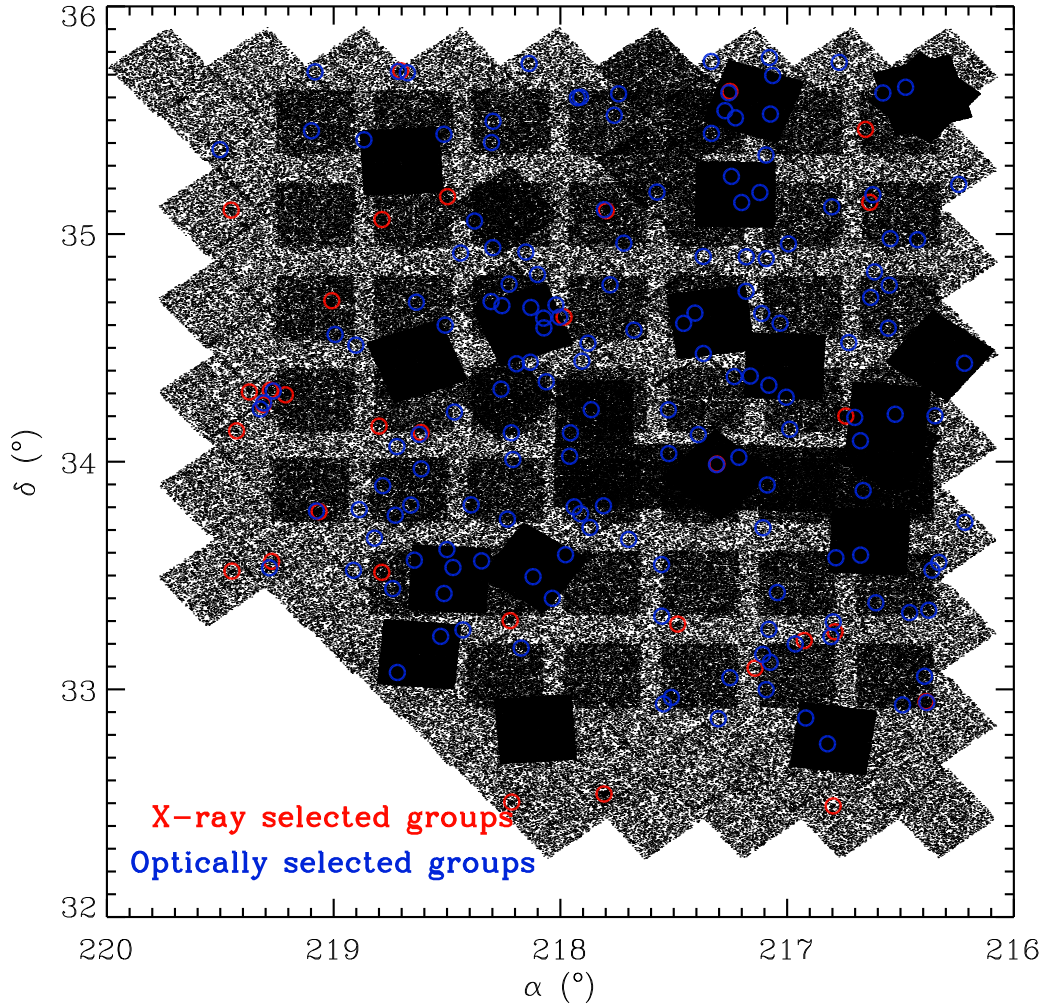


Figure 2.2 Positions of the 32 X-ray selected (red circles) and 162 optically selected (blue circles) galaxy groups in the Chandra full mosaic of Boötes ACIS-I fields. This mosaic includes the original 5ks observations of the X-Boötes survey and all the ACIS-I deeper Chandra observations of the field

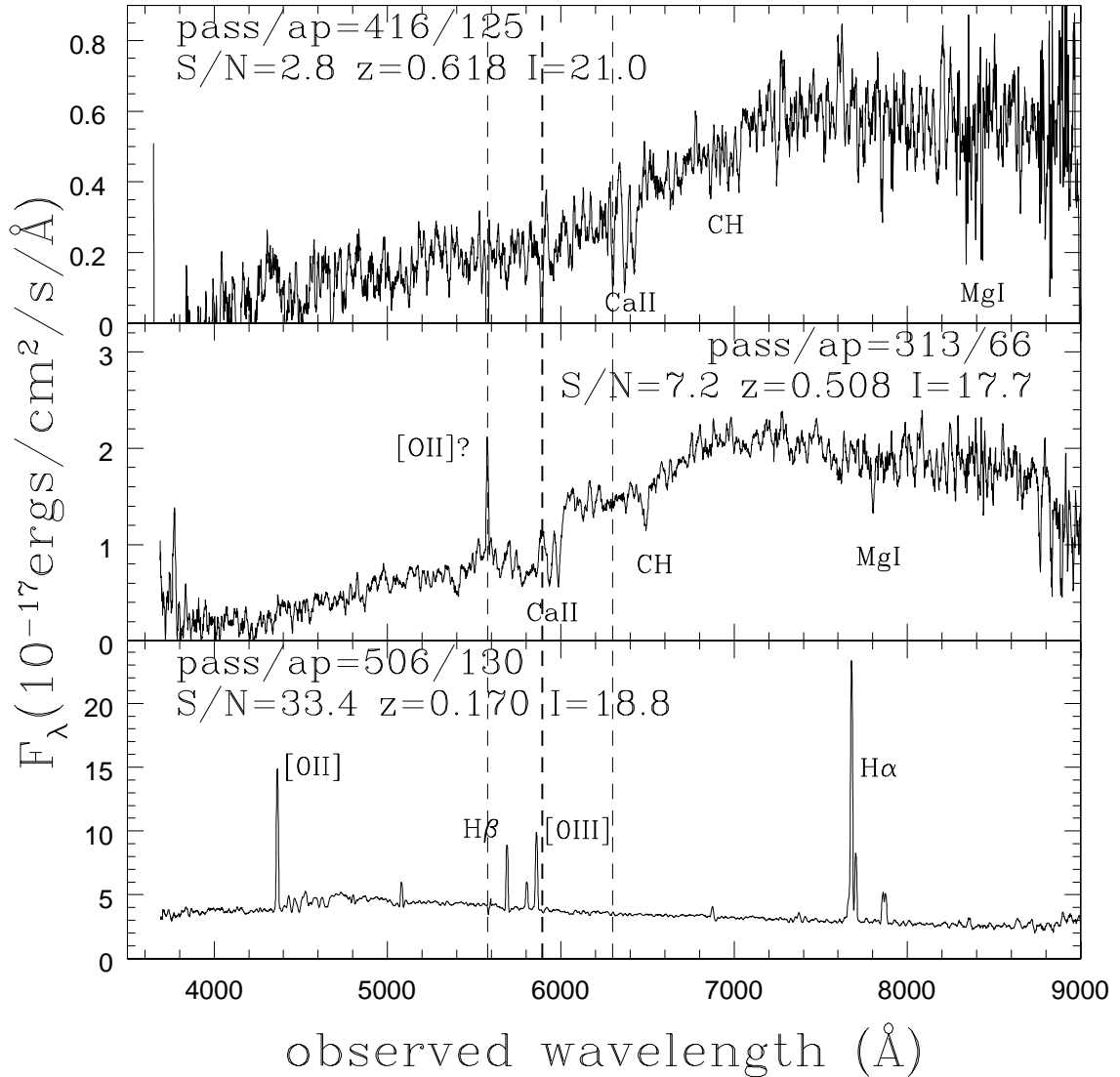


Figure 2.3 Three examples of the spectra of galaxies. The top, middle, and lower panels show spectra with continuum signal-to-noise ratios typical of the worst 5%, median, and best 5% of the spectra yielding redshifts, respectively. Several features are labeled, and the vertical lines mark the strong sky lines. The spectra are smoothed by an 11 pixel box car, which roughly halves the intrinsic spectral resolution (Original Figure 8 from Kochanek et al. 2012).

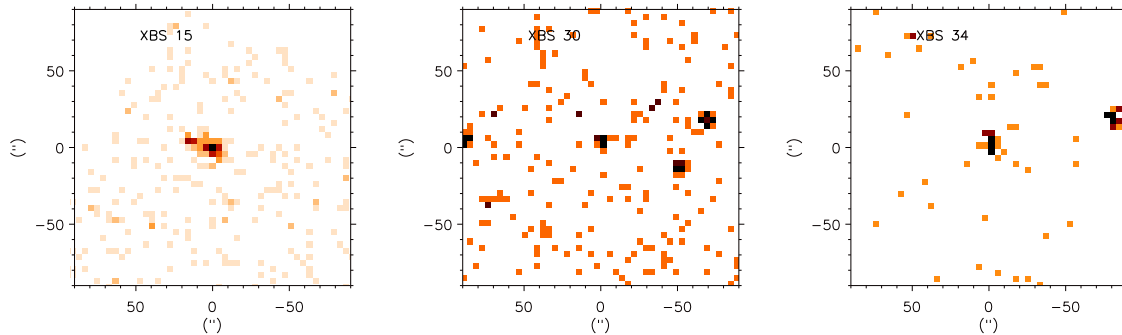


Figure 2.4 Chandra images, in the 0.5-2 keV energy band binned with 4'' resolution, for three sources originally classified by Kenter et al. (2005) as extended, that we found in deeper Chandra observations to be point-like or to have multiple point sources.

2.2 Samples

2.2.1 X-ray Selected Boötes Sample (XBS)

Using a wavelet decomposition, Kenter et al. (2005) detected 3293 point sources in the full 0.5-7 keV band with $n \geq 4$ X-ray counts. In addition, they detected 41¹ extended sources at an existence threshold equivalent to $\approx 3\sigma$, using 0.5-2 keV band images. Most of these extended sources are expected to be galaxy groups and poor clusters.

Additionally we include two extended sources selected by Michael Anderson in 2006 in his SAO REU² summer project on X-ray bright optically normal galaxies (XBONGS) in the Boötes field. Those sources were selected originally as point sources by Kenter et al. (2005). Those two sources together with the 41 detected by Kenter et al. (2005) compose our X-ray sample of galaxy groups in the Boötes field.

In addition to the 5 ks X-ray mosaic, we used all deeper Chandra observations of the Boötes field to confirm that extended sources were not multiple point sources and to better characterize the group properties.

To test that each object in the sample is a real galaxy group, we inspected the X-ray,

¹The original extended source list from Kenter et al. (2005) contains 43 objects. But, after determining their redshift, we verified that two sources were identified twice. They are XBS 01 and XBS 02 and XBS 16 and XBS 17.

²Research Experience for Undergraduate students

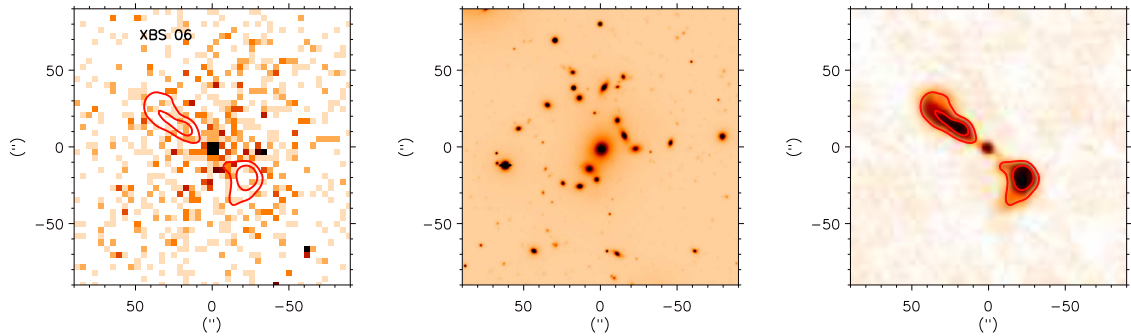


Figure 2.5 The extended X-ray source XBS 06 at $\alpha = 14:26:57.9$ and $\delta = 34:12:01$. This group has 2300 net X-ray counts, $L_X = 3.1 \times 10^{43}$ ergs/s in the 0.5-2 keV band and $N_{gals} = 50$. Left panel shows the ACIS-S 30 ks image (ObsId = 10495) in 0.5-2 keV band with the radio contours of the jets (red lines). It is possible to see a cavity in the X-ray emission, probably associated with the SW radio lobe. Middle panel presents the I-band image from NDWFS, where we can see the BCG at the center of the X-ray emission. Right panel is the FIRST-NRAO radio image which shows the BCG's radio lobes, which extend ≈ 110 kpc and 75 kpc.

optical and radio images of all 43 sources and ran the MARX³ simulations to determine how a point source with the same flux as the real source would appear at the same position in the detector. MARX provides detailed ray-trace simulations of how Chandra responds to a variety of astrophysical sources and can generate standard FITS event files and images as output. It contains detailed models for Chandra’s High Resolution Mirror Assembly (HRMA), the Chandra High Energy Transmission Grating (HETG), Low Energy Transmission Grating (LETG) and all the focal plane detectors.

The last column ($S_{14} \text{ Flux}^{0.5-2keV}$) of Table 1 from Kenter et al. (2005) is given as the input flux from the simulations. All simulated sources were compared with the real sources. The profile of the simulated and real sources were fitted to a Gaussian with the width as a free parameter. If the width fitted to the simulated source is consistent within 3σ or larger than the width fitted to the real one, we confirm it is indeed a point source. Figure 2.4 shows three examples of sources originally selected as extended which we classify as point sources. On the other hand, if the extension of the real source is larger than the simulated source, then it is classed as an extended source. Figure 2.5 shows an example of an extended source. After this procedure, we excluded 9 objects. The 32 sources confirmed as extended form our galaxy group catalog. Figure 2.2 shows the positions of the 32 candidates (red circles) in the X-Boötes field and Table A.1 provides the general information for the 32 X-ray selected galaxy groups: the group name; coordinates; Chandra ObsIDs; exposure time; the final redshift and uncertainties adopted in this work; the number of galaxies used to estimate the redshift and the technique applied for determining the redshift (§2.2.1).

Redshift Determination

We use the AGES data to determine the redshifts of the galaxy groups. Each system’s redshift was first estimated inside a 60 arcsecond radius aperture centered on the X-ray position. We use the following approach to estimate the galaxy group’s redshift. First, we try to identify each group in redshift space by applying a *gap-technique* (Katgert et al., 1996). After the group is identified in redshift space, then we measure its redshift with a biweight estimate. If we do not identify a group in redshift space, we apply the biweight estimate to all galaxies within 60 arcsecond of the X-ray position, no matter their redshift differences.

³<http://space.mit.edu/cxc/marx-4.5/index.html>

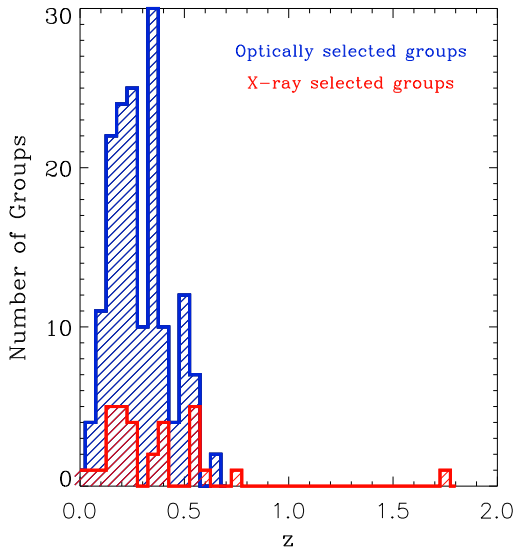


Figure 2.6 The redshift distribution of the 31 X-ray selected (red histogram) and 162 optically selected (blue histogram) groups in the Boötes field

The gap-technique (Katgert et al., 1996) identifies groups in redshift space. Two galaxies, which are adjacent in redshift, are determined to belong to the same group, if their velocity difference does not exceed a pre-determined value, called the velocity gap. We adopt a variable velocity gap referred to as a *density gap* (Adami et al., 1998; Lopes, 2007; Lopes et al., 2009a). The density gap width is given by the expression

$$\Delta z = 500\{1 + \exp[-(N - 6)/33]\}/c. \quad (2.1)$$

where N is the number of galaxies inside the 60 arcsecond radius aperture and c is the speed of light in km s^{-1} . For the purpose of the redshift determination, the gap-technique considers the system to be a galaxy group, if it has at least three galaxies identified. After a galaxy group is identified through the gap-technique, we determine its redshift through the biweight estimate (Beers et al., 1990), using only the galaxies selected as group members by the gap-technique. If more than one group of galaxies is identified, we use the group with the smallest offset from the X-ray centroid. After the redshift determination, we found two groups that were identified twice in X-rays by Kenter et al. (2005). They are groups XBS 01 and XBS 02, and XBS 16 and XBS 17. For our analysis, we keep the groups XBS

02 and XBS 17, because they have more galaxies identified as members compared to their duplicate identifications.

With the gap-technique, we are able to identify 17 of 32 extended sources in redshift space. For the other 15 systems, the biweight estimate is applied, considering all galaxies within 60 arcseconds of the X-ray center. If there is only one galaxy with a measured redshift, its redshift is taken as the redshift of the system. Applying only the biweight estimate, we are able to determine the redshifts for 10 of the 15 remaining groups. Since the gap-technique combined with the biweight estimate provides more reliable results than just the biweight estimate, we attempt to refine these ten redshifts determined only from the biweight analysis. To do this, we compute the 0.5 Mpc radius using the redshift estimated from the biweight analysis and we apply the gap-technique inside a fixed metric. If we identify a group in redshift space within 0.5 Mpc, we perform a biweight estimate using the galaxies now identified to be associated with the group. After this procedure, we are able to determine redshifts for 5 of the 10 previous groups with redshifts derived only through the biweight estimate. Finally there are five groups which do not have AGES data (XBS 04, 08, 18, 21 and 27). For XBS 04, we adopted the redshift determined from optical and IR spectra by Stanford et al. (2012). This cluster is at a very high redshift and was originally identified using the SDWFS (Spitzer Deep Wide Field Survey, Ashby et al., 2009) data and matched with the NDWFS data. There are seven members spectroscopically identified, one of them is a QSO observed in AGES. For XBS 08, we adopted the redshift of the BCG from the Sloan data as the group redshift. For XBS 18 and 27, we determined the redshift from the X-ray spectrum. XBS 21 has no estimated redshift. The redshift distribution of the 31 X-ray selected groups (red histogram) is represented in Figure 2.6 and the list of the groups with their respective redshifts and the technique applied is given in Table A.1.

To assure the reliability of the group redshifts (especially the groups XBS 05, 28, 29, 39, 41 and 52 for which the redshift was estimated based on only one or two galaxies), we identify the brightest galaxy of the group (BGG) with $M_R \leq M_R^* - 1$, inside an aperture of 60 arcseconds centered on the X-ray emission and compare its redshift with the redshift of the group. The adoption of this non-strict criteria is justified by the difficulty for some groups in identifying the BGG. For many groups there is no clear dominant central galaxy.

When the redshift difference $|cz_{group} - cz_{BGG}| \geq 300 \text{ km s}^{-1}$, we adopt the redshift of the BGG as the redshift of the system. We could identify the BGG in 28 of the 32 groups.

For these 28 groups, 16 have a group redshift consistent with the redshift of the brightest galaxy of the group, 6 only have the BGG redshift and the remaining 6 groups do not have a redshift consistent with the BGG redshift. For these 6 groups we adopt the redshift of the BGG as the redshift of the group. Table 2.1 shows the information for the BGGs. Thus, the final group sample contains 32 X-ray selected groups and we are able to determine the redshifts for 31 of these.

Table 2.1. Information of the Brightest Galaxy of the Group of the X-ray Selected Sample

Name	R.A. _{BGG} (deg)	Dec _{BGG} (deg)	z_{BGG}	M_R	Offset ^a (kpc)
XBS 02	216.387	32.9440	0.214	-22.62	23
XBS 05	216.655	35.4588	0.257	-21.53	15
XBS 06	216.749	34.1999	0.128	-23.90	49
XBS 07 ^b	216.786	33.2525	0.011	-20.51	2
XBS 08 ^c	216.797	32.4880	0.132	-23.19	96
XBS 09	216.931	33.2042	0.151	-21.83	112
XBS 11	217.251	35.6226	0.234	-23.15	49
XBS 13	217.310	33.9896	0.129	-23.85	55
XBS 14	217.482	33.2864	0.419	-23.78	12
XBS 17	217.798	35.1026	0.191	-22.71	87
XBS 20	217.980	34.6349	0.349	-23.36	71
XBS 22	218.220	33.3062	0.569	-24.50	103
XBS 25	218.615	34.1279	0.189	-22.93	20
XBS 26	218.705	35.7131	0.152	-20.88	21
XBS 28	218.788	33.5182	0.422	-23.49	83
XBS 29	218.810	34.1496	0.404	-20.28	174
XBS 32	219.019	34.6994	0.534	-24.23	271
XBS 33	219.057	33.7881	0.337	-23.49	146
XBS 35	219.211	34.2927	0.045	-21.47	5
XBS 36	219.271	33.5610	0.243	-23.66	25
XBS 37	219.279	34.3140	0.122	-23.59	4
XBS 38	219.319	34.2516	0.547	-24.14	125
XBS 39 ^c	219.380	34.3097	0.396	-19.75	144
XBS 41	219.429	34.1363	0.543	-24.28	24

Table 2.1 (cont'd)

Name	R.A. _{BGG} (deg)	Dec _{BGG} (deg)	z_{BGG}	M_R	Offset ^a (kpc)
XBS 42	219.448	33.5205	0.218	—	13
XBS 43	219.442	35.1138	0.576	-23.37	255
XBS 46	217.141	33.0890	0.196	-22.66	8
XBS 52	218.498	35.1645	0.599	-22.63	9

^aOffset between the X-ray position and the BGG

^bRedshift from NASA/IPAC Extragalactic Database (NED)

^cSpectroscopic redshift from SDSS DR8

^dBrand et al. (2006)

2.2.2 Optically Selected Boötes Sample (OBS)

To select galaxy groups and galaxy clusters using the optical data, we apply the Voronoi Tessellation technique (VT), already employed in the galaxy cluster identification (Ramella et al., 2001; Kim et al., 2002; Lopes, 2003; Lopes et al., 2004). The main advantage of this technique for the galaxy cluster selection is the fact that it does not bin the data, nor make any assumption about the source geometry. Hence, the algorithm is sensitive to irregular and elongated structures.

When VT is applied to a galaxy catalog, each galaxy is considered as a seed and has a Voronoi cell associated to it. The area of the cell is interpreted as the effective area occupied by a galaxy in the plane and its inverse provides the local density at that point. The galaxy group is identified by high density regions, i.e., regions comprised of cells small enough to give a density value higher than a chosen density threshold. Figure 2.7 shows an example of VT applied to the AGES data, in the redshift range between $0.20 < z \leq 0.24$. The red circles indicate the high density regions associated with group candidates.

In this Ph.D. thesis, we use the Voronoi Tessellation code developed by Ramella et al.

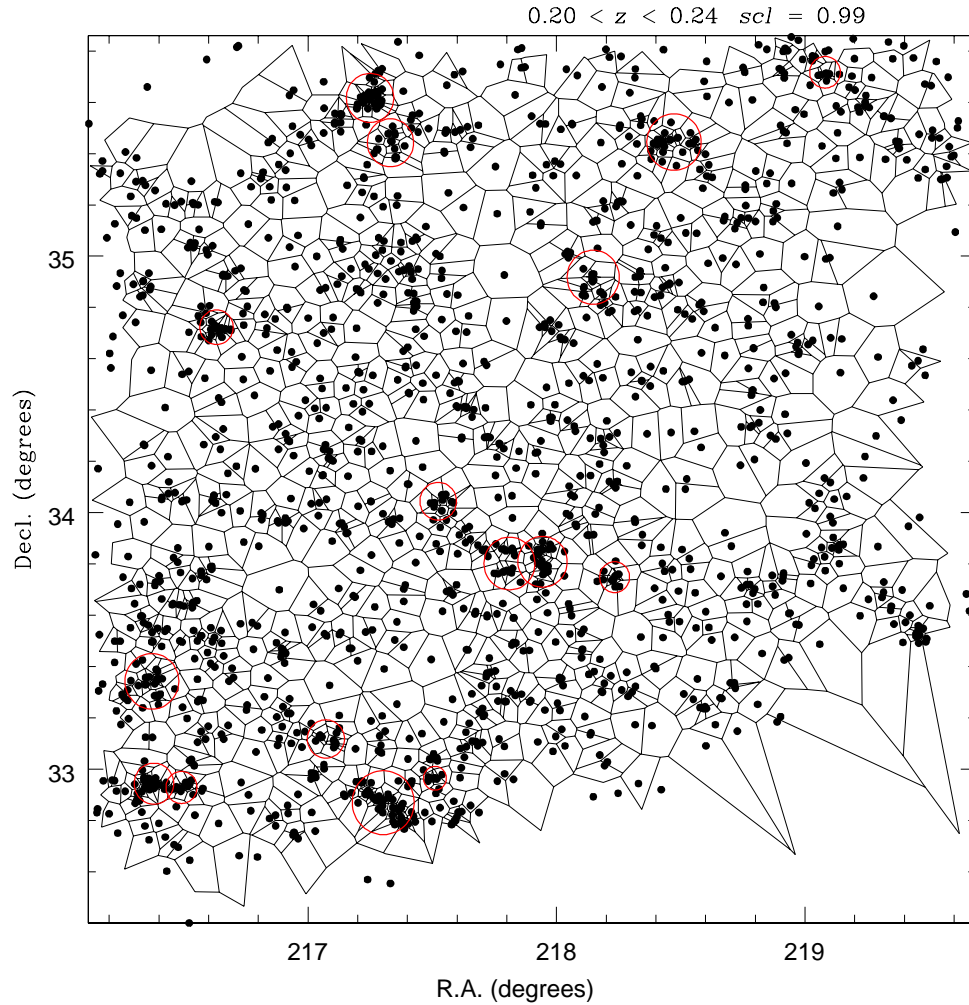


Figure 2.7 The Voronoi Tessellation technique applied to a sample of galaxies from AGES between $0.20 < z \leq 0.24$. Each point represents a galaxy surrounded by its associated Voronoi cell (demarcated by the polygons). The red circles indicate the overdensity regions associated to a group/cluster candidate.

(2001). This code utilizes the *triangle* C code by Shewchuk (1996) to generate the mosaic. The algorithm identifies the group candidates based on two criteria. The first is the density threshold, called search confidence level (*scl*). It identifies fluctuations denser than the background distribution. The second criterium calculates the probability that these overdensities are actually random fluctuations as a poissonian distribution (Kiang 1996). This criterium is called rejection confidence level (*rcl*). If the probability that the object is a random fluctuation is higher than the adopted *rcl*, then the object is rejected from the preliminary list generated by the first criteria. For our group selection, we set $scl = 0.99$ and $rcl = 0.95$.

As we have the galaxy spectroscopic data from AGES, we split the sample in non-overlapping redshifts slices. To choose the best width for the redshift slices, we run tests varying the width from $\Delta z = 0.01$ to $\Delta z = 0.06$. We notice that, for thin redshift slices (e.g. $\Delta z = 0.01$ and $\Delta z = 0.02$), the Voronoi Tessellation is only sensitive to large structures. This is due to the small number of Voronoi seeds, i.e. galaxies, in the field. On the other hand, for thick redshift slices (e.g. $\Delta z = 0.05$ and $\Delta z = 0.06$), the field is so crowded with galaxies that the VT is only sensitive to small structures. After the tests searching for the most appropriate width, we chose redshift slices of $\Delta z = 0.04$, starting at $z = 0.00$ and going up to $z = 1.00$. We run the VT code in each slice independently (for instance, from $0.00 < z \leq 0.04$, then $0.04 < z \leq 0.08$ and so on up to $z = 1.00$). Then, we eliminate double groups with coincident centroids at the same redshift, coming from different redshift slices. To be twice identified the object must be found in the edge of the slices. However, only a small fraction of systems are located in the borders of the redshift sections. Following this procedure, we select 162 galaxy group/cluster candidates between $0.00 \leq z \leq 1.00$. Table B.1 provides the general information for the 162 optically selected galaxy groups: the group name; coordinates; Chandra ObsIDs; exposure time; the final redshift and uncertainties adopted in this work and the number of galaxies used to estimate the redshift.

Redshift Determination

For each galaxy group candidate we compute the system's redshift using an aperture of 0.50 Mpc (considering the central redshift of the bin where the group was found). First, as we did for the X-ray selected sample, we identify the group in redshift space employing

the gap-technique. The same density gap described in Equation 2.1 was adopted to select the galaxy members. For the redshift determination we considered all galaxies within $\Delta z = \pm 0.020$ from the redshift bin in question. This allows that systems detected close to the redshift limits to have all galaxies selected. Once the group is identified in the redshift space, we compute the redshift of the system applying a biweight estimate, using only those galaxies selected as members by the gap-technique. Double systems (within 0.50 Mpc and with $|\Delta z| \leq 0.010$) are checked. We found no case where a system was detected twice.

The redshift distribution of the optically selected sample (blue histogram) is shown in Figure 2.6. From the 162 groups, 5 have $z \leq 0.05$, 105 have $0.05 < z \leq 0.35$ and 52 have $0.35 < z \leq 0.66$. The 5 groups with $z \leq 0.05$ have between 5 and 20 spectral members identified by the gapper technique inside 0.5 Mpc aperture. From the 105 groups with $0.05 < z \leq 0.35$, 23 have less than 5 spectrally identified members, 36 groups have between 5 and 10 members, 38 have between 10 and 20 members and 8 groups have more than 20 spectrally identified members inside 0.5 Mpc. From the 52 groups with $z > 0.35$, 25 have less than 5 members and 27 have more than 5 spectral identified members inside 0.5 Mpc. Judging by the number of spectroscopically identified members inside 0.5 Mpc, it seems that the high redshift groups are the one with lowest mass. This may be just a consequence of the spectral incompleteness of the data, since AGES data is only complete to $M^* + 1$ up to $z = 0.35$. Due to this fact, we do not use them in any further analysis, except in the L_X estimation, which is not affected by the optical spectral incompleteness.

After determining the redshift of the groups, we identify the BGG using the same non-strict criteria adopted for the X-ray selected sample: (i) the BGG must be within a maximum distance of 60 arcseconds from the optical baricenter of the galaxies; (ii) $M_R^{BGG} \leq M_R^* - 1$. Table 2.2 shows the information for the BGGs. We identified 70 BGGs from the 162 groups. From the 92 groups that do not have their BGG identified, 30 have less than 5 members identified, 66 have less than 10 members and 26 have more than 10 spectral identified members.

Several works (Mulchaey et al., 2006; Jeltama et al., 2006, 2007; Fassnacht et al., 2008) reported the difficulty to identify the BGG of groups. In Fassnacht et al. (2008), there is no clearly dominant central galaxy for some groups, instead in several of the groups the brightest and next brightest galaxies are separated by less than half a magnitude. Investigating intermediate-redshift groups, Mulchaey et al. (2006); Jeltama et al. (2006,

2007) have found systems for which the intergroup medium (IGM) is detected in X-ray, but no dominant BGG was identified. The lack of a dominant BGG in some groups may be due to seeing these groups at an earlier stage of their evolution (Jeltema et al., 2007), or it may be due to incomplete spectral information where the BGG has not yet been identified as a group member, which can be the case for the 15 groups with $z > 0.35$ and no BGG found. Besides, as mentioned before, there are groups with no dominant bright galaxy. Since we used $M_R^{BGG} \leq M_R^* - 1$ as one of the criterion to select the BGG, we restricted our BGG identification only to relatively bright galaxies. So, any group from our sample, which consist in reality of some few faint galaxies, have no BGG identified according to our selection criteria.

Table 2.2. Information of the Brightest Galaxy of the Group of the Optically Selected Sample

Name	R.A. _{BGG} (deg)	Dec _{BGG} (deg)	z_{BGG}	M_R	Offset ^a (kpc)
OBS 011	217.974960	34.703056	0.084	-22.99	0.38136
OBS 015 ^{XBS06}	216.749	34.1999	0.128	-23.90	49
OBS 018 ^{XBS13}	217.310	33.9896	0.129	-23.85	55
OBS 025	218.406235	33.803822	0.119	-22.98	32.445
OBS 031 ^{XBS37}	219.279	34.3140	0.122	-23.59	4
OBS 040	217.198929	35.139313	0.193	-23.12	129.967
OBS 042 ^{XBS17}	217.798	35.1026	0.191	-22.71	87
OBS 046	217.954880	34.125874	0.178	-22.86	120.028
OBS 047	218.141510	35.761074	0.185	-23.57	37.512
OBS 049 ^{XBS25}	218.615	34.1279	0.189	-22.93	20
OBS 051 ^{XBS02}	216.387	32.9440	0.214	-22.62	23
OBS 054	216.628128	34.725197	0.210	-23.38	39.387
OBS 056 ^{XBS11}	217.251	35.6226	0.234	-23.15	49
OBS 062	217.941193	33.794586	0.227	-23.57	191.417
OBS 069	216.584946	35.619041	0.255	-23.36	199.25
OBS 074	217.077255	35.775486	0.248	-22.85	136.381
OBS 076	217.367798	34.464771	0.256	-23.17	89.0664
OBS 077	217.551163	32.929638	0.242	-23.13	145.492
OBS 078	217.672134	34.577343	0.266	-23.21	101.5
OBS 088 ^{XBS36}	219.271	33.5610	0.243	-23.66	25
OBS 089	216.353836	33.526001	0.307	-23.07	109.584
OBS 090	216.554520	34.587589	0.313	-23.13	144.362
OBS 094	218.225632	34.781761	0.310	-23.01	143.395
OBS 096	216.217682	33.733707	0.359	-23.92	234.142

Table 2.2 (cont'd)

Name	R.A. _{BGG} (deg)	Dec _{BGG} (deg)	z_{BGG}	M_R	Offset ^a (kpc)
OBS 097	216.422836	34.974201	0.328	-22.86	117.49
OBS 098	216.522324	34.207325	0.345	-23.07	68.1582
OBS 099	216.678772	33.589542	0.320	-23.19	14.091
OBS 100	216.677582	34.092598	0.352	-23.02	177.142
OBS 104	217.236206	34.374931	0.329	-23.27	146.452
OBS 105	217.398712	34.121120	0.326	-23.74	122.705
OBS 107	217.552521	33.319813	0.320	-23.14	109.91
OBS 108	217.780640	34.776344	0.351	-23.47	149.85
OBS 109	217.879852	34.514534	0.328	-23.16	217.786
OBS 110	217.960205	34.024746	0.351	-24.38	89.91
OBS 111 ^{XBS20}	217.980	34.6349	0.349	-23.36	71
OBS 114	218.498962	34.603100	0.351	-23.54	68.931
OBS 115	218.634277	34.699661	0.351	-23.71	185.814
OBS 116	218.663910	33.807800	0.328	-23.42	74.5056
OBS 117	218.783447	33.892605	0.328	-23.68	68.7744
OBS 118	218.888596	33.788582	0.342	-23.38	191.529
OBS 119 ^{XBS33}	219.057	33.7881	0.337	-23.49	146
OBS 120	216.477188	35.645294	0.388	-23.37	169.303
OBS 122	216.963303	33.204350	0.364	-23.78	82.8468
OBS 123	217.042328	33.426163	0.362	-22.95	33.6336
OBS 124	217.090836	32.999863	0.366	-23.78	58.5048
OBS 125	218.073944	34.630028	0.373	-23.51	143.354
OBS 127	218.103714	34.825027	0.368	-23.00	176.13
OBS 130	218.719330	33.074081	0.374	-23.49	18.7308

Table 2.2 (cont'd)

Name	R.A. _{BGG} (deg)	Dec _{BGG} (deg)	z_{BGG}	M_R	Offset ^a (kpc)
OBS 131	219.322342	34.225040	0.398	-23.23	42.1902
OBS 132	217.073059	35.527420	0.417	-23.92	150.228
OBS 133	217.059555	35.703033	0.414	-23.45	59.832
OBS 134	217.095657	35.342731	0.416	-23.09	146.678
OBS 138	217.572189	33.548302	0.426	-23.21	138.621
OBS 139	218.475021	33.535511	0.445	-22.91	180.367
OBS 141	217.031769	34.607597	0.472	-23.56	28.6896
OBS 143	216.726028	34.520699	0.525	-23.17	216.486
OBS 144	216.807236	33.231239	0.501	-23.60	55.584
OBS 148	218.057510	34.351318	0.513	-23.66	330.211
OBS 149	218.192474	34.426102	0.494	-23.06	227.999
OBS 150	218.210617	34.015083	0.503	-23.73	111.402
OBS 152	218.436203	34.916748	0.489	-23.92	285.246
OBS 153	218.612808	33.968521	0.497	-23.01	81.1668
OBS 154	216.989258	34.142220	0.570	-22.91	288.992
OBS 155	217.978241	33.591709	0.558	-23.37	19.587
OBS 157	218.715836	35.714584	0.542	-23.99	15.444
OBS 158	218.902847	34.509998	0.523	-23.37	200.912
OBS 159	219.307510	34.258556	0.543	-23.93	177.772
OBS 160	217.698715	33.661171	0.571	-22.85	3.9624
OBS 162	218.499405	33.616322	0.662	-23.80	169.608

Chapter 3

Methodology

In this chapter, we present the techniques applied to determine the dynamical, optical and X-ray properties for both samples of galaxy groups. For each group, we used the AGES observations to estimate velocity dispersion (σ_{gr}), physical radii (R_{500} and R_{200}) and mass (M_{500} and M_{200}). Using the optical photometric data from the NDWFS, we derived richness (N_{gals}) and optical luminosity (L_{opt}). Finally, we estimated the X-ray luminosity (L_X) and X-ray temperature (T_X) using the X-Boötes survey.

3.1 Virial Analysis

With the redshifts estimated, we calculate the dynamical properties of the groups, including velocity dispersion, physical radius and total mass. To do this, we perform a virial analysis. Lopes et al. (2009a) showed that if a survey is complete to at least M^*+1 , the velocity dispersion (σ_{gr}) and the corresponding mass estimates for galaxy groups and clusters are reliable, while if the survey is shallower, those masses may be underestimated. Therefore, we apply the virial analysis only for the groups with $z \leq 0.35$, where AGES is complete to M^*+1 . We also require the galaxy group to have at least five galaxy members. After excluding the interlopers, we have 14 X-ray selected and 67 optically selected groups to $z \leq 0.35$ with at least 5 galaxy members.

The first step before starting the virial analysis is to eliminate the interlopers. To do so, we use a technique called “shifting-gapper” (Lopes et al., 2009a), applied to all galaxies with spectra available within R_{500} centered on the X-ray coordinates. The R_{500} of each

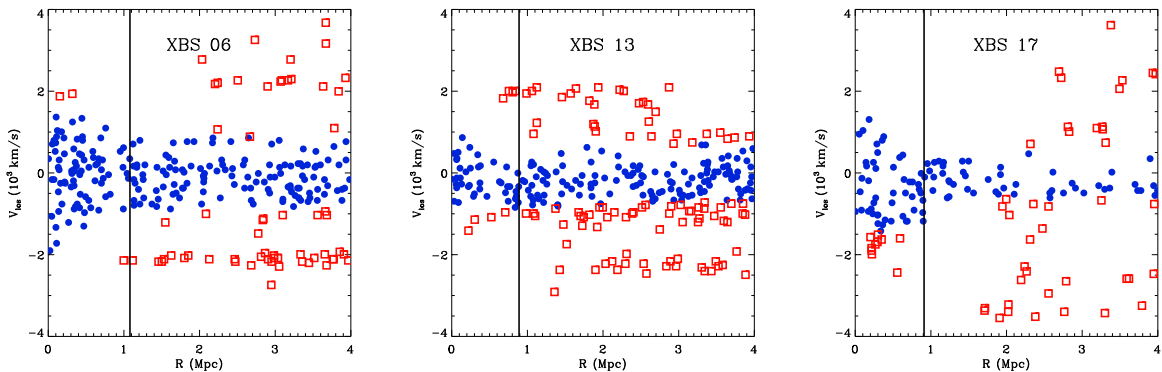


Figure 3.1 Phase-space diagrams of the three most massive X-ray selected galaxy groups shown as examples. The velocity and radial offsets are with respect to the group center. We apply a shifting-gapper procedure for the selection of group members (filled blue circles) and exclusion of interlopers (open red squares). The vertical line is the R_{500} of the group. The large number of members at large radii sensitive to the group velocity illustrate the large structure in which these groups reside

group is determined from the L_X - M_{500} relation for groups from Eckmiller et al. (2011), using the X-ray luminosities; how we estimated L_X is discussed in Section 3.3. We convert M_{500} to R_{500} using the equation:

$$M_{500} = 500 \times \frac{4\pi}{3} \rho_c R_{500}^3, \quad (3.1)$$

where ρ_c is the critical density of the Universe at the redshift of the group.

The principle of the “shifting-gapper” technique is the same as for the gapper technique used to estimate the redshifts of the groups, except for two differences: (i) we apply the procedure in radial bins from the center of the group; (ii) the size of the velocity gap between two galaxies adjacent in velocity depends on the velocity limits of each group (as shown in Equation 3.2). This method makes no assumption about the dynamical state of the group. The procedure applied is very similar to the one used in Lopes et al. (2009a). The most important difference is that we do not run the interloper rejection to a radius of 4 Mpc, but instead we stop at R_{500} . The reason why we perform the analysis only inside R_{500} is because for poor groups, 4 Mpc is much larger than the virial radius (the mean R_{500} of our samples is ≈ 0.56 Mpc).

We start the “shifting-gapper” technique selecting all galaxies within R_{500} from the group center and with $|cz - cz_{group}| \leq 4000 \text{ km s}^{-1}$, where z_{group} is the redshift of the group estimated in Section 2.2.1 and 2.2.2. We run the gap technique in radial bins of 0.35 Mpc width or larger (if it does not exceed R_{500}) to guarantee the selection of at least 15 galaxies in each annulus. In the first radial bin, we order the galaxies by velocity and run the gap technique. A galaxy is excluded as an outlier, if the velocity difference between it and the adjacent galaxy exceeds the velocity gap given by:

$$\Delta z = \frac{|v_{lo} - v_{hi}|}{10} \times \{1 + \exp[-(N - 6)/3]\}/c. \quad (3.2)$$

where v_{lo} and v_{hi} are, respectively, the lower and higher velocity limits of the galaxies in the group measured inside 0.5 Mpc. These velocity limits are symmetric.

If no group is found in the first radial bin, we keep all the galaxies, v_{lo} and v_{hi} and we reanalyze them with the galaxies of the next annulus. If a group is identified according to Eq. 3.2, we keep all the galaxies selected as members within v_{lo} and v_{hi} . Then, we update the values of v_{lo} and v_{hi} , using only the member galaxies. For the next annulus, we use these new values for v_{lo} and v_{hi} . We repeat this routine until we reach R_{500} .

Figure 3.1 illustrates the results of the outliers removal for the three most massive groups in the X-ray sample. In each panel, the filled circles represent the group members and the open squares represent the rejected interlopers. The vertical line marks R_{500} for each group from the L_X - M_{500} relation (Eckmiller et al., 2011). In Figure 3.1, we extended the interloper rejection analysis to larger radii to show the large scale structure in which these groups reside. For these cases, the result of the outlier exclusion inside R_{500} is not altered, if we extend the analysis to large radii.

In Appendices C and D, we present, respectively, the X-ray and optical galaxy group catalogs to $z \leq 0.35$. For each group, we show the galaxy number density profile and the spatial distribution of galaxy members and interlopers for each group. In the numeric density profiles, we can see that even the least massive groups present a density peak over the galaxy background distribution, reinforcing that these systems are real galaxy groups. In the spatial distribution of galaxy members and interlopers, we also see a clump of galaxy members inside R_{500} for all 14 X-ray and 67 optical groups. The colors of the galaxy members and interlopers represent their velocities. Through the colors of the symbols, it is possible to verify that these central galaxy clumps are not a projection effect, but a real

agglomeration of galaxies at the same distance.

After the interloper exclusion, these groups were subjected to a virial analysis to derive σ_{gr} , R_{500} , R_{200} , M_{500} and M_{200} , similar to the one adopted by Girardi et al. (1998), Popesso et al. (2005, 2007), Biviano et al. (2006) and Lopes et al. (2009a). First, the line-of-sight velocity dispersion of all group members within an aperture R_A is computed applying a biweight estimate. The aperture R_A is defined as the radial offset of the most distant group member. Then, the velocity dispersion is corrected by velocity errors. Following Girardi et al. (1998), we obtain a first estimate of the projected virial radius and, then, the deprojected virial mass:

$$M_V = \frac{3\pi\sigma_p^2 R_{PV}}{2G}. \quad (3.3)$$

This is Eq. 5 from Girardi et al. (1998), where G is the gravitational constant, $3\pi/2$ is the deprojection factor, σ_p is the line-of-sight velocity dispersion and R_{PV} and M_V are, respectively, the projected virial radius and mass.

Next, we apply the surface pressure term correction to the mass estimate (The and White, 1986). Then, we obtain an estimate of R_{200} considering the virial mass density:

$$R_{200} = R_A \left(\frac{\rho_V}{200\rho_c(z)} \right)^{1/2.4} \quad (3.4)$$

where $\rho_V = 3M_V/(4\pi R_A^3)$ after the surface pressure correction, $\rho_c(z)$ is the critical density at redshift z and the exponent of the equation is the one describing a Navarro, Frenk & White (NFW) profile near R_{200} (Katgert et al., 2004). To obtain M_{200} , we assume a NFW profile and interpolate (when $R_{200} < R_A$) or extrapolate (when $R_{200} > R_A$) M_V from R_A to R_{200} . Then, we use the definition of M_{200}^1 to compute a final estimation of R_{200} . If we substitute 200 for 500 in the equations above, we derive R_{500} and M_{500} .

In the further analysis, we adopt the R_{500} estimated through the virial analysis. The results of the virial analysis are represented in Figure 3.2 and given in Tables E.1 and F.1. We find that the 14 groups have total masses which range over two magnitudes, from $M_{500} = 3 \times 10^{12} M_\odot$ to $2 \times 10^{14} M_\odot$. The X-Boötes groups have velocity dispersion estimates of $110 < \sigma_{gr} < 650 \text{ km s}^{-1}$. The 67 optically selected groups have masses spreading from $M_{500} = 10^{12} M_\odot$ to $M_{500} = 2.5 \times 10^{14} M_\odot$ and velocity dispersion between 100 km s^{-1}

¹ $M_{200} = 200 \times \frac{4\pi}{3} \rho_c(z) R_{200}^3$

$$\lesssim \sigma_{gr} \leq 700 \text{ km s}^{-1}.$$

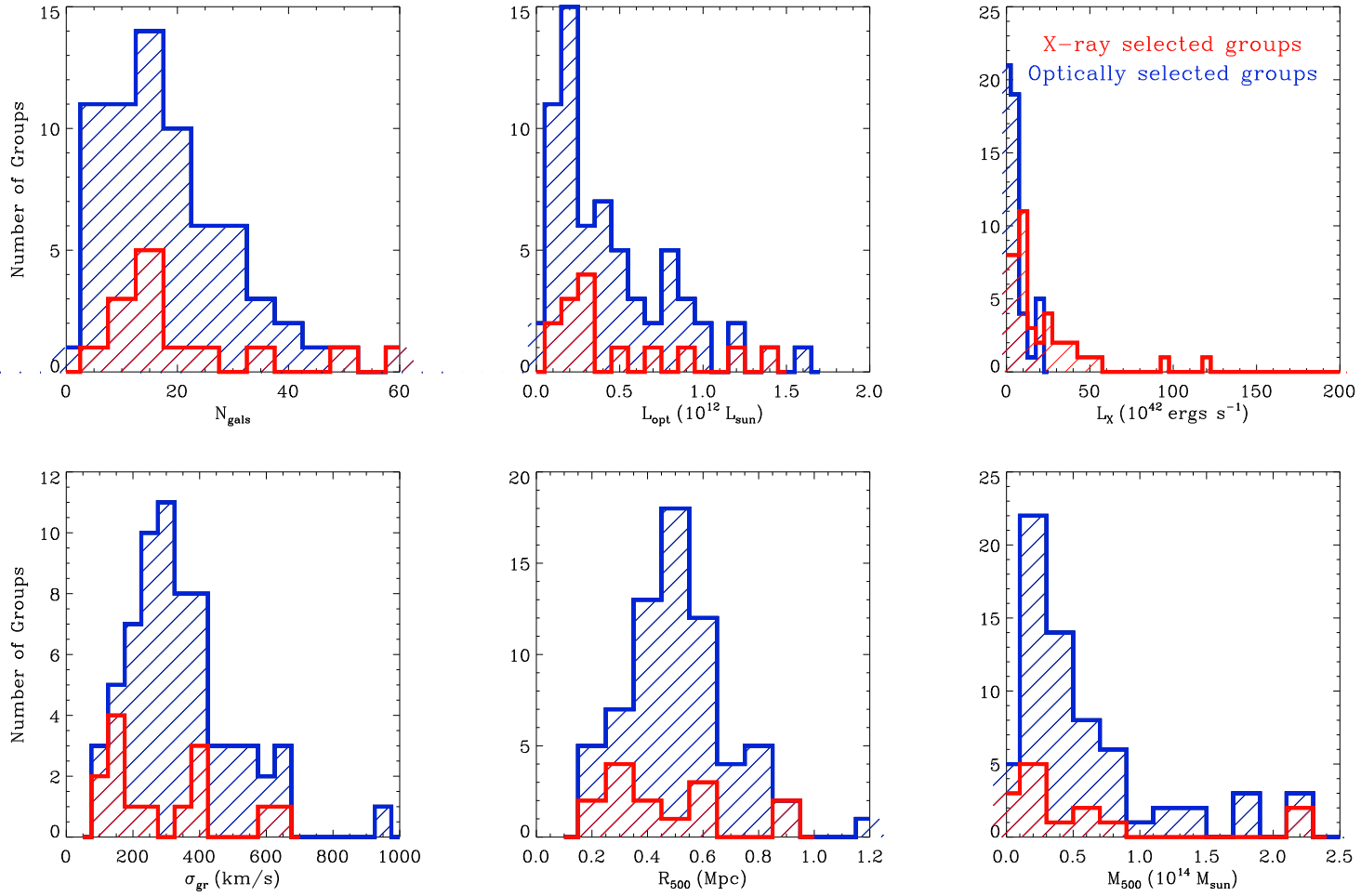


Figure 3.2 Distribution of N_{gals} , L_{opt} , L_X , σ_{gr} , R_{500} and M_{500} for the x-ray (red histograms) and optically (blue histograms) selected samples.

3.2 Optical Properties Determination

For each group with mass estimates, we derive the richness and optical luminosity. Using the photometric data from the NDWFS, we apply the same procedure used in Lopes et al. (2006) and Lopes et al. (2009a). Our richness (N_{gals}) is defined as the number of galaxies with $m_R^* - 1 \leq m_R \leq m_R^* + 2$ inside R_{500} , where m_R^* is the characteristic apparent magnitude in R band of the cluster luminosity function. The optical luminosity was also estimated inside R_{500} . We adopt the values for the bright end of the Schechter luminosity function, obtained by Popesso et al. (2006). They found the slope of the bright end $\alpha = -1.09$ and $M^* = -21.83$ inside R_{200} . This value of M^* is already converted for $z = 0$ using the cosmology adopted in this work. For different redshifts we apply an evolutionary correction for M^* from Yee and López-Cruz (1999):

$$M^*(z) = M^*(0) - Qz, \quad (3.5)$$

where $Q = -1.4$.

The first step in estimating the group richness is to convert M^* into m^* and calculate the apparent radius in arcseconds for R_{500} . As we are only interested in galaxies with magnitudes between $m_R^* - 1 \leq m_R \leq m_R^* + 2$, we selected all objects inside R_{500} with magnitudes between $m_R^* - 1 + k_s \leq m_R \leq m_R^* + 2 + k_e$, where k_e and k_s are, respectively, the k correction for elliptical and spiral (Sbc) galaxies. Considering the k correction in the magnitude limits, we can guarantee that all galaxies inside $m_R^* - 1 \leq m_R \leq m_R^* + 2$ are selected. We define N_{grp} as the number of galaxies inside R_{500} and within the magnitude range established previously.

Next we need to estimate the galaxy background contribution and subtract it from N_{grp} . We used 20 fields each with 0.5° in aperture spread randomly inside a 1° annulus, 3 Mpc distant from the center of each galaxy group. In each field, we counted the number of galaxies within the same magnitude range used to extract N_{grp} . The background contribution of galaxies (N_{bkg}) is given by the median number in the 20 fields. To avoid the border effect and contamination by other systems, fields with galaxy counts higher than 3σ or lower than 2σ from the median, were excluded. Finally, the corrected galaxy counts in the group, N_{cor} , is equal to $N_{grp} - N_{bkg}$, where N_{bkg} is normalized by the source area.

Next, we apply the k correction to the galaxies inside R_{500} , following a bootstrap pro-

cedure. This method consists of randomly selecting N_{cor} galaxies from N_{grp} galaxies and applying the k correction to each one. An elliptical k correction is applied to X percent of the N_{cor} galaxies, while a Sbc k correction is applied to $100 - X$ percent. This percentage X of k_e depends on the redshift. We assume that at $z \leq 0.15$ galaxy clusters and groups are composed of 80% early-type galaxies (E and S0), while at $0.15 < z \leq 0.30$ the percentage drops to 50% and for $z > 0.30$, it is equal to 30% (Dressler et al., 1997; Smith et al., 2005; Lopes et al., 2009a). Then, with the corrected magnitudes, we can count the number of galaxies in the range $m_R^* - 1 \leq m_R \leq m_R^* + 2$. We repeat this procedure 100 times. The final value of N_{gals} is provided by the median of the 100 procedures. The richness uncertainty ($\sigma_{N_{gals}}$) is a combination of the uncertainties in the background count (σ_{bkg}) and the bootstrap procedure (σ_{boot}). Thus, $\sigma_{N_{gals}}$ is equal to $\sqrt{\sigma_{bkg}^2 + \sigma_{boot}^2}$.

We applied the same bootstrap procedure to estimate the optical luminosity for each group. Using bins of $\Delta mag = 0.02$, we generated a magnitude distribution for the N_{cor} galaxies inside R_{500} with magnitudes within $m_R^* - 1 \leq m_R \leq m_R^* + 2$. The total optical luminosity (L_{opt}) of each system is given by:

$$L_{opt} = \sum_{i=1}^n N_i 10^{-0.4R_i}, \quad (3.6)$$

where N_i is the corrected counts for each magnitude bin R_i . Then, we transformed the optical luminosity in absolute magnitude (M_{grp}^R) and applied the k correction. To obtain the optical luminosity in solar units, we used the following equation:

$$L_{opt} = 10^{-0.4(M_{grp}^R - M_{\odot}^R)} \quad (3.7)$$

where $M_{\odot}^R = 4.42$ (Blanton and Roweis, 2007). The results for L_{opt} and N_{gals} are shown in Figure 3.2 and listed in Tables E.1 and F.1. The X-Boötes groups have optical luminosities $10^{11} L_{\odot} < L_{opt} < 10^{12} L_{\odot}$, with 9 groups ($\sim 65\%$) having $L_{opt} \leq 0.5 \times 10^{12} L_{\odot}$. Richnesses are in the range $5 < N_{gals} < 60$. The optical luminosity range of the OBS groups is $2 \times 10^9 \lesssim L_{opt} \leq 1.4 \times 10^{12} L_{\odot}$ and richness range is $1 \lesssim N_{gals} \leq 50$. Hence, as expected, the L_{opt} and N_{gals} have values typical of galaxy groups.

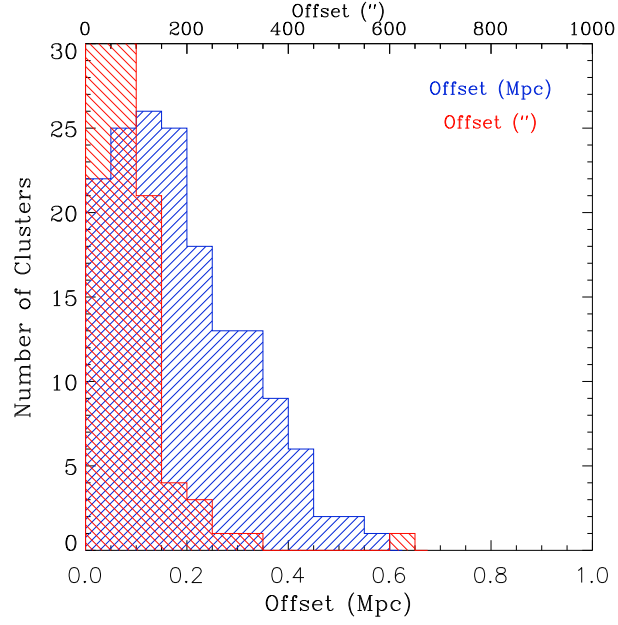


Figure 3.3 Optical and X-ray coordinates offset distribution for the optically selected sample. The lower x-axis shows the radial offsets in Mpc (blue histogram), while the upper x-axis shows the offsets in arcsecond unit (red histogram).

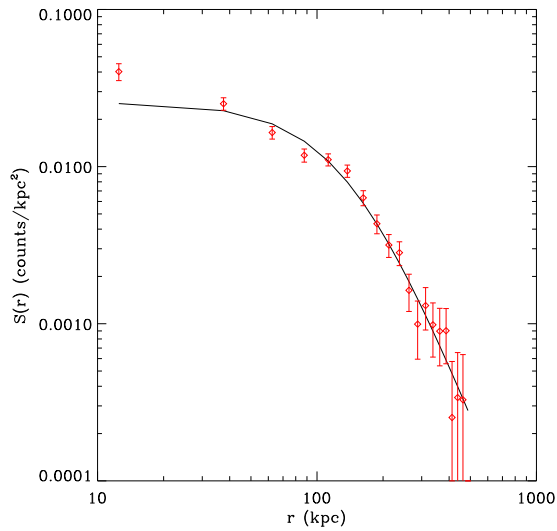


Figure 3.4 Surface brightness profile of the brightest group XBS 06. The β -Model (black line) is characterized by $r_c = 143.3 \pm 3.22$ kpc, $\beta = 0.76 \pm 0.02$ and $S_0 = 0.03 \pm 0.0006$ counts/kpc².

3.3 X-ray Properties Determination

To determine the X-ray luminosity in the 0.5-2 keV energy band for all the groups with determined redshift, we follow the procedure described in Böhringer et al. (2000). The analysis of the X-ray emission for each group consists basically of measuring the net source counts in a specified region of the galaxy group and then converting the count rate into X-ray flux and luminosity.

Before we start to evaluate the X-ray luminosity, we need to determine the center of the X-ray emission for the optically selected groups. These groups have their optical center defined by the VT as the baricenter of the optical emission, which in most of the cases is not coincident with the center of the X-ray emission or with the BGG. For the groups that have their BGG identified ($\sim 40\%$ of the sample), we adopt the BGG as the center of the group. But, even for the groups with identified BGG, we must check if the BGG lies on the center of the X-ray emission.

To re-center the coordinates of the groups, we use the task `funcen` from the package `Funtools`². The X-ray emission center is defined by the baricenter of the photon distribution inside a 0.5 Mpc aperture from the old coordinates. Figure 3.3 shows the offsets between the optical and X-ray coordinates. The red histogram shows the offsets in arcsecond, while the blue histogram presents the offsets in Mpc.

We can see that most of the offsets are smaller than 0.3 Mpc. All groups with identified BGG have offsets smaller than 0.15 Mpc. On the other hand, all the groups with offsets larger than 0.3 Mpc have no BGG identified and less than 10 galaxy members. Their raw counts inside 0.5 Mpc are less than 200 photons, which makes the task of distinguishing the source emission from the background very hard. Due to this reason the X-ray center of those systems was determined by eye.

After recentering the coordinates of the optically selected sample, we proceed to estimate the X-ray luminosity. The first step is to estimate the background counts used to obtain the net source counts for each group. The background contribution in the 0.5-2 keV band is evaluated in an annulus centered on the central coordinates of the group, with inner and outer radii equal, respectively, to $0.5 \text{ Mpc} + 1 \text{ arcminute}$ and $0.5 \text{ Mpc} + 2 \text{ arcminute}$ for groups with $R_{500} \leq 0.5 \text{ Mpc}$, and inner and outer radii equal to $1 \text{ Mpc} + 1 \text{ arcminute}$

²Available in the webpage <http://www.cfa.harvard.edu/~john/funtools>.

and 1 Mpc + 2 arcminute for those with $R_{500} > 0.5$ Mpc. The annulus is divided into 12 equal sectors. We obtain the count rate of each sector by dividing the photon counts by the average exposure time of each sector. We excluded all counts coming from the point sources cataloged in Kenter et al. (2005) from both the background and source counts. In addition, we visually inspected the deep fields in the Boötes region to eliminate the point sources that were not cataloged by Kenter et al. (2005). To avoid the survey border effect and the contamination by other extended sources inside the ring, the median sector count rate was determined and sectors with lower than 2σ or higher than 3σ deviation from the median of all the sectors were discarded from further calculations. The final background count rate is given by the median count rates of the remaining sectors.

The X-ray count rates of the galaxy groups are estimated inside 0.5 Mpc as well as R_{500} , when possible. The background count rate normalized by the source area is subtracted from the source count rate. To convert the net count rates to X-ray flux in the 0.5-2 keV energy band, we use the PIMMS³ software package routine. We calculate the conversion factor from count rates to flux for a source assuming a given spectral model, temperature, abundance and hydrogen column density. We adopted the astrophysical plasma emission code APEC (Smith et al., 2001) to represent the intra-group medium, with a metallicity equal to $0.3Z_{\odot}$ and a temperature of 1 keV. The hydrogen column density (21 cm) in the direction of each group was obtained from Dickey and Lockman (1990). Once the redshift of the group is known, we determine the luminosity, L_{X1} , based on the measured flux. We use this luminosity to better estimate the temperature of the gas using the L_X - T_X relation from Sun (2012):

$$E(z)^{-1}L_X = L_0 \left(\frac{T_X}{2.5keV} \right)^{2.74} \quad (3.8)$$

where T_X is in keV, L_0 is equal to 0.3334×10^{44} ergs s^{-1} and $E(z) = \sqrt{\Omega_m(1+z)^3 + \Omega_\Lambda}$. The temperature estimate allows the calculation of a new flux and new luminosity. We repeat this procedure iteratively, until the difference between the temperatures of the two last iterations is less than 0.1 keV. Usually, the temperature converges in two or three iterations. The k -correction from Böhringer et al. (2000) is applied to obtain the rest-frame X-ray luminosity. To convert the X-ray luminosity in the 0.5-2 keV energy band into bolometric luminosity, we used `xspec` to simulate the spectrum of each group with

³Available on the HEASARC-NASA website

the appropriate n_{H} column density, redshift, temperature and abundance. We assumed a thermal plasma model and a photoelectric absorption model for the IGM. We calculated the ratio between the bolometric (0.1-100 keV) and 0.5-2 keV energy band luminosity and multiplied the rest-frame X-ray luminosity of the group by this ratio, to convert it to bolometric luminosity. The results are shown in Figure 3.2 and listed in Table G.1.

We consider that a group has a reliable X-ray emission, if its counts are higher than 3σ the background deviation. As expected, all X-ray selected groups have reliable X-ray emission. In the optically selected sample, 64 groups have reliable emission, 24 are upper limits and 74 have no X-ray emission.

We also extract the X-ray surface brightness profiles for the groups. Using **SHERPA**⁴, we fit a β -model (Cavaliere and Fusco-Femiano, 1976) to the surface brightness profile:

$$S(r) = S_0 \left(1 + \frac{r^2}{r_c^2} \right)^{-3\beta + \frac{1}{2}} \quad (3.9)$$

where r_c is the core radius and S_0 is the central surface brightness. The background was estimated using the same annulus for the X-ray luminosity estimation. The background region of each group was chosen to be free from contamination of extended sources and far from the detector edge. The counts from point sources were excluded from both the background and source regions. Figure 3.4 shows the β -model fit for the group XBS 06. We were able to extract the parameters of the β -model from the surface brightness profiles for 11 of 32 XBS groups and 11 from the 162 OBS groups, which have at least 200 counts. For groups with counts below 200 photons, it was not possible to determine these parameters. The results are shown in Table G.1. We find that the 11 XBS groups have β slopes between 0.4 and 0.9, while the core radius ranges from 22 to 143 kpc. The 11 OBS groups have β slopes between 0.3 and 0.9 and core radius between 10 to 380 kpc.

Of these 11 XBS groups, we could determine the gas temperature (T_{X}) for 9. And from the 11 OBS groups with brightness profile extracted, we were able to estimate T_{X} for 4 of them. We use CIAO to extract the spectrum of each group inside 0.5 Mpc and R_{500} , using the blank sky fields to subtract the background. The background region has the same area as its respective source region. The procedure differs from our X-ray luminosity and X-ray surface brightness profile analysis, since now it is necessary to use the blank sky to subtract the background, because most of data used to extract the spectra are the

⁴<http://cxc.harvard.edu/sherpa4.4/index.html>

smaller fields from ACIS-S observations. After extracting the spectrum, we used `XSPEC` to fit a thermal model and obtain the temperature of the gas. As we did to convert X-ray luminosity in the 0.5-2 keV energy band into bolometric luminosity, we assume a thermal plasma and photoelectric absorption model for the intra-group medium. We use the n_{H} column density and redshift of each group. As a first trial, we chose T_{X} to be 1 keV and the heavy element abundance to be $0.3Z_{\odot}$ and then constrained those parameters by the spectral fit. We were able to fit the spectrum of 9 groups. The gas temperatures of the XBS groups range from 0.6 to 4 keV, while OBS groups have T_{X} between 0.8 and 3.5 keV. The results are shown in Table G.1.

Chapter 4

Results

4.1 Comparison Between The Samples Selected In Optical and X-ray

After selecting and estimating the dynamical, optical and X-ray properties of the XBS and OBS, we perform a comparative investigation to understand the similarities and differences between the two catalogs. It is well known that there are different methods for selecting galaxy groups and clusters, and each of them can cause a bias in the scaling relations and mass function determination. The optical selection, methods for instance, are generally more sensitive to projection effects than the X-ray selection method. On the other hand, the latter requires that the intracluster gas has already been heated to a detectable level. It is clear that understanding the selection effects and the biases due to different group selection techniques is crucial for interpreting the scientific results obtained from such different group samples.

The first difference between the two catalogs that calls our attention is their sample sizes. While, the XBS has only 32 identified groups, the OBS has 162 systems. To understand this difference, we run a recovering test to find the optical counterparts of the XBS groups. For each X-ray selected system, we look for its optical counterpart assuming that the maximum radial offset between the centroids of the groups cannot exceed 0.5 Mpc and the redshift difference (Δz) must be equal or lower than 0.001. The results of the test are shown in Figures 4.1 and 4.2. There are 10 groups found in both catalogs, 22 groups found only in the X-ray selected sample and 152 found only in the optically selected sample. There is

a small overlap of the samples X-ray selected and optically selected. Only $\sim 31\%$ of the X-ray selected groups were found in the optical sample, while $\sim 6\%$ optical systems were identified in the X-rays. The 10 common groups to the two catalogs are assigned in all tables of this thesis.

From Figures 4.1 and 4.2, we can notice that all the common groups have redshifts higher than $z = 0.1$, X-ray luminosities between $10^{42} - 10^{44}$ ergs s^{-1} and the number of members inside 0.5 Mpc radius ($N_{\text{menmb}}^{0.5\text{Mpc}}$) between 25-50. The selection of groups at low redshifts ($z \ll 0.1$) is hard for small area surveys. In our case, we do not expect to observe many clusters with $L_X > 10^{44}$ ergs s^{-1} , since their numeric density is equal to 10^{-6} Mpc $^{-3}$ ¹ and our Chandra survey observations cover only 9 square degrees. Besides the small probability, their projected size would make them very hard to be detected using both techniques, the VT (in the optical spectroscopic data) and the wavelet transform (in the X-ray data). For instance, a cluster with L_X equal to 10^{44} ergs s^{-1} has typically $R_{500} \approx 1$ Mpc. At $z = 0.05$, the projected R_{500} is equivalent to 17 arcminutes, which is the size of the Chandra detector ACIS-I ($16.9' \times 16.9'$). So, clusters more massive and/or at lower redshifts would have their X-ray emission spread in a large area, becoming difficult to distinguish their emission from the background. From the optical point of view, the problem to detect those massive clusters is similar to the X-ray selection. Their galaxies would be scattered in a large area, so the VT would not measure any overdensity compared to the the background distribution. That is why we only expect to identify poor groups at very low redshifts with the Boötes. Besides, the Boötes region was chosen to be mapped because this area had no bright star or galaxy cluster known previously. We can encounter the same issue to detect poor groups. That is also why there are groups only selected either in the optical sample or in the X-ray sample.

¹This is equivalent to say that at $z = 0.1$ we expect to find one cluster of $L_X = 10^{44}$ ergs s^{-1} per 13 square degrees.

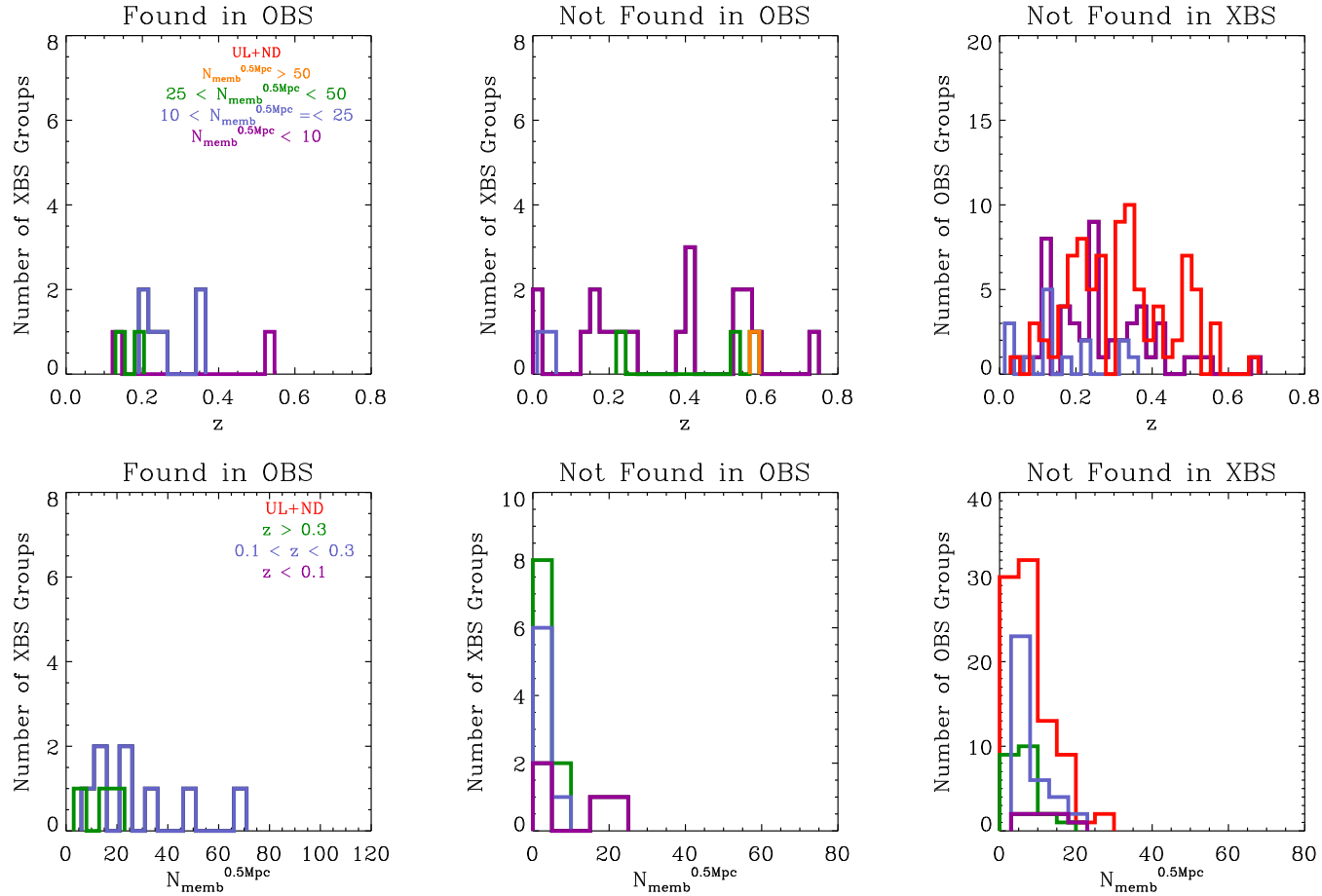


Figure 4.1 Analysis of the X-ray and optically selected systems. The upper panels show the redshift distribution split in three ranges based on the number of members inside 0.5 Mpc ($N_{\text{memb}}^{0.5\text{Mpc}}$): $N_{\text{memb}}^{0.5\text{Mpc}} < 10$ (purple histogram); $10 \leq N_{\text{memb}}^{0.5\text{Mpc}} < 25$ (blue histogram); $25 \leq N_{\text{memb}}^{0.5\text{Mpc}} < 50$ (green histogram). The upper limits and groups with no X-ray emission are shown in red. From the left to the right, we present the distributions of XBS groups found in the optical sample, the XBS groups not found in the optical sample and the OBS groups not found in the X-ray sample. The lower panels show the $N_{\text{memb}}^{0.5\text{Mpc}}$ distribution split in three redshift ranges: $z < 0.1$ (purple histogram); $0.1 \leq z < 0.3$ (blue histogram); $z > 0.3$ (green histogram).

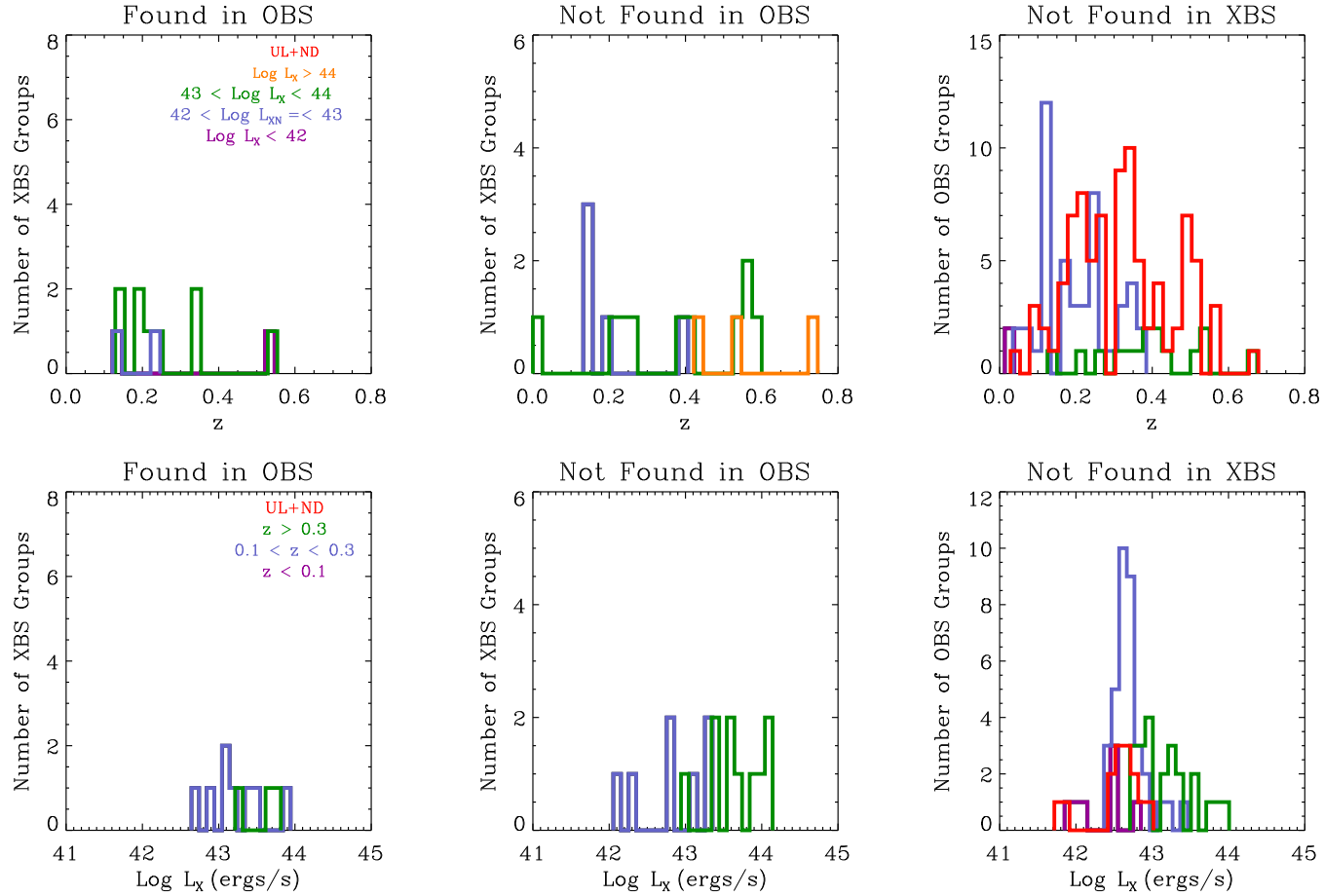


Figure 4.2 Analysis of the X-ray and optically selected systems, similar to Fig. 4.1, but now as a function of L_X . The upper panels show the redshift distribution split in four ranges of X-ray luminosity inside 0.5 Mpc (L_X): $\text{Log } L_X < 42$ (purple histogram); $42 \leq \text{Log } L_X < 43$ (blue histogram); $43 \leq \text{Log } L_X < 44$ (green histogram); $\text{Log } L_X > 44$ (orange histogram). The upper limits and groups with no X-ray emission are shown in red. The lower panels show the $\text{Log } L_X$ distribution split in three redshift ranges: $z < 0.1$ (purple histogram); $0.1 \leq z < 0.3$ (blue histogram); $z > 0.3$ (green histogram).

In Figures 4.1 and 4.2, we can split the X-ray selected groups not found in OBS in three regimes: (i) low redshifts ($z < 0.1$) with $N_{\text{memb}}^{0.5\text{Mpc}}$ lower than 25 and X-ray luminosities lower than 10^{42} ergs s^{-1} ; (ii) intermediate redshifts ($0.1 \leq z < 0.3$) with $N_{\text{memb}}^{0.5\text{Mpc}}$ lower than 10 and L_X between $10^{42} - 10^{43}$ ergs s^{-1} ; (iii) high redshifts ($z > 0.3$) with $N_{\text{memb}}^{0.5\text{Mpc}}$ lower than 10 and L_X lower than 10^{43} ergs s^{-1} . One feature common to the groups in the three ranges of redshift is the small number of members inside the 0.5 Mpc aperture. Among the 22 XBS groups lost in the optical selection, 6 have no galaxy observed by AGES. They are groups XBS 04, 08, 18, 21, 27 and 39. One (XBS 07) is at a low redshift ($z = 0.011$). Seven groups have only one galaxy identified in AGES, the BGG. Since the VT considers a group only the systems with at least three galaxies, these four systems (XBS 05, 28, 29, 35, 41, 42 and 52) could never be considered a group according to the VT definition. But, even systems with three or more galaxies identified may be rejected by the optical selection. If a group with few members is located in a redshift slice crowded with galaxies and its surface density compared to the background is too low or at the same level, it will be rejected as a poisson fluctuation. This is the case for groups XBS 9, 14, 22, 26, 32, 43 and 46.

The 152 optically selected groups not found in XBS can also be split into three redshift ranges: (i) low redshifts with $N_{\text{memb}}^{0.5\text{Mpc}}$ lower than 25 and L_X lower than 10^{43} ergs s^{-1} ; (ii) intermediate redshifts with $N_{\text{memb}}^{0.5\text{Mpc}}$ lower than 25 and L_X between $10^{42} - 10^{44}$ ergs s^{-1} ; (iii) high redshifts with $N_{\text{memb}}^{0.5\text{Mpc}}$ lower than 10 and L_X between $10^{42} - 10^{44}$ ergs s^{-1} . All upper limits and X-ray zero emission groups were not in the X-ray selection. Since the upper limits are below the threshold of 3σ adopted by Kenter et al. (2005), it was already expected that no upper limit would be present in the XBS. There are a total of 24 X-ray upper limits and 74 X-ray non-detected emission groups in the OBS, all of them lost in the X-ray selection. Another property important to explain the difference in numbers of groups selected in the two catalogs is the completeness of the X-Boötes Survey. According to Kenter et al. (2005), their on axis detection limit is $\approx 1 \times 10^{-14}$ cgs (0.5-2 keV) for sources that are demonstrably larger than the local PSF. Also, based on the surface density distribution per flux for galaxy clusters, the Log N -Log S relation, reported by Vikhlinin et al. (1998) and Rosati et al. (2002), their flux limit and the survey area, Kenter's extended source catalog is less than 50% complete. From the 152 OBS groups with reliable X-ray emission not found in XBS, 36 have $f_X \approx 10^{-14}$ cgs. There are 3 OBS groups not found in XBS located at $z < 0.05$. Most likely, they were lost in the X-ray selection, because their flux was spread in a large

area, becoming hard to distinguish their emission from the background. The remaining 13 present a clumpy X-ray emission, most of the X-ray radiation is associated to individual galaxy members.

After exploring the difference in size of the two selected samples, we want to investigate a second feature that characterizes the groups, which is their X-ray emission. In the optically selected sample, there are three classes of groups based on their X-ray emission, the reliables, upper limits and zero emission groups. It is well known that virialized clusters and groups present a hot intracluster gas which emits in the X-ray. So, the fact we detect systems with X-ray upper limit or no emission at all raises the following question: are these systems real? If they are real, why do we not detect their X-ray emission?

In the case the upper limits and zero emission groups are indeed real systems, there are two immediate hypotheses to explain their low X-ray emission or, in some cases, the lack of emission. First, the most simple one, the survey is too shallow to detect their flux. The second hypothesis is that those are young systems still undergoing the virialization process (Barkhouse et al., 2006; Fang et al., 2007; Popesso et al., 2007). So, their intragroup gas has not yet had time yet to be heated. To explore these two scenarios, we compare the velocity dispersion and spatial distribution of galaxies.

First, we stacked the surface galaxy and the phase-space distribution of the groups, using only the results of the shifting-gapper technique (Section 3.1). Figures 4.3 and 4.4 show, respectively, the stacked surface galaxy and the stacked phase space distributions of the reliable, upper limits, X-ray non-detectable emission and XBS groups.

From Figure 4.3 it is possible to see that the distribution of the OBS with reliable X-ray emission (left panels) and XBS (right panels) groups are very similar. In both redshift bins, they show a very well established center. On the other hand, the upper limits (middle left panels) do not show a clear center at $z < 0.15$, they present a elongated structure in the central region. It is true that there are not many galaxies, since there are only 24 upper limits in the optically selected sample, only 6 of them are located at $z < 0.15$ and they are typically very poor groups ($N_{\text{gals}} < 15$). If the members distribution observed in the upper limit groups is not an artifice of statistically small number of galaxies, this may be an evidence that the upper limits are not yet in equilibrium.

The upper limits at intermediate redshift (lower middle left panel of Figure 4.3) present a central structure, like a core region. It is not so concentrated as the center of the reliable

and XBS groups, but still the surface galaxy distribution of the upper limit groups is more similar to the latter than to the upper limits at low redshift. This feature may be just a selection effect, since in the bin of intermediate-high redshifts only the bright galaxies are detected. If it is not the case, this feature may indicate that the X-ray luminosity of these groups is an upper limit just because the survey is shallow.

The zero emission groups at low redshift (upper middle right panel of Figure 4.3) show a central structure, with the galaxies very spread around the center. It is very similar to what we see in the surface galaxy distribution of the X-ray upper limit systems at low redshift. On the other hand, the zero emission groups at intermediate redshift ($0.15 < z \leq 0.35$) present a very well established center, with the majority of the galaxies very concentrated in the central region, just like the reliable and XBS groups.

A common characteristic to all groups at intermediate redshifts (lower panels of Figure 4.3) is the the small number of galaxies at large radii from the center. This may be a consequence of the survey incompleteness. AGES is complete to $M^* + 1$ to $z = 0.35$, so at intermediate redshifts galaxies fainter than $M^* + 1$ start to be missed. Since, typically galaxies in the outskirts of the groups and clusters are spirals and dwarf ellipticals, which are generally fainter than the early-types from the core region, the loss of galaxies with $M_R < M^* + 1$ have significant impact in the galaxy counts in outer regions of groups and clusters.

Figure 4.4 displays the phase-space diagrams of the reliable (left panels), upper limit (middle left panels), zero emission (middle right panels) and XBS (right panels) groups. In the phase-space diagram of the XBS and reliable groups, it is possible to see the trumpet shaped pattern, a characteristic of the cluster infall regions. This trumpet shape can be seen in both bins of redshift. Galaxy systems are surrounded by infall regions where galaxies are bound to the system but are not in equilibrium. In the Cluster Infall Regions in Sloan Digital Sky Survey project (CIRCS), Rines and Diaferio (2006) have shown that X-ray selected clusters display a characteristic trumpet shaped pattern in the radius-velocity phase-space diagram. These patterns, termed caustics, were first predicted for a simple spherical infall onto clusters (Kaiser, 1987; Regos and Geller, 1989), but later works showed that these patterns actually reflect the dynamics of the infall region (Diaferio and Geller, 1997; Diaferio, 1999). In Rines and Diaferio (2010), the caustic technique to determine the system's mass was applied to groups. But, because they are typically less massive and have

few galaxy members, infall pattern might not be identifiable.

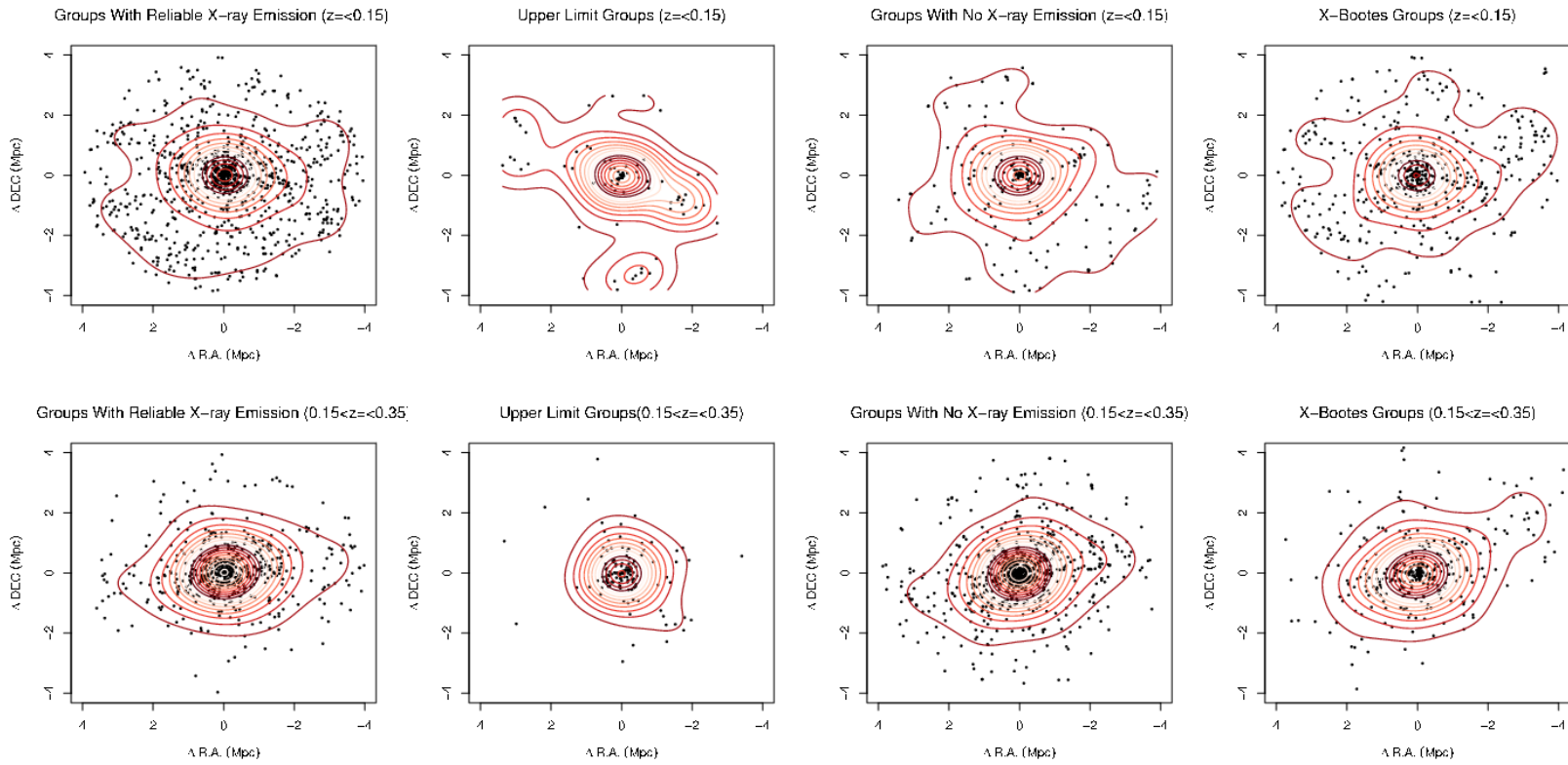


Figure 4.3 Stacked positions of the galaxy members. From left to the right, the panels show the stacked position of the reliable optically selected groups, upper limits, zero emission and X-ray selected groups. The stacked spatial distribution of groups is split in two bins of redshift: $z \leq 0.15$ (upper panels) and $0.15 < z \leq 0.35$ (lower panels).

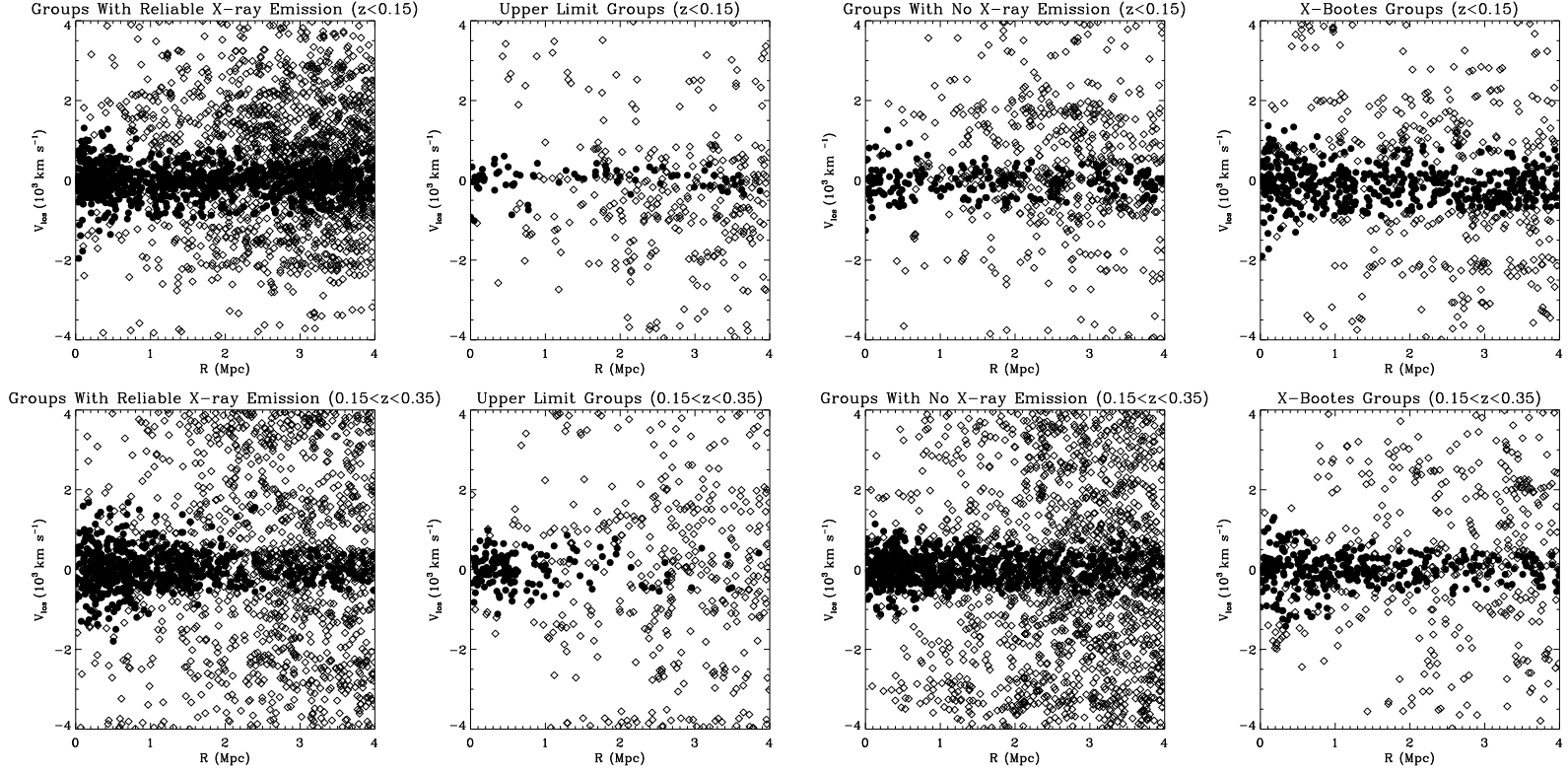


Figure 4.4 Stacked phase-space diagrams. From left to right, the panels show the stacked phase space diagrams of the reliable optically selected groups, upper limits, zero emission and X-ray selected groups. The filled circles represent the galaxies selected as members by the shifting-gapper and the open diamonds the galaxies excluded as interlopers. The stacked phase space diagram of groups is split in two bins of redshift: $z \leq 0.15$ (upper panels) and $0.15 < z \leq 0.35$ (lower panels).

In the low redshift bin, the galaxy members of the upper limit systems are displayed homogeneously along all radii. No matter at which distance from the center of the groups the galaxies are located, they all have velocity dispersion around $\pm 500 \text{ km s}^{-1}$. The upper limit groups at the intermediate bin of redshift have most of their galaxies concentrated at $R < 1 \text{ Mpc}$. The galaxy velocity dispersion in the line-of-sight spreads between $\pm 1000 \text{ km s}^{-1}$ and the infall pattern is not observed like in the reliable and XBS groups.

The zero emission groups display a phase-space diagram similar to the upper limits at both redshift bins. The only difference is the galaxy velocity dispersion in the line-of-sight, which has a broader range. From the surface galaxy distribution and the phase-space diagram, we have some evidence that the XBS and reliable groups are virialized systems. The upper limit and zero emission groups show a different configuration of the surface galaxy and phase-space distribution from the XBS and reliable groups. It is hard to make any affirmative about their dynamical state. Further investigations are needed to have a conclusive answer about their nature.

4.2 Scaling Relations

4.2.1 Optically Selected Sample

In this section, we explore the use of optical and X-ray properties as mass proxies for groups at $z < 0.35$. We compare M_{500} and σ_{gr} to optical (L_{opt}) and X-ray (L_X) luminosities by fitting an orthogonal regression (Akritas and Bershady, 1996). All the scaling relations obtained in this work are of the form:

$$\text{Log}_{10}(Y) = A + B \times \text{Log}_{10}(X). \quad (4.1)$$

The result of the scaling relations are summarized in Table 4.1. The columns give (1) the parameters in the relation (X - Y); (2) Sample(s) used; (3) the intercept (A); (4) the slope (B) and (5) the scatter in the Y parameter at a fixed X .

Figure 4.5 shows the comparison between σ_{gr} and L_{opt} (left panel) and between M_{500} derived from the velocity dispersion and L_{opt} (right panel). All properties were computed within R_{500} . We also compare the optically selected sample (black and red dots) with the Northern Sky Optical Cluster Survey (NoSOCS, gray stars) from Lopes et al. (2009a).

To make the NoSOCS sample comparable to the optically selected sample, the velocity dispersions were recomputed inside R_{500} .

We fit the relations for the OBS groups (black line), for NoSOCS sample (magenta line), Boötes and NoSOCS with no cut in mass (red line), with a mass cut of $M_{500} \leq 5 \times 10^{13} M_{\odot}$ (blue line) and with a mass cut of $M_{500} > 5 \times 10^{13} M_{\odot}$ (green line). The best fit values of the relations $L_{\text{opt}} - \sigma_{\text{gr}}$ and $L_{\text{opt}} - M_{500}$ for the OBS groups agree with the results for NoSOCS, although there is a large scatter in the relation for $\sigma_{\text{gr}} < 400 \text{ km s}^{-1}$ and $M_{500} < 5 \times 10^{13} M_{\odot}$. This can be explained by the fact that low mass systems have fewer than 10 galaxy members selected and their use leads to an increase in the scatter in the scaling relations.

Still in Figure 4.5, it is possible to notice two groups that are detached from the whole sample. The first group consists of four systems (OBS 021, 023, 036, 069) with σ_{gr} between 300-500 km s^{-1} and $L_{\text{opt}} < 1 \times 10^{11} L_{\odot}$. They seem to have low optical luminosity compared to their velocity dispersion. We inspected these four galaxy groups to check if they qualify as fossil group candidates. According to Jones et al. (2003), a fossil group is defined as a system with a $\Delta m_{12} = 2$ magnitude difference between the first and the second rank galaxies within $0.5R_{200}$ and an extended thermal X-ray halo with $L_{X,\text{bol}} > 10^{42} h_{50}^{-2} \text{ erg s}^{-1}$. These four groups have $L_{X,\text{bol}}$ between 3×10^{42} - $2.6 \times 10^{43} \text{ erg s}^{-1}$ and Δm_{12} between 1-1.5, so they are not fossil group candidates, according to this criteria. Another possibility is that their velocity dispersion is overestimated. We examine each group's phase-space diagram and no abnormality was found that could explain the overestimated velocity dispersion. Another factor that can cause the group mass and velocity dispersion to be overestimated is the presence of substructures.

Substructure is defined as the presence of two or more clumps of galaxies and/or gas within a galaxy cluster or group (Pinkney et al., 1996). The most obvious optical observational signature is a multimodality in the spatial or velocity distribution of galaxy members. The presence of substructure in clusters is interpreted as a clear sign of the incomplete relaxation process (Pinkney et al., 1996).

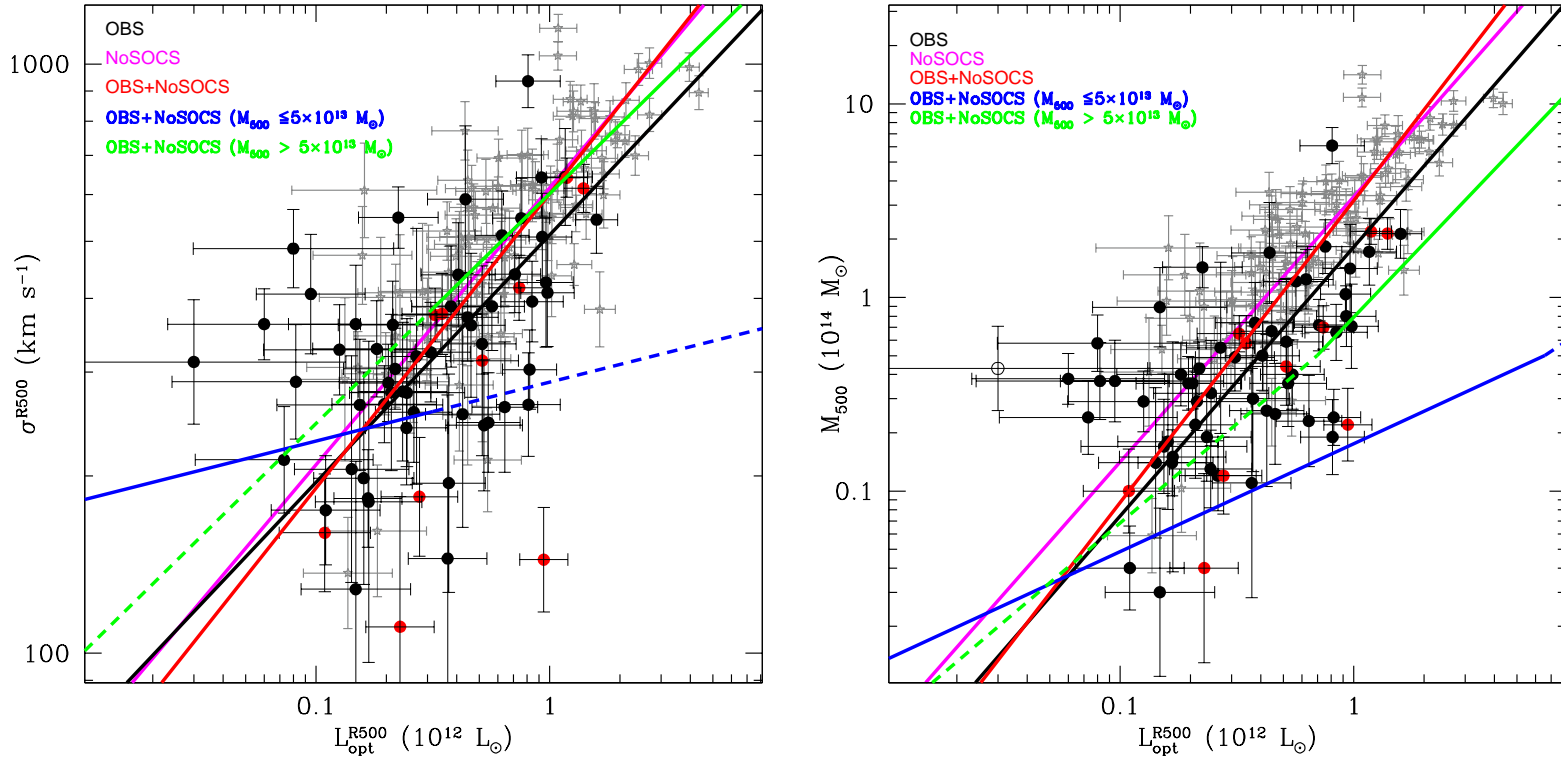


Figure 4.5 Comparison between optical properties for 68 optically selected groups at $z < 0.35$, with at least five member galaxies (black dots) and the NoSOCS sample of galaxy groups and clusters (gray stars). The red dots are the groups with X-ray counterparts. In the left panel, we show the relation between optical luminosity and velocity dispersion (σ - L_{opt}). In the right panel, we show the relation between optical luminosity and mass (M_{500} - L_{opt}). The black line is the orthogonal regression fit using only the OBS groups. The magenta line is the regression fit only for NoSOCS. The red, blue and green lines are, respectively, the orthogonal regression fit for both data sets (OBS and NoSOCS), with $M_{500} \leq 5 \times 10^{13} M_{\odot}$ and with $M_{500} > 5 \times 10^{13} M_{\odot}$.

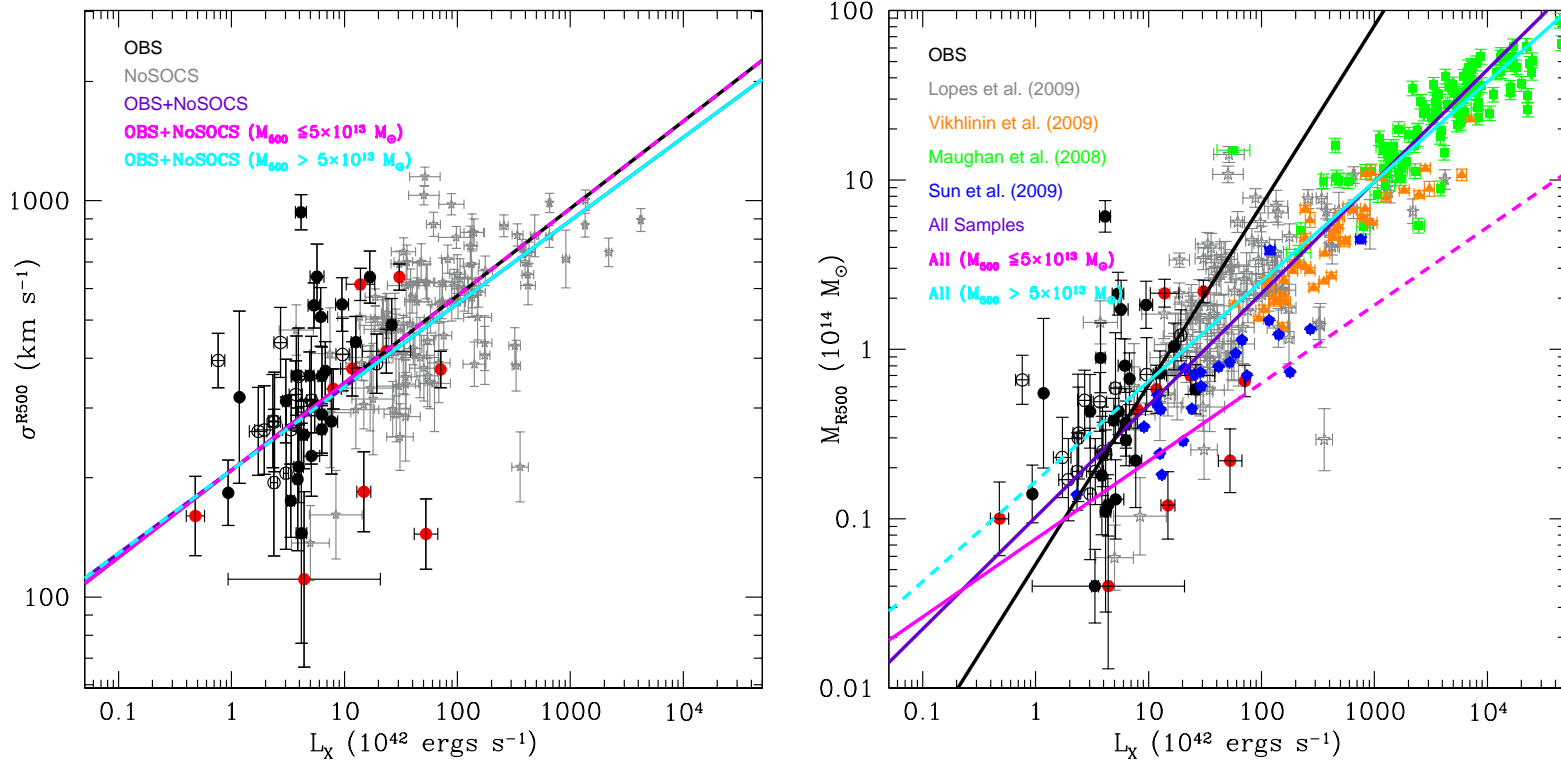


Figure 4.6 Comparison between X-ray properties for 50 OBS groups at $z < 0.35$ with X-ray emission and at least five member galaxies (black dots) and the NoSOCS sample (gray stars). The red dots are the OBS groups with X-ray counterparts. In the left panel, we show the relation between bolometric X-ray luminosity and velocity dispersion (σ - L_X). In the right panel, we show the relation between bolometric X-ray luminosity and total mass derived from the velocity dispersion (M_{500} - L_X) and we also include the results from Vikhlinin et al. (2009) (orange triangles), Maughan et al. (2008) (green squares) and Sun et al. (2009) (blue pentagons). The black line is the orthogonal regression fit using only the OBS groups. The purple, magenta and cyan lines are, respectively, the orthogonal regression fit for all data with no mass cut, with $M_{500} \leq 5 \times 10^{13} M_\odot$ and with $M_{500} > 5 \times 10^{13} M_\odot$.

To verify the possible effects of the presence of substructures on the scaling relations, we apply two tests which have been shown to be very efficient to detect disturbed galaxy distributions in galaxy clusters (Pinkney et al., 1996). The first test is called Δ or DS (Dressler and Shectman, 1988). This is a 3D statistical algorithm which looks for deviations of the local velocity mean and dispersion from the global values of the cluster. The second test is called $\beta - test$ (West et al., 1988) and it quantifies the overall symmetry of the galaxy distribution within a cluster about its center, on the premise that a substructure represents a localized asymmetry superposed on a symmetric distribution.

The substructure tests were applied only to groups with at least 5 members inside R_{200} . The system is considered to have substructures, if the statistical significance of the test is $\leq 5\%$. The test is positive for 17 from the 162 OBS groups ($\approx 10\%$). From the 17 groups with substructure, 11 are X-ray reliable emission groups, 2 are upper limit and 4 are X-ray non-detectable groups. From the 32 XBS groups, only 3 present substructure. All three are common to the OBS samples. The results of the substructure test are listed in the column of Tables E and F.

From the 68 groups used to fit the optical scaling relations, 14 ($\approx 20\%$) have substructure. This includes the four groups (OBS 021, 023, 036, 069) we mentioned before. To examine how the presence of substructure can influence the fit of the optical scaling relations, we excluded the groups positive to substructure from the new fit. For the $L_{\text{opt}} - \sigma_{\text{gr}}$ relation, we obtain $\text{Log}(\sigma_{\text{gr}}) = (2.70 \pm 0.05) + (0.45 \pm 0.10) \times \text{Log}(L_{\text{opt}})$. And for the $L_{\text{opt}} - M_{500}$ relation, we have $\text{Log}(M_{500}) = (0.30 \pm 0.13) + (1.47 \pm 0.25) \times \text{Log}(L_{\text{opt}})$. These values are consistent within 1σ with the results displayed in Table 4.1. So, although, the substructure cause the mass and velocity dispersion to be overestimated, we do not see any influence in the scaling relations fit. Probably, the effects of the presence of the substructure was diluted, since $\approx 80\%$ of sample used to fit the relations is free from any disturbance.

The second group that is detached from the rest of the sample in Fig. 4.5 is the few galaxy groups below $\sigma_{\text{gr}} = 200 \text{ km s}^{-1}$ (left panel) and below $M_{500} = 10^{13} M_{\odot}$ (right panel). These groups raise an old debate in the literature still not settled, whether the relations determined for clusters also hold true for poor clusters and groups. The scaling relations predicted by the self-similar models describe well the rich virialized clusters, because their evolution is driven dominantly by gravitational processes. But, going to smaller scales, other processes (e.g. feedback processes) start to play an important role in the evolution

of the poor clusters and groups. We will come back to this topic and discuss in more detail the presence of a break in the group scaling-relations in Section 4.2.2.

In Figure 4.6, we show the $L_X - \sigma_{\text{gr}}$ (left panel) and $L_X - M_{500}$ (right panel) relations. We use only the groups with reliable X-ray emission to fit the X-ray scaling relations. All properties were computed within R_{500} . We also compare the optically selected sample (black and red dots and open circles) with the samples from Lopes et al. (2009a) (gray stars), Vikhlinin et al. (2009) (orange triangles), Maughan et al. (2008) (green squares) and Sun et al. (2009) (blue pentagons). We fit the relations for the Boötes optically selected sample (black line), for all the samples (purple line) and for all the samples with mass cuts of $M_{500} \leq 5 \times 10^{13} M_\odot$ (magenta line) and $M_{500} > 5 \times 10^{13} M_\odot$ (cyan line).

The best fit values of the $L_X - \sigma_{\text{gr}}$ relation for the Boötes optically selected sample agree with the results for all the samples (NoSOCS and OBS combined), with the self-similar model predictions ($\sigma \propto L_X^{1/4}$) and with the results found in Section 4.2.2 for the XBS groups (Table 4.2, $\sigma_{\text{gr}} \propto L_X^{0.23 \pm 0.07}$). The slope of the $L_X - \sigma_{\text{gr}}$ relation for the OBS groups has a slope of 0.22 ± 0.11 . When we considered the mass cut $M_{500} = 5 \times 10^{13} M_\odot$, the result is a similar slope for both high and low mass regimes (0.21 and 0.22, respectively).

For the $L_X - M_{500}$ relation (right panel of Figure 4.6), the best fit values for the Boötes optically selected sample do not agree either with the results found for all the samples (with mass cut or not) nor with the results found for the XBS groups (Table 4.2). They also disagree with the self-similar model prediction ($L_X \propto M_{\text{Tot}}^{3/4}$). According to the $L_X - M_{500}$ relation fitted to all samples ($L_X \propto M_{500}^{0.66 \pm 0.02}$), it seems that there are some systems with $L_X > 10^{42} \text{ erg s}^{-1}$ and $M_{500} > 10^{13} M_\odot$ that have low X-ray luminosity compared to their masses. These are not only the upper limit systems, but also groups with reliable X-ray emission, which are responsible for causing the steepening of the OBS $L_X - M_{500}$ relation.

Other works (Barkhouse et al., 2006; Fang et al., 2007; Popesso et al., 2007) have reported the detection of an optically selected cluster population that deviate from the X-ray scaling relations. Two scenarios have been invoked to explain this behavior: (i) those cluster are severely affected by projection effects, caused by filamentary large-scale structures along the line-of-sight; (ii) those are young clusters detected in a initial evolutionary stage, when they are still undergoing the virialization process.

To better understand the nature of these groups and explore the two scenarios above, we inspect the residual distribution of the $L_X - M_{500}$ relation along the L_X axis. We define

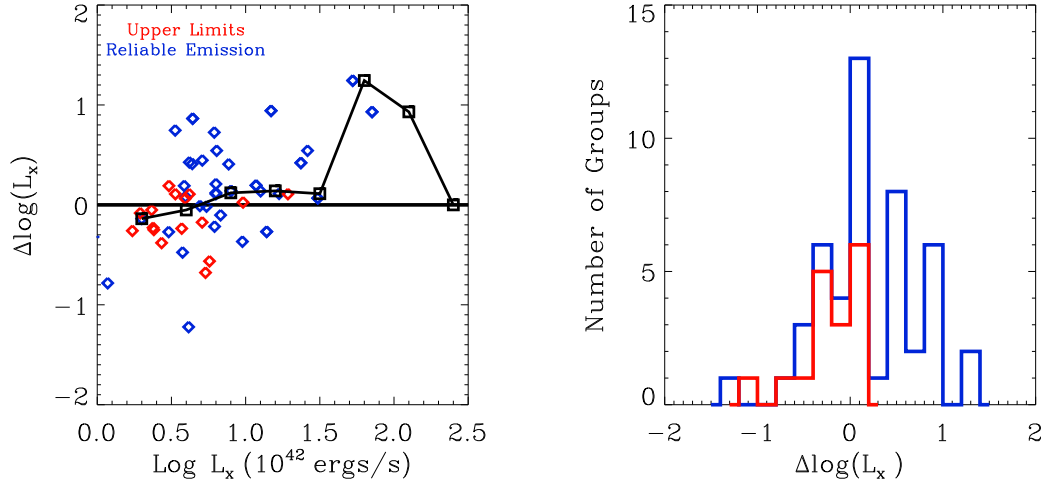


Figure 4.7 The X-ray luminosity residuals $\Delta\text{Log}(L_X)$ from the best fit L_X - M_{500} relation of all 5 samples (see Table 4.1), vs. the X-ray luminosity. Open squares represent the median of the luminosity residual per X-ray luminosity bin. The right panel shows the luminosity distribution. In both panels, the groups with X-ray reliable emission are represented in blue and the upper limits in red.

the residual as $\Delta\text{Log}(L_X) = \text{Log}(L_{X,m}) - \text{Log}(L_{X,p})$, where $L_{X,m}$ is the measured X-ray luminosity and $L_{X,p}$ is the X-ray luminosity predicted by the second L_X - M_{500} relation from Table 4.1 ($L_X \propto M_{500}^{0.66 \pm 0.02}$, fitted for all samples of groups and clusters). The negative residual values indicate that the group has a low X-ray luminosity compared to its mass. We designate X-ray underluminous groups as those systems (with reliable X-ray emission or upper limits) whose residual is negative.

Figure 4.7 shows the residual distribution of the L_X - M_{500} relation. The groups with reliable X-ray emission are represented in blue and the upper limits in red. Twenty one ($\approx 43\%$) OBS groups from the L_X - M_{500} relation have a negative residual. Of these 21, 11 are upper limits and 10 have reliable X-ray emission, all with $L_X \lesssim 10^{43} \text{ erg s}^{-1}$. Ten percent of the systems with negative residual have L_X at least 3 times less luminous than they should be. As we can notice, the underluminous systems have L_X values typical of groups and poor clusters.

To verify the possibility that mass is overestimated, we checked for the presence of sub-

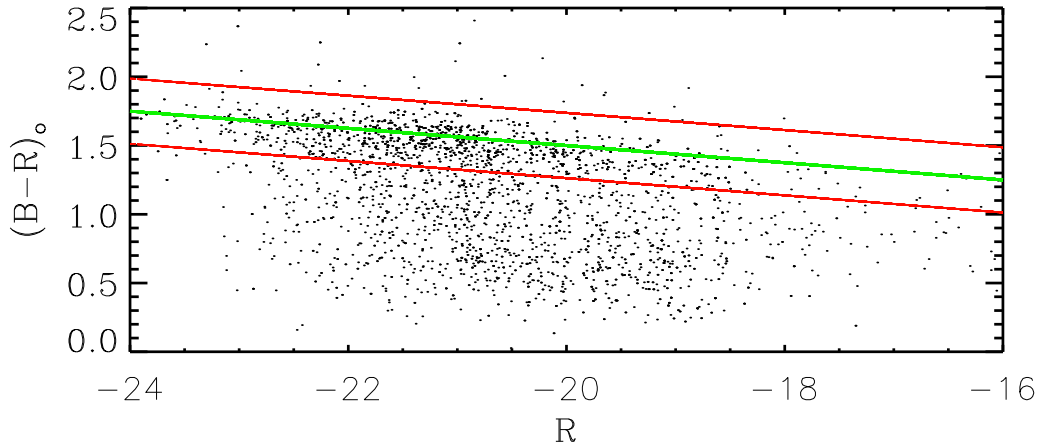


Figure 4.8 The Color-Magnitude Diagram of the Reliable Groups (OBS and XBS). The green line is the best fit of the red sequence. The red lines delimit the 2σ confident level region.

structure. From the 21 underluminous groups, 9 are positive for the presence of substructure (7 with reliable X-ray emission and 2 upper limits). So the presence of substructure may be causing the mass to be overestimated, making these systems seem to be underluminous. In the case of the two upper limit groups, the presence of substructure may be also additional evidence that these two systems are not evolved yet.

To what regards to the other 12 groups, it is not explained yet why they deviate so severely from the L_X - M_{500} relation. If these groups are indeed still young forming systems, we should expect other evidence of their evolutionary stage. To look for other traces of the underluminous group nature, we analyze their galaxy population. To compare the galaxy population composition of the normal and underluminous groups, we decide to split the galaxies according to their colors, in red and blue populations. To do that, we use only the XBS and OBS groups with reliable X-ray emission and which do not deviate from the L_X - M_{500} relation to fit the red sequence from the color-magnitude diagram. We fit the this sequence using only galaxies with M_R between -23 and -20. Figure 4.8 shows the red sequence of the color-magnitude stacked relation of all the XBS and OBS groups with reliable emission which do not deviate from the L_X - M_{500} relation. The green line shows the

best fit and the red line the 2σ interval.

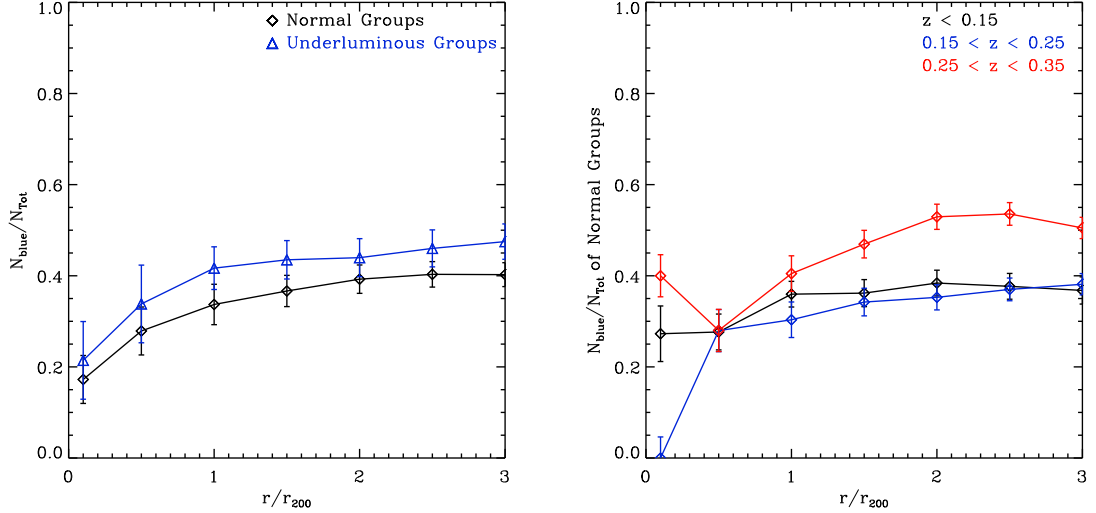


Figure 4.9 The fraction of Blue Galaxies Inside the Groups. The left panel shows the fraction of blue galaxies as a function of the distance from the center of the underluminous (blue triangle) and normal (black diamond) groups. The right panel displays the fraction of blue galaxies of the normal groups per bin of redshift: $z \leq 0.15$ (in black), $0.15 < z \leq 0.25$ (in blue), $0.25 < z \leq 0.35$ (in red).

Using the fit from Figure 4.8, a galaxy is considered to be red if its color is consistent within 2σ with the fit of the red sequence, while a galaxy is considered to be blue if its color is bluer than 2σ of the fit. We use only galaxies with positive colors and $M_R \leq M^* + 1$. Figure 4.9 shows the stacked fraction of blue (left panel) of the normal (black diamonds) and underluminous (blue triangles) groups as a function of R_{200} . The normal sample here consists of all XBS groups and the OBS that have reliable X-ray emission and a positive residual in the L_X - M_{500} relation. While, the called underluminous groups in Figure 4.9 are all the X-ray zero emission and upper limit groups and the reliable with negative residual and no substructure.

As we can already expect, the galaxy population of the reliable groups are dominated by red galaxies. The overall stacked blue fraction of normal groups is 0.39 ± 0.03 . If, we consider that the majority of the blue galaxy population consists of spirals, then this is in agreement with the overall spiral fraction within the virial radius found by Helsdon and

Ponman (2003) ($F_s = 0.425 \pm 0.035$). Considering the distance to the group's center, the population of blue galaxies decreases smoothly until they fall within R_{200} , when it changes abruptly from $\approx 35\%$ to less than 20% at the central region ($0.1R_{200}$). The same behavior can be observed in the underluminous groups, although they have higher blue fractions than normal groups. Their total stacked blue fraction is 0.46 ± 0.05 . The blue population keeps constant between 45-40% until reaches R_{200} , when it starts to decrease abruptly. From R_{200} to $0.5R_{200}$, it drops from 40% to 30%. Then, from $0.5R_{200}$ to $0.1R_{200}$ it reaches 20%.

The right panel of Figure 4.9 shows the stacked fraction of blue galaxies of the normal groups as a function of R_{200} per bins of redshift ($z \leq 0.15$, $0.15 < z \leq 0.25$, $0.25 < z \leq 0.35$). It is possible to see an evolution in the blue galaxy population of the normal systems, in which groups are becoming bluer with the increase of the redshift. At low ($z \leq 0.15$) and intermediate ($0.15 < z \leq 0.25$) redshifts, the blue fractions of normal groups are almost the same, 0.36 ± 0.05 and 0.37 ± 0.04 , respectively. But, at the high redshift bin ($0.25 < z \leq 0.35$) the blue fraction jumps to 0.50 ± 0.04 . This fraction is consistent with the underluminous group's overall blue fraction.

As we mentioned before, blue galaxies consist typically of spiral and irregular galaxies with high star formation rate, also termed late-type. While red galaxies are generally elliptical and S0 galaxies with little star formation, called early-type galaxies. In the group and cluster environment, several different processes (e.g. ram-pressure stripping, strangulation, mergers, tidal stripping from the cluster's potential) are acting to transform late-type in early-type galaxies. Hence, young groups are expected to have their galaxy population bluer than old clusters. This is the natural conclusion for the evolution seen in the right panel of Figure 4.9. Following this line, the higher blue fraction of the underluminous groups compared to the normal ones could be interpreted as an evidence to support the scenario that these are systems still in early evolutionary stages.

Other works (Barkhouse et al., 2006; Fang et al., 2007; Popesso et al., 2007) have shown the existence of an X-ray underluminous optically selected cluster population which deviates from the L_X - M_{Tot} relation. Using the RASS-SDSS data, Popesso et al. (2007), for instance, identified a population of X-ray underluminous systems in the Abell Catalog, called *Abell X-ray Underluminous* (AXU) clusters. They showed that the AXU clusters do not present more substructures than the other clusters from the Abell catalog and that

Table 4.1. Scaling Relations of Luminosity, Velocity Dispersion and Mass of the OBS Groups

Relation (X-Y)	Sample	A	B	$\sigma_{\text{LogY X}}$
$L_{\text{opt}}^{\text{R500}} - \sigma^{\text{R500}}$	OBS	2.71 ± 0.04	0.42 ± 0.09	0.31
	NoSOCS	2.79 ± 0.01	0.47 ± 0.04	0.22
	OBS, NoSOCS	2.78 ± 0.01	0.50 ± 0.04	0.23
	OBS, NoSOCS ($M_{500} > 5 \times 10^{13} M_{\odot}$)	2.78 ± 0.01	0.39 ± 0.03	0.23
	OBS, NoSOCS ($M_{500} \leq 5 \times 10^{13} M_{\odot}$)	2.46 ± 0.11	0.10 ± 0.18	0.38
$L_{\text{opt}}^{\text{R500}} - M_{500}$	OBS	0.26 ± 0.11	1.39 ± 0.22	0.29
	NoSOCS	0.52 ± 0.03	1.37 ± 0.13	0.19
	OBS, NoSOCS	0.50 ± 0.03	1.56 ± 0.10	0.21
	OBS, NoSOCS ($M_{500} > 5 \times 10^{13} M_{\odot}$)	0.48 ± 0.03	1.15 ± 0.09	0.21
	OBS, NoSOCS ($M_{500} \leq 5 \times 10^{13} M_{\odot}$)	-0.24 ± 0.54	0.66 ± 0.86	0.38
$L_{\text{X}}^{\text{R500}} - \sigma^{\text{R500}}$	OBS	2.32 ± 0.09	0.22 ± 0.11	0.79
	NoSOCS	2.36 ± 0.06	0.20 ± 0.03	0.49
	OBS, NoSOCS	2.32 ± 0.04	0.21 ± 0.02	0.58
	OBS, NoSOCS ($M_{500} > 5 \times 10^{13} M_{\odot}$)	2.32 ± 0.04	0.21 ± 0.02	0.58
	OBS, NoSOCS ($M_{500} \leq 5 \times 10^{13} M_{\odot}$)	2.32 ± 0.10	0.22 ± 0.15	0.80
$L_{\text{X}}^{\text{R500}} - M_{500}$	OBS	-1.27 ± 0.49	1.06 ± 0.60	0.75
	All	-0.99 ± 0.05	0.66 ± 0.02	0.75
	All ($M_{500} > 5 \times 10^{13} M_{\odot}$)	-0.78 ± 0.05	0.59 ± 0.02	0.74
	All ($M_{500} \leq 5 \times 10^{13} M_{\odot}$)	-1.12 ± 0.08	0.46 ± 0.09	0.78

their fraction of blue galaxies is slightly higher than the normal clusters. The biggest difference between these two types of systems is their galaxy member velocity distribution. In the AXU clusters, the velocity distribution in the outskirts is consistent with systems in accretion. Their results seem to support the interpretation that the AXU clusters are systems in formation undergoing a phase of mass accretion. Their low X-ray luminosity would be due to the still accreting intracluster gas or to an ongoing merging process.

4.2.2 X-ray Selected Sample

In this section, we explore the use of optical and X-ray properties as mass proxies at $z < 0.35$ for the XBS sample. We compare M_{500} and σ_{gr} to optical (L_{opt}) and X-ray (L_{X}) luminosities by fitting an orthogonal regression, as done before for the OBS groups. The result of the scaling relations are summarized in Table 4.2. The columns give (1) the parameters in the relation (X - Y); (2) Sample(s) used; (3) and (4) the intercept (A) and the slope (B) and their respective uncertainties and (5) the scatter in the Y parameter at a fixed (X).

Figure 4.10 shows the comparison between σ_{gr} and L_{opt} (left panel) and between M_{500} derived from the velocity dispersion and L_{opt} (right panel). All properties were computed within R_{500} . We also compare the X-Boötes sample (black dots) with the NoSOCS sample (gray stars) from Lopes et al. (2009a).

We fit the relations for the Boötes sample (black line), for the NoSOCS sample (magenta line), Boötes and NoSOCS with no cut in mass (red line), with a mass cut of $M_{500} \leq 5 \times 10^{13} M_{\odot}$ (blue line) and with a mass cut of $M_{500} > 5 \times 10^{13} M_{\odot}$ (green line). As shown in Table 4.2, the best fit values of the relations $L_{\text{opt}} - \sigma_{\text{gr}}$ and $L_{\text{opt}} - M_{500}$ for the Boötes sample do not agree with the results for NoSOCS. While the slope of the $L_{\text{opt}} - \sigma_{\text{gr}}$ relation for Boötes has a slope of 0.79 ± 0.09 , the relation for NoSOCS has a slope of 0.47 ± 0.04 . There is also a large scatter in the relation for $\sigma < 400 \text{ km s}^{-1}$. This can be explained by the fact that low mass systems have fewer than 10 galaxy members selected and the use of systems with fewer than 10 galaxies leads to an increase in the scatter in the scaling relations. Due to the large scatter and the few points below $M_{500} \leq 5 \times 10^{13} M_{\odot}$, it is not possible to say if there is a break in the $L_{\text{opt}} - \sigma_{\text{gr}}$ relation between the high and low-mass systems.

Optical scaling relations are generally more difficult to interpret, because their behavior cannot be described by simple physics scaling arguments. This comes from the fact that galaxy properties are the result of a complex non-linear process of formation and evolution.

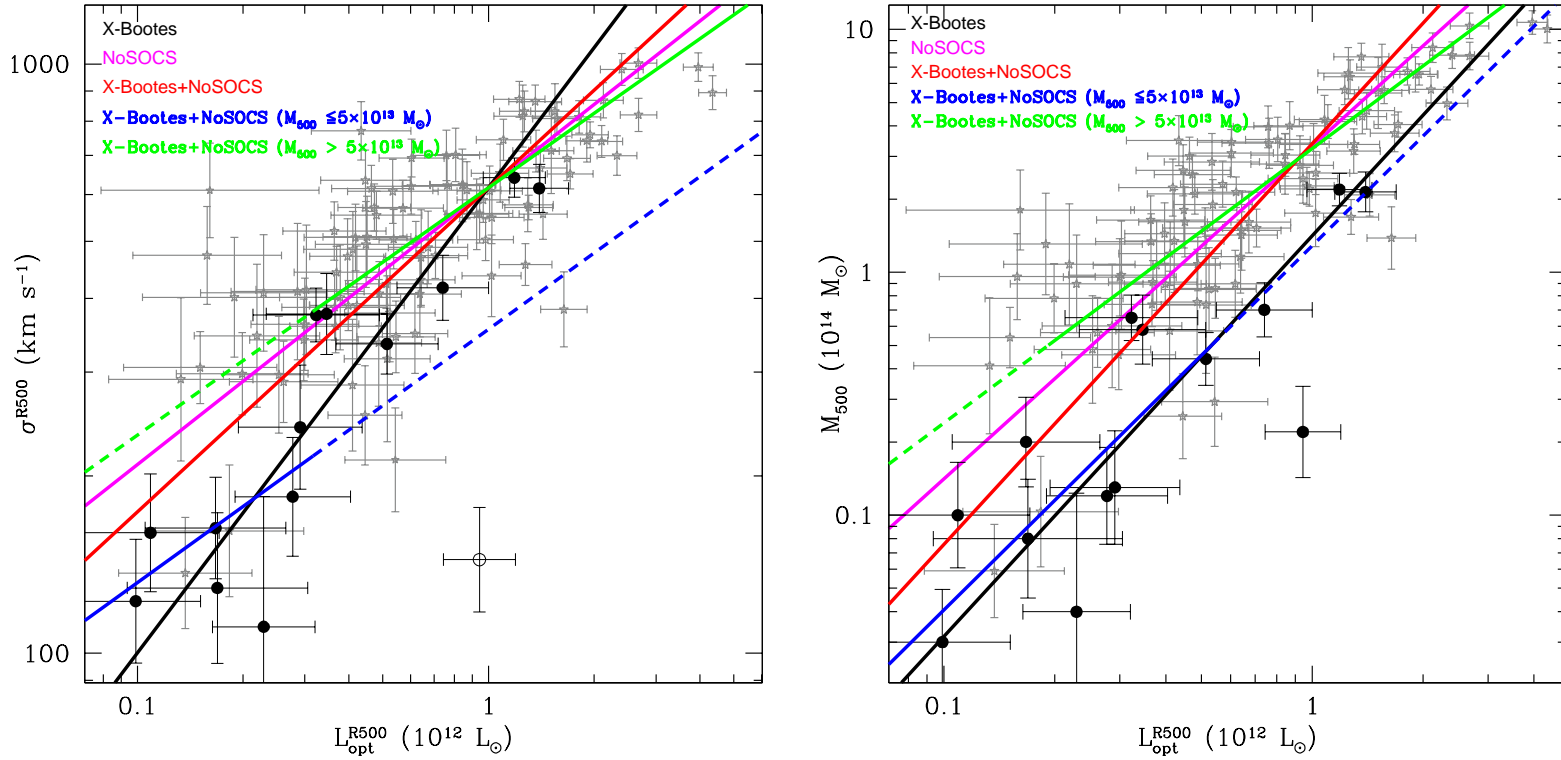


Figure 4.10 Comparison between optical properties for 14 X-Boötes groups at $z < 0.35$, with at least five member galaxies (black dots) and the NoSOCS sample of galaxy groups and clusters (gray stars). In the left panel, we show the relation between optical luminosity and velocity dispersion (σ - L_{opt}). In the right panel, we show the relation between optical luminosity and mass (M_{500} - L_{opt}). The black line is the orthogonal regression fit using only the X-Boötes data. The magenta line is the regression fit only for NoSOCS. The red, blue and green lines are, respectively, the orthogonal regression fit for both data sets (X-Boötes and NoSOCS), both data sets with $M_{500} \leq 5 \times 10^{13} M_{\odot}$ and both data sets with $M_{500} > 5 \times 10^{13} M_{\odot}$.

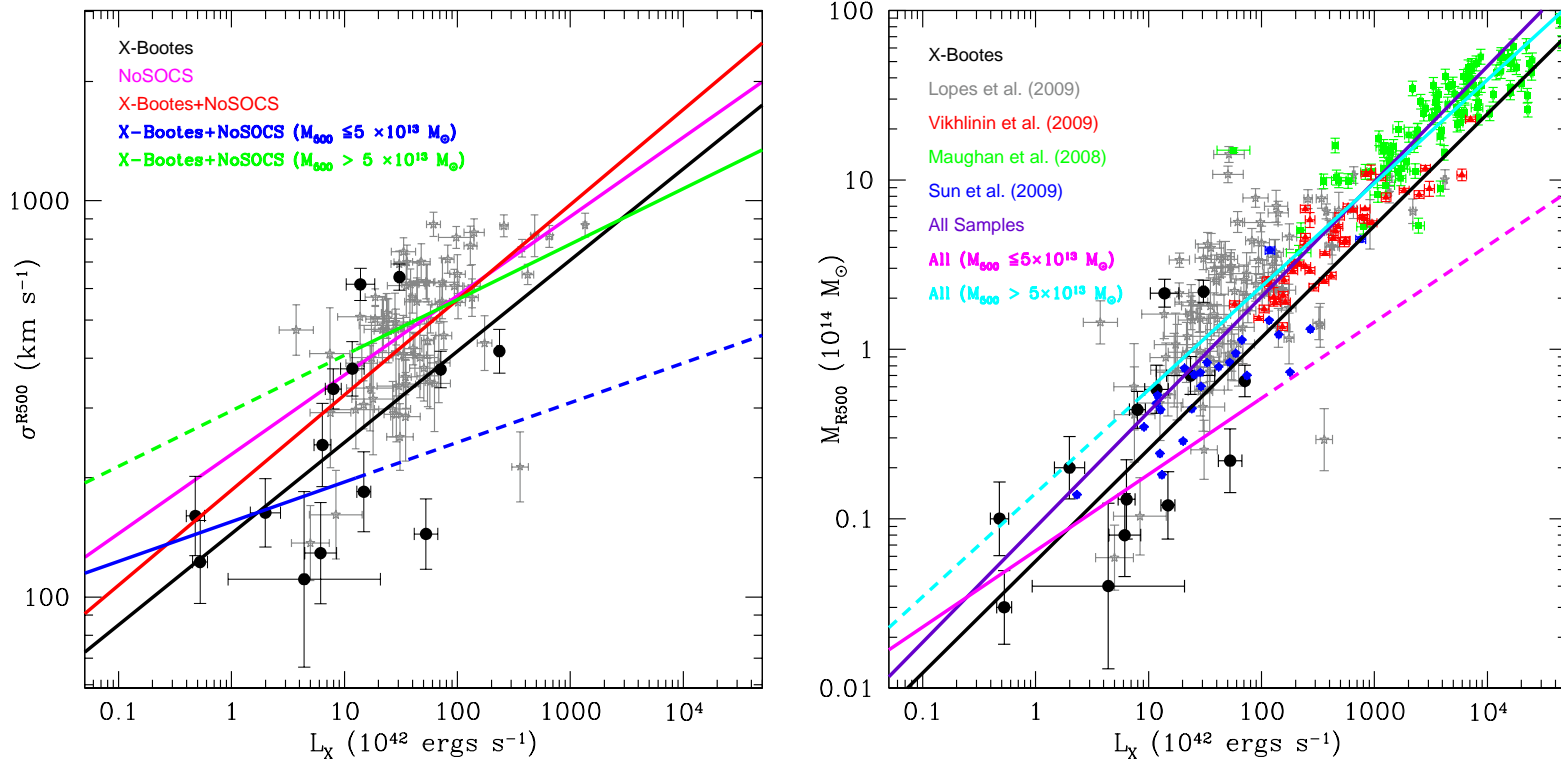


Figure 4.11 Comparison between X-ray properties for 14 X-Boötes groups at $z < 0.35$, with at least five member galaxies (black dots) and the NoSOCS sample (gray stars). In the left panel, we show the relation between bolometric X-ray luminosity and velocity dispersion (σ - L_X). In the right panel, we show the relation between bolometric X-ray luminosity and total mass derived from the velocity dispersion (M_{500} - L_X) and we also include the results from Vikhlinin et al. (2009) (red triangles), Maughan et al. (2008) (green squares) and Sun et al. (2009) (blue pentagons). The black line is the orthogonal regression fit using only the X-Boötes data. The purple, magenta and cyan lines are, respectively, the orthogonal regression fit for all data, all data with $M_{500} \leq 5 \times 10^{13} M_\odot$ and all data with $M_{500} > 5 \times 10^{13} M_\odot$.

According to the self-similar model prediction, the $M_{\text{Tot}}-L_{\text{opt}}$ relation has a predicted power law slope equal to one. For this to be true, the mass-to-light ratio must be constant for the sample. As most studies indicate (e.g. Lopes et al., 2009b), there is an increase of M/L_{opt} with the mass of the cluster. The straightforward result of the dependence of M/L_{opt} on the mass is that the power law slope of the $M_{\text{Tot}}-L_{\text{opt}}$ relation will not be the same for galaxy groups and clusters.

In Figure 4.11, we show the $L_X - \sigma_{\text{gr}}$ (left panel) and L_X-M_{500} (upper panel) relations. All properties were computed within R_{500} . We also compare the X-Boötes sample (black dots) with the samples from Lopes et al. (2009a) (gray stars), Vikhlinin et al. (2009) (red triangles), Maughan et al. (2008) (green squares) and Sun et al. (2009) (blue pentagons). We fit the relations for the Boötes sample (black line), for all the samples (purple line) and for all the samples with mass cuts of $M_{500} \leq 5 \times 10^{13} M_{\odot}$ (magenta line) and $M_{500} > 5 \times 10^{13} M_{\odot}$ (cyan line). It is important to note that differently from X-Boötes and NoSOCS samples, where masses were determined using galaxy dynamics, Vikhlinin et al. (2009); Sun et al. (2009); Maughan et al. (2008) estimated the M_{500} using X-ray data. To verify how the results change if these samples are neglected, we fit the L_X-M_{500} relation using only the X-Boötes and NoSOCS samples. The best fit values are $M_{500} \propto L_X^{0.76 \pm 0.07}$ (for no mass cut), $M_{500} \propto L_X^{0.37 \pm 0.13}$ (for $M_{500} \leq 5 \times 10^{13} M_{\odot}$) and $M_{500} \propto L_X^{0.50 \pm 0.05}$ (for $M_{500} > 5 \times 10^{13} M_{\odot}$). These values are consistent within 1σ with the results displayed in Table 4.2.

Since the X-Boötes sample was X-ray selected, it is clearly not volume limited, but flux limited and therefore various correlations could be subject to Malmquist bias. To test the Malmquist bias in the $L_X - \sigma_{\text{gr}}$ and L_X-M_{500} relations, we choose two volumes ($z = 0.20$ and $z = 0.35$) and determine the limiting X-ray luminosity ($L_X = 1.12 \times 10^{42}$ and $L_X = 4.01 \times 10^{42}$ ergs s^{-1} , respectively) equivalent to the limiting flux of the X-Boötes survey for extended sources ($f_X = 1 \times 10^{-14}$ erg s^{-1} cm^{-2}) in each volume. For $z \leq 0.35$ and $L_X > 4.01 \times 10^{42}$ ergs s^{-1} , the best fit values² are $\sigma_{\text{gr}} \propto L_X^{0.16 \pm 0.12}$ and $M_{500} \propto L_X^{0.83 \pm 0.59}$. And for $z \leq 0.20$ and $L_X > 1.12 \times 10^{42}$ ergs s^{-1} , the best fit values³ are $\sigma_{\text{gr}} \propto L_X^{0.42 \pm 0.27}$ and $M_{500} \propto L_X^{1.13 \pm 0.65}$. The resulting power law exponents of the scaling relations are consistent with the best fit values found for the X-Boötes sample (see Table 4.2). The uncertainties on the fits are large and these are directly linked to the small number of sources used to fit

²In this fit, the groups XBS 07, XBS 26 and XBS 35 were excluded

³In this fit, the groups XBS 02, XBS 07, XBS 11, XBS 33, XBS 35 and XBS 36 were excluded

the relations. For this reason, we cannot conclude that we are not entirely free from the Malmquist bias, but the tests suggest that we are not dominated by it. To investigate it in details, more data and large samples are necessary.

The best fit values of the relation $L_X - \sigma_{\text{gr}}$ for the Boötes sample agree with the results for all the samples (NoSOCS and X-Boötes combined), with the self-similar model predictions ($\sigma \propto L_X^{1/4}$) and with the results found in Figure 8 of Fassnacht et al. (2008), in Mahdavi and Geller (2001) ($\sigma_{\text{gr}} \propto L_X^{0.23^{+0.02}_{-0.03}}$) and in Helsdon and Ponman (2000) ($\sigma_{\text{gr}} \propto L_X^{0.21 \pm 0.03}$). The slope of the $L_X - \sigma_{\text{gr}}$ relation for Boötes has a slope of 0.23 ± 0.07 . When we considered the mass cut $M_{500} = 5 \times 10^{13} M_{\odot}$, the result is a similar slope for both high and low mass regimes (0.14 and 0.10, respectively). For the high mass systems, the slope may have been flattened by 6 clusters from the NoSOCS sample. They have high values for L_X (10^{44} - 10^{45} ergs s^{-1}) compared to their velocity dispersions (700-1000 km s^{-1}). When these 6 clusters are excluded from the fit, the relation has a slope of 0.25 ± 0.05 . In the low mass regime ($M_{500} \leq 5 \times 10^{13} M_{\odot}$), the slope of the relation is obtained using 16 groups and therefore the result is uncertain. So, based on these results, we can not conclude if there is a break in the $L_X - \sigma_{\text{gr}}$ relation.

Although we are unable to determine the existence of a break in the $L_X - \sigma_{\text{gr}}$ relation, there are a set of galaxy groups with $\sigma_{\text{gr}} \leq 200$ km s^{-1} that has an offset in an opposite direction to what would be expected if we consider the effects of feedback processes over the intragroup medium. In the presence of an AGN outburst, for instance, a fraction of the intragroup gas could be expelled from the group gravitational potential. As a direct consequence, the group L_X would decrease, but the velocity dispersion would remain unaltered. But, what is observed from the left panel of Figure 4.11 is that groups with $\sigma_{\text{gr}} \leq 200$ km s^{-1} have higher L_X in comparison with their σ_{gr} . This same phenomenon was observed before by dell'Antonio et al. (1994); Mahdavi et al. (2000); Mahdavi and Geller (2001); Helsdon et al. (2005); Rines and Diaferio (2010).

If the velocity dispersion values estimated from the galaxy velocities in the line of sight (see Section 3.1) are a fair estimate of the 'real' velocity dispersion, then some process must have reduced the velocity dispersion of the galaxies in these systems. Helsdon et al. (2005) suggested three scenarios to explain the reduction of the galaxy velocity dispersion. The first possibility is the dynamical friction, which leads to a transfer of energy from a large orbiting body to the dark matter particles through which it moves. The second possibility

is that orbital energy may be converted into internal energy of galaxies, through tidal interactions. This effect is not significant in clusters, because the orbital velocities of galaxies are substantially higher than their internal velocity dispersion. The third possibility is that much of the orbital motion of the galaxy groups takes place in the plane of the sky and does not contribute to the line of sight velocity dispersion. Tovmassian et al. (2002) showed that it is expected to find elongation and an anisotropic velocity dispersion tensor in many systems, since groups generally form within cosmic filaments.

For the L_X - M_{500} relation (right panel of Figure 4.11), the best fit values for the X-Boötes sample agree with the results found for all the samples with no mass cut and for with the mass cut of $M_{500} > 5 \times 10^{13} M_\odot$. However, in the low mass regime ($M_{500} \leq 5 \times 10^{13} M_\odot$), the slope of 0.45 ± 0.08 does not agree with the steeper slopes (0.61-0.68) found for the other samples. It is clear in Figure 4.11 that there is a break in the L_X - M_{500} relation between low and high mass systems. Thus, galaxy groups cannot be described by the same power law as galaxy clusters.

A large number of researchers (e.g., Reiprich and Böhringer, 2002; Ettori et al., 2002; Maughan et al., 2006; Maughan, 2007; Vikhlinin et al., 2009; Pratt et al., 2009) have measured the slope for L_X - M_{Tot} relation as 0.5-0.7, which is flatter than the self-similar predictions of $M_{\text{Tot}} \propto L_X^{3/4}$. These works show that the ICM is heavily affected by non-gravitational processes. Since L_X comes from the hot ICM, any change in the amount of hot gas in the system will influence the L_X . But, the feedback processes cannot explain the steep L_X - M_{500} relation for low mass systems. If we consider the L_X - M_{500} relation for clusters (purple and cyan lines in Figure 4.11), the groups show an excess of L_X compared to M_{500} . Since the M_{500} of the X-Boötes groups were derived from the velocity dispersion (see Section 3.1), reduction in the velocity dispersion will provoke a reduction in M_{500} . As we mentioned before, dynamical friction, tidal interactions between the galaxy members of the group and projection effects can decrease the velocity dispersion values. These effects are not significant in clusters, causing the L_X - M_{500} to be steeper for groups than for clusters.

4.3 X-ray Luminosity Function

Using the survey solid angle, we calculate the number of groups per flux bin, the LogN-LogS relation, for the Boötes group sample which is complete to $f_X = 1 \times 10^{-14} \text{ ergs s}^{-1} \text{ cm}^{-2}$.

Table 4.2. Scaling Relations of Luminosity, Velocity Dispersion and Mass of the XBS Groups

Relation (X-Y)	Sample	A	B	$\sigma_{\text{LogY X}}$
$L_{\text{opt}}^{\text{R500}} - \sigma^{\text{R500}}$	XBS	2.79 ± 0.05	0.79 ± 0.09	0.15
	NoSOCS	2.79 ± 0.01	0.47 ± 0.04	0.22
	XBS, NoSOCS	2.79 ± 0.01	0.55 ± 0.04	0.21
	XBS, NoSOCS ($M_{500} > 5 \times 10^{13} M_{\odot}$)	2.79 ± 0.01	0.42 ± 0.03	0.21
	XBS, NoSOCS ($M_{500} \leq 5 \times 10^{13} M_{\odot}$)	2.55 ± 0.24	0.43 ± 0.36	0.47
$L_{\text{opt}}^{\text{R500}} - M_{500}$	XBS	0.15 ± 0.12	1.65 ± 0.17	0.23
	NoSOCS	0.52 ± 0.03	1.37 ± 0.13	0.19
	XBS, NoSOCS	0.53 ± 0.04	1.65 ± 0.12	0.20
	XBS, NoSOCS ($M_{500} > 5 \times 10^{13} M_{\odot}$)	0.51 ± 0.03	1.13 ± 0.08	0.19
	XBS, NoSOCS ($M_{500} \leq 5 \times 10^{13} M_{\odot}$)	0.11 ± 0.37	1.50 ± 0.50	0.29
$L_{\text{X}}^{\text{R500}} - \sigma^{\text{R500}}$	XBS	2.16 ± 0.07	0.23 ± 0.07	0.30
	NoSOCS	2.36 ± 0.06	0.20 ± 0.03	0.49
	XBS, NoSOCS	2.27 ± 0.05	0.24 ± 0.03	0.57
	XBS, NoSOCS ($M_{500} > 5 \times 10^{13} M_{\odot}$)	2.47 ± 0.04	0.14 ± 0.02	1.01
	XBS, NoSOCS ($M_{500} \leq 5 \times 10^{13} M_{\odot}$)	2.19 ± 0.05	0.10 ± 0.05	1.38
$L_{\text{X}}^{\text{R500}} - M_{500}$	XBS	-1.25 ± 0.21	0.66 ± 0.21	0.34
	All	-1.05 ± 0.05	0.68 ± 0.02	0.74
	All ($M_{500} > 5 \times 10^{13} M_{\odot}$)	-0.85 ± 0.05	0.61 ± 0.02	0.74
	All ($M_{500} \leq 5 \times 10^{13} M_{\odot}$)	-1.19 ± 0.08	0.45 ± 0.08	0.76

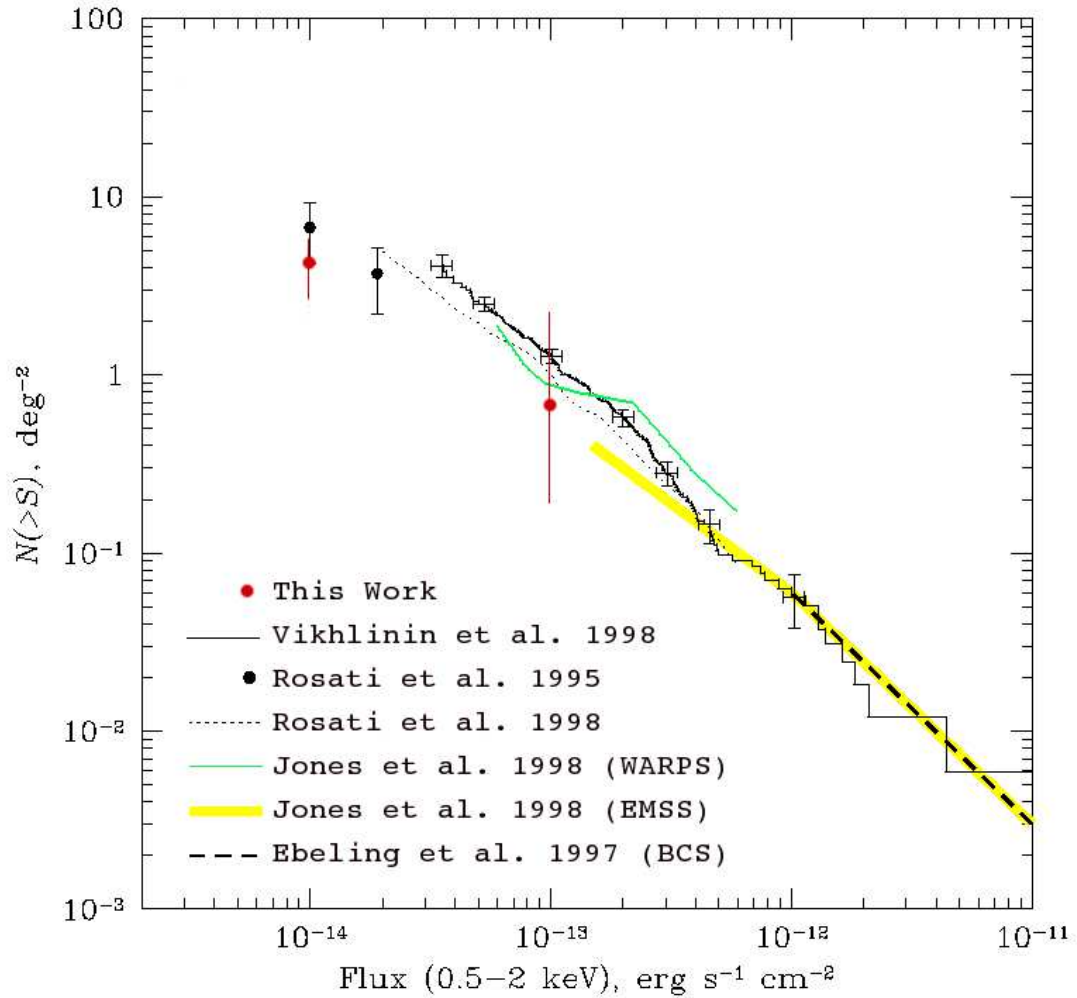


Figure 4.12 Log N -Log S relation. The results from X-Boötes survey are shown as the red dots including error bars. Vertical error bars represent the uncertainty in the number of groups. We compare our results with other surveys: Vikhlinin et al. (1998) (black solid histogram with several individual points including error bars); Rosati et al. (1995) (black dot); Rosati et al. (1998) (black short dashed line); WARPS (green solid line); EMSS (yellow heavy solid line) and BCS (black long dashed line).

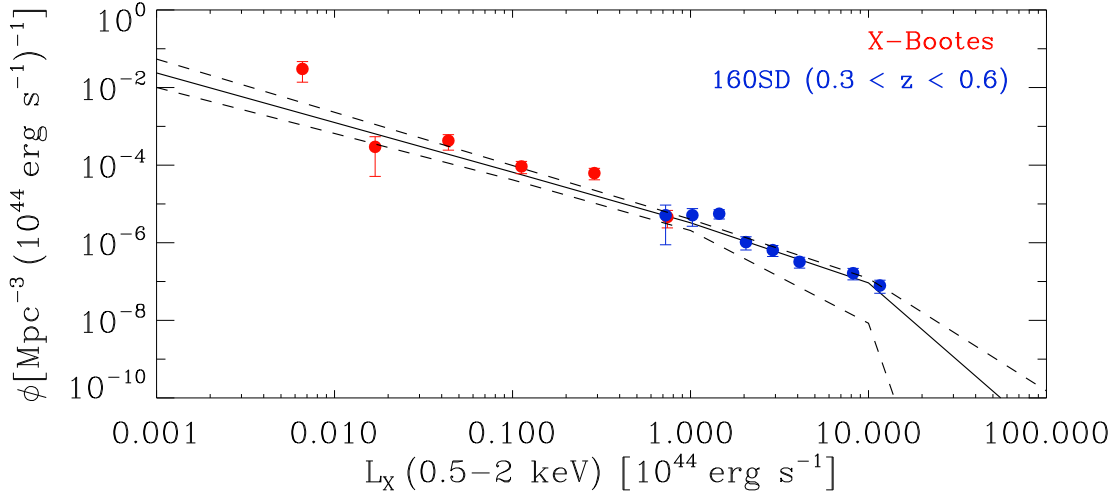


Figure 4.13 Determinations of the group/cluster X-ray luminosity function measured by X-Boötes (red circles) and 160SD (blue circles). The Schechter fit for the nonparametric data points is represented by the black line. The dashed lines represent the 1σ uncertainty region of the Schechter fit, assuming the errors for L_X^* and α are correlated. The data point uncertainties are $\pm 1\sigma$.

Table 4.3. Expected Number of Groups Between $L_X^{\min} < L_X < L_X^{\max}$ Inside a Volume
($z_{\min} < z < z_{\max}$)

$L_X^{\min} - L_X^{\max}$	N_{exp}				
	(ergs s^{-1})	$0 < z \leq 0.046$	$0.046 < z \leq 0.114$	$0.114 < z \leq 0.238$	$0.238 < z \leq 0.319$
$10^{41} - 10^{42}$		1178	17		
$10^{42} - 5 \times 10^{42}$		474	6673	386	
$5 \times 10^{42} - 10^{43}$		147	2067	16419	11

Kenter et al. (2005) estimated that the X-Boötes survey on axis detection limit is $\approx 1 \times 10^{-14}$ cgs (0.5-2 keV) for sources that are just demonstrably larger than the PSF. Since all the extended sources were detected at an existence significance threshold equivalent to $\approx 3\sigma$ and their Gaussian fitted profile have width broader than the local PSF⁴, our sample also is 100% complete.

The derived cumulative Log N -Log S plot is shown in Figure 4.12. We also show the cluster counts derived in: Vikhlinin et al. (1998), EMSS Jones et al. (1998), the ROSAT All-Sky survey sample of X-ray brightest clusters (BCS; Ebeling et al. (1997)), the WARPS survey (Jones et al., 1998) and the ROSAT cluster sample from Rosati et al. (1995, 1998). Our cumulative numerical density of groups spans one order of magnitude in flux. At the faint end, our results are in excellent agreement with the samples of nearby clusters from Rosati et al. (1995,1998), Vikhlinin et al. (1998) and WARPS.

The Log N -Log S relation predicts the number of systems that future large X-ray surveys will observe. The eROSITA all sky survey, in particular, will have an average exposure time of 3 ks and will be complete to $f_X = 3 \times 10^{-14}$ ergs s^{-1} cm^{-2} . Thus, it will be able to observe clusters with masses as small as $3.5 \times 10^{14} h^{-1} M_\odot$ to $z = 2$. Based on Figure 4.12, eROSITA will detect 100,000-130,000 galaxy groups and clusters brighter than $f_X = 3 \times 10^{-14}$ ergs s^{-1} cm^{-2} to $z = 2$, which agrees with the predictions made by Chon and Böhringer (2012) and Pillepich et al. (2012).

With the eROSITA flux limit it will be possible to observe groups which are more luminous than $L_X = 10^{41}$ ergs s^{-1} to $z = 0.046$, groups with $L_X = 10^{42}$ ergs s^{-1} to $z = 0.114$, groups with $L_X = 5 \times 10^{42}$ ergs s^{-1} to $z = 0.238$ and groups with $L_X = 10^{43}$ ergs s^{-1} to $z = 0.319$. To estimate how these groups are distributed in bins of luminosity within a given volume, we build the X-ray luminosity function (XLF).

The differential luminosity function is defined as

$$\phi(L_X, z) = \frac{d^2 N}{dV dL_X}(L_X, z), \quad (4.2)$$

where N is the number of clusters of luminosity L_X in a volume V at a redshift z . Schmidt (1968) was the first to propose the $1/V_{max}$ technique for deriving a nonparametric repre-

⁴During the wavelet detection, Kenter et al. (2005) compared all detected sources with the local PSF. The profile of a detected source was fitted to a Gaussian with the width as a free parameter. The source was only considered extended, if the free parameter fitted width were larger than the local PSF width.

sensation of the differential cluster XLF. Later, this technique was generalized by Avni and Bahcall (1980). Here, we follow the procedure described in Mullis et al. (2004) to fit the XLF, using the X-Boötes sample. We divide the observed luminosity range into bins of width ΔL , within each of which there are N_j observed groups. The luminosity binning is uniform in log space. The XLF is estimated by summing the density contributions of each group in the given luminosity and redshift bin:

$$\phi(L_X, z) = \frac{1}{\Delta L} \sum_{i=1}^{N_j} \frac{1}{V_{max}(L_{X,i})} \quad (4.3)$$

where $L_{X,i}$ is the luminosity of a group and V_{max} is the total comoving volume in which a group with $L_{X,i}$ could have been detected above the flux limits of the survey. The total comoving volume is defined by

$$V_{max}(L_X) = \int_{z_{min}}^{z_{max}} \Omega(f_X(L_X, z)) \frac{dV(z)}{dz} dz. \quad (4.4)$$

$\Omega(f_X)$ is the survey solid angle written as a function of the X-ray flux and $dV(z)/dz$ is the differential comoving volume element per steradians. To fit the group XLF, we adopt the Schechter function (Schechter, 1976),

$$\phi(L_X) = AL_X^{-\alpha} \exp\left(\frac{-L_X}{L_X^*}\right). \quad (4.5)$$

This is the parametric representation of the group/cluster XLF, where L_X^* is the characteristic luminosity marking the transition between the power-law and exponential regimes, α is the faint-end slope, $A = \phi^*/L_X^{1-\alpha}$ and ϕ^* is the normalization in units of Mpc^{-3} .

Typical values of L_X^* are between $10^{44} - 10^{45}$ ergs s^{-1} , depending on the cosmological model adopted. Since the Boötes sample goes only to a maximum of $L_X = 10^{44}$ ergs s^{-1} , we add the 160SD low redshift sample from Mullis et al. (2004) to our data to be able to fit L_X^* . In Figure 4.13, we show the XLF fit (black line) for the X-Boötes (red circles) and 160SD (blue circles) samples. The dashed lines indicate the 1σ region of the Schechter fit assuming the errors for L_X^* and α are correlated. The data are plotted at the center of each luminosity bin. The uncertainties on the data points are $\pm 1\sigma$, based on Poissonian errors for the number of groups per luminosity bin (Gehrels, 1986).

We find $L_X^* = (1.44 \pm 1.12) \times 10^{45}$ ergs s^{-1} , $\alpha = 1.28 \pm 0.09$ and $\phi^* = (1.65 \pm 0.32) \times 10^{-6}$ Mpc^{-3} (10^{44} ergs s^{-1}) $^{-1}$. The value found for L_X^* is compatible with what was found by

Böhringer et al. (2002) for the REFLEX sample ($L_X^* = 1.02_{-0.09}^{+0.11} \times 10^{45}$ ergs s⁻¹)⁵. The normalization $\phi^* = 5.75 \times 10^{-7}$ and the slope $\alpha = 1.69 \pm 0.045$ for the REFLEX differ from what we found here, because the REFLEX sample does not extend as low as $L_X = 10^{41} - 10^{42}$ ergs s⁻¹, the faint end of our XLF.

With the XLF parametrized, we can estimate the expected number of groups (N_{exp}) for a given range of luminosity inside a given volume. Assuming there is no evolution in the XLF, N_{exp} can be computed by integrating the luminosity function $\phi(L_X)$ over a given volume and a luminosity interval, according to this equation:

$$N_{exp} = \int_{L_X^{min}}^{L_X^{max}} \int_{z_{min}}^{z_{max}} \phi(L_X) \Omega(f_X(L_X, z)) \frac{dV(z)}{dz} dz dL_X. \quad (4.6)$$

Assuming that the eROSITA all sky survey will be complete to $f_X = 3 \times 10^{-14}$ ergs s⁻¹ cm⁻², we adopt $\Omega(f_X(L_X, z)) = 4\pi$. To integrate N_{exp} , we consider four intervals of redshift ($0 < z \leq 0.046$, $0.046 < z \leq 0.114$, $0.114 < z \leq 0.238$ and $0.238 < z \leq 0.319$) and three intervals of luminosity ($10^{41} \leq L_X \leq 10^{42}$, $10^{42} \leq L_X \leq 5 \times 10^{42}$ and $5 \times 10^{42} \leq L_X \leq 10^{43}$ ergs s⁻¹ cm⁻²). The results, listed in Table 4.3, show that with eROSITA it will be possible to detect approximately 27,400 groups within $z = 0.32$. Approximately 1800 of these groups between $10^{41} \leq L_X \leq 10^{43}$ ergs s⁻¹ will be within $z = 0.046$, which corresponds to a luminosity distance (D_L) of 200 Mpc. Thus, since groups trace the large scale filaments, the eROSITA survey by determining the locations of groups will map the large scale structures and filaments throughout the local universe.

⁵This value is converted for $\Omega_m = 0.3, \Omega_\Lambda = 0.7$ and $H_0 = 70$ km s⁻¹ Mpc⁻¹.

Chapter 5

Discussion

In this Ph.D. thesis, we have been working to understand the nature of galaxy groups. Due to the small number of galaxy members ($N < 5 - 50$), the faint X-ray flux and low background contrast, this task proved to be very challenging. We have selected two group catalogs using different selection techniques, in two wavelength regimes (X-ray and optical). The first is the XBS sample, which consists of 32 galaxy groups with $z \leq 1.75$, M_{500} between $10^{12} - 10^{14} M_{\odot}$ and L_X ranging from $10^{42} - 10^{45} \text{ erg s}^{-1}$. From the 32 groups, 28 have a BGG identified and 3 tested positive for the presence of substructure. All the groups in the sample are below $z \lesssim 0.7$ with one exception, the group XBS 04. This system is at a very high redshift ($z = 1.75$) and was detected in the IR by Stanford et al. (2012). XBS 04 is beyond the observational expectation of the X-Boötes surveys, which was designed to cover an area with no previously known massive cluster or bright stars.

The second sample contains the 162 OBS groups with $z \leq 0.66$, M_{500} between $10^{12} - 10^{14} M_{\odot}$ and L_X between $10^{41} - 10^{43} \text{ erg s}^{-1}$. Because every selection technique has its own bias, we have two catalogs with very distinct group populations. The two catalogs have a very small overlap. Only 10 systems are found in both samples. This corresponds to less than 6% of the optically selected groups and less than 31% of the X-ray selected one. A similar discrepancy between two catalogs selected in the same region, but at different wavelengths was also reported by Rasmussen et al. (2006); Connelly et al. (2012).

The optically selected samples presents two distinct types of groups: (i) the X-ray luminous groups that are highly dominated by a population of red galaxies; (ii) upper limits and systems with no X-ray detection that have a higher fraction of blue galaxies in

comparison with the former and are also typically less massive.

From the 162 OBS groups, 70 have their BGG identified: 26 are X-ray reliable groups, 8 are X-ray upper limits and 36 are X-ray non-detected systems. Between 45-50% of the identified BGGs for the X-ray upper limits and non-detectable groups are at $z > 0.35$. From 17 presenting substructure, two are X-ray upper limits and four are X-ray non-detected groups, with five of them having no BGG identified. The combination of the presence of substructure, the absence of a dominant bright galaxy and their faint or zero X-ray emission strongly support the interpretation that those four groups are indeed young systems. Since the X-Boötes survey is shallow (5 ks), it is hard to affirm if the remaining upper limit and X-ray non-detected groups have truly such low or any X-ray emission. To have a conclusive answer deeper X-ray data is necessary.

Studying the optical and X-ray scaling relations of galaxy groups and clusters, we have found a break between the low and high mass regime (Figure 4.11). Also, the L_X - M_{500} relation fitted for the OBS groups is steeper ($M_{500} \propto L_X^{1.06}$) than the self-similar model prediction ($M \propto L_X^{3/4}$) and to all other relations found in this thesis. A subsample of the OBS groups appear to have low X-ray luminosity compared to their masses. Hence, either these systems are young groups that did not collapse their intragroup gas, or part of their gas was removed.

One possible hypothesis to explain the break in the scaling relation is the strong influence of non-gravitational processes over the intragroup medium in low mass systems. Feedback effects have a more severe impact in groups and poor clusters, because of their shallow gravitational potential. Important information to elucidate the feedback impact on the IGM is the AGN incidence in dense environments. As a next step in studying the galaxy groups in the Boötes region, we will investigate the relations between the AGN fraction and the group's velocity dispersion and the AGN fraction and local surface density of galaxies. We want to explore how frequent is the presence of AGN in low-mass systems and if there is a high AGN fraction in the groups that deviate from the X-ray scaling relations, which could explain the low X-ray emission of these systems.

Best (2004), Popesso and Biviano (2006), Arnold et al. (2009) and Martini et al. (2009) have shown that AGNs are more frequent in groups and poor clusters than in rich clusters. If this information holds true, the galaxy group evolution is tightly connected to the galaxies of the system. In Popesso and Biviano (2006), the relation found between the AGN fraction

and the velocity dispersion of groups and clusters suggest that the evolution of AGNs may be connected to the evolution of galaxy systems. The high merging rate of low velocity dispersion galaxy systems can produce starburst events in galaxies, followed by the AGN formation. AGN feedback may also be crucial to the star formation extinction in galaxy groups (Cooper et al., 2006) and may provide extra entropy to the ICM (Ettori et al., 2004). The hierarchical growth of galaxy systems causes the increase in their velocity dispersion, which suppresses merging processes and the AGN formation in galaxy clusters.

Best (2004) has shown that the AGN fraction increases with the local surface density of galaxies. The environmental dependence of the AGN fraction strongly supports the argument that galaxy interaction and mergers provide the triggering mechanism for the AGN activity (Heckman et al., 1986). Because of the small velocity dispersion of galaxy groups, interactions, especially, galaxy mergers are more common than in very rich and virialized environments like the central region of rich clusters. Works showing the increase of the AGN fraction in the central region of groups and in outskirts of clusters provide extra support to this model.

Trejo-Alonso et al. (2014) have investigated two cluster samples from Abell’s catalog (Popesso et al., 2007): an X-ray underluminous and a “normal” X-ray emitting cluster sample. The aim was to verify if the ICM was indeed important to model the red sequence in the color-magnitude diagram (CMR). They found that in all ranges of redshift ($0.05 \leq z \leq 0.20$) the red sequence of underluminous clusters has a less steep slope and large spread than the so-called “normal” clusters. According to Trejo-Alonso et al. (2014), the interpretation of the results is that galaxies evolve differently in environments with distinct ICM properties. This can be a consequence of the different dynamical stages of the systems. In the initial phase of the structure formation, a dense ICM is expected to increase the star formation in massive galaxies through the dynamical pressure. In this scenario, the brightest galaxies in the “normal” clusters will have higher metallicities compared to their X-ray underluminous counterparts, which will, consequently, generate CMR with different slopes.

Understanding how the environment affects the galaxy evolution and how feedback processes change the IGM is very important to build a more complete picture of the group evolution. Unlike the rich and virialized clusters which are well described by self-similar models, galaxy groups have a more complex evolution with the contribution of non-gravitational

processes. The break in the scaling-relations is strong evidence of that. In this context, the scaling relations are not just important mass calibrators for large observational surveys, but also an important tool to diagnose the evolutionary stage of galaxy systems.

The connection between galaxy evolution and the presence of hot IGM in low mass groups suggests a link. As for clusters, it is believed that the principal source of hot gas in the IGM is the primordial gas which has fallen into the group potential. But, as suggested by O’Sullivan et al. (2014), one possibility is that star-forming driven galactic winds could contribute to the formation of the IGM. Another is that intergalactic HI could be shock heated by collisions within the group. The latter process is observed in one system, Stephan’s Quintet (HCG 92), in which an infalling spiral galaxy has collided with a tidal HI filament, heating it to a temperature of ~ 0.6 keV (van der Hulst and Rots, 1981; Sulentic et al., 2001; Trinchieri et al., 2003; O’Sullivan et al., 2009).

If our subsample of upper limit and X-ray non-detected groups are proven to be systems still undergoing virialization, they are perfect candidates to investigate the origin of the IGM in low mass groups. Besides the low X-ray luminosity, they have high fractions of blue galaxies compared to the groups with reliable emission and less than 45% have a BGG identified. Combining the deep X-ray observations and radio continuum imaging, it is possible to investigate the origin and the current state of the intragroup medium. Considering that low mass groups are the building blocks to the rich clusters (Peebles, 1970; Gonzalez et al., 2005), understanding the development of the hot IGM is clearly central to any study of structure formation involving groups.

Chapter 6

Conclusions

In this last chapter, the main conclusions of this thesis are summarized.

We have presented two galaxy group samples. We have used the extended source catalog from Kenter et al. (2005) to build the X-ray selected galaxy group catalog. Applying a Voronoi Tessellation, we have constructed an optically selected group catalog. Group redshifts are measured from the AGES (Kochanek et al., 2012) spectroscopic data. Because AGES is complete to $M^* + 1$ galaxies to $z = 0.35$, we applied the virial analysis only to systems with $z \leq 0.35$. Our final sample comprises 32 X-ray selected systems at $z < 1.75$, with 14 below $z = 0.35$ and 162 optically selected groups at $z < 0.66$, with 65 below $z = 0.35$.

For groups with at least five galaxy members inside R_{500} , we apply a virial analysis to estimate velocity dispersions and to obtain the radii (R_{200} and R_{500}) and total masses (M_{200} and M_{500}). To derive the group richness and the optical luminosity, we use photometric data from the NDWFS (Jannuzi and Dey, 1999). The X-ray luminosity for each group is determined from the Chandra X-ray observations.

After measuring the group's properties, we compared the two selected samples. These catalogs have a very small overlap, being only 10 groups common to both catalogs. From the 150 optically selected groups not found in X-ray, 24 have X-ray upper limit detection and 74 have no X-ray detection at all. The identification of X-ray upper limits and non-detected groups raises the question of whether these are really bound systems, and not just the result of projection effect. X-ray upper limit and non-detected groups are typically low mass systems, with fewer than 45% of their BGGs identified. The inspection of their

stacked phase-space diagram and galaxy surface distribution has shown that upper limits have a less concentrated and well determined center than the XBS and OBS groups with reliable X-ray emission. On the other hand, X-ray non-detectable groups display a galaxy distribution very similar to the XBS and OBS groups with reliable X-ray emission.

We have examined the group’s properties as proxies for the group mass. It is important to understand how well these observables measure the total mass, because they will often be used as mass proxies in large surveys (e.g. eROSITA). First, we have presented the scaling relations of optically selected groups, comparing them with samples from the literature. The OBS fit of the optical scaling relations are in good agreement with the theoretical expectations and other samples in the literature.

In the X-ray scaling relations, the fit of the L_X - M_{500} relation for the OBS sample is too steep compared to the self similar model prediction and to the other samples from literature, including the XBS groups. Twenty-one OBS (reliable and upper limits) groups are found to be underluminous according to the residual of the L_X - M_{500} relation. In these 21 underluminous groups, 8 are positive for the presence of substructure, which can be an evidence of their early evolutionary stage. Looking for other traces of the nature of underluminous groups, we analyze their galaxy population. In comparison with XBS and OBS groups with reliable X-ray emission, the underluminous groups present a higher fraction of blue galaxies.

Exploring the scaling relations built with the XBS groups and comparing them with samples from the literature, we find a break in the $L_X - M_{500}$ relation at approximately $M_{500} = 5 \times 10^{13} M_\odot$. A possible explanation for this break can be the dynamical friction, tidal interactions and projection effects which reduce the velocity dispersion values of the galaxy groups. We also examine the $L_X - \sigma_{gr}$, $L_{opt} - M_{500}$ and $L_{opt} - \sigma_{gr}$ relations. But, due to the large scatter in these relations, it is difficult to determine if there is a break between cluster and group samples.

By extending the $\text{Log}N$ - $\text{Log}S$ and the luminosity function to the group regime, we predict the number of groups that the new X-ray survey, eROSITA, will detect per interval of luminosity and distance. eROSITA will observe a total of 27,400 galaxy groups within $z = 0.32$ with L_X between 10^{41} - 10^{43} ergs s^{-1} . The galaxy groups will be a powerful tool for eROSITA to map the large scale structure in the local universe.

Bibliography

- Abell, G. O. (1958). The Distribution of Rich Clusters of Galaxies. *ApJS*, 3:211.
- Abell, G. O., Corwin, Jr., H. G., and Olowin, R. P. (1989). A catalog of rich clusters of galaxies. *ApJS*, 70:1–138.
- Adami, C., Mazure, A., Biviano, A., Katgert, P., and Rhee, G. (1998). The ESO nearby Abell cluster survey. IV. The fundamental plane of clusters of galaxies. *A&A*, 331:493–505.
- Akritis, M. G. and Bershad, M. A. (1996). Linear Regression for Astronomical Data with Measurement Errors and Intrinsic Scatter. *ApJ*, 470:706.
- Allen, S. W., Evrard, A. E., and Mantz, A. B. (2011). Cosmological Parameters from Observations of Galaxy Clusters. *ARAA*, 49:409–470.
- Anderson, M. E., Bregman, J. N., Butler, S. C., and Mullis, C. R. (2009). Redshift Evolution in the Iron Abundance of the Intracluster Medium. *ApJ*, 698:317–323.
- Arnold, T. J., Martini, P., Mulchaey, J. S., Berti, A., and Jeltama, T. E. (2009). Active Galactic Nuclei in Groups and Clusters of Galaxies: Detection and Host Morphology. *ApJ*, 707:1691–1706.
- Ashby, M. L. N., Stern, D., Brodwin, M., Griffith, R., Eisenhardt, P., Kozłowski, S., Kochanek, C. S., Bock, J. J., Borys, C., Brand, K., Brown, M. J. I., Cool, R., Cooray, A., Croft, S., Dey, A., Eisenstein, D., Gonzalez, A. H., Gorjian, V., Grogin, N. A., Ivison, R. J., Jacob, J., Jannuzi, B. T., Mainzer, A., Moustakas, L. A., Röttgering, H. J. A., Seymour, N., Smith, H. A., Stanford, S. A., Stauffer, J. R., Sullivan, I., van Breugel, W., Willner, S. P., and Wright, E. L. (2009). The Spitzer Deep, Wide-field Survey. *ApJ*, 701:428–453.

- Avni, Y. and Bahcall, J. N. (1980). On the simultaneous analysis of several complete samples - The V/V_{\max} and V_e/V_a variables, with applications to quasars. *ApJ*, 235:694–716.
- Bahcall, N. A., Fan, X., and Cen, R. (1997). Constraining Ω with Cluster Evolution. *ApJ*, 485:L53–L56.
- Balestra, I., Tozzi, P., Ettori, S., Rosati, P., Borgani, S., Mainieri, V., Norman, C., and Viola, M. (2007). Tracing the evolution in the iron content of the intra-cluster medium. *A&A*, 462:429–442.
- Balogh, M., Bower, R. G., Smail, I., Ziegler, B. L., Davies, R. L., Gaztelu, A., and Fritz, A. (2002a). Galaxy properties in low X-ray luminosity clusters at $z=0.25$. *MNRAS*, 337:256–274.
- Balogh, M. L., Smail, I., Bower, R. G., Ziegler, B. L., Smith, G. P., Davies, R. L., Gaztelu, A., Kneib, J.-P., and Ebeling, H. (2002b). Distinguishing Local and Global Influences on Galaxy Morphology: A Hubble Space Telescope Comparison of High and Low X-Ray Luminosity Clusters. *ApJ*, 566:123–136.
- Barkhouse, W. A., Green, P. J., Vikhlinin, A., Kim, D.-W., Perley, D., Cameron, R., Silverman, J., Mossman, A., Burenin, R., Jannuzi, B. T., Kim, M., Smith, M. G., Smith, R. C., Tananbaum, H., and Wilkes, B. J. (2006). ChaMP Serendipitous Galaxy Cluster Survey. *ApJ*, 645:955–976.
- Bartelmann, M. (2010). TOPICAL REVIEW Gravitational lensing. *Classical and Quantum Gravity*, 27(23):233001.
- Bauer, A. E., Grützbauch, R., Jørgensen, I., Varela, J., and Bergmann, M. (2011). Star formation in the XMMU J2235.3-2557 galaxy cluster at $z=1.39$. *MNRAS*, 411:2009–2018.
- Beers, T. C., Flynn, K., and Gebhardt, K. (1990). Measures of location and scale for velocities in clusters of galaxies - A robust approach. *AJ*, 100:32–46.
- Best, P. N. (2004). The environmental dependence of radio-loud AGN activity and star formation in the 2dFGRS. *MNRAS*, 351:70–82.

- Biviano, A., Murante, G., Borgani, S., Diaferio, A., Dolag, K., and Girardi, M. (2006). On the efficiency and reliability of cluster mass estimates based on member galaxies. *A&A*, 456:23–36.
- Blanton, M. R. and Roweis, S. (2007). K-Corrections and Filter Transformations in the Ultraviolet, Optical, and Near-Infrared. *AJ*, 133:734–754.
- Boehringer, H., Braglia, F., Pierini, D., Biviano, A., Schuecker, P., Zhang, Y.-Y., Finoguenov, A., Pratt, G. W., Quintana, H., and Lynam, P. D. (2006). Unveiling the Structure of Galaxy Clusters with Combined ESO-VLT WFI, and XMM-Newton Observations. *The Messenger*, 123:49.
- Böhringer, H., Collins, C. A., Guzzo, L., Schuecker, P., Voges, W., Neumann, D. M., Schindler, S., Chincarini, G., De Grandi, S., Cruddace, R. G., Edge, A. C., Reiprich, T. H., and Shaver, P. (2002). The ROSAT-ESO Flux-limited X-Ray (REFLEX) Galaxy Cluster Survey. IV. The X-Ray Luminosity Function. *ApJ*, 566:93–102.
- Böhringer, H., Voges, W., Huchra, J. P., McLean, B., Giacconi, R., Rosati, P., Burg, R., Mader, J., Schuecker, P., Simiç, D., Komossa, S., Reiprich, T. H., Retzlaff, J., and Trümper, J. (2000). The Northern ROSAT All-Sky (NORAS) Galaxy Cluster Survey. I. X-Ray Properties of Clusters Detected as Extended X-Ray Sources. *ApJS*, 129:435–474.
- Brand, K., Brown, M. J. I., Dey, A., Jannuzi, B. T., Kochanek, C. S., Kenter, A. T., Fabricant, D., Fazio, G. G., Forman, W. R., Green, P. J., Jones, C. J., McNamara, B. R., Murray, S. S., Najita, J. R., Rieke, M., Shields, J. C., and Vikhlinin, A. (2006). The Chandra XBoötes Survey. III. Optical and Near-Infrared Counterparts. *ApJ*, 641:140–157.
- Carlberg, R. G., Yee, H. K. C., Ellingson, E., Morris, S. L., Abraham, R., Gravel, P., Pritchet, C. J., Smecker-Hane, T., Hartwick, F. D. A., Hesser, J. E., Hutchings, J. B., and Oke, J. B. (1997). The Average Mass Profile of Galaxy Clusters. *ApJ*, 485:L13–L16.
- Cavaliere, A. and Fusco-Femiano, R. (1976). X-rays from hot plasma in clusters of galaxies. *A&A*, 49:137–144.
- Cavaliere, A. G., Gursky, H., and Tucker, W. H. (1971). Extragalactic X-ray Sources and Associations of Galaxies. *Nature*, 231:437–438.

- Chon, G. and Böhringer, H. (2012). The ROSAT-ESO flux limited X-ray galaxy cluster survey (REFLEX II). I. Newly identified X-ray luminous clusters at $z \geq 0.2$. *A&A*, 538:A35.
- Clowe, D., Bradač, M., Gonzalez, A. H., Markevitch, M., Randall, S. W., Jones, C., and Zaritsky, D. (2006). A Direct Empirical Proof of the Existence of Dark Matter. *ApJ*, 648:L109–L113.
- Connelly, J. L., Wilman, D. J., Finoguenov, A., Hou, A., Mulchaey, J. S., McGee, S. L., Balogh, M. L., Parker, L. C., Saglia, R., Henderson, R. D. E., and Bower, R. G. (2012). Exploring the Diversity of Groups at $0.1 < z < 0.8$ with X-Ray and Optically Selected Samples. *ApJ*, 756:139.
- Cooper, M. C., Newman, J. A., Croton, D. J., Weiner, B. J., Willmer, C. N. A., Gerke, B. F., Madgwick, D. S., Faber, S. M., Davis, M., Coil, A. L., Finkbeiner, D. P., Guhathakurta, P., and Koo, D. C. (2006). The DEEP2 Galaxy Redshift Survey: the relationship between galaxy properties and environment at $z \sim 1$. *MNRAS*, 370:198–212.
- Cora, S. A. (2006). Metal enrichment of the intracluster medium: a three-dimensional picture of chemical and dynamical properties. *MNRAS*, 368:1540–1560.
- Dariush, A., Khosroshahi, H. G., Ponman, T. J., Pearce, F., Raychaudhury, S., and Hartley, W. (2007). The mass assembly of fossil groups of galaxies in the Millennium simulation. *MNRAS*, 382:433–442.
- Davé, R., Oppenheimer, B. D., and Sivanandam, S. (2008). Enrichment and pre-heating in intragroup gas from galactic outflows. *MNRAS*, 391:110–123.
- dell’Antonio, I. P., Geller, M. J., and Fabricant, D. G. (1994). X-ray and optical properties of groups of galaxies. *AJ*, 107:427–447.
- Desjardins, T. D., Gallagher, S. C., Tzanavaris, P., Mulchaey, J. S., Brandt, W. N., Charlton, J. C., Garmire, G. P., Gronwall, C., Hornschemeier, A. E., Johnson, K. E., Konstantopoulos, I. S., and Zabludoff, A. I. (2013). Intragroup and Galaxy-linked Diffuse X-Ray Emission in Hickson Compact Groups. *ApJ*, 763:121.

- Diaferio, A. (1999). Mass estimation in the outer regions of galaxy clusters. *MNRAS*, 309:610–622.
- Diaferio, A. and Geller, M. J. (1997). Infall Regions of Galaxy Clusters. *ApJ*, 481:633–643.
- Dickey, J. M. and Lockman, F. J. (1990). H I in the Galaxy. *ARAA*, 28:215–261.
- D’Onghia, E., Sommer-Larsen, J., Romeo, A. D., Burkert, A., Pedersen, K., Portinari, L., and Rasmussen, J. (2005). The Formation of Fossil Galaxy Groups in the Hierarchical Universe. *ApJ*, 630:L109–L112.
- Dressler, A. (1980). Galaxy morphology in rich clusters - Implications for the formation and evolution of galaxies. *ApJ*, 236:351–365.
- Dressler, A., Oemler, Jr., A., Couch, W. J., Smail, I., Ellis, R. S., Barger, A., Butcher, H., Poggianti, B. M., and Sharples, R. M. (1997). Evolution since $z = 0.5$ of the Morphology-Density Relation for Clusters of Galaxies. *ApJ*, 490:577–591.
- Dressler, A. and Shectman, S. A. (1988). Evidence for substructure in rich clusters of galaxies from radial-velocity measurements. *AJ*, 95:985–995.
- Ebeling, H., Edge, A. C., Fabian, A. C., Allen, S. W., Crawford, C. S., and Boehringer, H. (1997). The ROSAT Brightest Cluster Sample (BCS): The Cluster X-Ray Luminosity Function within $Z = 0.3$. *ApJ*, 479:L101.
- Eckmiller, H. J., Hudson, D. S., and Reiprich, T. H. (2011). Testing the low-mass end of X-ray scaling relations with a sample of Chandra galaxy groups. *A&A*, 535:A105.
- Eke, V. R., Frenk, C. S., Baugh, C. M., Cole, S., Norberg, P., Peacock, J. A., Baldry, I. K., Bland-Hawthorn, J., Bridges, T., Cannon, R., Colless, M., Collins, C., Couch, W., Dalton, G., de Propris, R., Driver, S. P., Efsthathiou, G., Ellis, R. S., Glazebrook, K., Jackson, C. A., Lahav, O., Lewis, I., Lumsden, S., Maddox, S. J., Madgwick, D., Peterson, B. A., Sutherland, W., and Taylor, K. (2004). Galaxy groups in the Two-degree Field Galaxy Redshift Survey: the luminous content of the groups. *MNRAS*, 355:769–784.

- Ettori, S., De Grandi, S., and Molendi, S. (2002). Gravitating mass profiles of nearby galaxy clusters and relations with X-ray gas temperature, luminosity and mass. *A&A*, 391:841–855.
- Ettori, S., Gastaldello, F., Leccardi, A., Molendi, S., Rossetti, M., Buote, D., and Meneghetti, M. (2010). Mass profiles and $c-M_{DM}$ relation in X-ray luminous galaxy clusters. *A&A*, 524:A68.
- Ettori, S., Tozzi, P., Borgani, S., and Rosati, P. (2004). Scaling laws in X-ray galaxy clusters at redshift between 0.4 and 1.3. *A&A*, 417:13–27.
- Evrard, A. E. (1989). Biased cold dark matter theory - Trouble from rich clusters? *ApJ*, 341:L71–L74.
- Fang, T., Gerke, B. F., Davis, D. S., Newman, J. A., Davis, M., Nandra, K., Laird, E. S., Koo, D. C., Coil, A. L., Cooper, M. C., Croton, D. J., and Yan, R. (2007). AEGIS: Chandra Observation of DEEP2 Galaxy Groups and Clusters. *ApJ*, 660:L27–L30.
- Fassnacht, C. D., Kocevski, D. D., Auger, M. W., Lubin, L. M., Neureuther, J. L., Jeltema, T. E., Mulchaey, J. S., and McKean, J. P. (2008). The X-Ray Properties of Moderate-Redshift Galaxy Groups Selected by Association with Gravitational Lenses. *ApJ*, 681:1017–1034.
- Felten, J. E., Gould, R. J., Stein, W. A., and Woolf, N. J. (1966). X-Rays from the Coma Cluster of Galaxies. *ApJ*, 146:955–958.
- Finoguenov, A., Reiprich, T. H., and Böhringer, H. (2001). Details of the mass-temperature relation for clusters of galaxies. *A&A*, 368:749–759.
- Forman, W., Kellogg, E., Gursky, H., Tananbaum, H., and Giacconi, R. (1972). Observations of the Extended X-Ray Sources in the Perseus and Coma Clusters from UHURU. *ApJ*, 178:309–316.
- Fuse, C. and Broming, E. (2013). The X-Ray Evolution of Hickson Compact Groups. *ApJ*, 764:175.
- Gehrels, N. (1986). Confidence limits for small numbers of events in astrophysical data. *ApJ*, 303:336–346.

- Giodini, S., Pierini, D., Finoguenov, A., Pratt, G. W., Boehringer, H., Leauthaud, A., Guzzo, L., Aussel, H., Bolzonella, M., Capak, P., Elvis, M., Hasinger, G., Ilbert, O., Kartaltepe, J. S., Koekemoer, A. M., Lilly, S. J., Massey, R., McCracken, H. J., Rhodes, J., Salvato, M., Sanders, D. B., Scoville, N. Z., Sasaki, S., Smolcic, V., Taniguchi, Y., Thompson, D., and COSMOS Collaboration (2009). Stellar and Total Baryon Mass Fractions in Groups and Clusters Since Redshift 1. *ApJ*, 703:982–993.
- Girardi, M., Giuricin, G., Mardirossian, F., Mezzetti, M., and Boschin, W. (1998). Optical Mass Estimates of Galaxy Clusters. *ApJ*, 505:74–95.
- Gonzalez, A. H., Tran, K.-V. H., Conbere, M. N., and Zaritsky, D. (2005). Galaxy Cluster Assembly at $z=0.37$. *ApJ*, 624:L73–L76.
- Goto, T., Yamauchi, C., Fujita, Y., Okamura, S., Sekiguchi, M., Smail, I., Bernardi, M., and Gomez, P. L. (2003). The morphology-density relation in the Sloan Digital Sky Survey. *MNRAS*, 346:601–614.
- Gunn, J. E. and Gott, III, J. R. (1972). On the Infall of Matter Into Clusters of Galaxies and Some Effects on Their Evolution. *ApJ*, 176:1.
- Gursky, H., Kellogg, E., Murray, S., Leong, C., Tananbaum, H., and Giacconi, R. (1971). A Strong X-Ray Source in the Coma Cluster Observed by UHURU. *ApJ*, 167:L81.
- Heath, D., Krause, M., and Alexander, P. (2007). Chemical enrichment of the intracluster medium by FR II radio sources. *MNRAS*, 374:787–792.
- Heckman, T. M., Smith, E. P., Baum, S. A., van Breugel, W. J. M., Miley, G. K., Illingworth, G. D., Bothun, G. D., and Balick, B. (1986). Galaxy collisions and mergers - The genesis of very powerful radio sources? *ApJ*, 311:526–547.
- Helsdon, S. F. and Ponman, T. J. (2000). Are X-ray properties of loose groups different from those of compact groups? *MNRAS*, 319:933–938.
- Helsdon, S. F. and Ponman, T. J. (2003). The morphology-density relation in X-ray-bright galaxy groups. *MNRAS*, 339:L29–L32.
- Helsdon, S. F., Ponman, T. J., and Mulchaey, J. S. (2005). Chandra Observations of Low Velocity Dispersion Groups. *ApJ*, 618:679–691.

- Helsdon, S. F., Ponman, T. J., O’Sullivan, E., and Forbes, D. A. (2001). X-ray luminosities of galaxies in groups. *MNRAS*, 325:693–706.
- Hilton, M., Lloyd-Davies, E., Stanford, S. A., Stott, J. P., Collins, C. A., Romer, A. K., Hosmer, M., Hoyle, B., Kay, S. T., Liddle, A. R., Mehrrens, N., Miller, C. J., Sahlén, M., and Viana, P. T. P. (2010). The XMM Cluster Survey: Active Galactic Nuclei and Starburst Galaxies in XMMXCS J2215.9-1738 at $z = 1.46$. *ApJ*, 718:133–147.
- Jannuzi, B. T. and Dey, A. (1999). The NOAO Deep Wide-Field Survey. In Weymann, R., Storrie-Lombardi, L., Sawicki, M., and Brunner, R., editors, *Photometric Redshifts and the Detection of High Redshift Galaxies*, volume 191 of *Astronomical Society of the Pacific Conference Series*, page 111.
- Jeltema, T. E., Mulchaey, J. S., Lubin, L. M., and Fassnacht, C. D. (2007). The Evolution of Galaxies in X-Ray-luminous Groups. *ApJ*, 658:865–883.
- Jeltema, T. E., Mulchaey, J. S., Lubin, L. M., Rosati, P., and Böhringer, H. (2006). X-Ray Properties of Intermediate-Redshift Groups of Galaxies. *ApJ*, 649:649–660.
- Johnson, K. E., Hibbard, J. E., Gallagher, S. C., Charlton, J. C., Hornschemeier, A. E., Jarrett, T. H., and Reines, A. E. (2007). The Infrared Properties of Hickson Compact Groups. *AJ*, 134:1522–1543.
- Jones, C. and Forman, W. (1984). The structure of clusters of galaxies observed with Einstein. *ApJ*, 276:38–55.
- Jones, L. R., Ponman, T. J., Horton, A., Babul, A., Ebeling, H., and Burke, D. J. (2003). The nature and space density of fossil groups of galaxies. *MNRAS*, 343:627–638.
- Jones, L. R., Scharf, C., Ebeling, H., Perlman, E., Wegner, G., Malkan, M., and Horner, D. (1998). The WARPS Survey. II. The $\log N$ – $\log S$ Relation and the X-Ray Evolution of Low-Luminosity Clusters of Galaxies. *ApJ*, 495:100.
- Kaiser, N. (1987). Clustering in real space and in redshift space. *MNRAS*, 227:1–21.
- Katgert, P., Biviano, A., and Mazure, A. (2004). The ESO Nearby Abell Cluster Survey. XII. The Mass and Mass-to-Light Ratio Profiles of Rich Clusters. *ApJ*, 600:657–669.

- Katgert, P., Mazure, A., Perea, J., den Hartog, R., Moles, M., Le Fevre, O., Dubath, P., Focardi, P., Rhee, G., Jones, B., Escalera, E., Biviano, A., Gerbal, D., and Giuricin, G. (1996). The ESO Nearby Abell Cluster Survey. I. Description of the dataset and definition of physical systems. *A&A*, 310:8–30.
- Kellogg, E., Gursky, H., Tananbaum, H., Giacconi, R., and Pounds, K. (1972). The Extended X-Ray Source at M87. *ApJ*, 174:L65.
- Kenter, A., Murray, S. S., Forman, W. R., Jones, C., Green, P., Kochanek, C. S., Vikhlinin, A., Fabricant, D., Fazio, G., Brand, K., Brown, M. J. I., Dey, A., Jannuzi, B. T., Najita, J., McNamara, B., Shields, J., and Rieke, M. (2005). XBootes: An X-Ray Survey of the NDWFS Bootes Field. II. The X-Ray Source Catalog. *ApJS*, 161:9–20.
- Kim, R. S. J., Kepner, J. V., Postman, M., Strauss, M. A., Bahcall, N. A., Gunn, J. E., Lupton, R. H., Annis, J., Nichol, R. C., Castander, F. J., Brinkmann, J., Brunner, R. J., Connolly, A., Csabai, I., Hindsley, R. B., Ivezić, Ž., Vogeley, M. S., and York, D. G. (2002). Detecting Clusters of Galaxies in the Sloan Digital Sky Survey. I. Monte Carlo Comparison of Cluster Detection Algorithms. *AJ*, 123:20–36.
- King, I. (1962). The structure of star clusters. I. an empirical density law. *AJ*, 67:471.
- Kochanek, C. S., Eisenstein, D. J., Cool, R. J., Caldwell, N., Assef, R. J., Jannuzi, B. T., Jones, C., Murray, S. S., Forman, W. R., Dey, A., Brown, M. J. I., Eisenhardt, P., Gonzalez, A. H., Green, P., and Stern, D. (2012). AGES: The AGN and Galaxy Evolution Survey. *ApJS*, 200:8.
- Konstantopoulos, I. S., Gallagher, S. C., Fedotov, K., Durrell, P. R., Heiderman, A., Elmegreen, D. M., Charlton, J. C., Hibbard, J. E., Tzanavaris, P., Chandar, R., Johnson, K. E., Maybhate, A., Zabludoff, A. E., Gronwall, C., Szathmary, D., Hornschemeier, A. E., English, J., Whitmore, B., Mendes de Oliveira, C., and Mulchaey, J. S. (2010). Galaxy Evolution in a Complex Environment: A Multi-wavelength Study of HCG 7. *ApJ*, 723:197–217.
- Leauthaud, A., Finoguenov, A., Kneib, J.-P., Taylor, J. E., Massey, R., Rhodes, J., Ilbert, O., Bundy, K., Tinker, J., George, M. R., Capak, P., Koekemoer, A. M., Johnston, D. E., Zhang, Y.-Y., Cappelluti, N., Ellis, R. S., Elvis, M., Giodini, S., Heymans, C., Le

- Fèvre, O., Lilly, S., McCracken, H. J., Mellier, Y., Réfrégier, A., Salvato, M., Scoville, N., Smoot, G., Tanaka, M., Van Waerbeke, L., and Wolk, M. (2010). A Weak Lensing Study of X-ray Groups in the Cosmos Survey: Form and Evolution of the Mass-Luminosity Relation. *ApJ*, 709:97–114.
- Lopes, P. A. A. (2003). *Intermediate Redshift Galaxy Clusters from DPOSS*. PhD thesis, Observatório Nacional Rua General José Cristino, 77, Rio de Janeiro, RJ 20921-400, Brazil.
- Lopes, P. A. A. (2007). Empirical photometric redshifts of luminous red galaxies and clusters in the Sloan Digital Sky Survey. *MNRAS*, 380:1608–1620.
- Lopes, P. A. A., de Carvalho, R. R., Capelato, H. V., Gal, R. R., Djorgovski, S. G., Brunner, R. J., Odewahn, S. C., and Mahabal, A. A. (2006). X-Ray Galaxy Clusters in NoSOCS: Substructure and the Correlation of Optical and X-Ray Properties. *ApJ*, 648:209–229.
- Lopes, P. A. A., de Carvalho, R. R., Gal, R. R., Djorgovski, S. G., Odewahn, S. C., Mahabal, A. A., and Brunner, R. J. (2004). The Northern Sky Optical Cluster Survey. IV. An Intermediate-Redshift Galaxy Cluster Catalog and the Comparison of Two Detection Algorithms. *AJ*, 128:1017–1045.
- Lopes, P. A. A., de Carvalho, R. R., Kohl-Moreira, J. L., and Jones, C. (2009a). NoSOCS in SDSS - I. Sample definition and comparison of mass estimates. *MNRAS*, 392:135–152.
- Lopes, P. A. A., de Carvalho, R. R., Kohl-Moreira, J. L., and Jones, C. (2009b). NoSOCS in SDSS - II. Mass calibration of low redshift galaxy clusters with optical and X-ray properties. *MNRAS*, 399:2201–2220.
- Mahdavi, A., Böhringer, H., Geller, M. J., and Ramella, M. (2000). The RASSCALs: An X-Ray and Optical Study of 260 Galaxy Groups. *ApJ*, 534:114–132.
- Mahdavi, A. and Geller, M. J. (2001). The L_X - σ Relation for Galaxies and Clusters of Galaxies. *ApJ*, 554:L129–L132.
- Martini, P., Sivakoff, G. R., and Mulchaey, J. S. (2009). The Evolution of Active Galactic Nuclei in Clusters of Galaxies to Redshift 1.3. *ApJ*, 701:66–85.

- Maughan, B. J. (2007). The L_X - Y_X Relation: Using Galaxy Cluster X-Ray Luminosity as a Robust, Low-Scatter Mass Proxy. *ApJ*, 668:772–780.
- Maughan, B. J., Giles, P. A., Randall, S. W., Jones, C., and Forman, W. R. (2012). Self-similar scaling and evolution in the galaxy cluster X-ray luminosity-temperature relation. *MNRAS*, 421:1583–1602.
- Maughan, B. J., Jones, C., Forman, W., and Van Speybroeck, L. (2008). Images, Structural Properties, and Metal Abundances of Galaxy Clusters Observed with Chandra ACIS-I at $0.1 < z < 1.3$. *ApJS*, 174:117–135.
- Maughan, B. J., Jones, L. R., Ebeling, H., and Scharf, C. (2006). The evolution of the cluster X-ray scaling relations in the Wide Angle ROSAT Pointed Survey sample at $0.6 < z < 1.0$. *MNRAS*, 365:509–529.
- Meekins, J. F., Fritz, G., Chubb, T. A., and Friedman, H. (1971). Physical Sciences: X-rays from the Coma Cluster of Galaxies. *Nature*, 231:107–108.
- Metcalf, L., Kneib, J.-P., McBreen, B., Altieri, B., Biviano, A., Delaney, M., Elbaz, D., Kessler, M. F., Leech, K., Okumura, K., Ott, S., Perez-Martinez, R., Sanchez-Fernandez, C., and Schulz, B. (2003). An ISOCAM survey through gravitationally lensing galaxy clusters. I. Source lists and source counts for A370, A2218 and A2390. *A&A*, 407:791–822.
- Miles, T. A., Raychaudhury, S., Forbes, D. A., Goudfrooij, P., Ponman, T. J., and Kozhurina-Platais, V. (2004). The Group Evolution Multiwavelength Study (GEMS): bimodal luminosity functions in galaxy groups. *MNRAS*, 355:785–793.
- Mittal, R., Hicks, A., Reiprich, T. H., and Jaritz, V. (2011). The L_X - T_{vir} relation in galaxy clusters: effects of radiative cooling and AGN heating. *A&A*, 532:A133.
- Mulchaey, J. S. (2000). X-ray Properties of Groups of Galaxies. *ARAA*, 38:289–335.
- Mulchaey, J. S., Davis, D. S., Mushotzky, R. F., and Burstein, D. (2003). An X-Ray Atlas of Groups of Galaxies. *ApJS*, 145:39–64.
- Mulchaey, J. S., Lubin, L. M., Fassnacht, C., Rosati, P., and Jeltama, T. E. (2006). X-Ray-selected Intermediate-Redshift Groups of Galaxies. *ApJ*, 646:133–142.

- Mulchaey, J. S. and Zabludoff, A. I. (1998). The Properties of Poor Groups of Galaxies. II. X-Ray and Optical Comparisons. *ApJ*, 496:73.
- Mullis, C. R., Vikhlinin, A., Henry, J. P., Forman, W., Gioia, I. M., Hornstrup, A., Jones, C., McNamara, B. R., and Quintana, H. (2004). Evolution of the Cluster X-Ray Luminosity Function. *ApJ*, 607:175–189.
- Murray, S. S., Kenter, A., Forman, W. R., Jones, C., Green, P. J., Kochanek, C. S., Vikhlinin, A., Fabricant, D., Fazio, G., Brand, K., Brown, M. J. I., Dey, A., Jannuzi, B. T., Najita, J., McNamara, B., Shields, J., and Rieke, M. (2005). XBootes: An X-Ray Survey of the NDWFS Bootes Field. I. Overview and Initial Results. *ApJS*, 161:1–8.
- Osmond, J. P. F. and Ponman, T. J. (2004). The GEMS project: X-ray analysis and statistical properties of the group sample. *MNRAS*, 350:1511–1535.
- O’Sullivan, E., Giacintucci, S., Vrtilek, J. M., Raychaudhury, S., and David, L. P. (2009). A Chandra X-ray View of Stephan’s Quintet: Shocks and Star Formation. *ApJ*, 701:1560–1568.
- O’Sullivan, E., Vrtilek, J. M., David, L. P., Giacintucci, S., Zezas, A., Ponman, T. J., Mamon, G. A., Nulsen, P., and Raychaudhury, S. (2014). Deep Chandra Observations of HCG 16 - II. The Development of the Intra-group Medium in a Spiral-Rich Group. *ArXiv e-prints*.
- Peebles, P. J. E. (1970). Structure of the Coma Cluster of Galaxies. *AJ*, 75:13.
- Pillepich, A., Porciani, C., and Reiprich, T. H. (2012). The X-ray cluster survey with eRosita: forecasts for cosmology, cluster physics and primordial non-Gaussianity. *MNRAS*, 422:44–69.
- Pinkney, J., Roettiger, K., Burns, J. O., and Bird, C. M. (1996). Evaluation of Statistical Tests for Substructure in Clusters of Galaxies. *ApJS*, 104:1.
- Ponman, T. (2003). Galaxy Groups - Introductory Review. In *Astronomische Nachrichten, Supplementary Issue 2, Vol. 324, Short Contributions of the Annual Scientific Meeting of the Astronomische Gesellschaft in Berlin*, page 44.

- Ponman, T. J., Allan, D. J., Jones, L. R., Merrifield, M., McHardy, I. M., Lehto, H. J., and Luppino, G. A. (1994). A possible fossil galaxy group. *Nature*, 369:462–464.
- Pope, E. C. D. (2009). Observable consequences of kinetic and thermal AGN feedback in elliptical galaxies and galaxy clusters. *MNRAS*, 395:2317–2325.
- Popesso, P. and Biviano, A. (2006). The AGN fraction-velocity dispersion relation in clusters of galaxies. *A&A*, 460:L23–L26.
- Popesso, P., Biviano, A., Böhringer, H., and Romaniello, M. (2007). RASS-SDSS galaxy cluster survey. V. The X-ray-underluminous Abell clusters. *A&A*, 461:397–410.
- Popesso, P., Biviano, A., Böhringer, H., Romaniello, M., and Voges, W. (2005). RASS-SDSS galaxy cluster survey. III. Scaling relations of galaxy clusters. *A&A*, 433:431–445.
- Popesso, P., Biviano, A., and Böhringer, H. and Romaniello, M. (2006). RASS-SDSS Galaxy cluster survey. IV. A ubiquitous dwarf galaxy population in clusters. *A&A*, 445:29–42.
- Pratt, G. W., Croston, J. H., Arnaud, M., and Böhringer, H. (2009). Galaxy cluster X-ray luminosity scaling relations from a representative local sample (REXCESS). *A&A*, 498:361–378.
- Predehl, P., Böhringer, H., Brunner, H., Brusa, M., Burwitz, V., Cappelluti, N., Churazov, E., Dennerl, K., Freyberg, M., Friedrich, P., Hasinger, G., Kendziorra, E., Kreykenbohm, I., Schmid, C., Wilms, J., Lamer, G., Meidinger, N., Mühlegger, M., Pavlinsky, M., Robrade, J., Santangelo, A., Schmitt, J., Schwobe, A., Steinmetz, M., Strüder, L., Sunyaev, R., and Tenzer, C. (2010). eROSITA on SRG. *X-ray Astronomy 2009; Present Status, Multi-Wavelength Approach and Future Perspectives*, 1248:543–548.
- Proctor, R. N., de Oliveira, C. M., Dupke, R., de Oliveira, R. L., Cypriano, E. S., Miller, E. D., and Rykoff, E. (2011). On the mass-to-light ratios of fossil groups. Are they simply dark clusters? *MNRAS*, 418:2054–2073.
- Ramella, M., Boschin, W., Fadda, D., and Nonino, M. (2001). Finding galaxy clusters using Voronoi tessellations. *A&A*, 368:776–786.

- Rasmussen, J., Ponman, T. J., Mulchaey, J. S., Miles, T. A., and Raychaudhury, S. (2006). First results of the XI Groups Project: studying an unbiased sample of galaxy groups. *MNRAS*, 373:653–665.
- Regos, E. and Geller, M. J. (1989). Infall patterns around rich clusters of galaxies. *AJ*, 98:755–765.
- Reiprich, T. H. and Böhringer, H. (2002). The Mass Function of an X-Ray Flux-limited Sample of Galaxy Clusters. *ApJ*, 567:716–740.
- Rines, K. and Diaferio, A. (2006). CIRS: Cluster Infall Regions in the Sloan Digital Sky Survey. I. Infall Patterns and Mass Profiles. *AJ*, 132:1275–1297.
- Rines, K. and Diaferio, A. (2010). Infall Regions and Scaling Relations of X-Ray Selected Groups. *AJ*, 139:580–593.
- Rosati, P., Borgani, S., and Norman, C. (2002). The Evolution of X-ray Clusters of Galaxies. *ARAA*, 40:539–577.
- Rosati, P., Della Ceca, R., Burg, R., Norman, C., and Giacconi, R. (1995). A first determination of the surface density of galaxy clusters at very low x-ray fluxes. *ApJ*, 445:L11–L14.
- Rosati, P., della Ceca, R., Norman, C., and Giacconi, R. (1998). The ROSAT Deep Cluster Survey: The X-Ray Luminosity Function Out to $z=0.8$. *ApJ*, 492:L21.
- Rykoff, E. S., Evrard, A. E., McKay, T. A., Becker, M. R., Johnston, D. E., Koester, B. P., Nord, B., Rozo, E., Sheldon, E. S., Stanek, R., and Welchler, R. H. (2008). The LX-M relation of clusters of galaxies. *MNRAS*, 387:L28–L32.
- Santos, M. R., Ellis, R. S., Kneib, J.-P., Richard, J., and Kuijken, K. (2004). The Abundance of Low-Luminosity Ly α Emitters at High Redshift. *ApJ*, 606:683–701.
- Sarazin, C. L. and White, III, R. E. (1988). The X-ray emission of normal elliptical galaxies - Steady state cooling flow models. *ApJ*, 331:102–115.
- Schechter, P. (1976). An analytic expression for the luminosity function for galaxies. *ApJ*, 203:297–306.

- Schmidt, M. (1968). Space Distribution and Luminosity Functions of Quasi-Stellar Radio Sources. *ApJ*, 151:393.
- Schneider, P. (2006). *Extragalactic Astronomy and Cosmology*.
- Smith, G. P., Treu, T., Ellis, R. S., and Moran, S. M. and Dressler, A. (2005). Evolution since $z = 1$ of the Morphology-Density Relation for Galaxies. *ApJ*, 620:78–87.
- Smith, R. K., Brickhouse, N. S., Liedahl, D. A., and Raymond, J. C. (2001). Collisional Plasma Models with APEC/APED: Emission-Line Diagnostics of Hydrogen-like and Helium-like Ions. *ApJ*, 556:L91–L95.
- Stanford, S. A., Brodwin, M., Gonzalez, A. H., Zeimann, G., Stern, D., Dey, A., Eisenhardt, P. R., Snyder, G. F., and Mancone, C. (2012). IDCS J1426.5+3508: Discovery of a Massive, Infrared-selected Galaxy Cluster at $z = 1.75$. *ApJ*, 753:164.
- Starikova, S., Cool, R., Eisenstein, D., Forman, W., Jones, C., Hickox, R., Kenter, A., Kochanek, C., Kravtsov, A., Murray, S. S., and Vikhlinin, A. (2011). Constraining Halo Occupation Properties of X-Ray Active Galactic Nuclei Using Clustering of Chandra Sources in the Boötes Survey Region. *ApJ*, 741:15.
- Strazzullo, V., Rosati, P., Pannella, M., Gobat, R., Santos, J. S., Nonino, M., Demarco, R., Lidman, C., Tanaka, M., Mullis, C. R., Nuñez, C., Rettura, A., Jee, M. J., Böhringer, H., Bender, R., Bouwens, R. J., Dawson, K., Fassbender, R., Franx, M., Perlmutter, S., and Postman, M. (2010). Cluster galaxies in XMMU J2235-2557: galaxy population properties in most massive environments at $z \sim 1.4$. *A&A*, 524:A17.
- Sulentic, J. W., Rosado, M., Dultzin-Hacyan, D., Verdes-Montenegro, L., Trinchieri, G., Xu, C., and Pietsch, W. (2001). A Multiwavelength Study of Stephan’s Quintet. *AJ*, 122:2993–3016.
- Sun, M. (2012). Hot gas in galaxy groups: recent observations. *New Journal of Physics*, 14(4):045004.
- Sun, M., Voit, G. M., Donahue, M., Jones, C., Forman, W., and Vikhlinin, A. (2009). Chandra Studies of the X-Ray Gas Properties of Galaxy Groups. *ApJ*, 693:1142–1172.

- Taylor, J. E. and Babul, A. (2005). The evolution of substructure in galaxy, group and cluster haloes - II. Global properties. *MNRAS*, 364:515–534.
- Temporin, S. and Fritze-von Alvensleben, U. (2006). Interpreting the galaxy group CG J1720-67.8 through evolutionary synthesis models. *A&A*, 447:843–861.
- The, L. S. and White, S. D. M. (1986). The mass of the Coma cluster. *AJ*, 92:1248–1253.
- Tovmassian, H. M., Yam, O., and Tiersch, H. (2002). On the X-Ray Emission of the Low-Mass Galaxy Groups. *ApJ*, 567:L33–L35.
- Trejo-Alonso, J. J., Caretta, C. A., Laganá, T. F., Sodr e, L., Cypriano, E. S., Lima Neto, G. B., and Mendes de Oliveira, C. (2014). Red sequence of Abell X-ray underluminous clusters. *MNRAS*, 441:776–783.
- Trinchieri, G., Sulentic, J., Breitschwerdt, D., and Pietsch, W. (2003). Stephan’s Quintet: The X-ray anatomy of a multiple galaxy collision. *A&A*, 401:173–183.
- Vajgel, B., Jones, C., Lopes, P. A. A., Forman, W. R., Murray, S. S., Goulding, A., and Andrade-Santos, F. (2014). X-Ray-selected Galaxy Groups in Bo tes. *ApJ*, 794:88.
- van der Hulst, J. M. and Rots, A. H. (1981). VLA observations of the radio continuum emission from Stephan’s Quintet. *AJ*, 86:1775–1780.
- Verdes-Montenegro, L., Yun, M. S., Williams, B. A., Huchtmeier, W. K., Del Olmo, A., and Perea, J. (2001). Where is the neutral atomic gas in Hickson groups? *A&A*, 377:812–826.
- Viana, P. T. P. and Liddle, A. R. (1996). The cluster abundance in flat and open cosmologies. *MNRAS*, 281:323.
- Vikhlinin, A., Forman, W., and Jones, C. (1999). Outer Regions of the Cluster Gaseous Atmospheres. *ApJ*, 525:47–57.
- Vikhlinin, A., Kravtsov, A. V., Burenin, R. A., Ebeling, H., Forman, W. R., Hornstrup, A., Jones, C., Murray, S. S., Nagai, D., Quintana, H., and Voevodkin, A. (2009). Chandra Cluster Cosmology Project III: Cosmological Parameter Constraints. *ApJ*, 692:1060–1074.

- Vikhlinin, A., McNamara, B. R., Forman, W., Jones, C., Quintana, H., and Hornstrup, A. (1998). A Catalog of 200 Galaxy Clusters Serendipitously Detected in the ROSAT PSPC Pointed Observations. *ApJ*, 502:558.
- Voit, G. M. (2005). Tracing Cosmic Evolution with Clusters of Galaxies. *RvMP*, 77:207–258.
- West, M. J., Oemler, Jr., A., and Dekel, A. (1988). Subclustering in rich clusters of galaxies and their environs. *ApJ*, 327:1–24.
- Wilman, D. J., Balogh, M. L., Bower, R. G., Mulchaey, J. S., Oemler, A., Carlberg, R. G., Eke, V. R., Lewis, I., Morris, S. L., and Whitaker, R. J. (2005a). Galaxy groups at $0.3 \leq z \leq 0.55$ - II. Evolution to $z \sim 0$. *MNRAS*, 358:88–100.
- Wilman, D. J., Balogh, M. L., Bower, R. G., Mulchaey, J. S., Oemler, A., Carlberg, R. G., Morris, S. L., and Whitaker, R. J. (2005b). Galaxy groups at $0.3 \leq z \leq 0.55$ - I. Group properties. *MNRAS*, 358:71–87.
- Xue, Y.-J. and Wu, X.-P. (2000). The L_X -T, L_X - σ , and σ -T Relations for Groups and Clusters of Galaxies. *ApJ*, 538:65–71.
- Yee, H. K. C. and López-Cruz, O. (1999). A Quantitative Measure of the Richness of Galaxy Clusters. *AJ*, 117:1985–1994.
- Zabludoff, A. I. and Mulchaey, J. S. (1998). The Properties of Poor Groups of Galaxies. I. Spectroscopic Survey and Results. *ApJ*, 496:39–72.
- Zwicky, F. (1933). Die Rotverschiebung von extragalaktischen Nebeln. *Helvetica Physica Acta*, 6:110–127.
- Zwicky, F. (1937). On the Masses of Nebulae and of Clusters of Nebulae. *ApJ*, 86:217.
- Zwicky, F. and Humason, M. L. (1961). Spectra and Other Characteristics of Interconnected Galaxies and of Galaxies in Groups and in Clusters. II. *ApJ*, 133:794.

Appendix A

X-ray Selected Galaxy Group Catalog - General Information

In this appendix, we list the general information about the 32 X-ray selected galaxy group catalog. Table A.1 provides: the group name; coordinates; Chandra ObsIDs; exposure time; final redshift and uncertainties adopted in this work; the number of galaxies used to estimate the redshift and the technique applied for determining the redshift (§2.2.1).

Table A.1. Information of position, redshift, and exposure for the 32 galaxy groups selected with the X-Boötes Survey.

Name	R.A. (J2000)	Dec. (J2000)	ObsId	Exposure (ks)	z	N_{spec}^a	Technique ^b																																																																																												
XBS 02	14:25:32.90	32:56:44	4268	4.7	0.215 ± 0.001	7	Gap (60")																																																																																												
			8456	5.1				XBS 04	14:26:32.51	35:08:21	3621	4.7	1.75 ^f	0	Spectrum	7381	4.6	XBS 05	14:26:37.04	35:27:34	7775 ^c	14.8	0.257	1	BGG ^d	3605	4.7	7002	4.4	XBS 06	14:26:57.90	34:12:01	10495 ^c	30.0	0.129 ± 0.004	17	Gap (60")	4224	4.7	7945	40.7	XBS 07	14:27:09.30	33:15:10	9895 ^c	30.6	0.011	1	BGG ^d	4255	5.0	XBS 08	14:27:13.78	32:28:57	7948 ^c	42.2	0.132	1	BGG ^d	4281	5.0	XBS 09	14:27:41.89	33:12:52	4258	4.6	0.151 ± 0.000^e	13	Gap (60")	XBS 11	14:29:00.60	35:37:34	3602	4.5	0.234 ± 0.001	9	Gap (60")	7000	4.4	7942	38.2	XBS 13	14:29:16.15	33:59:29	9434 ^c	24.8	0.129 ± 0.002	13	Gap (60")	10450	22.7	4228	4.5	6983	4.7	6997	9.6	XBS 14	14:29:55.87
XBS 04	14:26:32.51	35:08:21	3621	4.7	1.75 ^f	0	Spectrum																																																																																												
			7381	4.6				XBS 05	14:26:37.04	35:27:34	7775 ^c	14.8	0.257	1	BGG ^d	3605	4.7				7002	4.4				XBS 06	14:26:57.90	34:12:01	10495 ^c				30.0	0.129 ± 0.004				17	Gap (60")	4224	4.7	7945	40.7	XBS 07	14:27:09.30	33:15:10	9895 ^c	30.6	0.011	1	BGG ^d	4255	5.0	XBS 08	14:27:13.78	32:28:57	7948 ^c	42.2	0.132	1	BGG ^d	4281	5.0	XBS 09	14:27:41.89	33:12:52	4258	4.6	0.151 ± 0.000^e				13	Gap (60")				XBS 11	14:29:00.60	35:37:34	3602				4.5	0.234 ± 0.001				9	Gap (60")	7000	4.4	7942	38.2	XBS 13	14:29:16.15	33:59:29	9434 ^c
XBS 05	14:26:37.04	35:27:34	7775 ^c	14.8	0.257	1	BGG ^d																																																																																												
			3605	4.7																																																																																															
			7002	4.4																																																																																															
XBS 06	14:26:57.90	34:12:01	10495 ^c	30.0	0.129 ± 0.004	17	Gap (60")																																																																																												
			4224	4.7																																																																																															
			7945	40.7																																																																																															
XBS 07	14:27:09.30	33:15:10	9895 ^c	30.6	0.011	1	BGG ^d																																																																																												
			4255	5.0																																																																																															
XBS 08	14:27:13.78	32:28:57	7948 ^c	42.2	0.132	1	BGG ^d																																																																																												
			4281	5.0																																																																																															
XBS 09	14:27:41.89	33:12:52	4258	4.6	0.151 ± 0.000^e	13	Gap (60")																																																																																												
XBS 11	14:29:00.60	35:37:34	3602	4.5	0.234 ± 0.001	9	Gap (60")																																																																																												
			7000	4.4																																																																																															
			7942	38.2																																																																																															
XBS 13	14:29:16.15	33:59:29	9434 ^c	24.8	0.129 ± 0.002	13	Gap (60")																																																																																												
			10450	22.7																																																																																															
			4228	4.5																																																																																															
			6983	4.7																																																																																															
			6997	9.6																																																																																															
XBS 14	14:29:55.87	33:17:11	4253	4.6	0.419 ± 0.002	3	Gap (60")																																																																																												

Table A.1 (cont'd)

Name	R.A. (J2000)	Dec. (J2000)	ObsId	Exposure (ks)	z	N_{spec}^a	Technique ^b																																																																																																								
XBS 17	14:31:09.17	35:06:09	3624	4.6	0.194 ± 0.003	11	Gap (60'')																																																																																																								
			7378	4.4				XBS 18	14:31:13.81	32:32:25	10496 ^c	28.8	0.231 ± 0.018	0	Spectrum	9272	5.0	XBS 20	14:31:56.12	34:38:06	9896 ^c	50.9	0.350 ± 0.002	11	Gap (60'')	3648	4.6	XBS 21	14:32:51.50	32:30:18	4277	4.7	—	0	—	XBS 22	14:32:53.14	33:18:06	4246	4.7	0.569 ± 0.000^e	5	Gap (60'')	4252	4.6	XBS 25	14:34:27.43	34:07:46	4220	4.6	0.191 ± 0.002	4	Gap (60'')	7383	4.4	XBS 26	14:34:49.05	35:43:01	3598	4.7	0.152 ± 0.001	4	Gap (60'')	XBS 27	14:35:08.85	35:03:49	9435 ^c	44.6	0.730 ± 0.066	0	Spectrum	3626	4.7	7376	4.4	XBS 28	14:35:09.03	33:30:50	4247	4.7	0.422 ± 0.138	1	BGG ^d	7011	4.7	XBS 29	14:35:11.94	34:09:22	13132 ^c	27.7	0.404	1	BGG ^d	4219	4.7	7383	4.4	XBS 32	14:36:01.94	34:42:26	3643	4.7	0.534 ± 0.001	4	Gap (60'')	7003	4.4	XBS 33	14:36:15.44	33:46:50	4232
XBS 18	14:31:13.81	32:32:25	10496 ^c	28.8	0.231 ± 0.018	0	Spectrum																																																																																																								
			9272	5.0				XBS 20	14:31:56.12	34:38:06	9896 ^c	50.9	0.350 ± 0.002	11	Gap (60'')	3648	4.6	XBS 21	14:32:51.50	32:30:18	4277	4.7	—	0	—	XBS 22	14:32:53.14	33:18:06	4246	4.7	0.569 ± 0.000^e	5	Gap (60'')	4252	4.6	XBS 25	14:34:27.43	34:07:46	4220	4.6	0.191 ± 0.002	4	Gap (60'')	7383	4.4	XBS 26	14:34:49.05	35:43:01	3598	4.7	0.152 ± 0.001	4	Gap (60'')	XBS 27	14:35:08.85	35:03:49	9435 ^c	44.6	0.730 ± 0.066	0	Spectrum	3626	4.7				7376	4.4				XBS 28	14:35:09.03	33:30:50	4247	4.7	0.422 ± 0.138	1	BGG ^d	7011	4.7	XBS 29	14:35:11.94	34:09:22	13132 ^c				27.7	0.404				1	BGG ^d	4219	4.7	7383	4.4	XBS 32	14:36:01.94	34:42:26	3643	4.7	0.534 ± 0.001	4	Gap (60'')	7003	4.4	XBS 33	14:36:15.44
XBS 20	14:31:56.12	34:38:06	9896 ^c	50.9	0.350 ± 0.002	11	Gap (60'')																																																																																																								
			3648	4.6				XBS 21	14:32:51.50	32:30:18	4277	4.7	—	0	—	XBS 22	14:32:53.14	33:18:06	4246	4.7	0.569 ± 0.000^e	5	Gap (60'')	4252	4.6	XBS 25	14:34:27.43	34:07:46	4220	4.6	0.191 ± 0.002	4	Gap (60'')	7383	4.4	XBS 26	14:34:49.05	35:43:01	3598	4.7	0.152 ± 0.001	4	Gap (60'')	XBS 27	14:35:08.85	35:03:49	9435 ^c	44.6	0.730 ± 0.066	0	Spectrum	3626	4.7				7376	4.4				XBS 28	14:35:09.03	33:30:50	4247	4.7	0.422 ± 0.138	1	BGG ^d	7011	4.7	XBS 29	14:35:11.94	34:09:22	13132 ^c	27.7	0.404	1	BGG ^d	4219	4.7				7383	4.4	XBS 32	14:36:01.94	34:42:26		3643	4.7	0.534 ± 0.001			4	Gap (60'')	7003	4.4	XBS 33	14:36:15.44	33:46:50	4232	4.7	0.343 ± 0.001	6	Gap(60'')	6979	5.1		
XBS 21	14:32:51.50	32:30:18	4277	4.7	—	0	—																																																																																																								
XBS 22	14:32:53.14	33:18:06	4246	4.7	0.569 ± 0.000^e	5	Gap (60'')																																																																																																								
			4252	4.6				XBS 25	14:34:27.43	34:07:46	4220	4.6	0.191 ± 0.002	4	Gap (60'')	7383	4.4	XBS 26	14:34:49.05	35:43:01	3598	4.7	0.152 ± 0.001	4	Gap (60'')	XBS 27	14:35:08.85	35:03:49	9435 ^c	44.6	0.730 ± 0.066	0	Spectrum	3626	4.7	7376	4.4	XBS 28	14:35:09.03	33:30:50	4247	4.7	0.422 ± 0.138	1	BGG ^d	7011	4.7	XBS 29	14:35:11.94	34:09:22	13132 ^c	27.7	0.404	1	BGG ^d	4219	4.7	7383	4.4	XBS 32	14:36:01.94	34:42:26	3643	4.7	0.534 ± 0.001	4	Gap (60'')	7003	4.4	XBS 33	14:36:15.44	33:46:50	4232	4.7	0.343 ± 0.001	6	Gap(60'')	6979	5.1																																
XBS 25	14:34:27.43	34:07:46	4220	4.6	0.191 ± 0.002	4	Gap (60'')																																																																																																								
			7383	4.4				XBS 26	14:34:49.05	35:43:01	3598	4.7	0.152 ± 0.001	4	Gap (60'')	XBS 27	14:35:08.85	35:03:49	9435 ^c	44.6	0.730 ± 0.066	0	Spectrum	3626	4.7				7376	4.4				XBS 28	14:35:09.03	33:30:50	4247	4.7	0.422 ± 0.138	1	BGG ^d	7011	4.7	XBS 29	14:35:11.94	34:09:22	13132 ^c				27.7	0.404				1	BGG ^d	4219	4.7	7383	4.4	XBS 32	14:36:01.94	34:42:26	3643	4.7	0.534 ± 0.001	4	Gap (60'')	7003	4.4	XBS 33	14:36:15.44	33:46:50	4232	4.7	0.343 ± 0.001	6	Gap(60'')	6979	5.1																														
XBS 26	14:34:49.05	35:43:01	3598	4.7	0.152 ± 0.001	4	Gap (60'')																																																																																																								
XBS 27	14:35:08.85	35:03:49	9435 ^c	44.6	0.730 ± 0.066	0	Spectrum																																																																																																								
			3626	4.7																																																																																																											
			7376	4.4																																																																																																											
XBS 28	14:35:09.03	33:30:50	4247	4.7	0.422 ± 0.138	1	BGG ^d																																																																																																								
			7011	4.7																																																																																																											
XBS 29	14:35:11.94	34:09:22	13132 ^c	27.7	0.404	1	BGG ^d																																																																																																								
			4219	4.7																																																																																																											
			7383	4.4																																																																																																											
XBS 32	14:36:01.94	34:42:26	3643	4.7	0.534 ± 0.001	4	Gap (60'')																																																																																																								
			7003	4.4																																																																																																											
XBS 33	14:36:15.44	33:46:50	4232	4.7	0.343 ± 0.001	6	Gap(60'')																																																																																																								
			6979	5.1																																																																																																											

Table A.1 (cont'd)

Name	R.A. (J2000)	Dec. (J2000)	ObsId	Exposure (ks)	z	N_{spec}^a	Technique ^b
XBS 35	14:36:51.06	34:17:37	3659	4.7	0.045	1	BGG ^d
			7382	4.8			
XBS 36	14:37:05.56	33:33:44	4234	4.7	0.243 ± 0.000^e	4	Gap (60'')
XBS 37	14:37:07.06	34:18:48	3659	4.7	0.122 ± 0.001	5	Gap (60'')
XBS 38	14:37:14.35	34:15:03	4218	5.0	0.541 ± 0.002	8	Gap(60'')
XBS 39	14:37:29.18	34:18:22	3660	4.6	0.396 ± 0.000^e	1	BGG ^d
XBS 41	14:37:42.77	34:08:07	10461 ^c	100.0	0.543 ± 0.186	1	BGG ^d
			4218	5.0			
XBS 42	14:37:47.63	33:31:10	4249	4.6	0.218 ± 0.021	1	BGG ^d
XBS 43	14:37:48.49	35:06:17	3628	4.6	0.574 ± 0.002	3	Gap (0.5 Mpc)
XBS 46	14:28:33.80	33:05:35	4258	4.6	0.196 ± 0.000^e	3	Gap (60'')
XBS 52	14:43:35.94	35:09:51	3615	4.6	0.599 ± 0.015	1	BGG ^d
			7376	4.4			

^aNumber of galaxy redshifts used to estimate the group redshift

^bTechnique applied to estimate the group redshift

^cACIS-S observations.

^dBrightest Galaxy of the Group

^eRedshift uncertainties < 0.001

^fThis redshift was estimated by Stanford et al. (2012)

Appendix B

Optically Selected Galaxy Group Catalog - General Information

In this appendix, we list the general information about the 162 optically selected galaxy group catalog. Table B.1 provides: the group name; coordinates; Chandra ObsIDs; exposure time; final redshift and uncertainties adopted in this work and the number of galaxies used to estimate the redshift.

Table B.1. Information of position, redshift, and exposure for the 162 galaxy groups selected with the AGES data.

Name	R.A. (J2000)	Dec. (J2000)	ObsId	Exposure (ks)	z	N_{spec}^a
OBS 001	14:29:19.43	35:31:26.39	7942	38.2	0.029±0.001	20
			3607	4.5		
			7000	4.4		
OBS 002	14:29:49.43	34:36:21.59	7007	4.4	0.028±0.000	8
			3639	4.5		
			10454	30.3		
OBS 003	14:31:02.87	35:31:12.00	6993	4.4	0.013±0.000	11
			3608	4.6		
OBS 004	14:31:57.83	33:19:15.59	4252	4.6	0.035±0.001	14
OBS 005	14:33:18.95	34:44:31.20	7005	4.4	0.034±0.000	8
			3641	4.7		
			10456	31.8		
OBS 006	14:26:27.35	34:50:31.19	3637	4.7	0.099±0.000	3
OBS 007	14:25:33.84	33:03:25.19	4257	4.7	0.102±0.001	16
			8456	5.1		
OBS 008	14:29:27.84	34:54:00.00	7379	4.4	0.099±0.000	7
OBS 009	14:30:53.03	34:57:03.60	3639	4.7	0.128±0.000	5
			7378	4.4		
OBS 010	14:31:43.68	35:36:14.40	3600	4.7	0.084±0.001	4
			6993	4.4		
			3608	4.6		
OBS 011	14:31:53.99	34:42:11.00	3640	4.6	0.084±0.001	13
			7385	4.4		
OBS 012	14:33:11.27	35:29:45.59	6992	4.4	0.084±0.002	9

Table B.1 (cont'd)

Name	R.A. (J2000)	Dec. (J2000)	ObsId	Exposure (ks)	z	N_{spec}^a
			3609	5.0		
OBS 013	14:25:22.80	34:12:07.19	4225	4.7	0.169 ± 0.000	5
OBS 014	14:26:39.83	33:52:26.40	4226	4.7	0.157 ± 0.001	11
			6985	4.6		
OBS 015 ^{XBS06}	14:26:57.90	34:12:01	10495 ^c	30.0	0.129 ± 0.004	17
			4224	4.7		
			7945	40.7		
OBS 016	14:27:11.28	33:34:44.39	6987	5.1	0.151 ± 0.001	15
			10453	34.7		
			4240	4.6		
OBS 017	14:27:17.03	32:45:43.20	7948	42.2	0.133 ± 0.001	16
			4270	5.0		
			4267	4.6		
OBS 018 ^{XBS13}	14:29:16.15	33:59:29	9434 ^c	24.8	0.129 ± 0.002	13
			10450	22.7		
			4228	4.5		
			6983	4.7		
			6997	9.6		
OBS 019	14:28:27.36	34:39:00.00	3638	4.6	0.122 ± 0.001	13
			7008	4.8		
OBS 020	14:28:43.91	34:22:37.19	7944	40.4	0.127 ± 0.001	4
			3655	4.5		
			3650	4.5		
OBS 021	14:28:53.75	35:30:46.80	3607	4.5	0.129 ± 0.001	12

Table B.1 (cont'd)

Name	R.A. (J2000)	Dec. (J2000)	ObsId	Exposure (ks)	z	N _{spec} ^a
			7000	4.4		
			7982	38.2		
OBS 022	14:28:59.03	33:02:59.99	4259	4.5	0.129±0.001	13
			7014	4.7		
OBS 023	14:31:29.52	33:42:07.19	4229	4.6	0.123±0.001	3
			4237	4.6		
OBS 024	14:32:51.11	34:07:01.20	3657	4.7	0.127±0.001	4
			7384	4.4		
OBS 025	14:33:37.49	33:48:13.75	4236	4.6	0.123±0.002	29
			6981	4.7		
			4230	4.7		
OBS 026	14:33:50.16	34:12:50.40	3658	4.7	0.126±0.003	4
			4220	4.6		
OBS 027	14:34:41.75	35:42:43.20	3599	4.6	0.125±0.000	7
			3598	4.7		
OBS 028	14:35:31.20	35:24:50.40	10459	31.6	0.128±0.000	8
			3614	4.7		
OBS 029	14:35:58.08	34:33:21.59	7004	4.4	0.125±0.001	11
			3642	4.7		
OBS 030	14:36:23.75	35:27:14.39	3611	4.7	0.128±0.001	20
			3612	4.6		
OBS 031 ^{XBS37}	14:37:07.06	34:18:48	3659	4.7	0.122 ± 0.001	5
OBS 032	14:38:01.20	35:22:33.59	3612	4.6	0.125±0.003	5
OBS 033	14:24:56.15	35:12:46.80	3620	4.7	0.170±0.000	17

Table B.1 (cont'd)

Name	R.A. (J2000)	Dec. (J2000)	ObsId	Exposure (ks)	z	N_{spec}^a																																																																																														
OBS 034	14:24:53.03	34:25:58.79	10458	36.7	0.169±0.002	15																																																																																														
			3652	4.7			OBS 035	14:26:11.04	34:58:44.40	7381	4.6	0.164±0.000	3	3621	4.7	OBS 036	14:26:28.79	35:10:37.19	7381	4.6	0.172±0.001	4	3621	4.7	OBS 037	14:27:12.00	35:07:11.99	7380	4.4	0.187±0.003	6	3622	4.6	OBS 038	14:27:58.80	34:57:00.00	3622	4.6	0.188±0.001	4	7380	4.4	OBS 039	14:28:42.71	34:53:56.39	3634	4.5	0.192±0.001	3	OBS 040	14:28:47.74	35:08:21.52	7943	42.6	0.194±0.001	15	7379	4.4	3622	4.6	3618	4.5	OBS 041	14:30:59.75	35:37:01.20	6993	4.4	0.162±0.001	28	3008	4.6	OBS 042 ^{XBS17}	14:31:09.17	35:06:09	3624	4.6	0.194 ± 0.003	11	7378	4.4	OBS 043	14:31:38.39	34:26:34.80	7385	4.4	0.188±0.001	12	OBS 044	14:31:26.63	34:13:33.60	7385	4.4	0.178±0.001	10	6994	9.9	7384	4.4	OBS 045	14:31:39.11
OBS 035	14:26:11.04	34:58:44.40	7381	4.6	0.164±0.000	3																																																																																														
			3621	4.7			OBS 036	14:26:28.79	35:10:37.19	7381	4.6	0.172±0.001	4	3621	4.7	OBS 037	14:27:12.00	35:07:11.99	7380	4.4	0.187±0.003	6	3622	4.6	OBS 038	14:27:58.80	34:57:00.00	3622	4.6	0.188±0.001	4	7380	4.4	OBS 039	14:28:42.71	34:53:56.39	3634	4.5	0.192±0.001	3	OBS 040	14:28:47.74	35:08:21.52	7943	42.6	0.194±0.001	15	7379	4.4				3622	4.6			3618	4.5	OBS 041	14:30:59.75	35:37:01.20	6993	4.4	0.162±0.001	28	3008	4.6	OBS 042 ^{XBS17}	14:31:09.17	35:06:09	3624	4.6	0.194 ± 0.003	11	7378	4.4	OBS 043	14:31:38.39	34:26:34.80	7385	4.4	0.188±0.001	12	OBS 044	14:31:26.63	34:13:33.60	7385				4.4	0.178±0.001			10	6994	9.9	7384	4.4	OBS 045
OBS 036	14:26:28.79	35:10:37.19	7381	4.6	0.172±0.001	4																																																																																														
			3621	4.7			OBS 037	14:27:12.00	35:07:11.99	7380	4.4	0.187±0.003	6	3622	4.6	OBS 038	14:27:58.80	34:57:00.00	3622	4.6	0.188±0.001	4	7380	4.4	OBS 039	14:28:42.71	34:53:56.39	3634	4.5	0.192±0.001	3	OBS 040	14:28:47.74	35:08:21.52	7943	42.6	0.194±0.001	15	7379	4.4				3622	4.6			3618	4.5	OBS 041	14:30:59.75	35:37:01.20	6993	4.4	0.162±0.001	28	3008	4.6	OBS 042 ^{XBS17}	14:31:09.17	35:06:09	3624	4.6	0.194 ± 0.003	11	7378	4.4	OBS 043	14:31:38.39	34:26:34.80	7385	4.4	0.188±0.001	12	OBS 044	14:31:26.63	34:13:33.60	7385	4.4	0.178±0.001	10	6994	9.9				7384	4.4	OBS 045	14:31:39.11	35:36:21.59		3608	4.6		0.163±0.000	3			
OBS 037	14:27:12.00	35:07:11.99	7380	4.4	0.187±0.003	6																																																																																														
			3622	4.6			OBS 038	14:27:58.80	34:57:00.00	3622	4.6	0.188±0.001	4	7380	4.4	OBS 039	14:28:42.71	34:53:56.39	3634	4.5	0.192±0.001	3	OBS 040	14:28:47.74	35:08:21.52	7943	42.6	0.194±0.001	15	7379	4.4				3622	4.6			3618	4.5	OBS 041	14:30:59.75	35:37:01.20	6993	4.4	0.162±0.001	28	3008	4.6	OBS 042 ^{XBS17}	14:31:09.17	35:06:09	3624	4.6	0.194 ± 0.003	11	7378	4.4	OBS 043	14:31:38.39	34:26:34.80	7385	4.4	0.188±0.001	12	OBS 044	14:31:26.63	34:13:33.60	7385	4.4	0.178±0.001	10	6994	9.9				7384	4.4			OBS 045	14:31:39.11	35:36:21.59	3608	4.6	0.163±0.000	3												
OBS 038	14:27:58.80	34:57:00.00	3622	4.6	0.188±0.001	4																																																																																														
			7380	4.4			OBS 039	14:28:42.71	34:53:56.39	3634	4.5	0.192±0.001	3	OBS 040	14:28:47.74	35:08:21.52	7943	42.6	0.194±0.001	15	7379	4.4				3622	4.6			3618	4.5	OBS 041	14:30:59.75	35:37:01.20	6993	4.4	0.162±0.001	28	3008	4.6	OBS 042 ^{XBS17}	14:31:09.17	35:06:09	3624	4.6	0.194 ± 0.003	11	7378	4.4	OBS 043	14:31:38.39	34:26:34.80	7385	4.4	0.188±0.001	12	OBS 044	14:31:26.63	34:13:33.60	7385	4.4	0.178±0.001	10	6994	9.9				7384	4.4			OBS 045	14:31:39.11	35:36:21.59	3608	4.6	0.163±0.000	3																					
OBS 039	14:28:42.71	34:53:56.39	3634	4.5	0.192±0.001	3																																																																																														
OBS 040	14:28:47.74	35:08:21.52	7943	42.6	0.194±0.001	15																																																																																														
			7379	4.4																																																																																																
			3622	4.6																																																																																																
			3618	4.5																																																																																																
OBS 041	14:30:59.75	35:37:01.20	6993	4.4	0.162±0.001	28																																																																																														
			3008	4.6			OBS 042 ^{XBS17}	14:31:09.17	35:06:09	3624	4.6	0.194 ± 0.003	11	7378	4.4	OBS 043	14:31:38.39	34:26:34.80	7385	4.4	0.188±0.001	12	OBS 044	14:31:26.63	34:13:33.60	7385	4.4	0.178±0.001	10	6994	9.9	7384	4.4	OBS 045	14:31:39.11	35:36:21.59	3608	4.6	0.163±0.000	3																																																												
OBS 042 ^{XBS17}	14:31:09.17	35:06:09	3624	4.6	0.194 ± 0.003	11																																																																																														
			7378	4.4			OBS 043	14:31:38.39	34:26:34.80	7385	4.4	0.188±0.001	12	OBS 044	14:31:26.63	34:13:33.60	7385	4.4	0.178±0.001	10	6994	9.9				7384	4.4			OBS 045	14:31:39.11	35:36:21.59	3608	4.6	0.163±0.000	3																																																																
OBS 043	14:31:38.39	34:26:34.80	7385	4.4	0.188±0.001	12																																																																																														
OBS 044	14:31:26.63	34:13:33.60	7385	4.4	0.178±0.001	10																																																																																														
			6994	9.9																																																																																																
			7384	4.4																																																																																																
OBS 045	14:31:39.11	35:36:21.59	3608	4.6	0.163±0.000	3																																																																																														

Table B.1 (cont'd)

Name	R.A. (J2000)	Dec. (J2000)	ObsId	Exposure (ks)	z	N_{spec}^a
			6993	4.4		
OBS 046	14:31:49.16	34:07:33.14	6994	9.9	0.179±0.001	11
			4222	4.6		
OBS 047	14:32:33.96	35:45:39.86	3600	4.7	0.184±0.002	17
OBS 048	14:33:03.12	34:19:04.80	7384	4.4	0.191±0.002	17
			7385	4.4		
OBS 049 ^{XBS25}	14:34:27.43	34:07:46	4220	4.6	0.191 ± 0.002	4
			7383	4.4		
OBS 050	14:34:53.28	34:03:53.99	4219	4.7	0.191±0.001	8
OBS 051 ^{XBS02}	14:25:32.90	32:56:44	4268	4.7	0.215 ± 0.001	7
			8456	5.1		
OBS 052	14:25:29.27	33:20:34.79	4256	4.7	0.210±0.001	10
			6986	4.7		
OBS 053	14:25:57.84	32:55:44.40	8456	5.1	0.216±0.002	11
			4257	4.7		
OBS 054	14:26:30.75	34:43:30.70	7009	4.4	0.210±0.002	5
			3637	4.7		
OBS 055	14:28:17.28	33:07:04.80	4258	4.6	0.219±0.002	15
			4254	4.5		
OBS 056 ^{XBS11}	14:29:00.60	35:37:34	3602	4.5	0.234 ± 0.001	9
			7000	4.4		
			7942	38.2		
OBS 057	14:29:12.71	32:52:11.99	4266	4.5	0.217±0.001	3
OBS 058	14:29:19.68	35:26:31.20	3607	4.5	0.217±0.001	3

Table B.1 (cont'd)

Name	R.A. (J2000)	Dec. (J2000)	ObsId	Exposure (ks)	z	N_{spec}^a
			7000	4.4		
OBS 059	14:30:02.64	32:57:54.00	4259	4.5	0.202±0.001	8
			4265	4.6		
OBS 060	14:30:05.76	34:02:41.99	6998	9.6	0.226±0.002	4
OBS 061	14:31:14.64	33:48:07.19	4229	4.6	0.255±0.000	4
			6982	4.7		
			6999	9.6		
OBS 062	14:31:45.88	33:47:40.51	4229	4.6	0.226±0.002	19
			6982	4.7		
OBS 063	14:32:35.51	34:55:04.79	3632	4.6	0.220±0.001	3
OBS 064	14:32:56.15	33:44:56.40	4230	4.7	0.218±0.000	8
			6981	4.7		
OBS 065	14:33:53.52	35:26:41.99	3615	4.6	0.212±0.004	6
			3610	4.7		
OBS 066	14:36:19.43	35:43:01.19	3598	4.7	0.205±0.003	6
OBS 067	14:25:19.91	33:33:14.40	4241	4.7	0.242±0.001	6
OBS 068	14:25:50.40	33:19:58.80	4242	4.7	0.243±0.001	3
			4256	4.7		
OBS 069	14:26:20.38	35:37:08.54	3130	120.1	0.256±0.002	10
			3482	58.5		
			7002	4.4		
OBS 070	14:26:25.92	33:22:51.60	6986	4.7	0.248±0.002	3
			4242	4.7		
OBS 071	14:27:10.80	33:17:56.39	4255	5.0	0.242±0.001	7

Table B.1 (cont'd)

Name	R.A. (J2000)	Dec. (J2000)	ObsId	Exposure (ks)	z	N _{spec} ^a																																																																																																			
OBS 072	14:28:19.20	34:20:02.39	7944	40.4	0.267±0.002	3																																																																																																			
			3654	4.6			OBS 073	14:28:18.24	33:15:57.59	4254	4.5	0.243±0.002	4	OBS 074	14:28:18.54	35:46:31.74	3602	4.5	0.247±0.001	7	OBS 075	14:28:29.04	35:10:55.19	7943	42.6	0.245±0.000	7	OBS 076	14:29:28.27	34:27:53.17	3655	4.5	0.257±0.001	10	10454	30.3	3639	4.5	3649	4.6	3650	4.5	OBS 077	14:30:12.28	32:55:46.69	4265	4.6	0.243±0.002	3	OBS 078	14:30:41.31	34:34:38.43	7006	4.4	0.265±0.000	3	3649	4.6	OBS 079	14:32:32.39	34:26:06.00	3648	4.6	0.275±0.001	7	OBS 080	14:32:41.75	33:10:48.00	7012	4.7	0.250±0.001	6	4261	4.7	OBS 081	14:33:39.11	33:15:35.99	4251	4.6	0.245±0.001	5	OBS 082	14:34:06.71	33:13:58.80	7946	40.4	0.244±0.001	6	4251	4.6	OBS 083	14:34:37.44	33:34:08.40	4247	4.7	0.273±0.000	3	7946	40.4	4235	4.7	OBS 084	14:34:57.35	33:26:38.40	4247
OBS 073	14:28:18.24	33:15:57.59	4254	4.5	0.243±0.002	4																																																																																																			
OBS 074	14:28:18.54	35:46:31.74	3602	4.5	0.247±0.001	7																																																																																																			
OBS 075	14:28:29.04	35:10:55.19	7943	42.6	0.245±0.000	7																																																																																																			
OBS 076	14:29:28.27	34:27:53.17	3655	4.5	0.257±0.001	10																																																																																																			
			10454	30.3																																																																																																					
			3639	4.5																																																																																																					
			3649	4.6																																																																																																					
			3650	4.5																																																																																																					
OBS 077	14:30:12.28	32:55:46.69	4265	4.6	0.243±0.002	3																																																																																																			
OBS 078	14:30:41.31	34:34:38.43	7006	4.4	0.265±0.000	3																																																																																																			
			3649	4.6																																																																																																					
OBS 079	14:32:32.39	34:26:06.00	3648	4.6	0.275±0.001	7																																																																																																			
OBS 080	14:32:41.75	33:10:48.00	7012	4.7	0.250±0.001	6																																																																																																			
			4261	4.7																																																																																																					
OBS 081	14:33:39.11	33:15:35.99	4251	4.6	0.245±0.001	5																																																																																																			
OBS 082	14:34:06.71	33:13:58.80	7946	40.4	0.244±0.001	6																																																																																																			
			4251	4.6																																																																																																					
OBS 083	14:34:37.44	33:34:08.40	4247	4.7	0.273±0.000	3																																																																																																			
			7946	40.4																																																																																																					
			4235	4.7																																																																																																					
OBS 084	14:34:57.35	33:26:38.40	4247	4.7	0.264±0.000	3																																																																																																			
			7011	4.7																																																																																																					

Table B.1 (cont'd)

Name	R.A. (J2000)	Dec. (J2000)	ObsId	Exposure (ks)	z	N _{spec} ^a																																																																																																			
OBS 085	14:34:54.48	33:45:53.99	6980	5.1	0.243±0.001	4																																																																																																			
			4231	4.7			OBS 086	14:35:17.04	33:39:57.60	4235	4.7	0.252±0.000	5	OBS 087	14:35:38.15	33:31:19.19	4235	4.7	0.274±0.001	4	OBS 088 ^{XBS36}	14:37:05.56	33:33:44	4234	4.7	0.243 ± 0.000 ^e	4	OBS 089	14:25:24.91	33:31:33.60	6986	4.7	0.306±0.001	3	4241	4.7	OBS 090	14:26:13.08	34:35:15.32	7009	4.4	0.312±0.001	5	3637	4.7	OBS 091	14:27:42.48	32:51:50.39	7948	42.2	0.301±0.001	0	4258	4.6	OBS 092	14:28:01.44	34:16:40.79	7944	40.4	0.314±0.000	3	7387	4.4	3654	4.6	OBS 093	14:29:37.68	34:39:10.79	10454	30.3	0.309±0.002	4	7007	4.4	3639	4.5	OBS 094	14:32:54.15	34:46:54.34	7005	4.4	0.311±0.001	10	3641	4.7	OBS 095	14:33:31.20	35:03:25.19	3625	4.7	0.309±0.001	5	7277	4.8	OBS 096	14:24:52.24	33:44:01.34	4241	4.7	0.359±0.002	4	OBS 097	14:25:41.48	34:58:27.12	7381
OBS 086	14:35:17.04	33:39:57.60	4235	4.7	0.252±0.000	5																																																																																																			
OBS 087	14:35:38.15	33:31:19.19	4235	4.7	0.274±0.001	4																																																																																																			
OBS 088 ^{XBS36}	14:37:05.56	33:33:44	4234	4.7	0.243 ± 0.000 ^e	4																																																																																																			
OBS 089	14:25:24.91	33:31:33.60	6986	4.7	0.306±0.001	3																																																																																																			
			4241	4.7			OBS 090	14:26:13.08	34:35:15.32	7009	4.4	0.312±0.001	5	3637	4.7	OBS 091	14:27:42.48	32:51:50.39	7948	42.2	0.301±0.001	0	4258	4.6	OBS 092	14:28:01.44	34:16:40.79	7944	40.4	0.314±0.000	3	7387	4.4	3654	4.6	OBS 093	14:29:37.68	34:39:10.79	10454	30.3	0.309±0.002	4	7007	4.4	3639	4.5	OBS 094	14:32:54.15	34:46:54.34	7005	4.4	0.311±0.001	10	3641	4.7	OBS 095	14:33:31.20	35:03:25.19	3625	4.7	0.309±0.001	5	7277	4.8	OBS 096	14:24:52.24	33:44:01.34	4241	4.7	0.359±0.002	4	OBS 097	14:25:41.48	34:58:27.12	7381	4.6	0.329±0.001	7	3621	4.7																									
OBS 090	14:26:13.08	34:35:15.32	7009	4.4	0.312±0.001	5																																																																																																			
			3637	4.7			OBS 091	14:27:42.48	32:51:50.39	7948	42.2	0.301±0.001	0	4258	4.6	OBS 092	14:28:01.44	34:16:40.79	7944	40.4	0.314±0.000	3	7387	4.4				3654	4.6			OBS 093	14:29:37.68	34:39:10.79	10454				30.3	0.309±0.002			4	7007	4.4	3639	4.5	OBS 094	14:32:54.15	34:46:54.34	7005	4.4	0.311±0.001	10	3641	4.7	OBS 095	14:33:31.20	35:03:25.19	3625	4.7	0.309±0.001	5	7277	4.8	OBS 096	14:24:52.24	33:44:01.34	4241	4.7	0.359±0.002	4	OBS 097	14:25:41.48	34:58:27.12	7381	4.6	0.329±0.001	7	3621	4.7																								
OBS 091	14:27:42.48	32:51:50.39	7948	42.2	0.301±0.001	0																																																																																																			
			4258	4.6			OBS 092	14:28:01.44	34:16:40.79	7944	40.4	0.314±0.000	3	7387	4.4				3654	4.6			OBS 093	14:29:37.68	34:39:10.79	10454	30.3	0.309±0.002	4	7007	4.4				3639	4.5	OBS 094	14:32:54.15	34:46:54.34		7005	4.4		0.311±0.001	10	3641	4.7	OBS 095	14:33:31.20	35:03:25.19	3625	4.7	0.309±0.001	5	7277	4.8	OBS 096	14:24:52.24	33:44:01.34	4241	4.7	0.359±0.002	4	OBS 097	14:25:41.48	34:58:27.12	7381	4.6	0.329±0.001	7	3621	4.7																																	
OBS 092	14:28:01.44	34:16:40.79	7944	40.4	0.314±0.000	3																																																																																																			
			7387	4.4																																																																																																					
			3654	4.6																																																																																																					
OBS 093	14:29:37.68	34:39:10.79	10454	30.3	0.309±0.002	4																																																																																																			
			7007	4.4																																																																																																					
			3639	4.5																																																																																																					
OBS 094	14:32:54.15	34:46:54.34	7005	4.4	0.311±0.001	10																																																																																																			
			3641	4.7																																																																																																					
OBS 095	14:33:31.20	35:03:25.19	3625	4.7	0.309±0.001	5																																																																																																			
			7277	4.8																																																																																																					
OBS 096	14:24:52.24	33:44:01.34	4241	4.7	0.359±0.002	4																																																																																																			
OBS 097	14:25:41.48	34:58:27.12	7381	4.6	0.329±0.001	7																																																																																																			
			3621	4.7																																																																																																					

Table B.1 (cont'd)

Name	R.A. (J2000)	Dec. (J2000)	ObsId	Exposure (ks)	z	N _{spec} ^a
			3636	4.7		
OBS 098	14:26:05.35	34:12:26.36	7945	40.7	0.344±0.001	10
			7388	4.4		
			10451	12.1		
			3653	4.7		
OBS 099	14:26:42.90	33:35:22.35	10453	34.7	0.321±0.002	3
			4242	4.7		
			6986	4.7		
OBS 100	14:26:42.62	34:05:33.35	7945	40.7	0.352±0.000	22
			10451	12.1		
			4224	4.7		
OBS 101	14:28:25.44	33:42:32.39	4239	4.5	0.325±0.001	3
OBS 102	14:28:21.35	33:53:52.79	6984	4.7	0.330±0.001	6
			4227	4.6		
OBS 103	14:28:39.59	34:44:56.40	3634	4.5	0.352±0.002	6
OBS 104	14:28:56.68	34:22:29.75	3650	4.5	0.329±0.002	8
			3655	4.5		
OBS 105	14:29:35.68	34:07:16.03	3655	4.5	0.328±0.003	4
			7386	4.4		
OBS 106	14:30:05.51	34:13:44.40	3655	4.5	0.329±0.001	14
			7386	4.4		
OBS 107	14:30:12.60	33:19:11.32	4253	4.6	0.321±0.001	10
OBS 108	14:31:07.35	34:46:34.83	7006	4.4	0.352±0.002	12
			3640	4.6		

Table B.1 (cont'd)

Name	R.A. (J2000)	Dec. (J2000)	ObsId	Exposure (ks)	z	N_{spec}^a
OBS 109	14:31:31.16	34:30:52.32	3648	4.6	0.327 ± 0.003	7
OBS 110	14:31:50.45	34:01:29.08	4221	4.6	0.352 ± 0.002	11
			6999	9.6		
			6982	4.7		
OBS 111 ^{XBS20}	14:31:56.12	34:38:06	9896 ^c	50.9	0.350 ± 0.002	11
			3648	4.6		
OBS 112	14:33:23.28	33:33:46.79	7946	40.4	0.351 ± 0.001	18
			7010	4.7		
OBS 113	14:34:02.39	33:25:19.20	7946	40.4	0.326 ± 0.002	10
			4247	4.7		
OBS 114	14:33:59.75	34:36:11.15	7004	4.4	0.350 ± 0.001	8
			3647	4.6		
OBS 115	14:34:32.22	34:41:58.78	7004	4.4	0.353 ± 0.001	5
			3642	4.7		
OBS 116	14:34:39.33	33:48:28.08	4231	4.7	0.329 ± 0.003	16
			6980	5.1		
OBS 117	14:35:08.02	33:53:33.37	4231	4.7	0.327 ± 0.001	11
			6980	5.1		
OBS 118	14:35:33.26	33:47:18.89	4235	4.7	0.343 ± 0.002	7
OBS 119 ^{XBS33}	14:36:15.44	33:46:50	4232	4.7	0.343 ± 0.001	6
			6979	5.1		
OBS 120	14:25:54.52	35:38:43.05	3130	120.1	0.386 ± 0.002	16
			3482	58.5		
OBS 121	14:27:06.24	35:45:21.60	3603	4.7	0.390 ± 0.001	7

Table B.1 (cont'd)

Name	R.A. (J2000)	Dec. (J2000)	ObsId	Exposure (ks)	z	N _{spec} ^a
OBS 122	14:27:51.19	33:12:15.65	4254	4.5	0.364±0.001	3
			4258	4.6		
			7015	4.7		
OBS 123	14:28:10.15	33:25:34.18	4243	4.6	0.362±0.001	5
			6987	5.1		
OBS 124	14:28:21.79	32:59:59.50	4258	4.6	0.368±0.003	8
			4266	4.5		
OBS 125	14:32:17.74	34:37:48.09	7005	4.4	0.374±0.001	7
			3641	4.7		
			10456	31.8		
OBS 126	14:32:29.52	33:29:45.59	10452	34.3	0.374±0.000	9
			7010	4.7		
OBS 127	14:32:24.89	34:49:30.09	3632	4.6	0.367±0.002	4
			7005	4.4		
OBS 128	14:33:12.48	34:56:20.39	3625	4.7	0.368±0.001	3
			7377	4.8		
OBS 129	14:33:12.24	35:24:10.79	6992	4.4	0.378±0.001	6
			3609	5.0		
OBS 130	14:34:52.63	33:04:26.69	7947	42.6	0.375±0.002	6
			4262	4.6		
OBS 131	14:37:17.36	34:13:30.14	4218	5.0	0.398±0.001	9
OBS 132	14:28:17.53	35:31:38.71	3606	4.6	0.416±0.002	7
			7942	38.2		
			7001	4.4		

Table B.1 (cont'd)

Name	R.A. (J2000)	Dec. (J2000)	ObsId	Exposure (ks)	z	N_{spec}^a																																																																																																																		
OBS 133	14:28:14.29	35:42:10.92	3602	4.5	0.416±0.002	7																																																																																																																		
			7942	38.2			OBS 134	14:28:22.95	35:20:33.83	3618	4.5	0.417±0.001	8	OBS 135	14:28:58.79	35:15:10.79	7943	42.6	0.417±0.002	12	3618	4.5	OBS 136	14:29:20.40	35:45:25.19	3602	4.5	0.420±0.000	3	OBS 137	14:30:17.76	35:10:58.79	3617	4.2	0.423±0.002	5	OBS 138	14:30:17.32	33:32:53.88	4238	4.6	0.427±0.001	6	OBS 139	14:33:54.00	33:32:07.83	7946	40.4	0.445±0.001	7	4236	4.6	OBS 140	14:28:21.35	34:53:38.40	3634	4.5	0.475±0.001	3	OBS 141	14:28:07.62	34:36:27.35	7008	4.8	0.473±0.001	8	3638	4.6	OBS 142	14:26:11.75	34:46:26.39	7009	4.4	0.488±0.001	4	3637	4.7	OBS 143	14:26:54.24	34:31:14.51	3651	4.7	0.526±0.001	6	OBS 144	14:27:13.73	33:13:52.46	4255	5.0	0.501±0.002	4	OBS 145	14:28:26.88	33:09:10.79	4258	4.6	0.488±0.001	3	4254	4.5	OBS 146	14:31:38.39	33:46:22.79	4229	4.6	0.497±0.001	5	6982	4.7	OBS 147	14:32:17.51	34:35:16.80	7005	4.4	0.513±0.002	3	10456	31.8	OBS 148	14:32:13.80
OBS 134	14:28:22.95	35:20:33.83	3618	4.5	0.417±0.001	8																																																																																																																		
OBS 135	14:28:58.79	35:15:10.79	7943	42.6	0.417±0.002	12																																																																																																																		
			3618	4.5			OBS 136	14:29:20.40	35:45:25.19	3602	4.5	0.420±0.000	3	OBS 137	14:30:17.76	35:10:58.79	3617	4.2	0.423±0.002	5	OBS 138	14:30:17.32	33:32:53.88	4238	4.6	0.427±0.001	6	OBS 139	14:33:54.00	33:32:07.83	7946	40.4	0.445±0.001	7	4236	4.6	OBS 140	14:28:21.35	34:53:38.40	3634	4.5	0.475±0.001	3	OBS 141	14:28:07.62	34:36:27.35	7008	4.8	0.473±0.001	8	3638	4.6	OBS 142	14:26:11.75	34:46:26.39	7009	4.4	0.488±0.001	4	3637	4.7	OBS 143	14:26:54.24	34:31:14.51	3651	4.7	0.526±0.001	6	OBS 144	14:27:13.73	33:13:52.46	4255	5.0	0.501±0.002	4	OBS 145	14:28:26.88	33:09:10.79	4258	4.6	0.488±0.001	3	4254	4.5	OBS 146	14:31:38.39	33:46:22.79	4229	4.6	0.497±0.001	5	6982	4.7	OBS 147	14:32:17.51	34:35:16.80	7005	4.4	0.513±0.002	3	10456	31.8	OBS 148	14:32:13.80	34:21:04.74	7384	4.4	0.514±0.003	0											
OBS 136	14:29:20.40	35:45:25.19	3602	4.5	0.420±0.000	3																																																																																																																		
OBS 137	14:30:17.76	35:10:58.79	3617	4.2	0.423±0.002	5																																																																																																																		
OBS 138	14:30:17.32	33:32:53.88	4238	4.6	0.427±0.001	6																																																																																																																		
OBS 139	14:33:54.00	33:32:07.83	7946	40.4	0.445±0.001	7																																																																																																																		
			4236	4.6			OBS 140	14:28:21.35	34:53:38.40	3634	4.5	0.475±0.001	3	OBS 141	14:28:07.62	34:36:27.35	7008	4.8	0.473±0.001	8	3638	4.6	OBS 142	14:26:11.75	34:46:26.39	7009	4.4	0.488±0.001	4	3637	4.7	OBS 143	14:26:54.24	34:31:14.51	3651	4.7	0.526±0.001	6	OBS 144	14:27:13.73	33:13:52.46	4255	5.0	0.501±0.002	4	OBS 145	14:28:26.88	33:09:10.79	4258	4.6	0.488±0.001	3	4254	4.5	OBS 146	14:31:38.39	33:46:22.79	4229	4.6	0.497±0.001	5	6982	4.7	OBS 147	14:32:17.51	34:35:16.80	7005	4.4	0.513±0.002	3	10456	31.8	OBS 148	14:32:13.80	34:21:04.74	7384	4.4	0.514±0.003	0																																									
OBS 140	14:28:21.35	34:53:38.40	3634	4.5	0.475±0.001	3																																																																																																																		
OBS 141	14:28:07.62	34:36:27.35	7008	4.8	0.473±0.001	8																																																																																																																		
			3638	4.6			OBS 142	14:26:11.75	34:46:26.39	7009	4.4	0.488±0.001	4	3637	4.7	OBS 143	14:26:54.24	34:31:14.51	3651	4.7	0.526±0.001	6	OBS 144	14:27:13.73	33:13:52.46	4255	5.0	0.501±0.002	4	OBS 145	14:28:26.88	33:09:10.79	4258	4.6	0.488±0.001	3	4254	4.5	OBS 146	14:31:38.39	33:46:22.79	4229	4.6	0.497±0.001	5	6982	4.7	OBS 147	14:32:17.51	34:35:16.80	7005	4.4	0.513±0.002	3	10456	31.8	OBS 148	14:32:13.80	34:21:04.74	7384	4.4	0.514±0.003	0																																																									
OBS 142	14:26:11.75	34:46:26.39	7009	4.4	0.488±0.001	4																																																																																																																		
			3637	4.7			OBS 143	14:26:54.24	34:31:14.51	3651	4.7	0.526±0.001	6	OBS 144	14:27:13.73	33:13:52.46	4255	5.0	0.501±0.002	4	OBS 145	14:28:26.88	33:09:10.79	4258	4.6	0.488±0.001	3	4254	4.5	OBS 146	14:31:38.39	33:46:22.79	4229	4.6	0.497±0.001	5	6982	4.7	OBS 147	14:32:17.51	34:35:16.80	7005	4.4	0.513±0.002	3	10456	31.8	OBS 148	14:32:13.80	34:21:04.74	7384	4.4	0.514±0.003	0																																																																		
OBS 143	14:26:54.24	34:31:14.51	3651	4.7	0.526±0.001	6																																																																																																																		
OBS 144	14:27:13.73	33:13:52.46	4255	5.0	0.501±0.002	4																																																																																																																		
OBS 145	14:28:26.88	33:09:10.79	4258	4.6	0.488±0.001	3																																																																																																																		
			4254	4.5			OBS 146	14:31:38.39	33:46:22.79	4229	4.6	0.497±0.001	5	6982	4.7	OBS 147	14:32:17.51	34:35:16.80	7005	4.4	0.513±0.002	3	10456	31.8	OBS 148	14:32:13.80	34:21:04.74	7384	4.4	0.514±0.003	0																																																																																									
OBS 146	14:31:38.39	33:46:22.79	4229	4.6	0.497±0.001	5																																																																																																																		
			6982	4.7			OBS 147	14:32:17.51	34:35:16.80	7005	4.4	0.513±0.002	3	10456	31.8	OBS 148	14:32:13.80	34:21:04.74	7384	4.4	0.514±0.003	0																																																																																																		
OBS 147	14:32:17.51	34:35:16.80	7005	4.4	0.513±0.002	3																																																																																																																		
			10456	31.8			OBS 148	14:32:13.80	34:21:04.74	7384	4.4	0.514±0.003	0																																																																																																											
OBS 148	14:32:13.80	34:21:04.74	7384	4.4	0.514±0.003	0																																																																																																																		

Table B.1 (cont'd)

Name	R.A. (J2000)	Dec. (J2000)	ObsId	Exposure (ks)	z	N_{spec}^a
OBS 149	14:32:46.19	34:25:33.96	3657	4.7	0.494 ± 0.001	4
OBS 150	14:32:50.54	34:00:54.29	4230	4.7	0.504 ± 0.001	5
			6981	4.7		
OBS 151	14:33:14.16	34:42:35.99	10456	31.8	0.490 ± 0.001	4
			7005	4.4		
			3641	4.7		
OBS 152	14:33:44.68	34:55:00.29	3631	4.6	0.492 ± 0.002	4
OBS 153	14:34:27.07	33:58:06.67	4231	4.7	0.494 ± 0.002	4
			6980	5.1		
OBS 154	14:27:57.42	34:08:31.99	7387	4.4	0.569 ± 0.001	7
			3654	4.6		
OBS 155	14:31:54.77	33:35:30.15	10452	34.3	0.558 ± 0.000	4
			4245	4.6		
			4237	4.6		
OBS 156	14:32:30.47	34:40:44.40	10456	31.8	0.532 ± 0.001	6
			7005	4.4		
			3641	4.7		
OBS 157	14:34:51.80	35:42:52.50	3598	4.7	0.543 ± 0.001	4
OBS 158	14:35:36.68	34:30:35.99	3646	4.7	0.522 ± 0.001	4
OBS 159 ^{XBS38}	14:37:14.35	34:15:03	4218	5.0	0.541 ± 0.002	8
OBS 160	14:30:47.69	33:39:40.21	4238	4.6	0.570 ± 0.001	3
OBS 161	14:28:51.11	34:01:08.40	4223	4.5	0.655 ± 0.001	6
			6997	9.6		
			10450	22.7		

Table B.1 (cont'd)

Name	R.A. (J2000)	Dec. (J2000)	ObsId	Exposure (ks)	z	N_{spec}^a
OBS 162	14:33:59.85	33:36:58.75	7946	40.4	0.662 ± 0.000	3
			4236	4.6		

^aNumber of galaxy redshifts used to estimate the group redshift

^bRedshift uncertainties < 0.001

Appendix C

X-ray Selected Extended Source Catalog For $z \leq 0.35$

In this appendix, we present the catalog of the 14 X-ray selected galaxy groups to $z = 0.35$ with at least 5 members inside R_{500} . For each group, we show the density profile of the AGES galaxies centered in the central coordinates of the galaxy group and the spatial distribution of galaxies in the Δ R.A. vs. Δ Dec diagram.

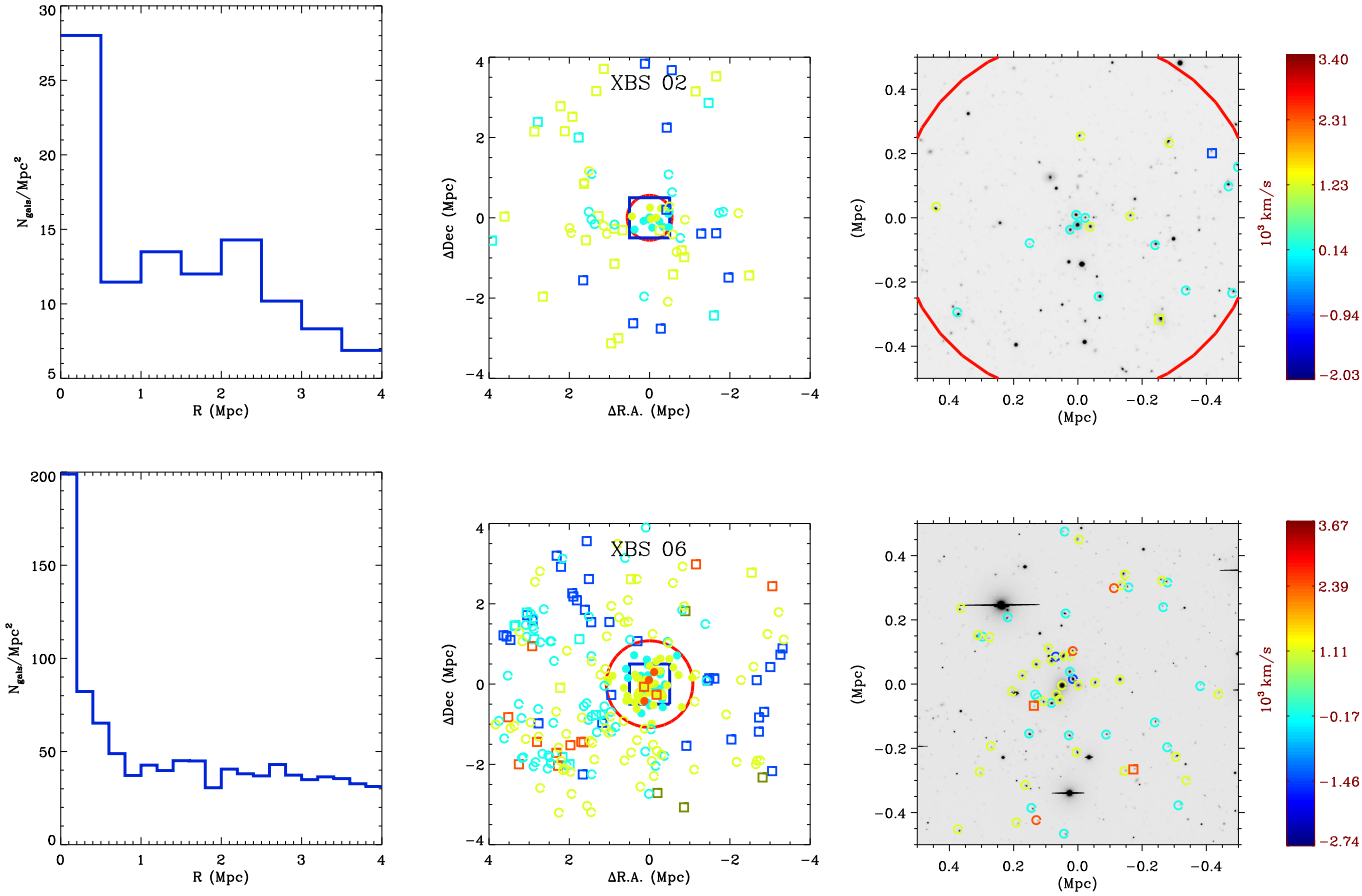
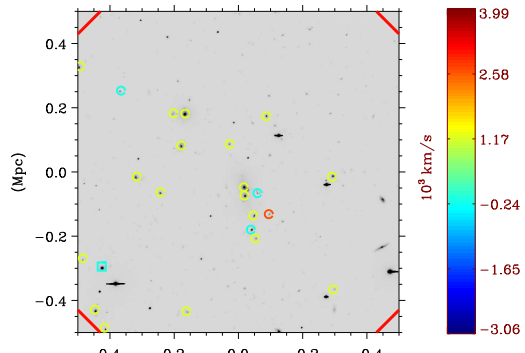
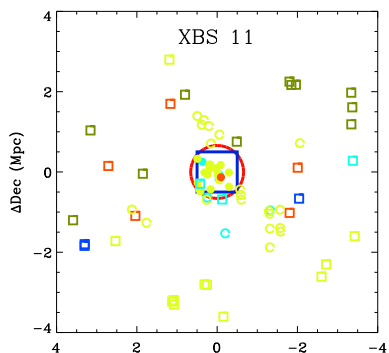
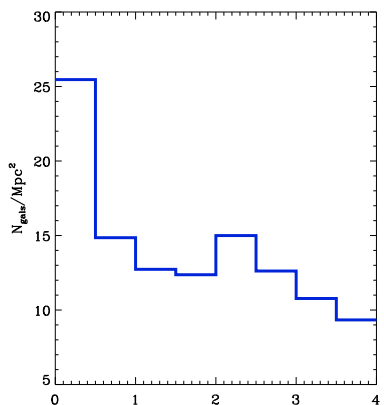
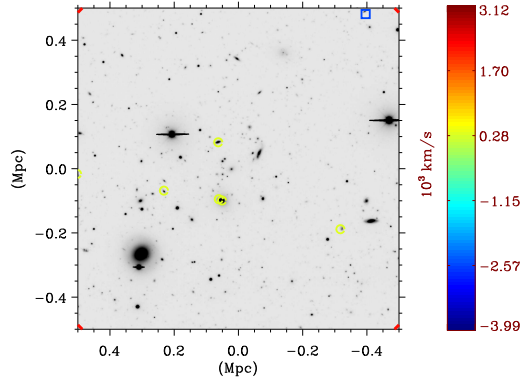
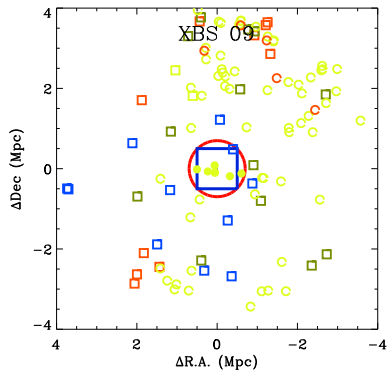
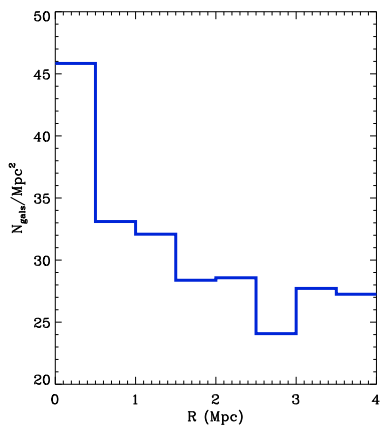
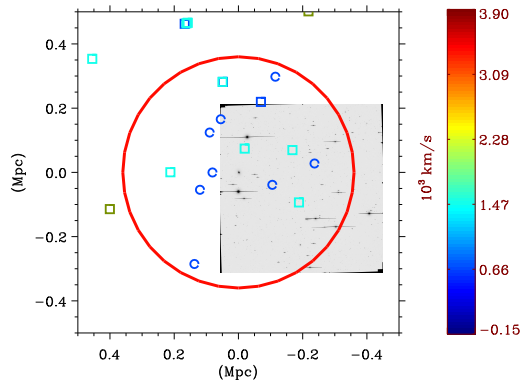
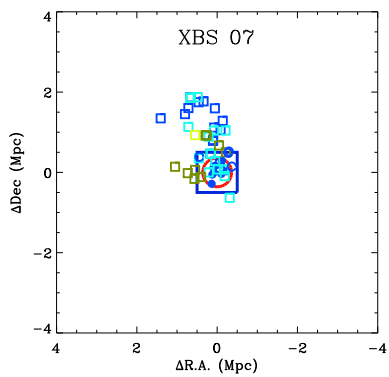
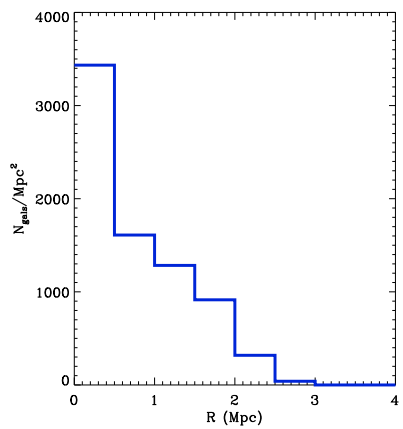
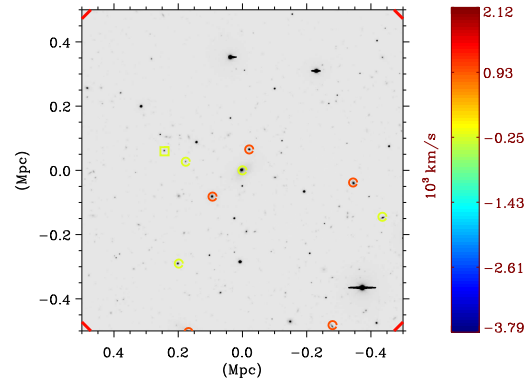
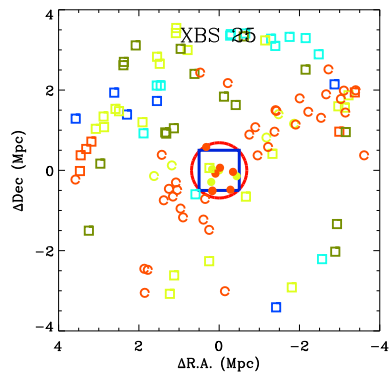
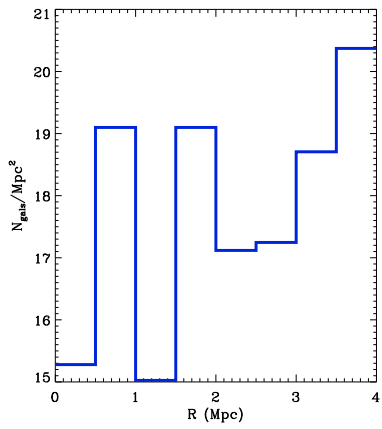
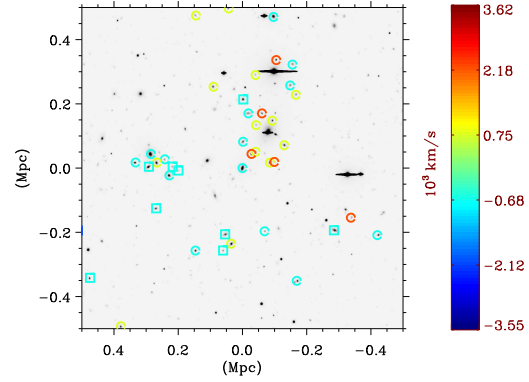
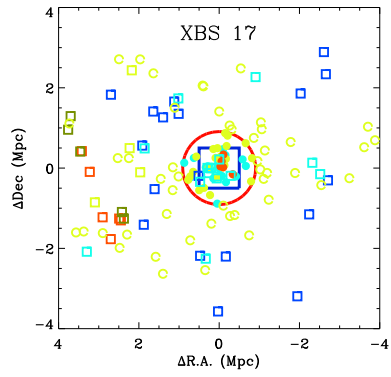
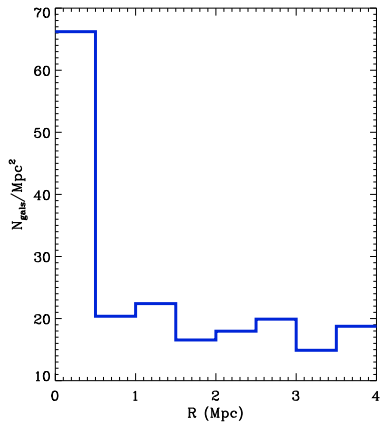
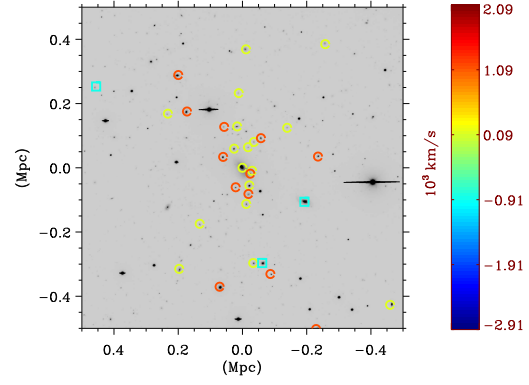
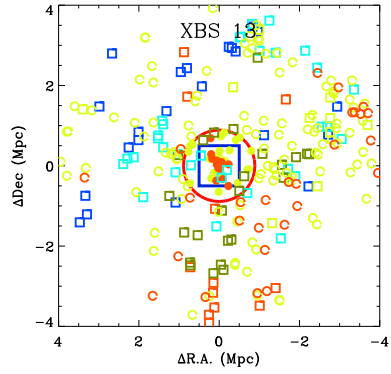
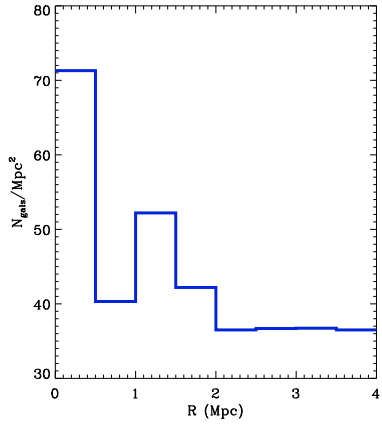
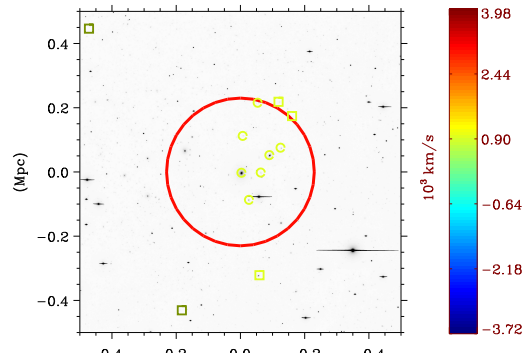
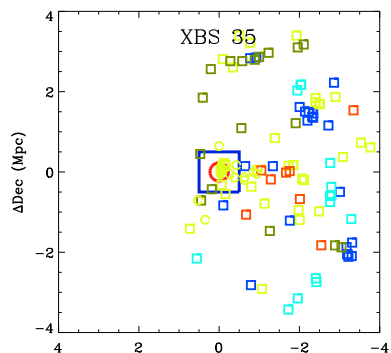
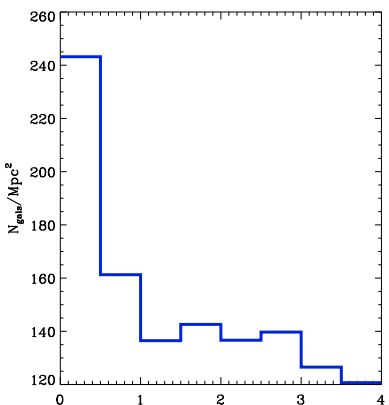
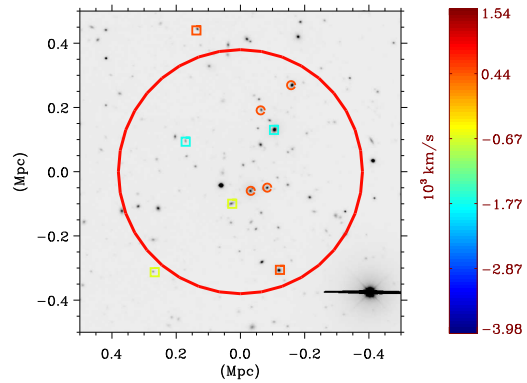
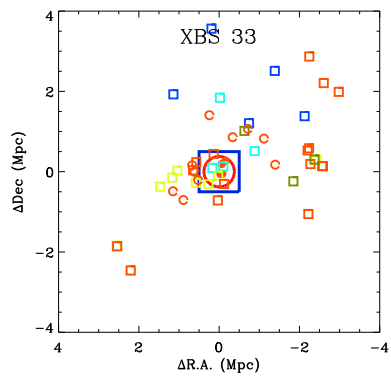
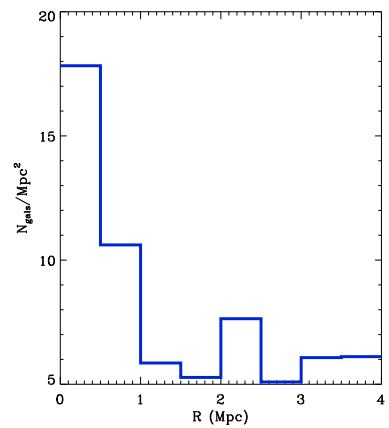
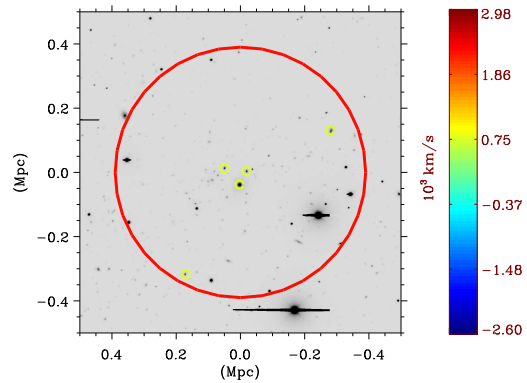
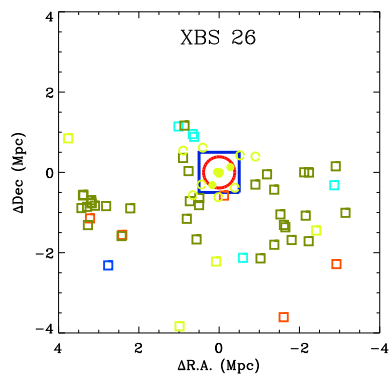
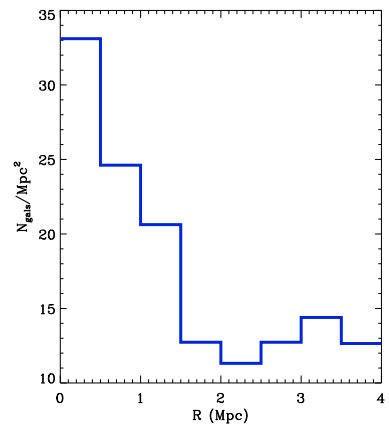
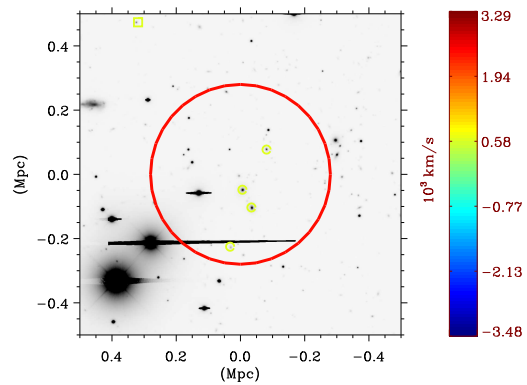
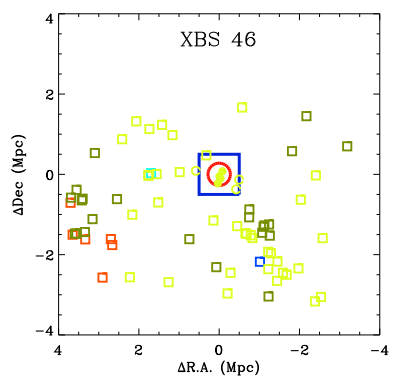
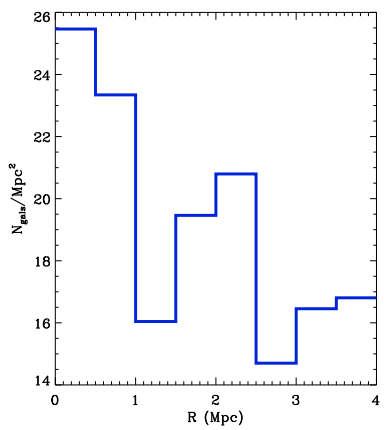
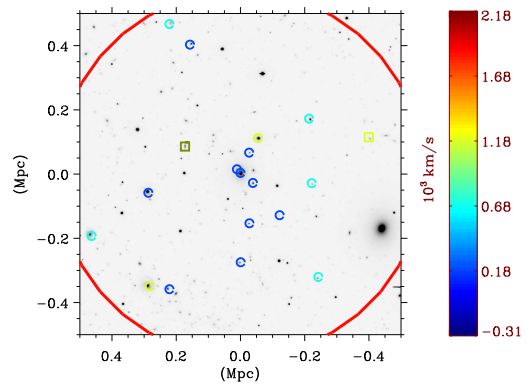
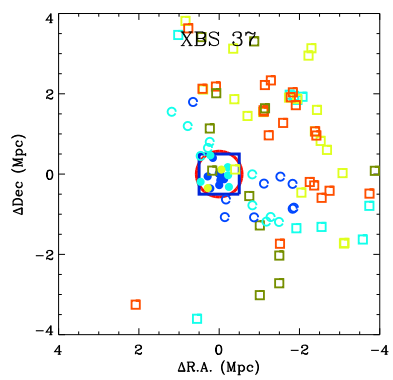
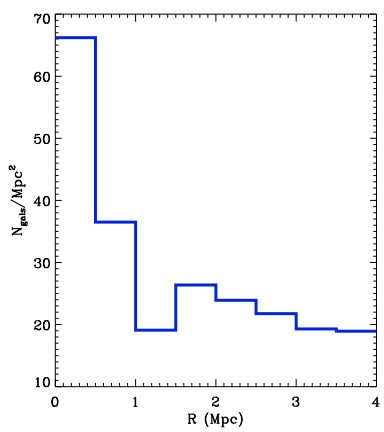
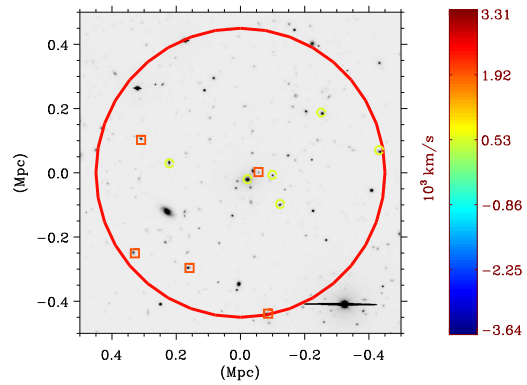
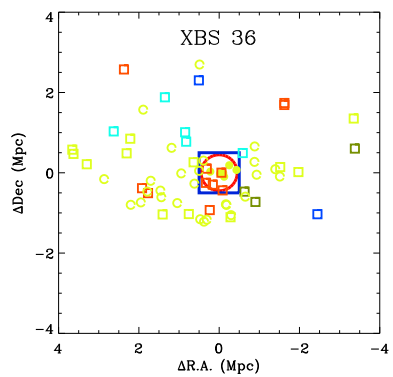
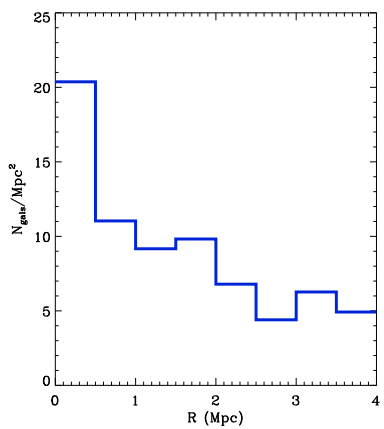


Figure C.1 The left panel in each row is the density profile for the AGES galaxies centered on the central coordinates of the galaxy group. The middle panel is the $\Delta\text{R.A.}$ vs. ΔDec diagram. The filled circles are the galaxy members inside R_{500} (big red circle) used to estimate σ . The open circles are galaxy members outside R_{500} . The open squares are the rejected interlopers. The colors of the symbols represent the difference in velocity between the group and the galaxies. The color scale is represented by the color bar (in units of 10^3 km s^{-1}) on the right side of the the right panel. The right panel is the zoom in region of the 1 Mpc blue box of the middle panel with I band NDWFS image in the background. The open circles are the galaxy members inside R_{500} used to estimate σ . The open squares are the rejected interlopers. The symbol colors follow the same scale of the color bar on the right.









Appendix D

Optically Selected Extended Source Catalog For $z \leq 0.35$

In this appendix, we present the catalog of the 68 optical selected galaxy groups to $z = 0.35$ with at least 5 members inside R_{500} . For each group, we show the density profile of the AGES galaxies centered in the central coordinates of the galaxy group and the spatial distribution of galaxies in the $\Delta R.A.$ vs. ΔDec diagram.

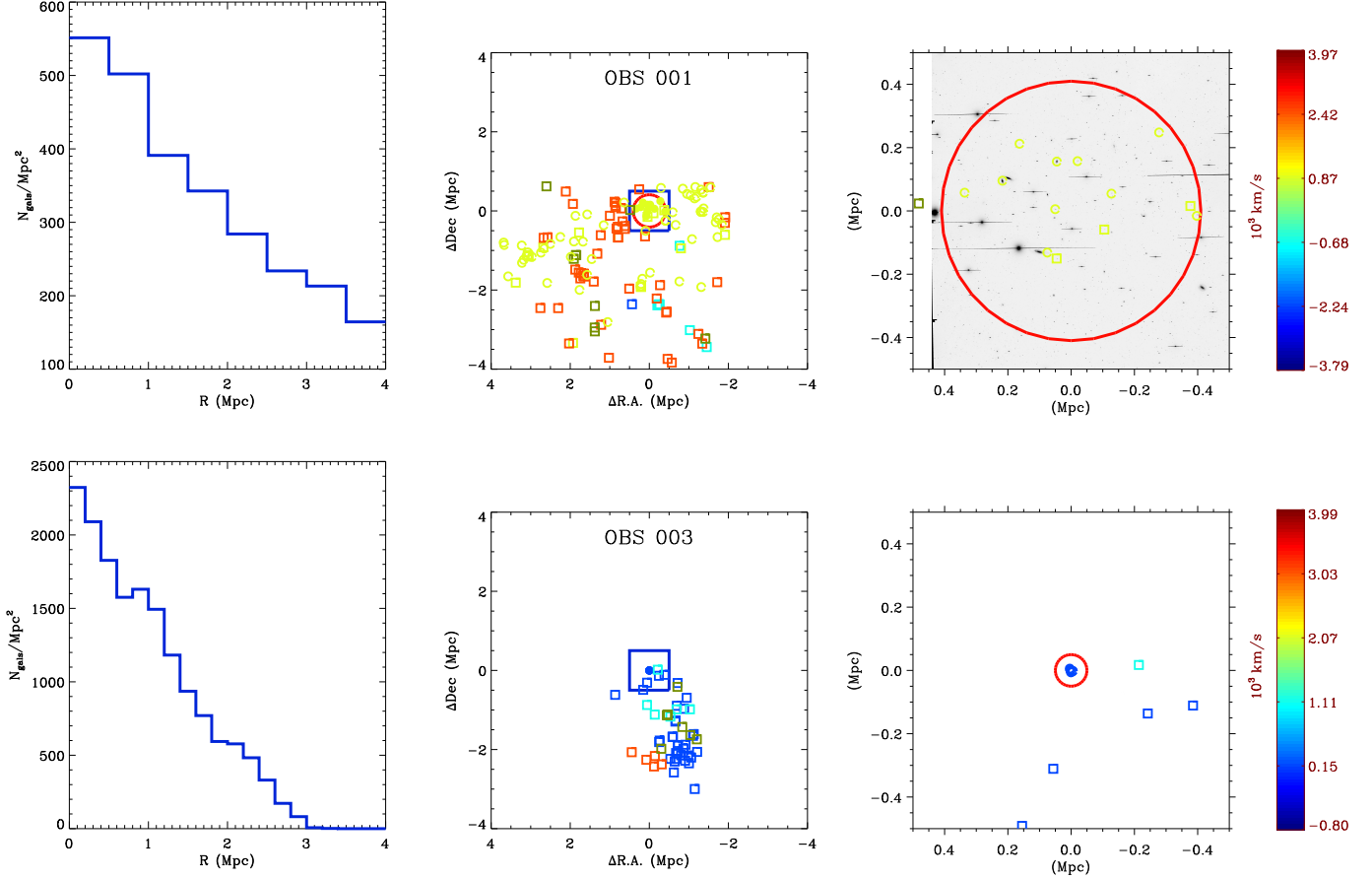


Figure D.1 The left panel in each row is the density profile for the AGES galaxies centered on the central coordinates of the galaxy group. The middle panel is the $\Delta R.A.$ vs. ΔDec diagram. The filled circles are the galaxy members inside R_{500} (big red circle) used to estimate σ . The open circles are galaxy members outside R_{500} . The open squares are the rejected interlopers. The colors of the symbols represent the difference in velocity between the group and the galaxies. The color scale is represented by the color bar (in units of 10^3 km s^{-1}) on the right side of the the right panel. The right panel is the zoom in region of the 1 Mpc blue box of the middle panel with I band NDWFS image in the background. The open circles are the galaxy members inside R_{500} used to estimate σ . The open squares are the rejected interlopers. The symbol colors follow the same scale of the color bar on the right.

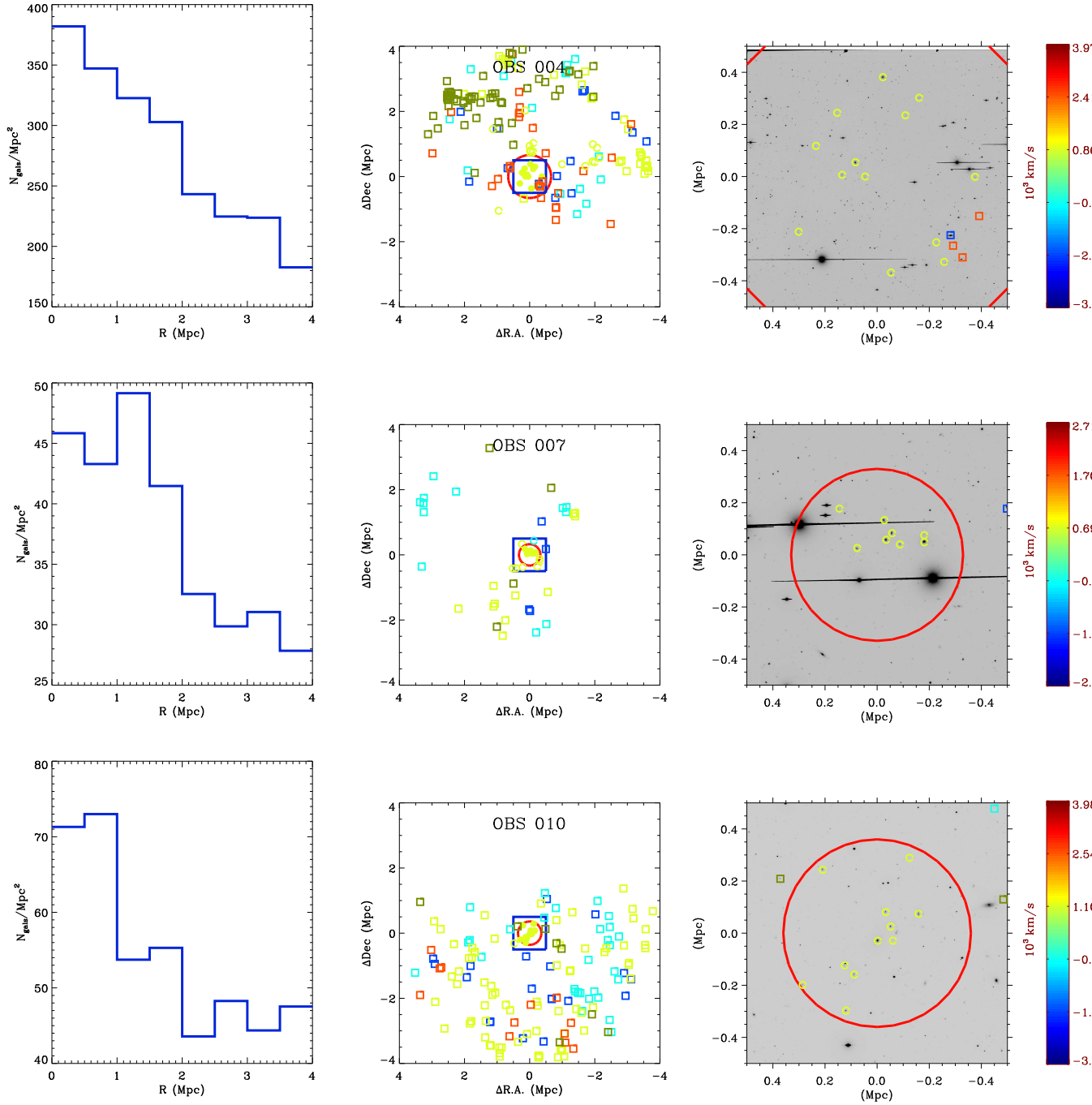


Figure D.2 Continuation of Figure D.1

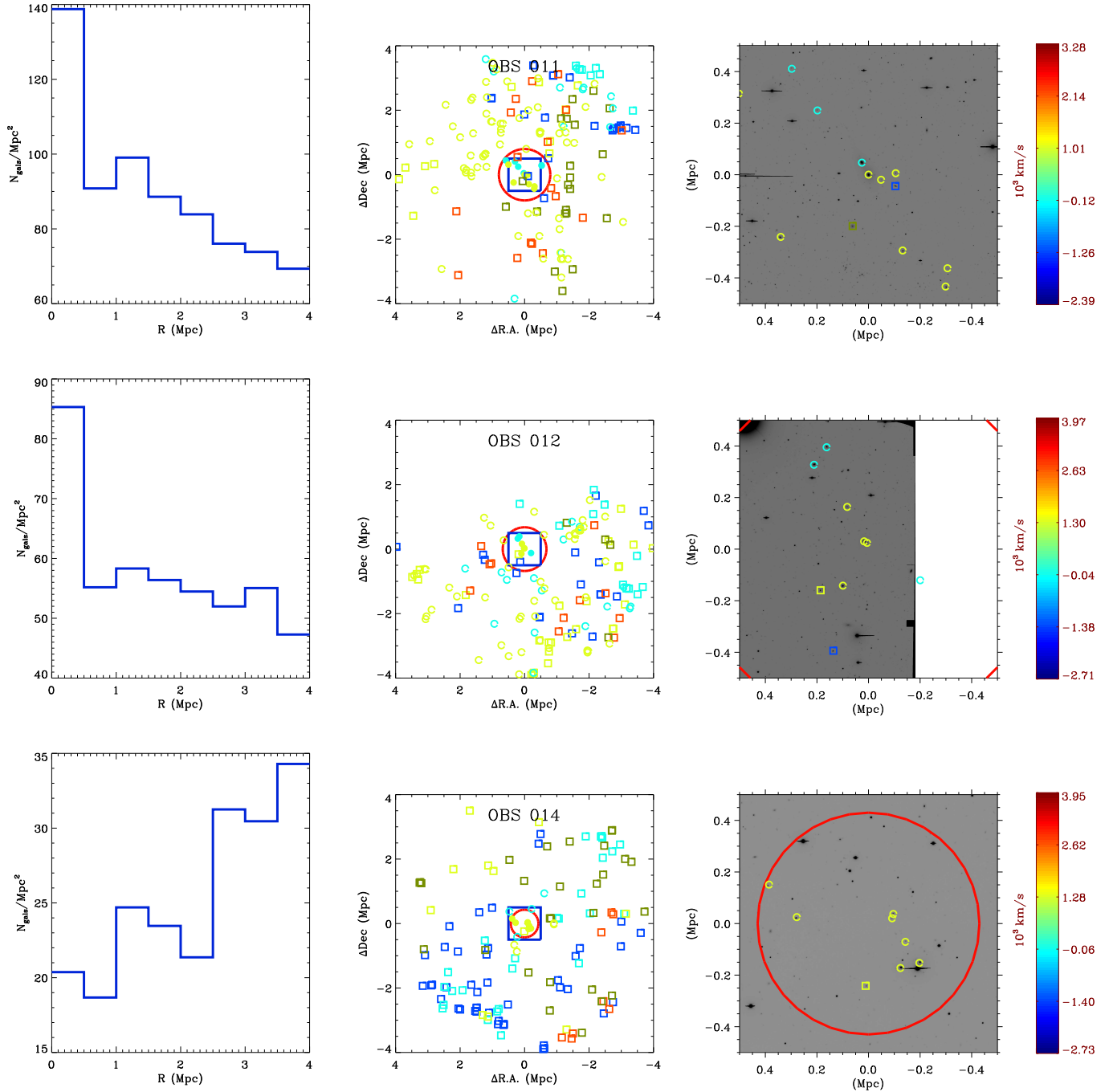


Figure D.3 Continuation of Figure D.1

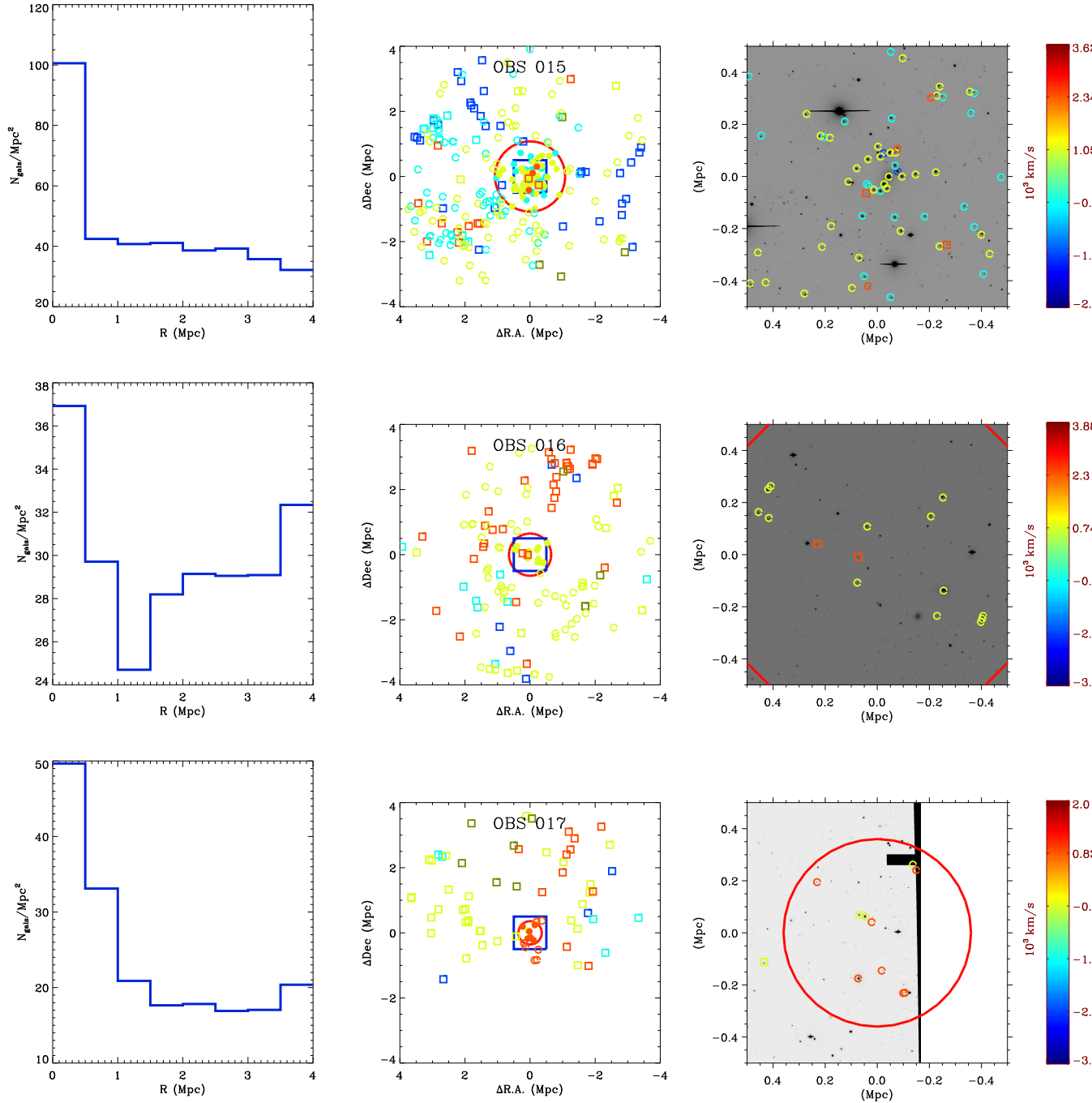


Figure D.4 Continuation of Figure D.1

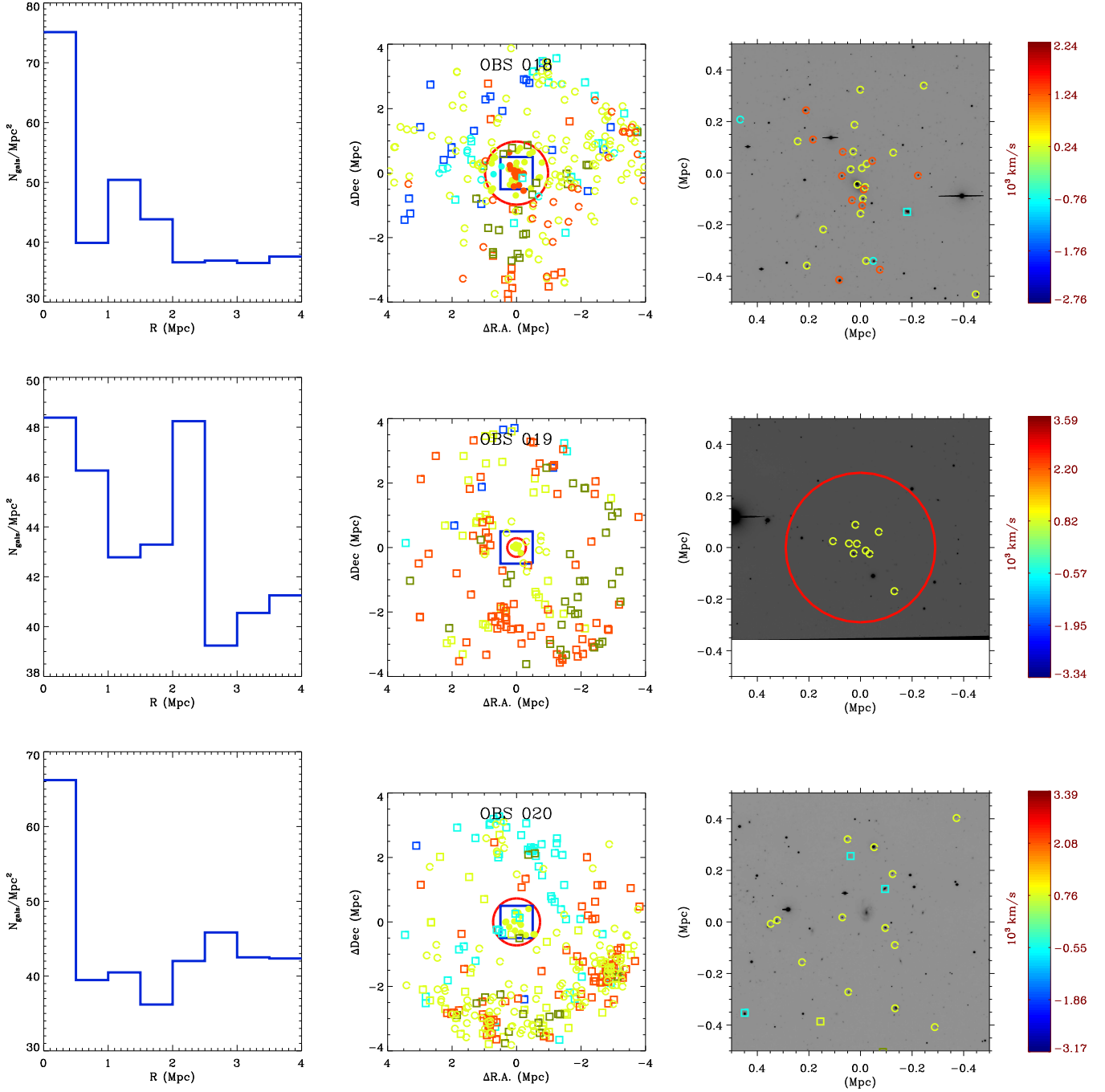


Figure D.5 Continuation of Figure D.1

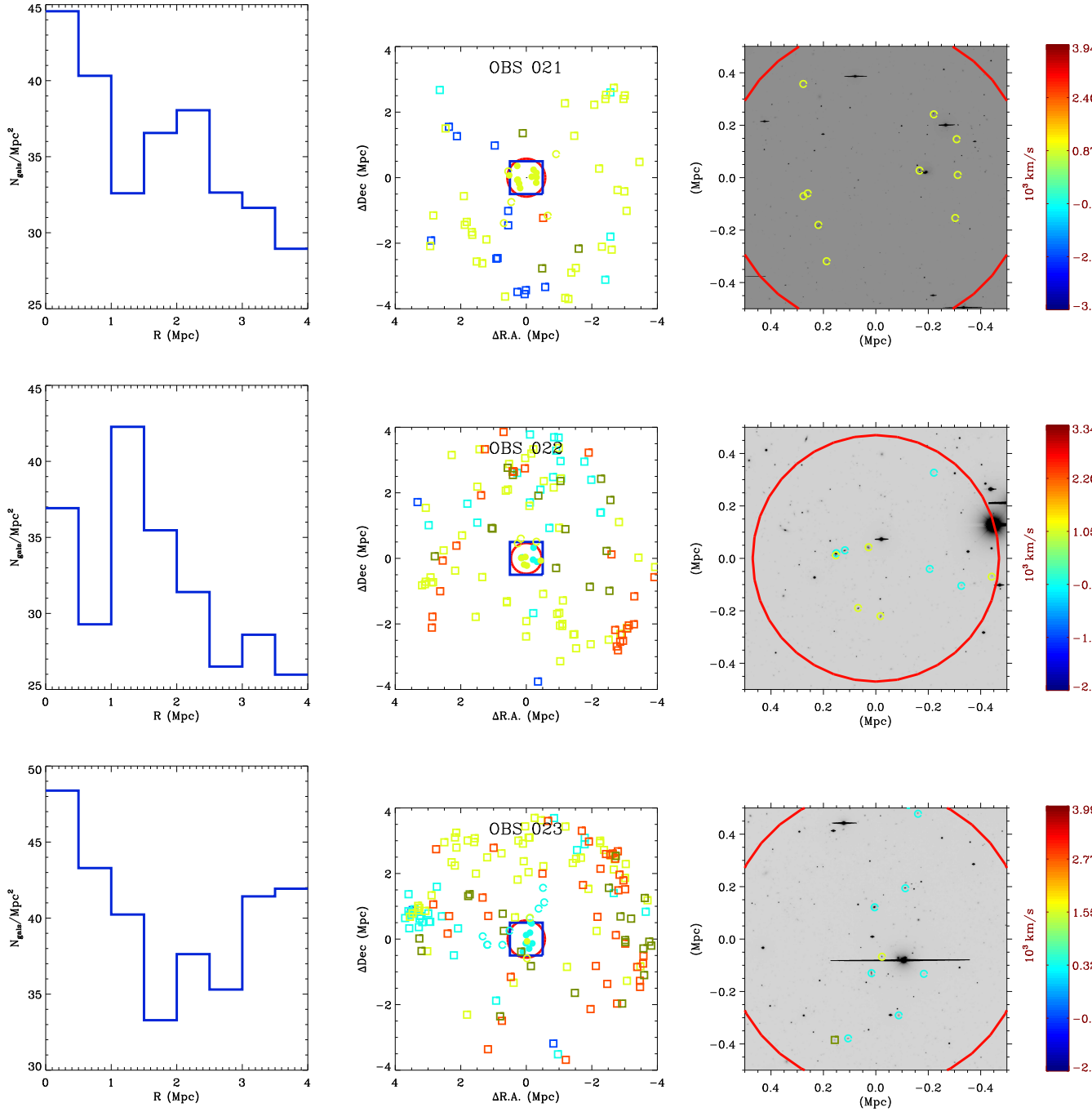


Figure D.6 Continuation of Figure D.1

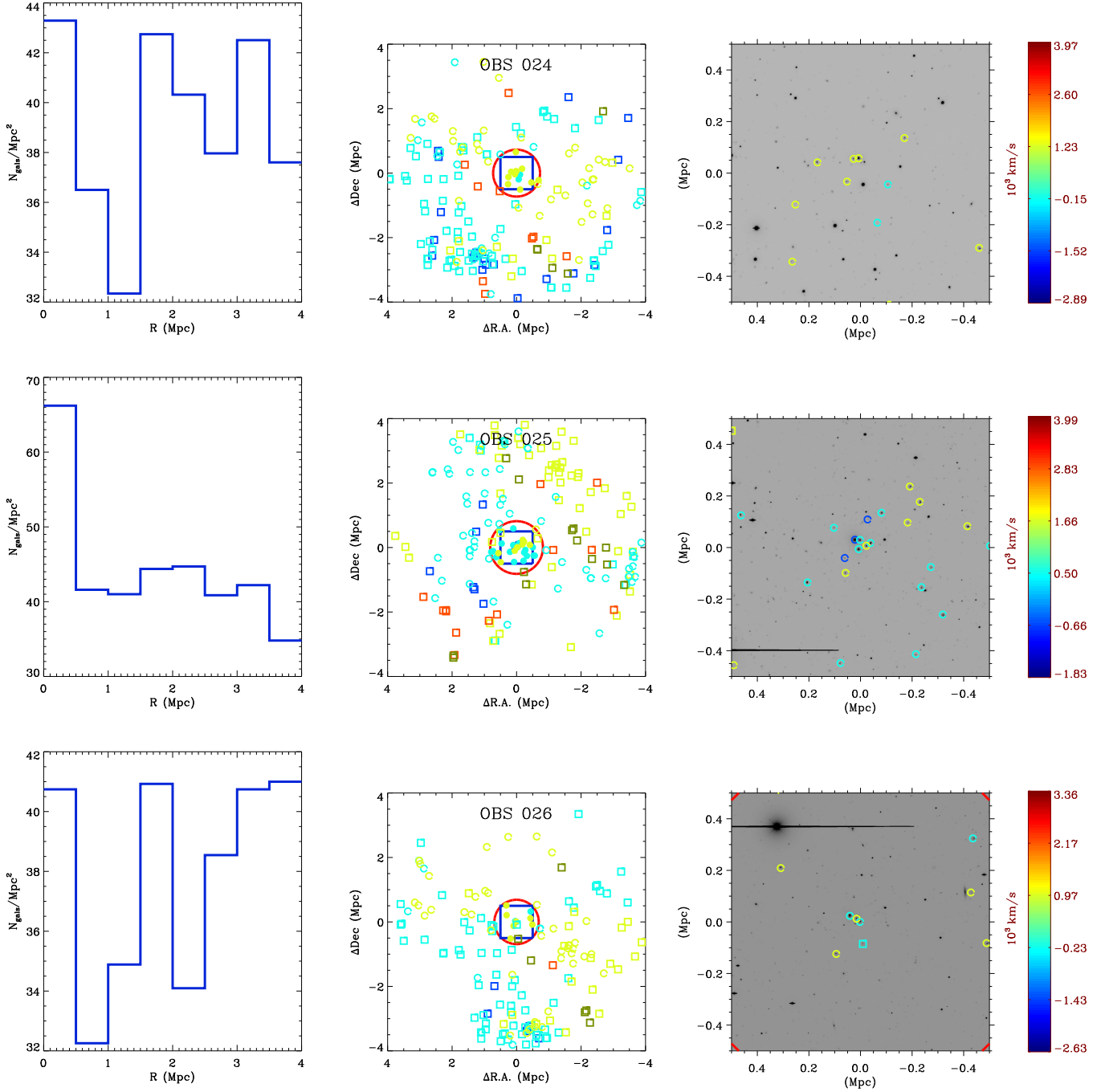


Figure D.7 Continuation of Figure D.1

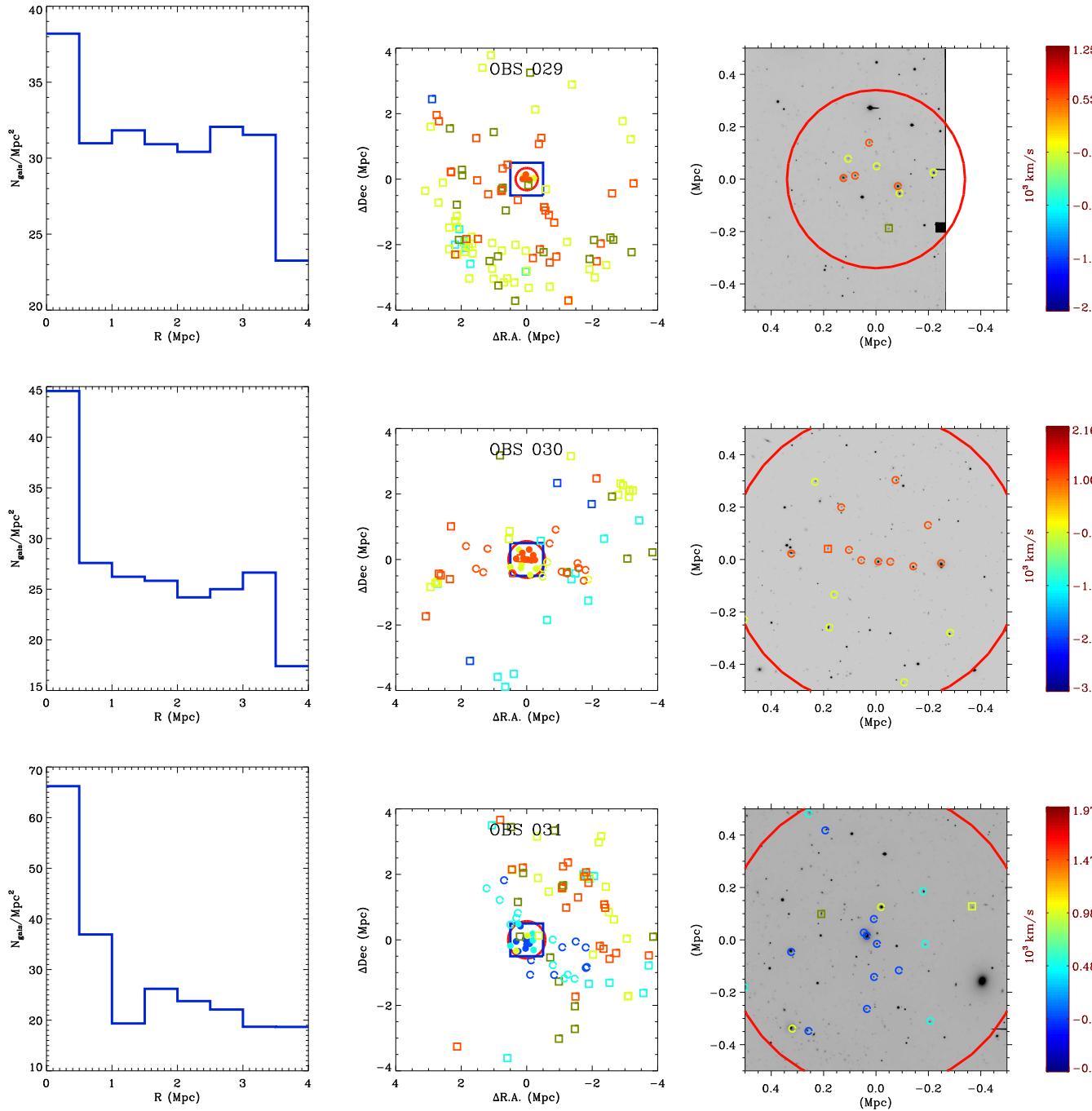


Figure D.8 Continuation of Figure D.1

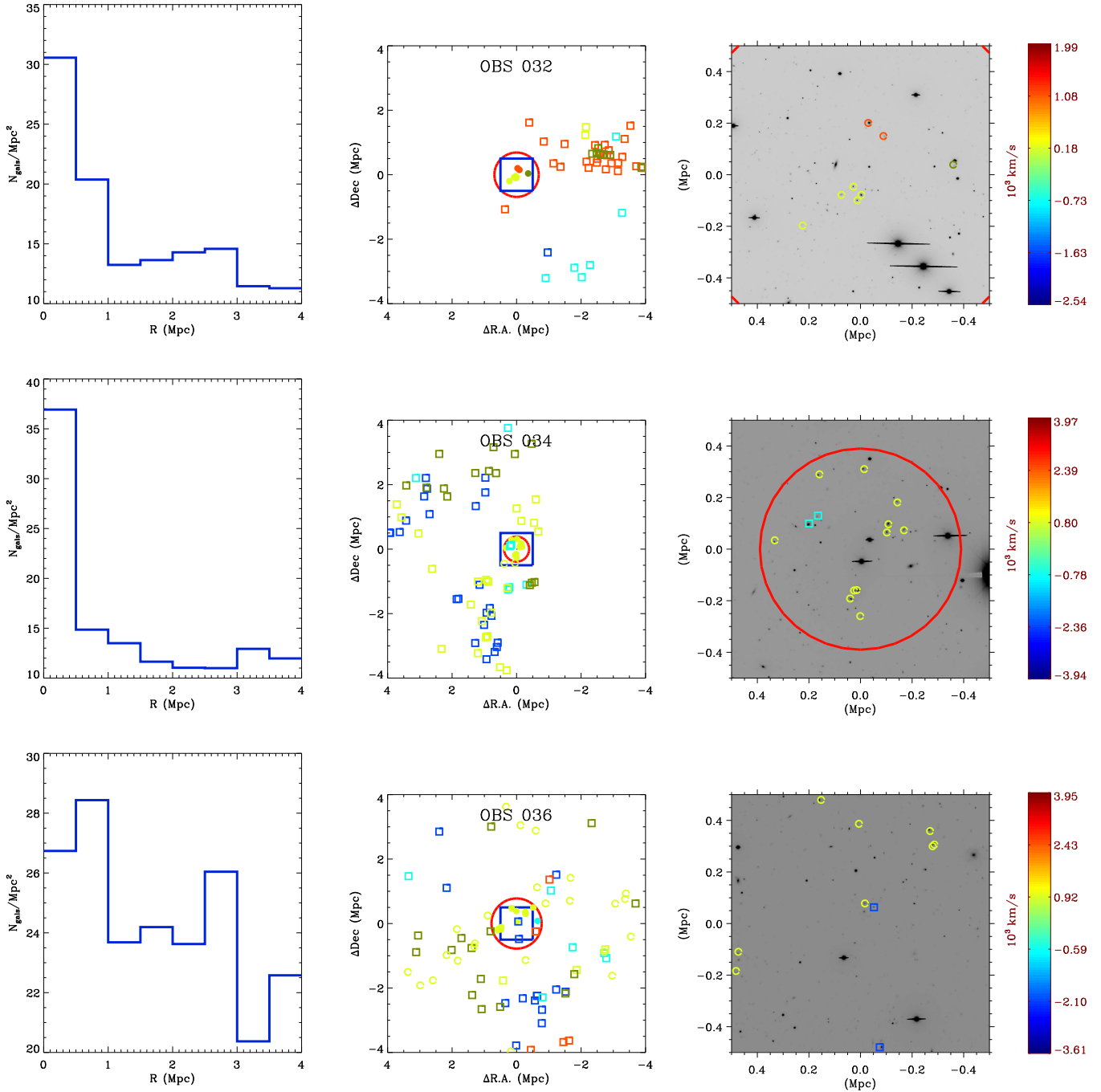


Figure D.9 Continuation of Figure D.1

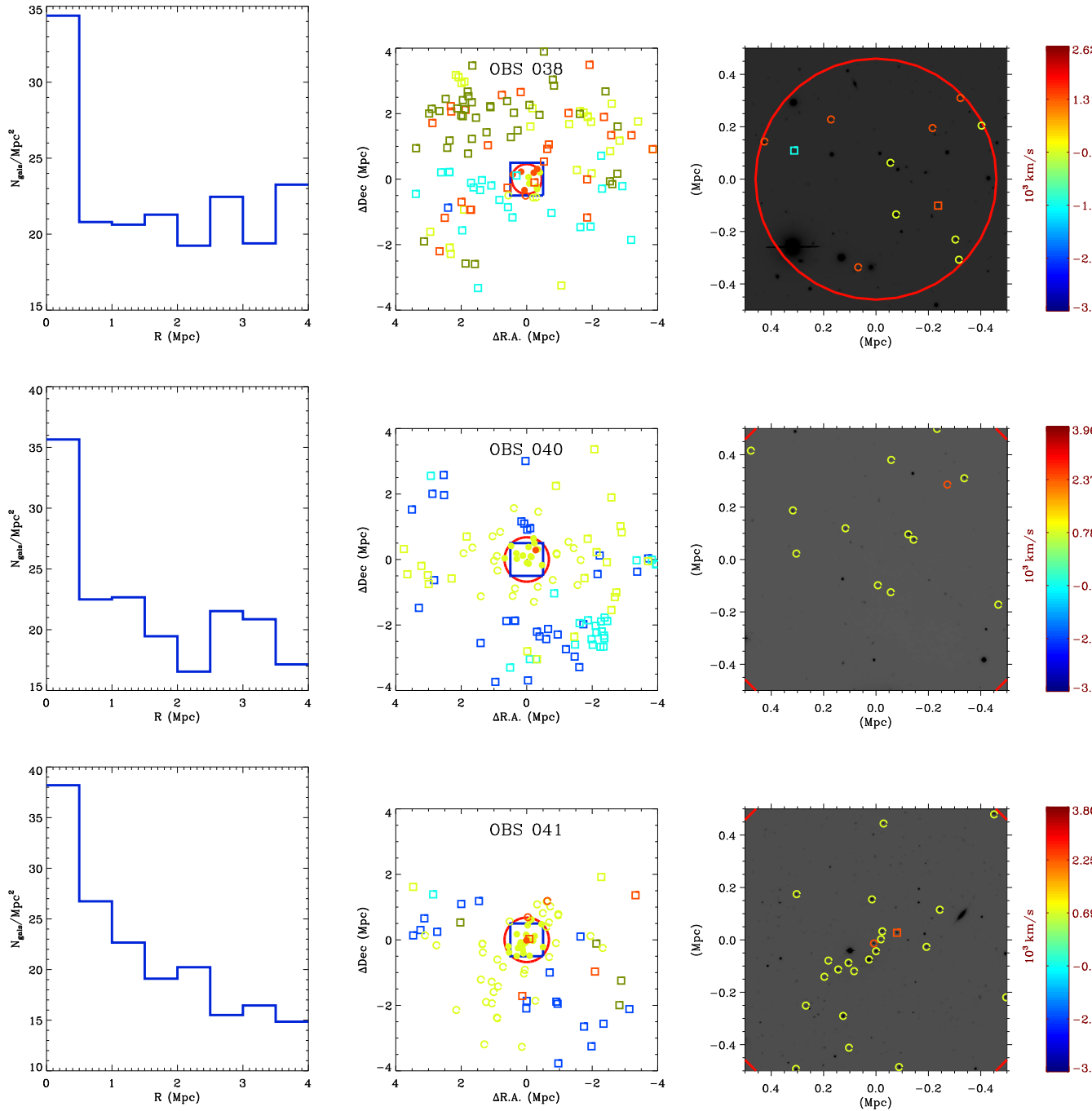


Figure D.10 Continuation of Figure D.1

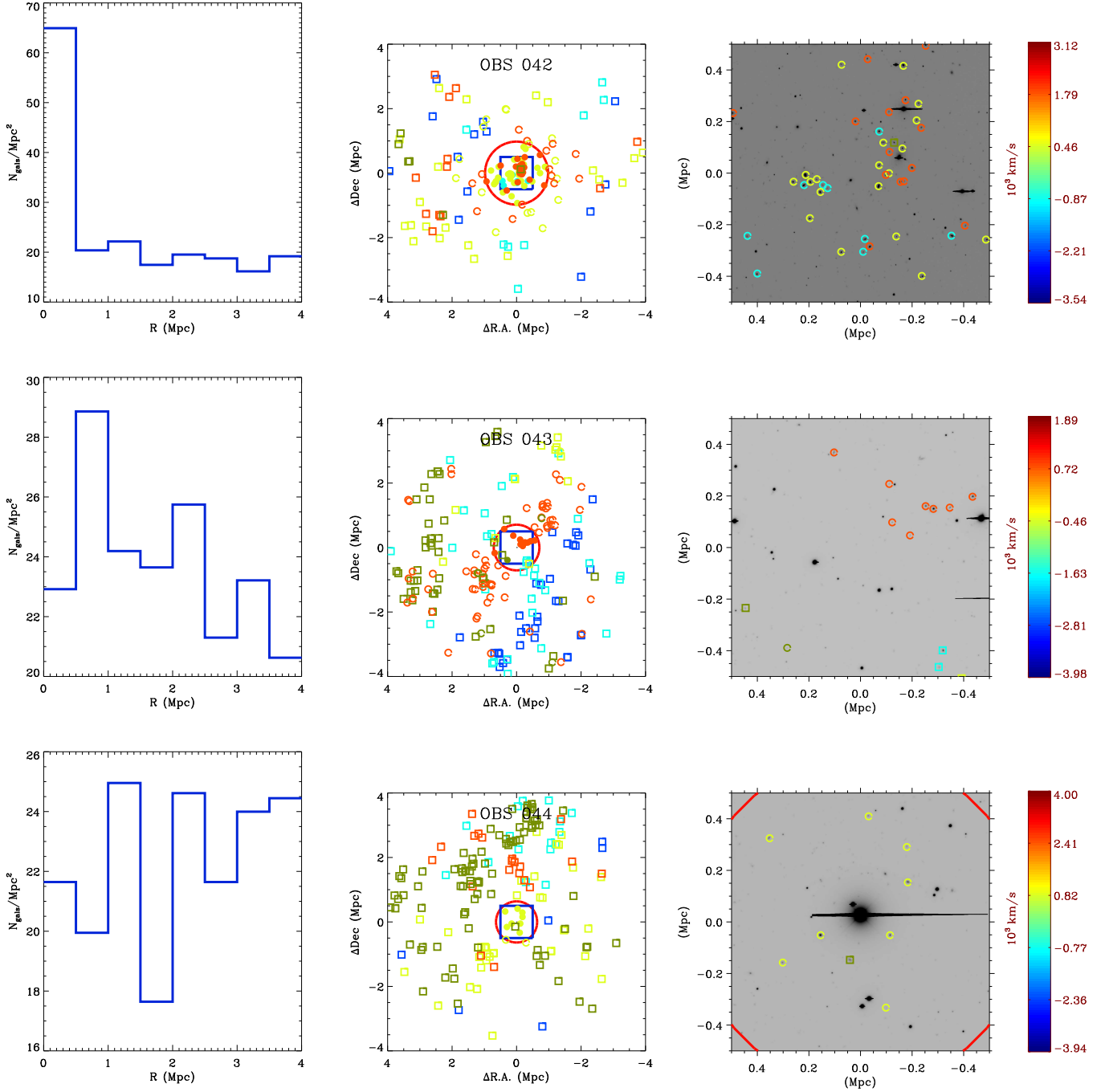


Figure D.11 Continuation of Figure D.1

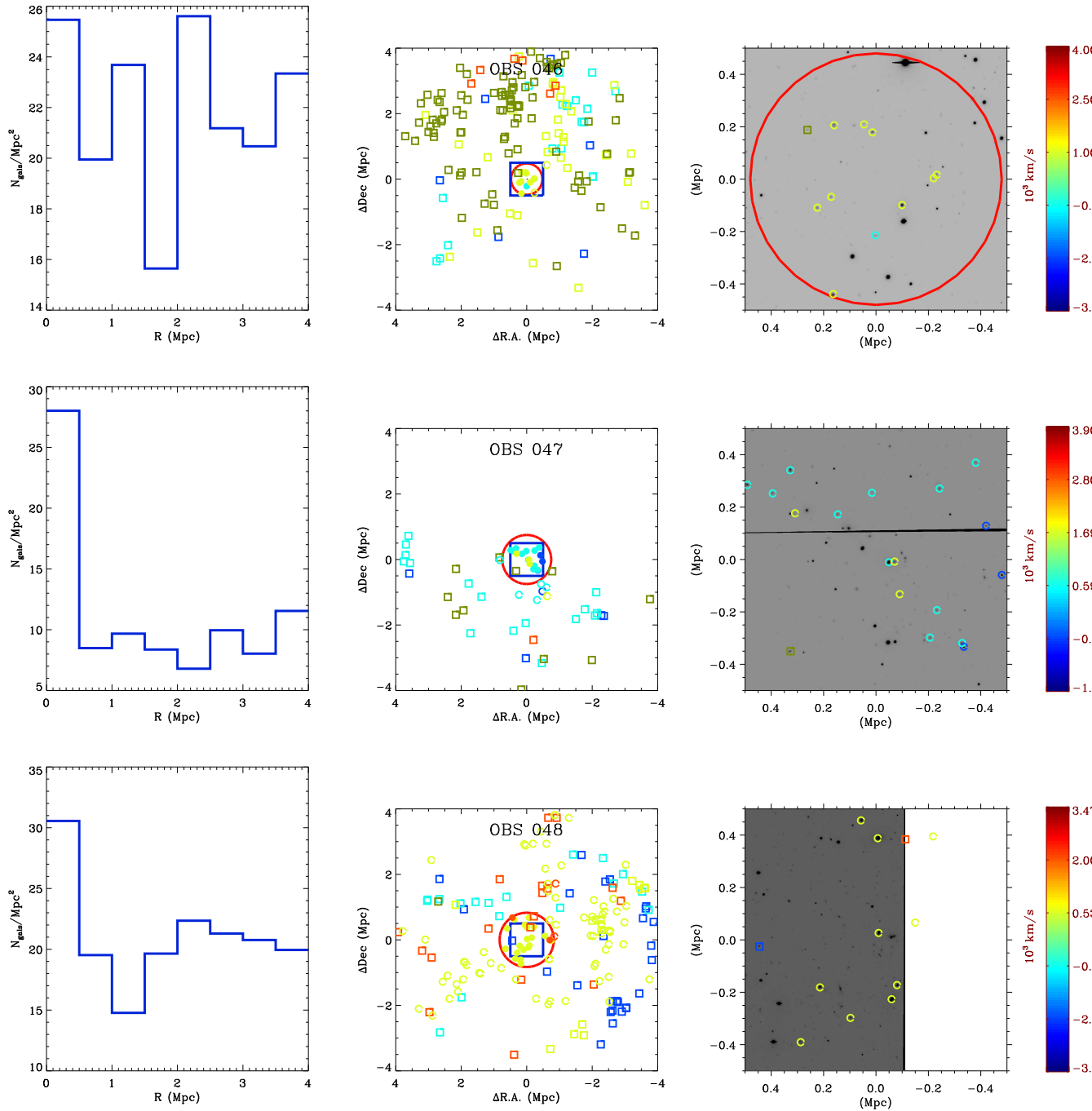


Figure D.12 Continuation of Figure D.1

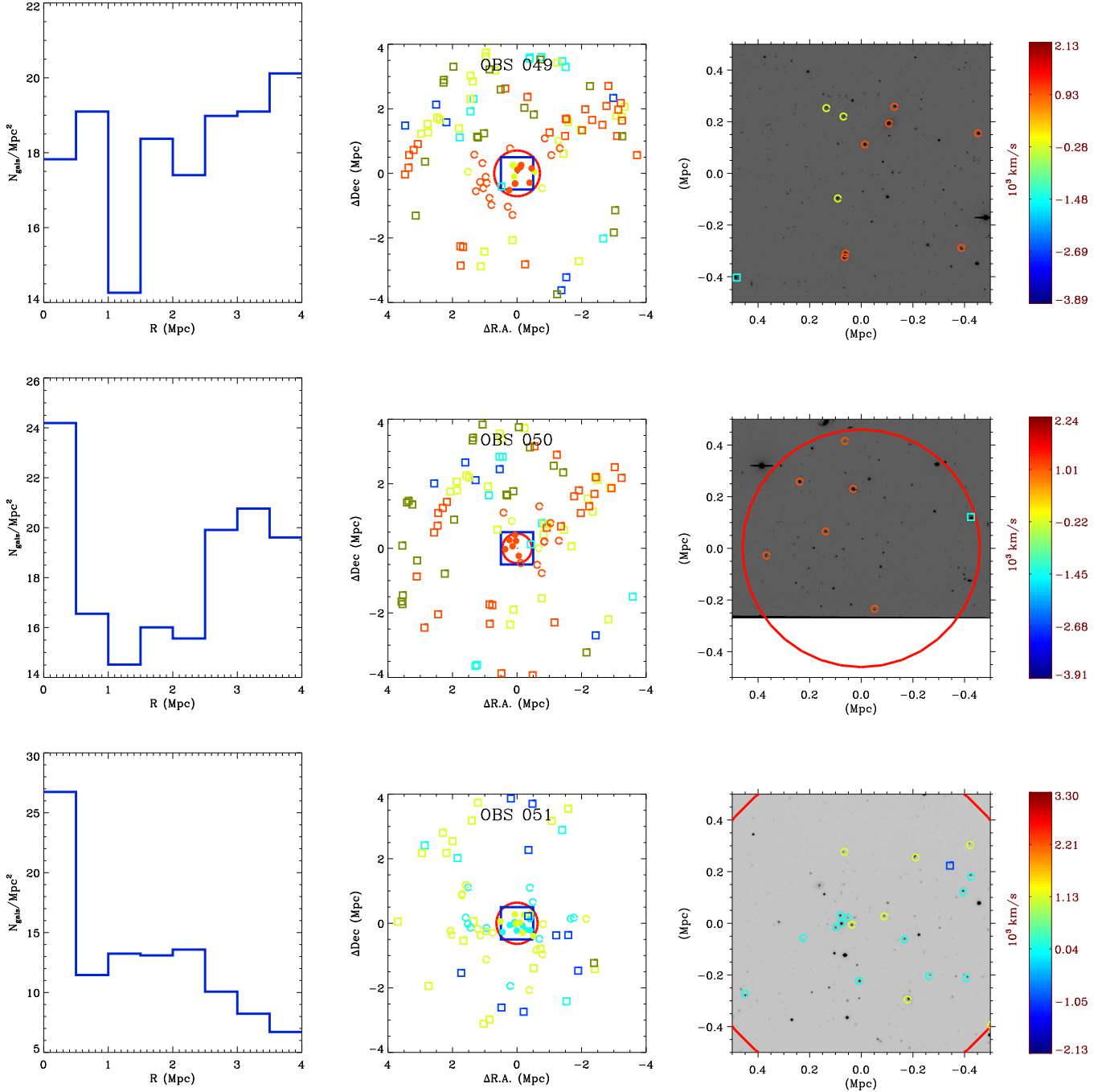


Figure D.13 Continuation of Figure D.1

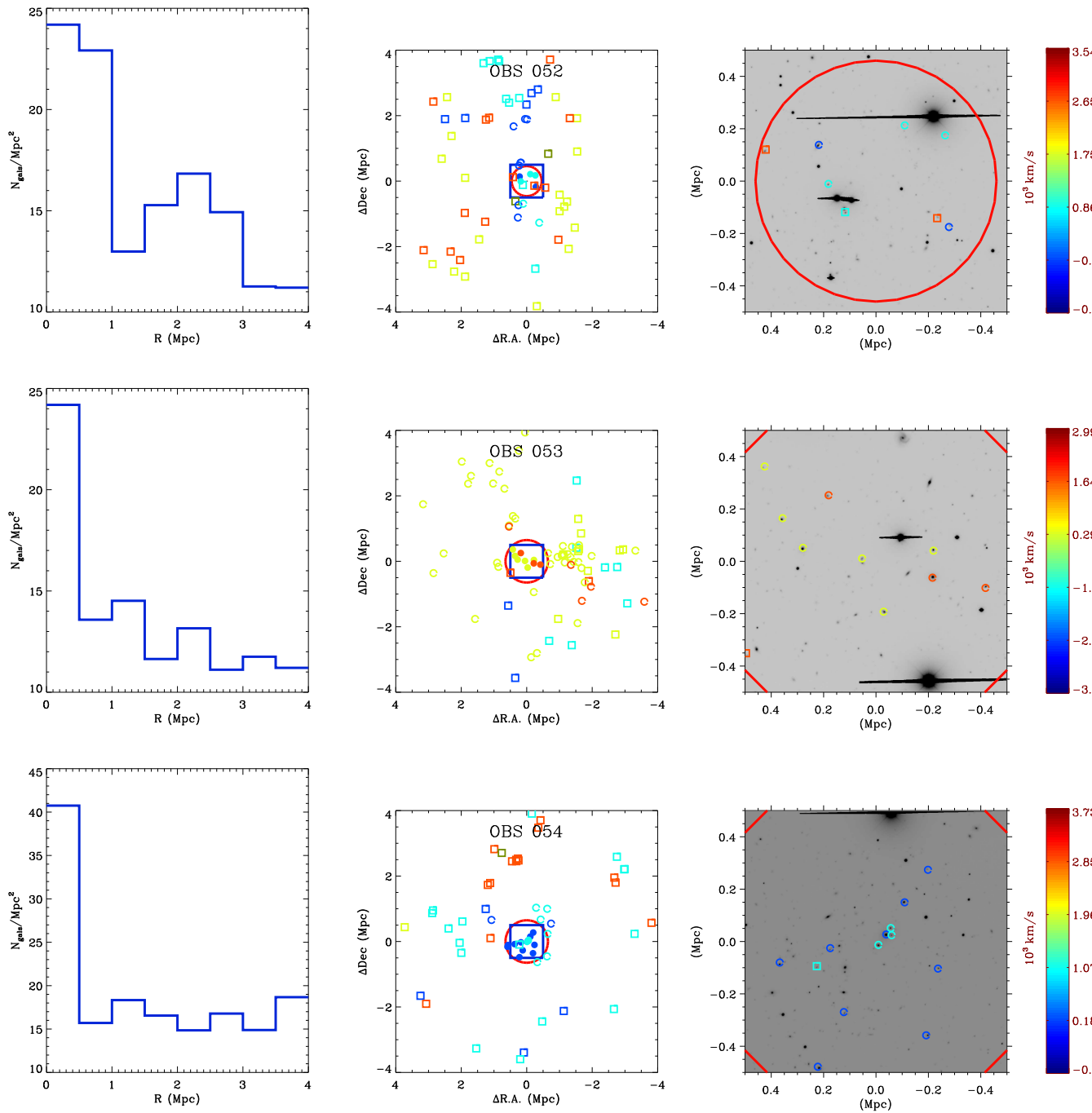


Figure D.14 Continuation of Figure D.1

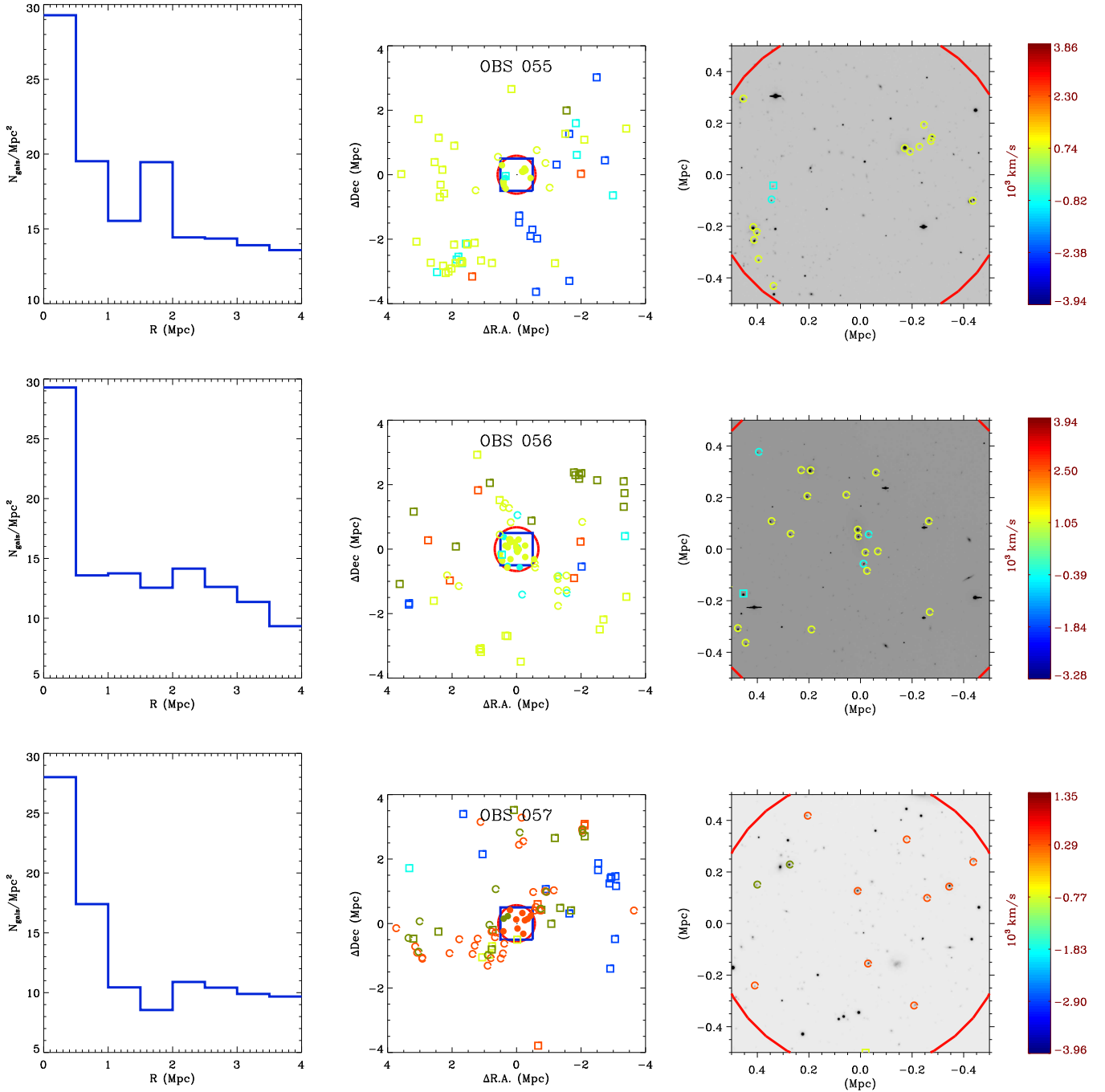


Figure D.15 Continuation of Figure D.1

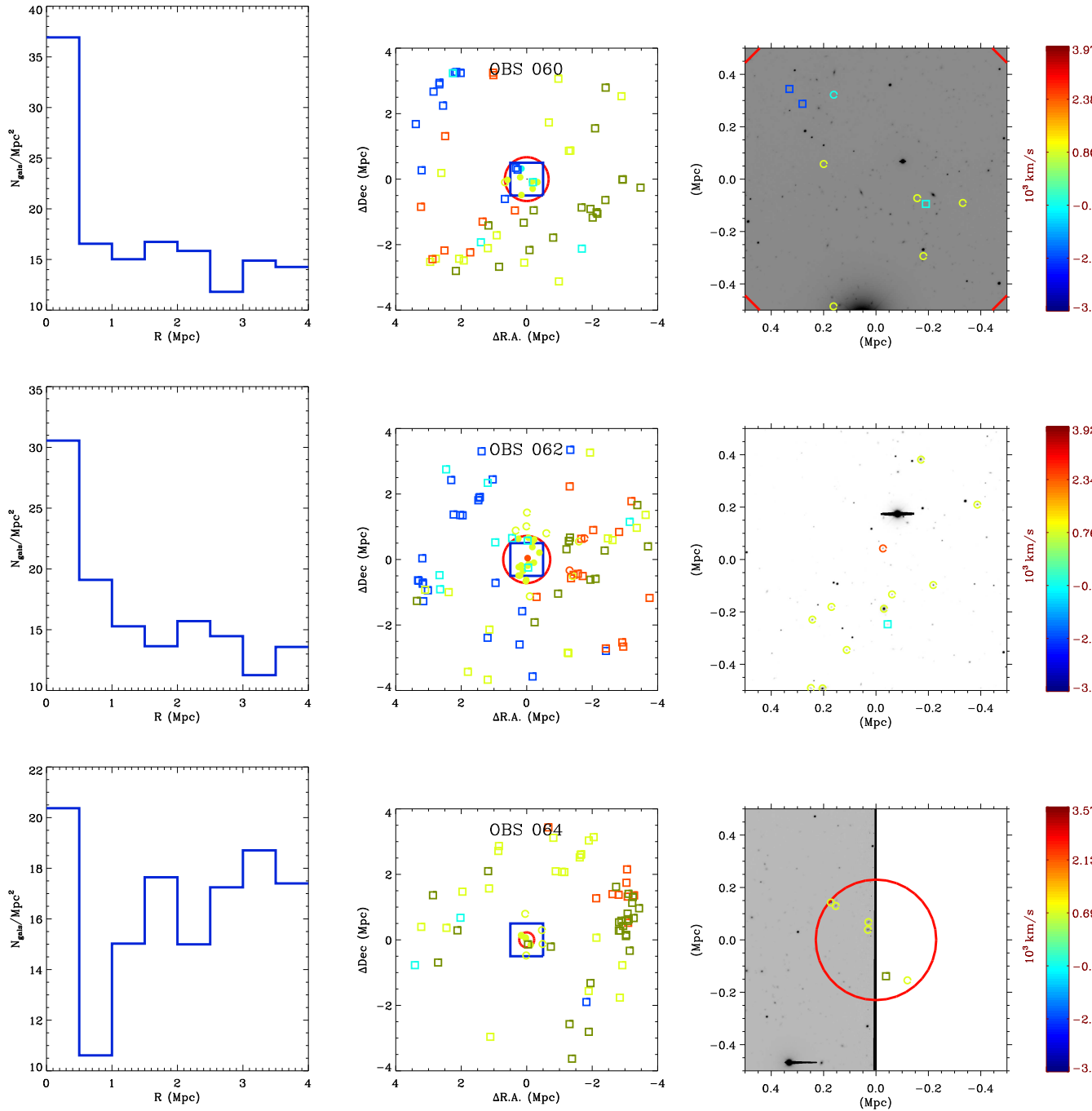


Figure D.16 Continuation of Figure D.1

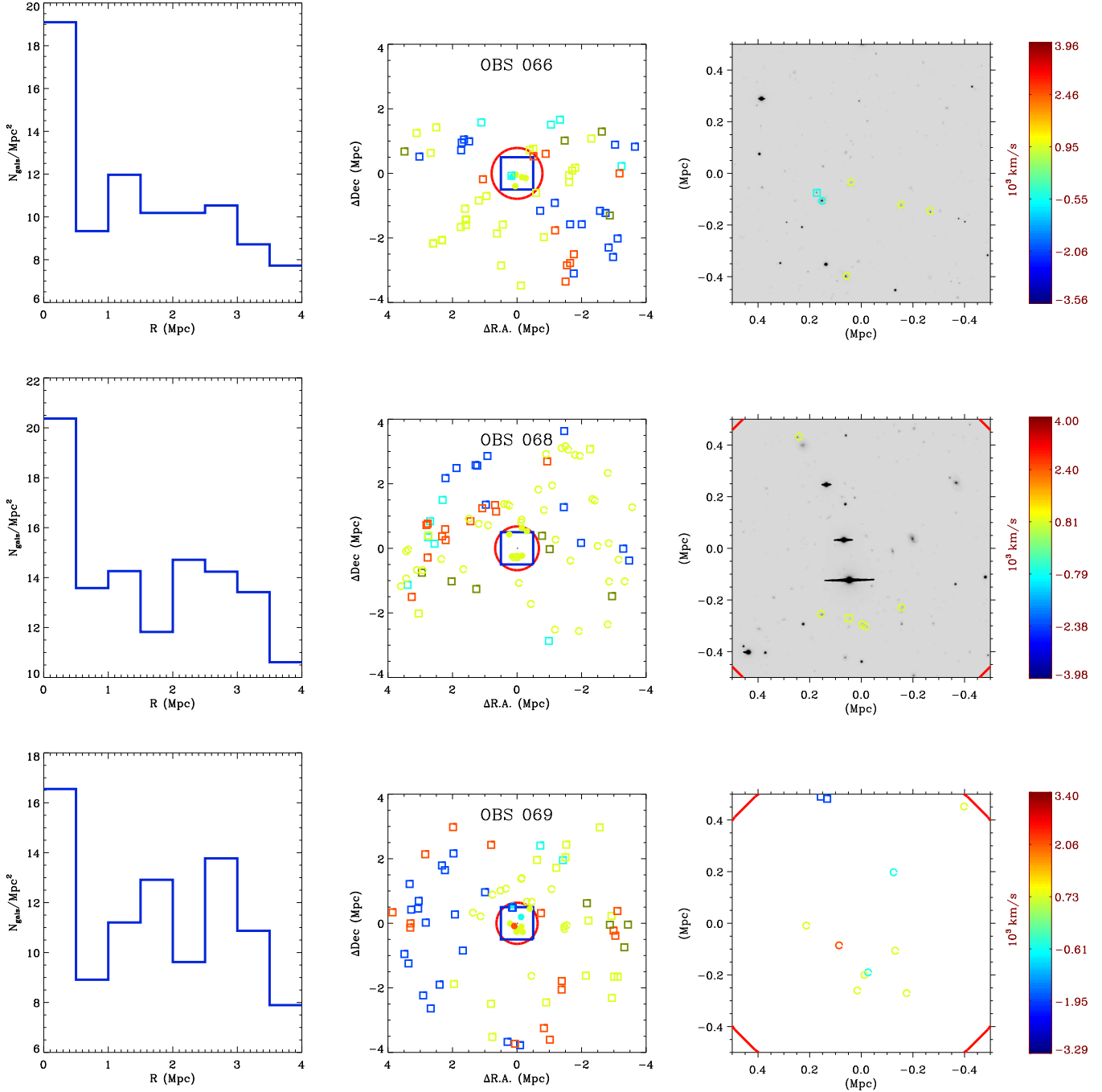


Figure D.17 Continuation of Figure D.1

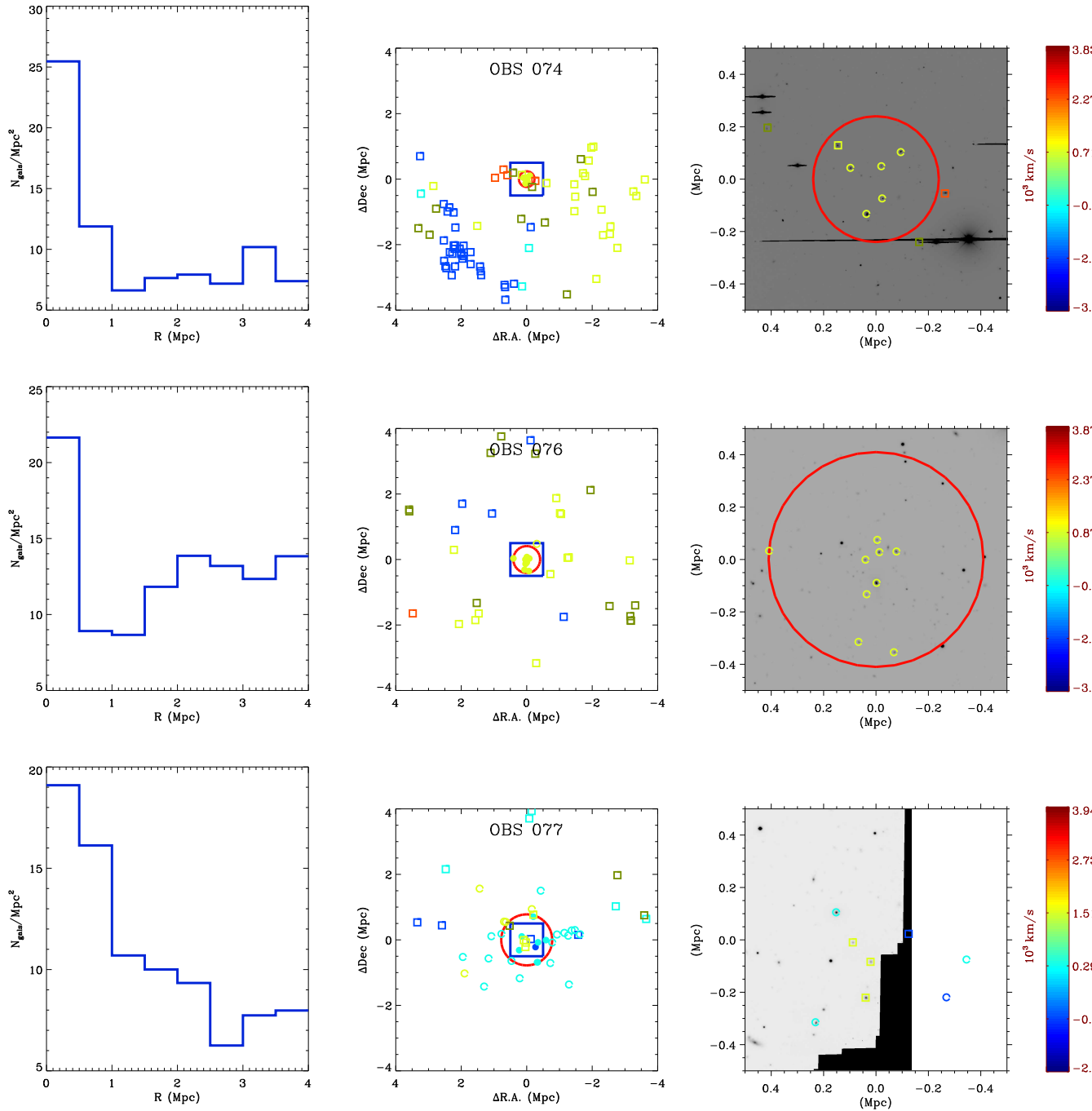


Figure D.18 Continuation of Figure D.1

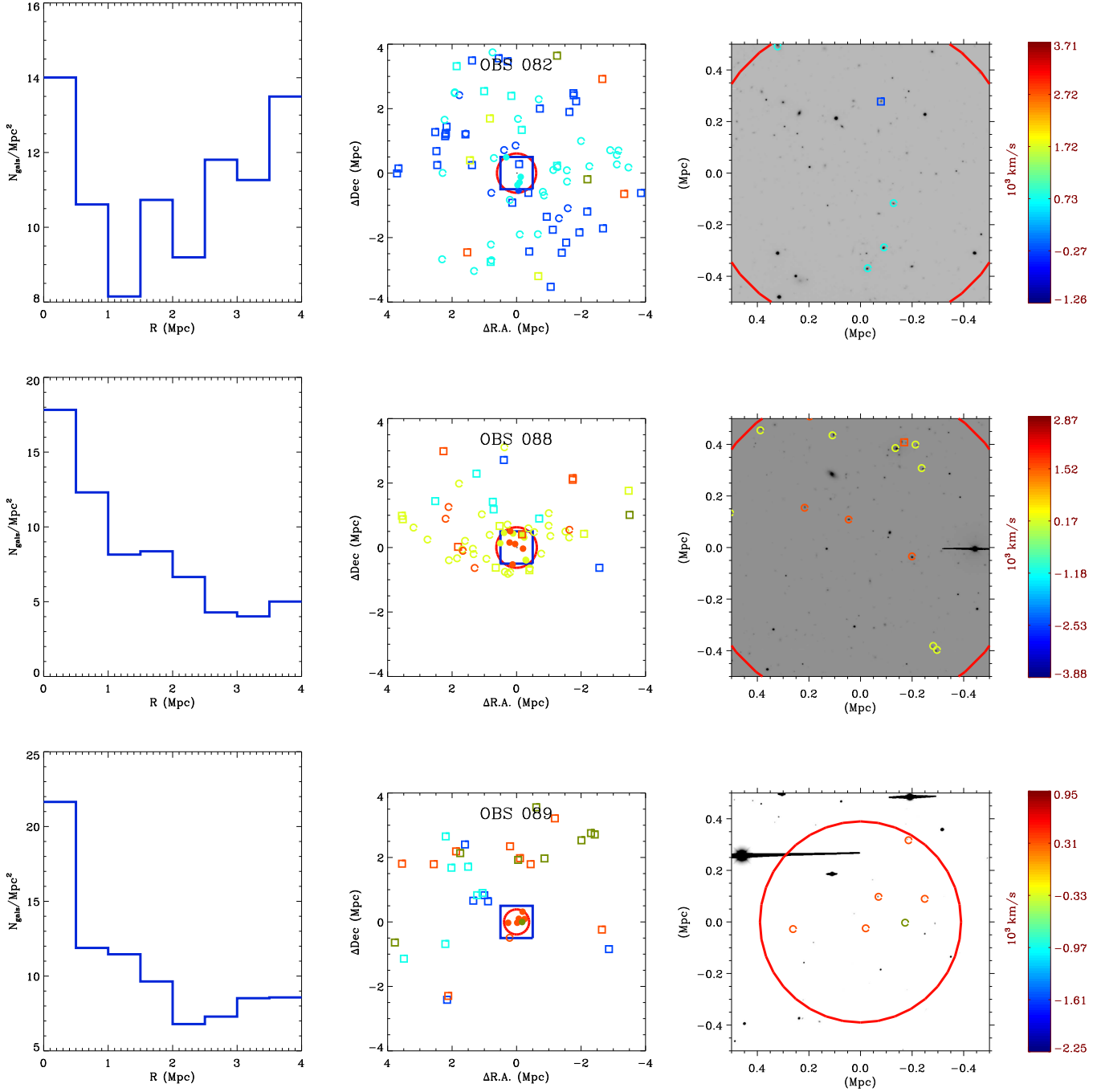


Figure D.19 Continuation of Figure D.1

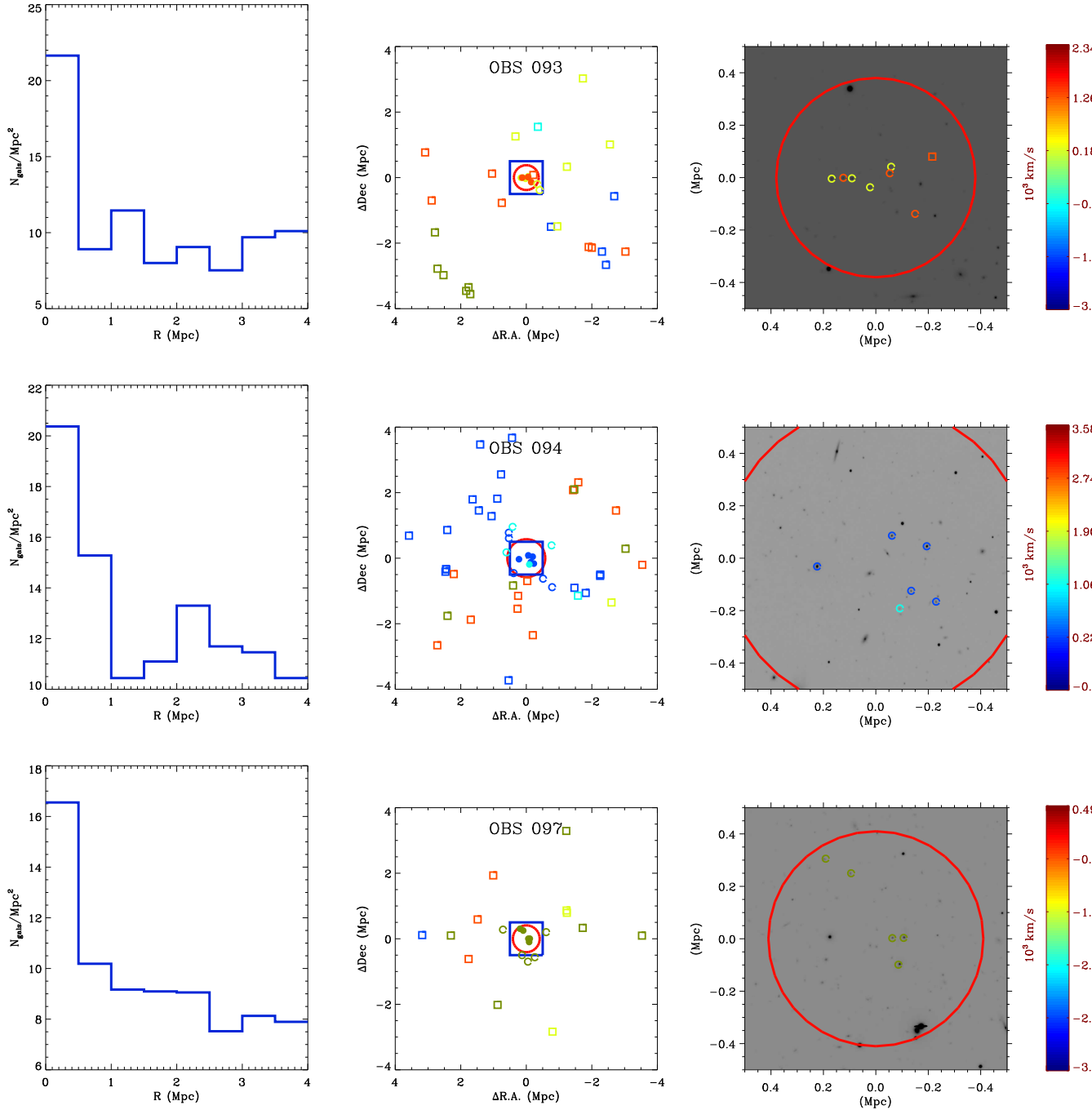


Figure D.20 Continuation of Figure D.1

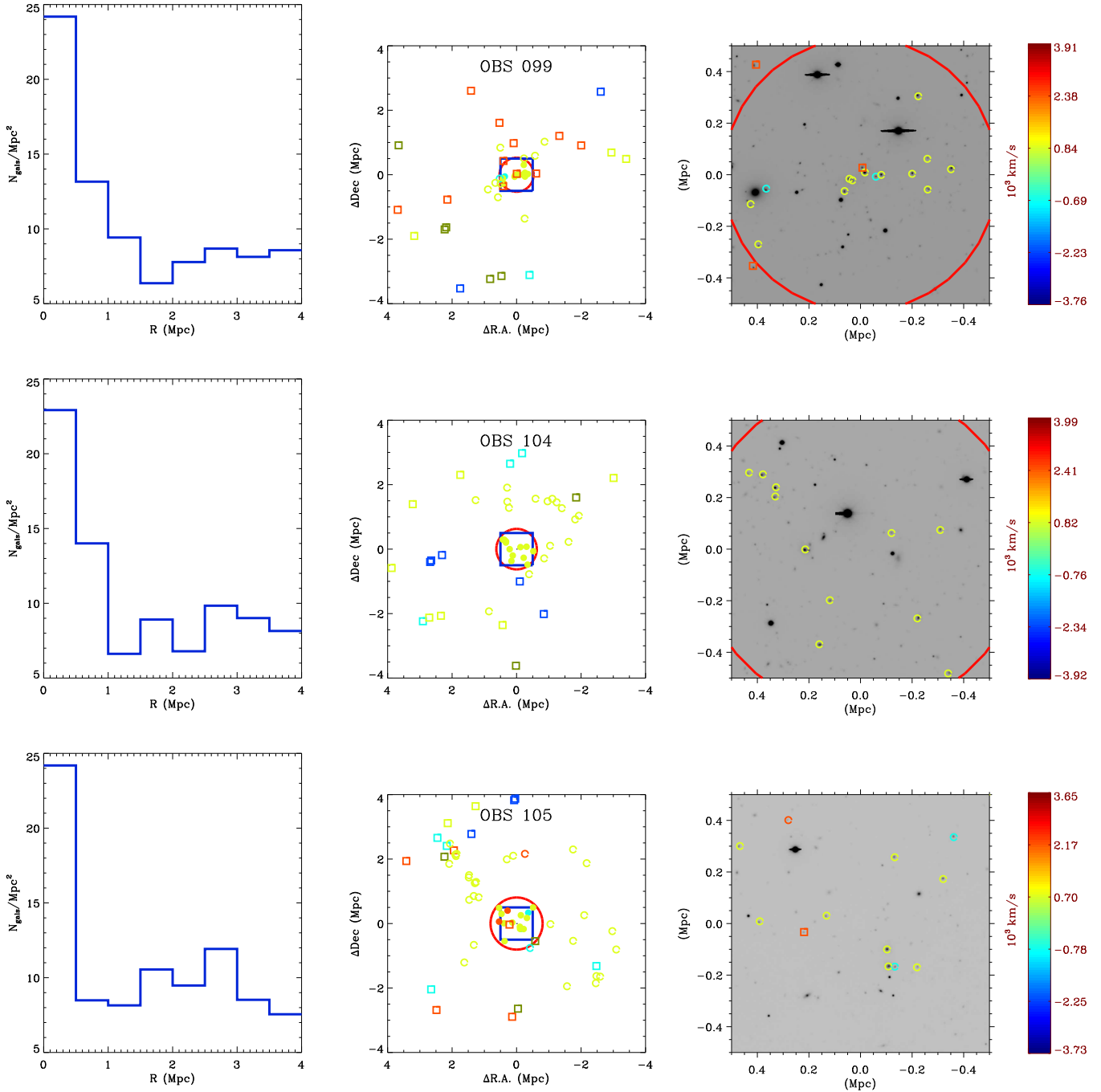


Figure D.21 Continuation of Figure D.1

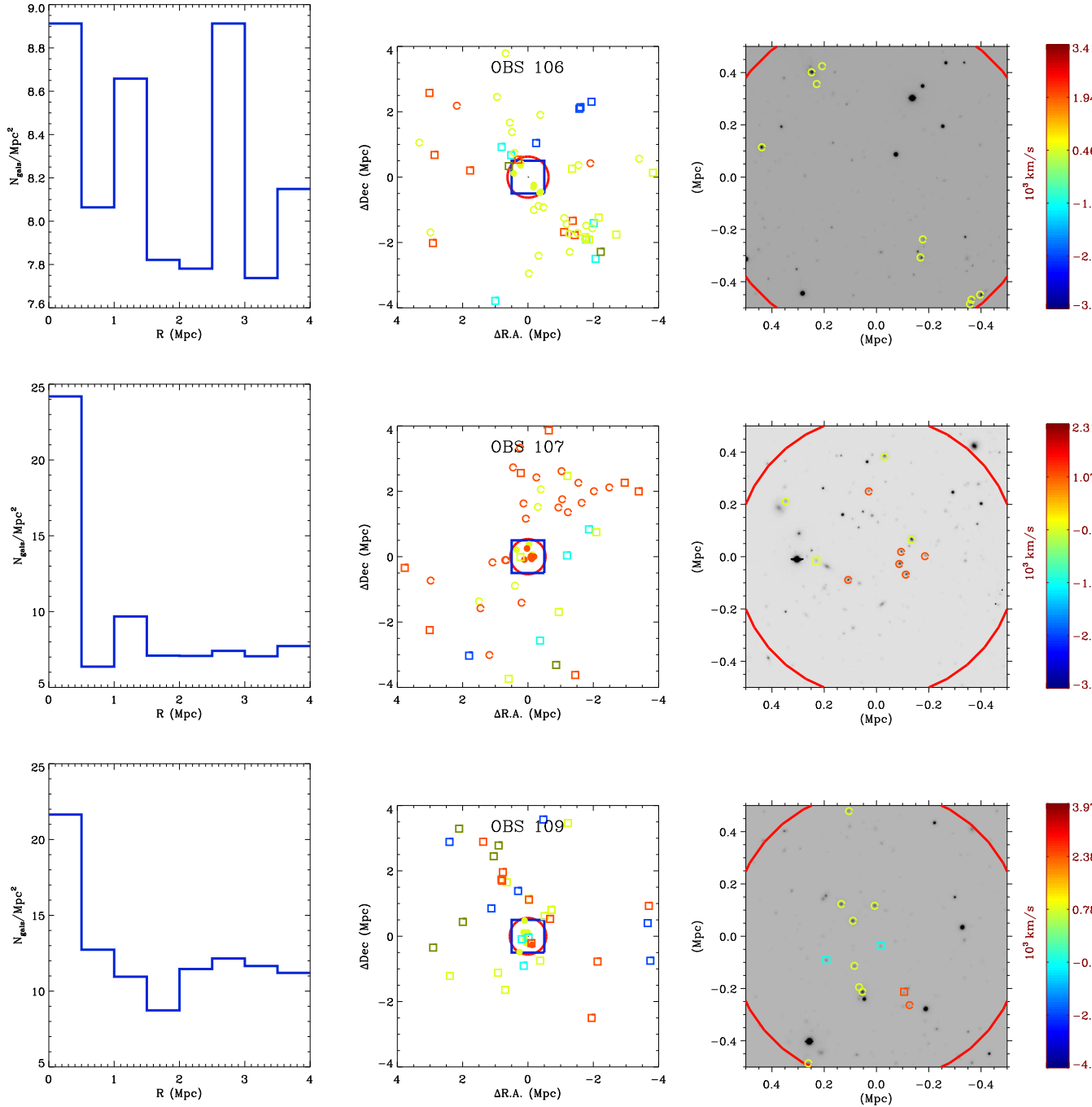


Figure D.22 Continuation of Figure D.1

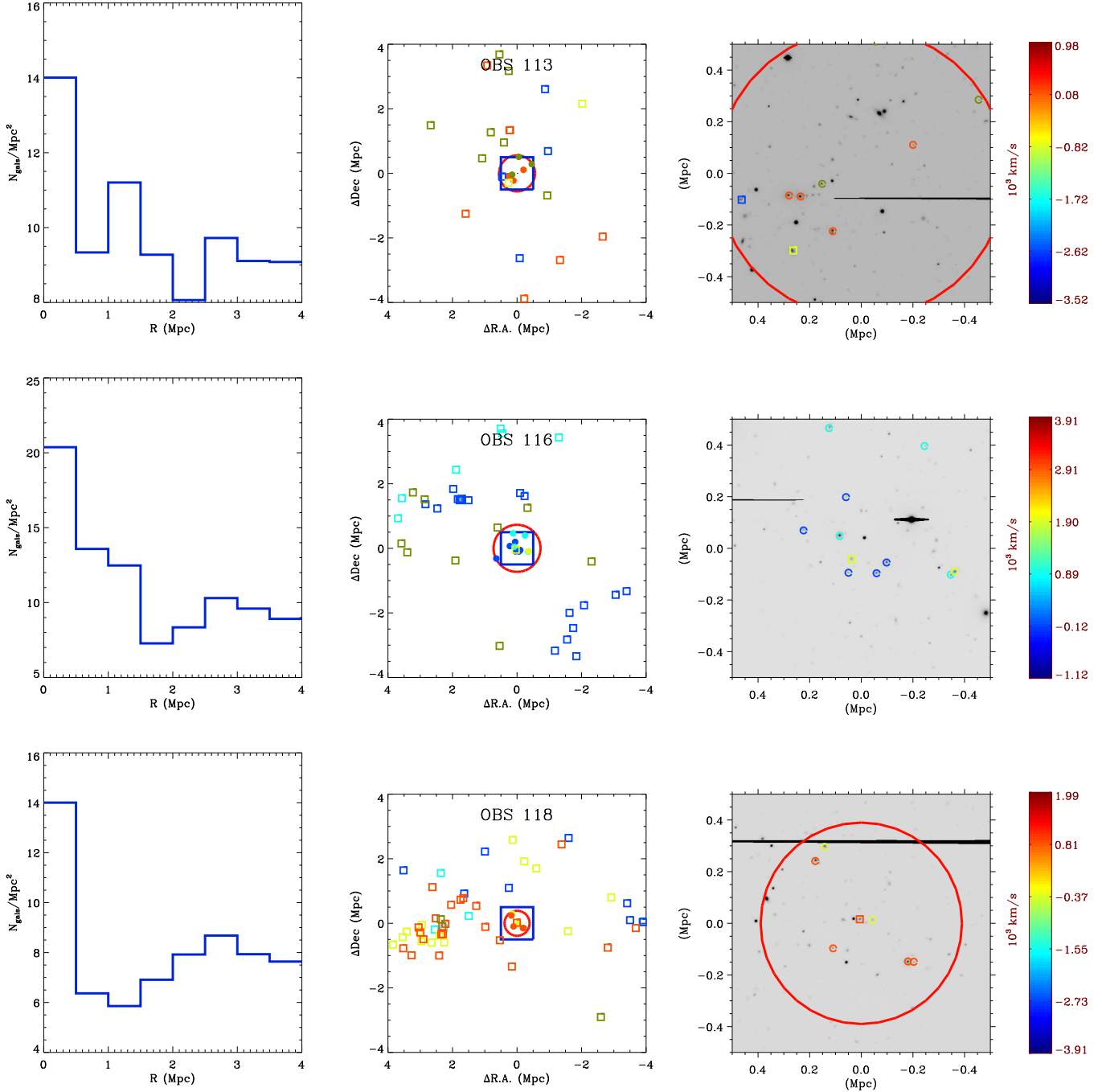


Figure D.23 Continuation of Figure D.1

Appendix E

X-ray Selected Galaxy Group Catalog - Optical and Dynamical Properties

In this appendix, we list the dynamical and optical properties for the 14 X-ray selected groups with at least 5 galaxy members and $z \leq 0.35$. Table E.1 contains: the group name; number of galaxies used to compute the velocity dispersion (N_σ); velocity dispersion (σ_{gr}); physical radius (R_{500}); total mass (M_{500}); optical luminosity (L_{opt}) and richness (N_{gals}).

Table E.1. Dynamical and Optical Properties For The 14 X-ray Selected Groups with $z \leq 0.35$ and at least 5 Galaxy Members

Name	N_σ	σ_{gr} (km s ⁻¹)	R_{500} (Mpc)	M_{500} (10 ¹⁴ M _⊙)	L_{opt} (10 ¹² L _⊙)	N_{gals}	Substructure
XBS 02	17	184 ⁺⁶⁰ ₋₂₅	0.32 ^{+0.07} _{-0.03}	0.12 ^{+0.08} _{-0.03}	0.28±0.11	15±0.8	Yes
XBS 06	81	641 ⁺⁵⁸ ₋₄₁	0.88 ^{+0.05} _{-0.04}	2.19 ^{+0.39} _{-0.28}	1.19±0.24	50±3.3	No
XBS 07	9	160 ⁺⁵² ₋₂₁	0.33 ^{+0.07} _{-0.03}	0.10 ^{+0.07} _{-0.03}	0.11±0.05	9±0.4	No
XBS 09	7	242 ⁺⁹⁹ ₋₁₈	0.34 ^{+0.10} _{-0.03}	0.13 ^{+0.11} _{-0.03}	0.29±0.12	14±0.3	No
XBS 11	22	417 ⁺⁶⁹ ₋₃₇	0.58 ^{+0.06} _{-0.04}	0.70 ^{+0.23} _{-0.13}	0.74±0.22	23±2.1	Yes
XBS 13	42	375 ⁺⁴⁸ ₋₃₁	0.59 ^{+0.05} _{-0.03}	0.65 ^{+0.17} _{-0.11}	0.32±0.13	17±1.7	No
XBS 17	49	615 ⁺⁶⁶ ₋₄₉	0.85 ^{+0.06} _{-0.05}	2.14 ^{+0.46} _{-0.35}	1.40±0.27	59±2.2	No
XBS 25	11	377 ⁺⁸⁹ ₋₃₀	0.55 ^{+0.09} _{-0.03}	0.58 ^{+0.28} _{-0.10}	0.35±0.14	13±1.2	No
XBS 26	13	163 ⁺⁴³ ₋₂₂	0.39 ^{+0.07} _{-0.04}	0.20 ^{+0.11} _{-0.06}	0.17±0.08	11±0.6	No
XBS 33	14	144 ⁺⁴¹ ₋₁₈	0.38 ^{+0.07} _{-0.03}	0.22 ^{+0.13} _{-0.06}	0.94±0.22	34±0.8	No
XBS 35	7	123 ⁺⁴⁴ ₋₁₅	0.21 ^{+0.05} _{-0.02}	0.03 ^{+0.02} _{-0.01}	0.10±0.04	9±0.2	No
XBS 36	6	111 ⁺⁷⁴ ₋₃₉	0.23 ^{+0.10} _{-0.05}	0.04 ^{+0.06} _{-0.03}	0.23±0.08	14±0.1	No

Table E.1 (cont'd)

Name	N_σ	σ_{gr} (km s ⁻¹)	R_{500} (Mpc)	M_{500} (10 ¹⁴ M _⊙)	L_{opt} (10 ¹² L _⊙)	N_{gals}	Substructure
XBS 37	17	335 ⁺⁵¹ ₋₂₇	0.52 ^{+0.05} _{-0.03}	0.44 ^{+0.14} _{-0.08}	0.51±0.17	21±0.9	Yes
XBS 46	7	129 ⁺⁵² ₋₂₄	0.28 ^{+0.08} _{-0.04}	0.08 ^{+0.06} _{-0.03}	0.17±0.10	7±0.2	No

Appendix F

Optically Selected Galaxy Group Catalog - Optical and Dynamical Properties

In this appendix, we list the dynamical and optical properties for the 67 optically selected groups with at least 5 galaxy members and $z \leq 0.35$. Table E.1 contains: the group name; number of galaxies used to compute the velocity dispersion (N_σ); velocity dispersion (σ_{gr}); physical radius (R_{500}); total mass (M_{500}); optical luminosity (L_{opt}) and richness (N_{gals}).

Table F.1. Dynamical and Optical Properties For The 67 Optically Selected Groups
with $z \leq 0.35$ and at least 5 Galaxy Members

Name	N_σ	σ_{gr} (km s ⁻¹)	R_{500} (Mpc)	M_{500} (10 ¹⁴ M _⊙)	L_{opt} (10 ¹² L _⊙)	N_{gals}	Structure
OBS 001	10	183 ⁺⁴⁶ ₋₂₃	0.36 ^{+0.06} _{-0.03}	0.14 ^{+0.07} _{-0.04}	0.17±0.06	16±0.4	No
OBS 003	9	160 ⁺⁵² ₋₂₂	0.33 ^{+0.07} _{-0.03}	0.10 ^{+0.07} _{-0.03}	0.11±0.05	9±0.4	No
OBS 004	13	319 ⁺³⁰⁶ ₋₁₃	0.57 ^{+0.37} _{-0.02}	0.55 ^{+1.06} _{-0.06}	0.27±0.09	18±3.6	No
OBS 007	8	128 ⁺⁷⁷ ₋₅₁	0.21 ^{+0.08} _{-0.06}	0.03 ^{+0.04} _{-0.02}	0.15±0.08	6±0.1	No
OBS 010	11	205 ⁺¹⁰⁰ ₋₈₁	0.36 ^{+0.12} _{-0.10}	0.14 ^{+0.14} _{-0.11}	0.14±0.08	9±0.3	No
OBS 011	13	372 ⁺⁸⁴ ₋₄₃	0.60 ^{+0.09} _{-0.05}	0.67 ^{+0.31} _{-0.16}	0.44±0.13	24±1.5	No
OBS 012	7	407 ⁺¹⁴² ₋₄₈	0.49 ^{+0.12} _{-0.04}	0.37 ^{+0.26} _{-0.10}	0.09±0.05	11±0.8	No
OBS 014	7	87 ⁺³⁷ ₋₁₉	0.17 ^{+0.06} _{-0.03}	0.02 ^{+0.02} _{-0.01}	0.09±0.08	2±0.1	Yes
OBS 015 ^{XBS06}	81	641 ⁺⁵⁸ ₋₄₁	0.88 ^{+0.05} _{-0.04}	2.19 ^{+0.39} _{-0.28}	1.19±0.24	50±3.3	No
OBS 016	14	327 ⁺⁷⁷ ₋₃₈	0.45 ^{+0.07} _{-0.04}	0.29 ^{+0.14} _{-0.07}	0.13±0.09	4±0.7	Yes
OBS 017	10	257 ⁺⁷⁰ ₋₃₀	0.33 ^{+0.06} _{-0.03}	0.12 ^{+0.07} _{-0.03}	0.26±0.10	13±0.3	No
OBS 018 ^{XBS13}	42	375 ⁺⁴⁸ ₋₃₁	0.59 ^{+0.05} _{-0.03}	0.65 ^{+0.17} _{-0.11}	0.32±0.13	17±1.7	No

Table F.1 (cont'd)

Name	N_σ	σ_{gr} (km s ⁻¹)	R_{500} (Mpc)	M_{500} (10 ¹⁴ M _⊙)	L_{opt} (10 ¹² L _⊙)	N_{gals}	Structure
OBS 019	8	175 ⁺⁵⁹ ₋₁₆	0.24 ^{+0.05} _{-0.02}	0.04 ^{+0.03} _{-0.01}	0.11±0.06	6±0.2	No
OBS 020	15	265 ⁺⁵⁰ ₋₃₀	0.48 ^{+0.06} _{-0.04}	0.36 ^{+0.14} _{-0.09}	0.20±0.10	13±1.1	No
OBS 021	11	289 ⁺⁸¹ ₋₄₉	0.49 ^{+0.09} _{-0.06}	0.37 ^{+0.21} _{-0.13}	0.08±0.10	3±0.9	No
OBS 022	10	361 ⁺⁸⁷ ₋₃₆	0.45 ^{+0.07} _{-0.03}	0.29 ^{+0.14} _{-0.06}	0.21±0.11	8±1.1	Yes
OBS 023	9	312 ⁺¹⁰⁴ ₋₄₇	0.51 ^{+0.12} _{-0.05}	0.43 ^{+0.29} _{-0.14}	0.03±0.04	4±1.7	Yes
OBS 024	13	198 ⁺¹⁰⁶ ₋₅₈	0.38 ^{+0.14} _{-0.08}	0.18 ^{+0.19} _{-0.10}	0.16±0.08	13±1.0	No
OBS 025	31	549 ⁺⁷⁵ ₋₅₆	0.76 ^{+0.07} _{-0.05}	1.43 ^{+0.40} _{-0.30}	0.22±0.09	20±4.3	No
OBS 026	7	194 ⁺¹⁰² ₋₆₄	0.45 ^{+0.16} _{-0.10}	0.30 ^{+0.32} _{-0.20}	0.37±0.13	14±1.3	No
OBS 029	8	241 ⁺⁹³ ₋₁₄	0.34 ^{+0.09} _{-0.02}	0.13 ^{+0.10} _{-0.02}	0.24±0.10	12±0.7	No
OBS 030	16	304 ⁺⁶³ ₋₃₃	0.51 ^{+0.07} _{-0.04}	0.43 ^{+0.18} _{-0.09}	0.22±0.11	12±1.3	No
OBS 031 ^{XBS37}	17	335 ⁺⁵¹ ₋₂₇	0.52 ^{+0.05} _{-0.03}	0.44 ^{+0.14} _{-0.08}	0.51±0.17	21±0.9	Yes
OBS 032	8	642 ⁺¹⁷⁷ ₋₁₇	0.69 ^{+0.13} _{-0.02}	1.04 ^{+0.58} _{-0.08}	0.92±0.23	32±1.1	Yes

Table F.1 (cont'd)

Name	N_σ	σ_{gr} (km s ⁻¹)	R_{500} (Mpc)	M_{500} (10 ¹⁴ M _⊙)	L_{opt} (10 ¹² L _⊙)	N_{gals}	Structure
OBS 034	11	278 ⁺¹⁰⁴ ₋₄₆	0.38 ^{+0.10} _{-0.04}	0.19 ^{+0.14} _{-0.06}	0.23±0.10	14±0.4	Yes
OBS 036	13	362 ⁺⁶⁸ ₋₃₂	0.49 ^{+0.06} _{-0.03}	0.38 ^{+0.15} _{-0.08}	0.06±0.06	9±1.6	No
OBS 038	11	314 ⁺¹⁴⁹ ₋₈₃	0.56 ^{+0.18} _{-0.10}	0.59 ^{+0.57} _{-0.32}	0.51±0.18	18±1.5	No
OBS 040	13	388 ⁺¹²⁰ ₋₆₃	0.60 ^{+0.12} _{-0.07}	0.74 ^{+0.46} _{-0.25}	0.38±0.15	17±2.3	No
OBS 041	26	288 ⁺⁵⁷ ₋₂₉	0.48 ^{+0.06} _{-0.03}	0.36 ^{+0.14} _{-0.08}	0.20±0.10	10±1.1	No
OBS 042 ^{XBS17}	49	615 ⁺⁶⁶ ₋₄₉	0.85 ^{+0.06} _{-0.05}	2.14 ^{+0.46} _{-0.35}	1.40±0.27	59±2.2	No
OBS 043	12	277 ⁺¹⁰² ₋₅₈	0.45 ^{+0.12} _{-0.07}	0.32 ^{+0.26} _{-0.14}	0.24±0.14	7±1.0	Yes
OBS 044	8	362 ⁺¹⁰⁴ ₋₆₃	0.64 ^{+0.12} _{-0.08}	0.89 ^{+0.52} _{-0.32}	0.15±0.10	8±1.9	No
OBS 046	11	328 ⁺⁸³ ₋₄₁	0.49 ^{+0.08} _{-0.04}	0.40 ^{+0.20} _{-0.10}	0.18±0.11	6±1.7	No
OBS 047	17	512 ⁺¹¹⁸ ₋₅₉	0.71 ^{+0.11} _{-0.06}	1.24 ^{+0.58} _{-0.30}	0.62±0.17	30±3.9	No
OBS 048	21	388 ⁺⁷⁷ ₋₅₇	0.71 ^{+0.09} _{-0.07}	1.21 ^{+0.48} _{-0.36}	0.57±0.18	27±3.6	No
OBS 049 ^{XBS25}	11	377 ⁺⁸⁹ ₋₃₀	0.55 ^{+0.09} _{-0.03}	0.58 ^{+0.28} _{-0.10}	0.35±0.14	13±1.2	No

Table F.1 (cont'd)

Name	N_σ	σ_{gr} (km s ⁻¹)	R_{500} (Mpc)	M_{500} (10 ¹⁴ M _⊙)	L_{opt} (10 ¹² L _⊙)	N_{gals}	Structure
OBS 050	6	213 ⁺⁶⁴ ₋₂₄	0.41 ^{+0.09} _{-0.03}	0.24 ^{+0.15} _{-0.06}	0.07±0.06	6±0.8	No
OBS 051 ^{XBS02}	17	184 ⁺⁶⁰ ₋₂₅	0.32 ^{+0.07} _{-0.03}	0.12 ^{+0.08} _{-0.03}	0.28±0.11	15±0.8	Yes
OBS 052	5	244 ⁺⁹⁵ ₋₃₀	0.47 ^{+0.12} _{-0.04}	0.36 ^{+0.28} _{-0.09}	0.52±0.20	20±1.8	No
OBS 053	5	145 ⁺⁴⁴ ₋₁₄₁	0.32 ^{+0.08} _{-0.21}	0.11 ^{+0.08} _{-0.22}	0.37±0.14	13±0.5	No
OBS 054	14	440 ⁺⁸⁸ ₋₄₄	0.59 ^{+0.08} _{-0.04}	0.72 ^{+0.29} _{-0.15}	0.71±0.18	32±1.1	Yes
OBS 055	14	439 ⁺¹²³ ₋₅₆	0.52 ^{+0.10} _{-0.05}	0.50 ^{+0.28} _{-0.13}	0.41±0.15	24±1.8	No
OBS 056 ^{XBS11}	22	417 ⁺⁶⁹ ₋₃₇	0.58 ^{+0.06} _{-0.04}	0.70 ^{+0.23} _{-0.13}	0.74±0.22	23±2.1	Yes
OBS 057	11	246 ⁺⁵⁸ ₋₃₇	0.49 ^{+0.08} _{-0.05}	0.40 ^{+0.20} _{-0.13}	0.55±0.17	26±2.1	No
OBS 060	7	426 ⁺¹⁴⁹ ₋₆₇	0.73 ^{+0.17} _{-0.08}	1.41 ^{+1.00} _{-0.48}	0.96±0.26	38±3.4	No
OBS 062	13	324 ⁺⁸⁵ ₋₄₁	0.52 ^{+0.09} _{-0.04}	0.49 ^{+0.26} _{-0.13}	0.31±0.12	22±1.6	No
OBS 064	5	90 ⁺³⁴ ₋₁₆	0.15 ^{+0.04} _{-0.02}	0.01 ^{+0.01} _{0.00}	0.02±0.02	3±0.2	No
OBS 065	21	935 ⁺¹⁰⁵ ₋₈₇	1.20 ^{+0.09} _{-0.08}	6.08 ^{+1.44} _{-1.17}	0.81±0.26	36±11.4	No

Table F.1 (cont'd)

Name	N_σ	σ_{gr} (km s ⁻¹)	R_{500} (Mpc)	M_{500} (10 ¹⁴ M _⊙)	L_{opt} (10 ¹² L _⊙)	N_{gals}	Structure
OBS 066	5	589 ⁺²¹⁹ ₋₁₂₀	0.79 ^{+0.20} _{-0.12}	1.70 ^{+1.26} _{-0.78}	0.44±0.16	19±2.0	No
OBS 068	7	277 ⁺¹⁰⁵ ₋₆₄	0.39 ^{+0.10} _{-0.06}	0.22 ^{+0.17} _{-0.11}	0.21±0.08	13±0.7	No
OBS 069	8	486 ⁺¹⁰⁰ ₋₄₈	0.54 ^{+0.08} _{-0.04}	0.58 ^{+0.26} _{-0.13}	0.08±0.08	9±2.0	Yes
OBS 076	8	264 ⁺⁹⁰ ₋₄₅	0.36 ^{+0.09} _{-0.05}	0.17 ^{+0.12} _{-0.07}	0.15±0.13	7±1.3	No
OBS 077	12	544 ⁺⁹¹ ₋₅₂	0.84 ^{+0.10} _{-0.06}	2.13 ^{+0.76} _{-0.48}	1.59±0.33	46±5.3	No
OBS 082	5	181 ⁺¹⁹⁹ ₋₂₈	0.34 ^{+0.27} _{-0.05}	0.15 ^{+0.35} _{-0.06}	0.17±0.09	10±0.9	No
OBS 088 ^{XBS36}	6	111 ⁺⁷⁴ ₋₃₉	0.23 ^{+0.10} _{-0.05}	0.04 ^{+0.06} _{-0.03}	0.23±0.08	14±0.1	No
OBS 089	6	254 ⁺¹⁴⁴ ₋₈₂	0.41 ^{+0.16} _{-0.09}	0.26 ^{+0.30} _{-0.17}	0.42±0.15	20±0.8	No
OBS 093	7	360 ⁺¹⁸⁸ ₋₁₅	0.40 ^{+0.14} _{-0.02}	0.25 ^{+0.26} _{-0.04}	0.46±0.15	16±1.4	No
OBS 094	6	262 ⁺⁹² ₋₄₁	0.39 ^{+0.09} _{-0.05}	0.23 ^{+0.16} _{-0.09}	0.64±0.21	20±1.6	No
OBS 099	14	303 ⁺⁶⁴ ₋₃₀	0.39 ^{+0.06} _{-0.03}	0.24 ^{+0.10} _{-0.06}	0.82±0.22	28±1.6	No
OBS 104	10	395 ⁺⁸⁸ ₋₃₇	0.55 ^{+0.08} _{-0.04}	0.66 ^{+0.30} _{-0.14}	0.84±0.26	29±2.9	No

Table F.1 (cont'd)

Name	N_σ	σ_{gr} (km s ⁻¹)	R_{500} (Mpc)	M_{500} (10 ¹⁴ M _⊙)	L_{opt} (10 ¹² L _⊙)	N_{gals}	Structure
OBS 105	15	547 ⁺¹¹⁰ ₋₆₁	0.77 ^{+0.10} _{-0.06}	1.83 ^{+0.74} _{-0.43}	0.75±0.21	35±5.3	No
OBS 106	9	227 ⁺⁶⁹ ₋₃₇	0.32 ^{+0.07} _{-0.05}	0.13 ^{+0.08} _{-0.06}	-10.00±0.03	3±0.9	No
OBS 107	9	264 ⁺⁷⁵ ₋₃₁	0.36 ^{+0.07} _{-0.04}	0.19 ^{+0.11} _{-0.06}	0.81±0.25	19±1.7	No
OBS 109	8	509 ⁺¹²⁰ ₋₅₃	0.58 ^{+0.10} _{-0.04}	0.80 ^{+0.40} _{-0.18}	0.93±0.27	25±3.0	Yes
OBS 113	7	409 ⁺¹³⁵ ₋₃₇	0.56 ^{+0.13} _{-0.06}	0.71 ^{+0.48} _{-0.23}	0.98±0.26	32±2.5	No
OBS 116	10	643 ⁺¹⁹⁷ ₋₄₅	0.76 ^{+0.16} _{-0.04}	1.72 ^{+1.07} _{-0.29}	1.16±0.31	40±5.4	No
OBS 119 ^{XBS33}	14	144 ⁺⁴¹ ₋₁₈	0.38 ^{+0.07} _{-0.03}	0.22 ^{+0.13} _{-0.06}	0.94±0.22	34±0.8	No

Appendix G

X-ray Selected Galaxy Group Catalog - X-ray Properties

In this appendix, we list the X-ray properties for the 31 X-ray selected groups with determined redshift. Table G.1 contains: the group name; the bolometric X-ray luminosity inside 0.5 Mpc aperture (L_X^{bol}); X-ray temperature (T_X); the core radius (r_{c_i}); β slope and the central surface brightness (S_0).

Table G.1. X-ray Properties Inside 0.5 Mpc

Name	L_X^{bol} (10^{42} ergs s^{-1})	T_X (keV)	r_c (kpc)	β	S_0 (counts/kpc)
XBS02	9.35±2.13	0.82±1.38	35.07±4.75	0.61±0.08	0.0027±0.0004
XBS04	156.00±70.20	—	—	—	—
XBS05	14.00±4.85	—	—	—	—
XBS06	300.65±1.12	3.53±0.69	143.28±3.22	0.76±0.02	0.0255±0.0006
XBS07	0.48±0.89	0.66±0.05	—	—	—
XBS08	1.14±0.17	—	—	—	—
XBS09	6.38±1.11	—	57.40±28.36	0.51±0.25	0.0008±0.0004
XBS11	23.53±11.64	1.99±0.55	67.58±9.80	0.48±0.07	0.0087±0.0013
XBS13	71.18±0.51	2.18±0.54	22.05±1.79	0.43±0.03	0.0366±0.0030
XBS14	49.17±9.53	—	—	—	—
XBS17	13.86±4.02	—	89.40±14.39	0.40±0.06	0.0010±0.0002
XBS18	22.20±1.22	3.37±0.23	28.38±18.87	0.48±0.32	0.0873±0.0581
XBS20	16.40±8.25	1.36±0.20	64.20±11.24	0.59±0.10	0.0106±0.0019
XBS22	39.91±7.74	—	—	—	—
XBS25	11.75±2.78	—	—	—	—
XBS26	1.99±0.62	—	—	—	—
XBS27	106.10±9.5	3.63±0.74	95.37±44.82	0.94±0.44	0.0161±0.0076
XBS28	111.07±12.91	—	—	—	—
XBS29	8.76±26.60	—	—	—	—
XBS32	113.87±30.51	—	—	—	—
XBS33	52.73±12.75	—	—	—	—
XBS35	0.53±0.08	—	—	—	—
XBS36	4.40±6.82	—	—	—	—
XBS37	7.97±1.29	—	—	—	—

Table G.1 (cont'd)

Name	L_X^{bol} (10^{42} ergs s^{-1})	T_X (keV)	r_c (kpc)	β	S_0 (counts/kpc)
XBS38	48.90 ± 11.39	—	—	—	—
XBS39	24.96 ± 6.45	—	—	—	—
XBS41	25.47 ± 4.07	4.02 ± 1.08	109.75 ± 85.61	0.48 ± 0.37	0.0039 ± 0.0030
XBS42	21.03 ± 4.66	—	40.11 ± 2.85	0.81 ± 0.06	0.0061 ± 0.0004
XBS43	82.50 ± 17.24	—	—	—	—
XBS46	6.15 ± 1.99	—	—	—	—
XBS52	35.09 ± 26.02	—	—	—	—

Appendix H

Optically Selected Galaxy Group Catalog - X-ray Properties

In this appendix, we list the X-ray properties for the 162 optically selected groups with determined redshift. Table G.1 contains: the group name; the bolometric X-ray luminosity inside 0.5 Mpc aperture (L_X^{bol}); X-ray temperature (T_X); the core radius (r_c); β slope; the central surface brightness (S_0) and the emission classification.

Table H.1. X-ray Properties Inside 0.5 Mpc

Name	L_X^{bol} (10^{42} ergs s^{-1})	T_X (keV)	r_c (kpc)	β	S_0 (counts/kpc)	Emission
OBS 001	0.93±0.02	—	—	—	—	Reliable
OBS 002	—	—	—	—	—	No Emission
OBS 003	0.71±0.01	—	—	—	—	Reliable
OBS 004	1.18±0.03	—	—	—	—	Reliable
OBS 005	3.10±0.06	—	—	—	—	Reliable
OBS 006	<3.09	—	—	—	—	Upper Limit
OBS 007	—	—	—	—	—	No Emission
OBS 008	<0.52	—	—	—	—	Upper Limit
OBS 009	<3.79	—	—	—	—	Upper Limit
OBS 010	<3.04	—	—	—	—	Upper Limit
OBS 011	6.78±0.29	—	—	—	—	Reliable
OBS 012	—	—	—	—	—	No Emission
OBS 013	2.40±0.25	—	—	—	—	Reliable
OBS 014	—	—	—	—	—	No Emission
OBS 015 ^{XBS06}	30.65±1.12	3.53±0.69	143.28±3.22	0.76±0.02	0.0255±0.0006	Reliable
OBS 016	—	—	—	—	—	No Emission

Table H.1 (cont'd)

Name	L_X^{bol} (10^{42} ergs s^{-1})	T_X (keV)	r_c (kpc)	β	S_0 (counts/kpc)	Emission
OBS 017	4.37 ± 0.33	—	—	—	—	Reliable
OBS 018 ^{XBS13}	71.18 ± 0.51	2.18 ± 0.54	22.05 ± 1.79	0.43 ± 0.03	0.0366 ± 0.0030	Reliable
OBS 019	3.35 ± 0.24	—	—	—	—	Reliable
OBS 020	6.30 ± 0.44	—	—	—	—	Reliable
OBS 021	6.31 ± 0.36	—	—	—	—	Reliable
OBS 022	6.31 ± 0.47	—	—	—	—	Reliable
OBS 023	3.03 ± 0.20	—	—	—	—	Reliable
OBS 024	3.86 ± 0.25	—	—	—	—	Reliable
OBS 025	—	—	—	—	—	No Emission
OBS 026	< 2.38	—	—	—	—	Upper Limit
OBS 027	4.59 ± 0.36	—	—	—	—	Reliable
OBS 028	< 3.26	—	—	—	—	Upper Limit
OBS 029	—	—	—	—	—	No Emission
OBS 030	5.45 ± 0.42	—	—	—	—	Reliable
OBS 031 ^{XBS37}	7.97 ± 1.29	—	—	—	—	Reliable
OBS 032	16.81 ± 0.86	—	—	—	—	Reliable

Table H.1 (cont'd)

Name	L_X^{bol} (10^{42} ergs s^{-1})	T_X (keV)	r_c (kpc)	β	S_0 (counts/kpc)	Emission
OBS 033	—	—	—	—	—	No Emission
OBS 034	<2.33	—	52.06±17.24	0.27±0.09	0.0010±0.0003	Upper Limit
OBS 035	—	—	—	—	—	No Emission
OBS 036	4.92±0.44	—	—	—	—	Reliable
OBS 037	<5.01	—	—	—	—	Upper Limit
OBS 038	<5.09	—	—	—	—	Upper Limit
OBS 039	—	—	—	—	—	No Emission
OBS 040	—	—	—	—	—	No Emission
OBS 041	—	—	—	—	—	No Emission
OBS 042 ^{XBS17}	13.86±4.02	—	89.40±14.39	0.40±0.06	0.0010±0.0002	Reliable
OBS 043	—	—	—	—	—	No Emission
OBS 044	3.76±0.35	—	—	—	—	Reliable
OBS 045	3.20±0.29	—	—	—	—	Reliable
OBS 046	—	—	—	—	—	No Emission
OBS 047	—	—	—	—	—	No Emission
OBS 048	—	—	—	—	—	No Emission

Table H.1 (cont'd)

Name	L_X^{bol} (10^{42} ergs s^{-1})	T_X (keV)	r_c (kpc)	β	S_0 (counts/kpc)	Emission
OBS 049 ^{XBS25}	11.75±2.78	—	—	—	—	Reliable
OBS 050	3.94±0.39	—	—	—	—	Reliable
OBS 051 ^{XBS02}	9.35±2.13	0.82±1.38	35.07±4.75	0.61±0.08	0.0027±0.0004	Reliable
OBS 052	—	—	—	—	—	No Emission
OBS 053	4.17±0.45	—	—	—	—	Reliable
OBS 054	12.62±1.16	—	—	—	—	Reliable
OBS 055	<2.71	—	—	—	—	Upper Limit
OBS 056 ^{XBS11}	23.53±11.64	1.99±0.55	67.58±9.80	0.48±0.07	0.0087±0.0013	Reliable
OBS 057	—	—	—	—	—	No Emission
OBS 058	—	—	—	—	—	No Emission
OBS 059	—	—	—	—	—	No Emission
OBS 060	—	—	—	—	—	No Emission
OBS 061	<2.87	—	—	—	—	Upper Limit
OBS 062	<3.71	—	—	—	—	Upper Limit
OBS 063	—	—	—	—	—	No Emission
OBS 064	—	—	—	—	—	No Emission

Table H.1 (cont'd)

Name	L_X^{bol} (10^{42} ergs s^{-1})	T_X (keV)	r_c (kpc)	β	S_0 (counts/kpc)	Emission
OBS 065	4.13±0.46	—	—	—	—	Reliable
OBS 066	—	—	—	—	—	No Emission
OBS 067	8.09±0.90	—	—	—	—	Reliable
OBS 068	7.68±0.96	—	—	—	—	Reliable
OBS 069	26.14±2.16	—	50.48±14.62	0.34±0.10	0.0055±0.0016	Reliable
OBS 070	—	—	—	—	—	No Emission
OBS 071	5.05±0.65	—	—	—	—	Reliable
OBS 072	4.58±0.59	—	—	—	—	Reliable
OBS 073	3.43±0.49	—	—	—	—	Reliable
OBS 074	—	—	—	—	—	No Emission
OBS 075	—	—	—	—	—	No Emission
OBS 076	—	—	—	—	—	No Emission
OBS 077	<5.36	—	—	—	—	Upper Limit
OBS 078	—	—	—	—	—	No Emission
OBS 079	—	—	—	—	—	No Emission
OBS 080	5.18±0.76	—	—	—	—	Reliable

Table H.1 (cont'd)

Name	L_X^{bol} (10^{42} ergs s^{-1})	T_X (keV)	r_c (kpc)	β	S_0 (counts/kpc)	Emission
OBS 081	—	—	—	—	—	No Emission
OBS 082	—	—	—	—	—	No Emission
OBS 083	<3.59	—	—	—	—	Upper Limit
OBS 084	—	—	—	—	—	No Emission
OBS 085	4.93 ± 0.56	—	—	—	—	Reliable
OBS 086	5.75 ± 0.73	—	—	—	—	Reliable
OBS 087	—	—	—	—	—	No Emission
OBS 088 ^{XBS36}	4.40 ± 6.82	—	—	—	—	Reliable
OBS 089	—	—	—	—	—	No Emission
OBS 090	—	—	—	—	—	No Emission
OBS 091	19.67 ± 2.21	—	—	—	—	Reliable
OBS 092	—	—	—	—	—	No Emission
OBS 093	<3.92	—	—	—	—	Upper Limit
OBS 094	—	—	—	—	—	No Emission
OBS 095	6.60 ± 0.81	—	—	—	—	Reliable
OBS 096	8.48 ± 1.31	—	—	—	—	Reliable

Table H.1 (cont'd)

Name	L_X^{bol} (10^{42} ergs s^{-1})	T_X (keV)	r_c (kpc)	β	S_0 (counts/kpc)	Emission
OBS 097	—	—	—	—	—	No Emission
OBS 098	—	—	—	—	—	No Emission
OBS 099	<4.17	—	67.68 ± 22.26	0.45 ± 0.15	0.0044 ± 0.0015	Upper Limit
OBS 100	—	—	—	—	—	No Emission
OBS 101	—	—	—	—	—	No Emission
OBS 102	—	—	—	—	—	No Emission
OBS 103	<5.68	—	—	—	—	Upper Limit
OBS 104	—	—	—	—	—	No Emission
OBS 105	9.51 ± 1.27	—	—	—	—	Reliable
OBS 106	5.10 ± 0.84	—	—	—	—	Reliable
OBS 107	—	—	—	—	—	No Emission
OBS 108	—	—	—	—	—	No Emission
OBS 109	6.17 ± 0.86	—	—	—	—	Reliable
OBS 110	—	—	—	—	—	No Emission
OBS 111 ^{XBS20}	16.40 ± 8.25	1.36 ± 0.20	64.20 ± 11.24	0.59 ± 0.10	0.0106 ± 0.0019	Reliable
OBS 112	8.72 ± 1.31	—	—	—	—	Reliable

Table H.1 (cont'd)

Name	L_X^{bol} (10^{42} ergs s^{-1})	T_X (keV)	r_c (kpc)	β	S_0 (counts/kpc)	Emission
OBS 113	—	—	—	—	—	No Emission
OBS 114	—	—	—	—	—	No Emission
OBS 115	<7.89	—	—	—	—	Upper Limit
OBS 116	—	—	—	—	—	No Emission
OBS 117	15.00±2.21	—	—	—	—	Reliable
OBS 118	—	—	—	—	—	No Emission
OBS 119 ^{XBS33}	52.73±12.75	—	—	—	—	Reliable
OBS 120	—	—	—	—	—	No Emission
OBS 121	13.32±2.16	—	—	—	—	Reliable
OBS 122	8.55±1.42	—	—	—	—	Reliable
OBS 123	—	—	—	—	—	No Emission
OBS 124	7.10±1.22	—	—	—	—	Reliable
OBS 125	—	—	—	—	—	No Emission
OBS 126	—	—	—	—	—	No Emission
OBS 127	—	—	—	—	—	No Emission
OBS 128	17.98±2.40	—	—	—	—	Reliable

Table H.1 (cont'd)

Name	L_X^{bol} (10^{42} ergs s^{-1})	T_X (keV)	r_c (kpc)	β	S_0 (counts/kpc)	Emission
OBS 129	18.97±2.83	—	—	—	—	Reliable
OBS 130	<3.00	—	—	—	—	Upper Limit
OBS 131	<7.47	—	—	—	—	Upper Limit
OBS 132	—	—	—	—	—	No Emission
OBS 133	37.63±4.90	—	—	—	—	Reliable
OBS 134	—	—	—	—	—	No Emission
OBS 135	—	—	—	—	—	No Emission
OBS 136	23.09±4.36	—	—	—	—	Reliable
OBS 137	<9.28	—	—	—	—	Upper Limit
OBS 138	91.00±9.38	—	—	—	—	Reliable
OBS 139	<4.27	—	—	—	—	Upper Limit
OBS 140	—	—	—	—	—	No Emission
OBS 141	—	—	—	—	—	No Emission
OBS 142	—	—	—	—	—	No Emission
OBS 143	<5.66	—	—	—	—	Upper Limit
OBS 144	20.80±2.83	—	—	—	—	Reliable

Table H.1 (cont'd)

Name	L_X^{bol} (10^{42} ergs s $^{-1}$)	T_X (keV)	r_c (kpc)	β	S_0 (counts/kpc)	Emission
OBS 145	—	—	—	—	—	No Emission
OBS 146	<4.82	—	—	—	—	Upper Limit
OBS 147	—	—	—	—	—	No Emission
OBS 148	—	—	—	—	—	No Emission
OBS 149	—	—	—	—	—	No Emission
OBS 150	—	—	—	—	—	No Emission
OBS 151	—	—	—	—	—	No Emission
OBS 152	—	—	—	—	—	No Emission
OBS 153	—	—	—	—	—	No Emission
OBS 154	—	—	—	—	—	No Emission
OBS 155	—	—	—	—	—	No Emission
OBS 156	73.92±10.35	—	55.90±38.76	0.84±0.58	0.0063±0.0044	Reliable
OBS 157	51.89±7.82	—	—	—	—	Reliable
OBS 158	—	—	—	—	—	No Emission
OBS 159 ^{XBS38}	48.90±11.39	—	—	—	—	Reliable
OBS 160	—	—	—	—	—	No Emission

Table H.1 (cont'd)

Name	L_X^{bol} (10^{42} ergs s^{-1})	T_X (keV)	r_c (kpc)	β	S_0 (counts/kpc)	Emission
OBS 161	—	—	—	—	—	No Emission
OBS 162	37.99 ± 8.10	—	—	—	—	Reliable